



HYPERSPECTRAL IMAGING FOR DETECTION OF CORROSION ON INTERMEDIATE LEVEL NUCLEAR WASTE CONTAINERS

by

WILLIAM GEORGE ROWLEY

A thesis submitted to the University of Birmingham for the degree of
DOCTOR OF PHILOSOPHY

School of Metallurgy and Materials
College of Engineering and Physical Sciences
University of Birmingham
September 2018

UNIVERSITY OF
BIRMINGHAM

University of Birmingham Research Archive

e-theses repository

This unpublished thesis/dissertation is copyright of the author and/or third parties. The intellectual property rights of the author or third parties in respect of this work are as defined by The Copyright Designs and Patents Act 1988 or as modified by any successor legislation.

Any use made of information contained in this thesis/dissertation must be in accordance with that legislation and must be properly acknowledged. Further distribution or reproduction in any format is prohibited without the permission of the copyright holder.

ABSTRACT

Intermediate level nuclear waste (ILW) will be stored above ground in 304L stainless steel (SS) containers for the next 100 years. During this period, the containers need to be monitored for atmospheric pitting corrosion - a known precursor of atmospherically induced stress corrosion cracking. Hyperspectral (HS) and optical imaging of pitting corrosion products from droplet experiments have been investigated towards developing a system for long term monitoring of atmospheric pitting corrosion of stainless steel containers in ILW stores.

Common corrosion products were first identified via Raman spectroscopic mapping as akaganeite (β -FeOOH) and lepidocrocite (γ -FeOOH), with a secondary presence of layered double hydroxide (green rust).

HS and optical methods were then compared for their efficacy at rust detection. Whilst it was not possible to identify specific corrosion species using HS imaging, HS images of rust under pitted droplets provided better contrast with the background steel than colour photography due to species having lower absorbance than the near infrared (850 nm) than red (650 nm).

Finally, the relationship between rust area and pit volume was determined by comparing colour photography (rust area) with confocal laser scanning microscopy (pit volume). A good correlation was present for samples exposed to a fixed relative humidity (RH) for MgCl₂ droplets and CaCl₂ droplets with small pit volumes. Poor correlation was found for samples exposed to natural fluctuations in RH. It was concluded that optical methods are viable for the detection of rust, but less effective for quantification of pit volumes.

Dedicated to my family and friends

*Two roads diverged in a yellow wood,
And sorry I could not travel both
And be one traveler, long I stood
And looked down one as far as I could
To where it bent in the undergrowth;*

*Then took the other, as just as fair,
And having perhaps the better claim,
Because it was grassy and wanted wear;
Though as for that the passing there
Had worn them really about the same,*

*And both that morning equally lay
In leaves no step had trodden black.
Oh I kept the first for another day!
Yet knowing how way leads on to way,
I doubted if I should ever come back.*

*I shall be telling this with a sigh
Somewhere ages and ages hence:
Two roads diverged in a wood, and I-
I took the one less traveled by,
And that has made all the difference*

-‘The Road not Taken’, Robert Frost[1]

ACKNOWLEDGEMENTS

I owe thanks to the advice and support of a great many people, without whom this project would not have been possible:

First and foremost my supervisors Professor Alison Davenport, whose guidance, support and patience have been limitless during the course of this project.

Secondly, my supervisor Professor Hamid Dehghani, his insight and experience have been invaluable for the imaging sections of this project.

I would also like to thank the Nuclear Decommissioning Authority for making this project possible and my industrial supervisor David Hambley from NNL for much productive discussion and the perspective of industry.

To my friends and colleagues Steven, Angus, Sarah, Haval, Flaviu, Rowena, Sophie, Qi and Berenika in Metallurgy and Materials and Sophie in Computer Science who I've had the fortune to call on for many hours of productive discussion

Last but not least I'd like to thank my friends and family for their unwavering support and encouragement over these past few years.

Table of Contents

1. INTRODUCTION	1
2. LITERATURE REVIEW	3
2.1 Interim storage of intermediate level nuclear waste	3
2.1.1 Overview	3
2.1.2 Conditions within waste stores	4
2.1.3 Temperature and humidity	4
2.1.4 Aerosol deposition	5
2.2 Stainless Steel	6
2.3 Corrosion	7
2.3.1 Overview	7
2.3.2 Passivity	8
2.3.3 Pitting corrosion of stainless steel	8
2.3.4 Atmospheric pitting corrosion	11
2.3.5 Atmospherically induced stress corrosion cracking	16
2.4 Corrosion products of iron	17
2.4.1 Formation and transformation of the iron oxides	18
2.4.2 Characterisation of iron oxides and oxide-hydroxides	20
2.4.3 Atmospheric corrosion products of iron alloys	21
2.4.4 Corrosion products of stainless steel	22
2.5 Corrosion detection and monitoring	23
2.5.1 Principles of imaging and spectroscopy	24

2.5.2	Hyperspectral imaging.....	26
2.5.3	Image analysis	28
2.6	Summary	32
3.	Methodology.....	33
3.1	Droplet experiments.....	33
3.1.1	Materials and sample preparation	33
3.1.2	Solution preparation	34
3.1.3	Droplet deposition	35
3.1.4	Exposure to fixed environmental conditions	36
3.1.5	Exposure to fluctuating ambient environmental conditions.....	37
3.2	Photography	38
3.3	Iron oxide syntheses	39
3.4	Characterisation and Spectroscopy	40
3.4.1	X-ray diffraction	40
3.4.2	UV-VIS-NIR spectroscopy.....	40
3.4.3	Fourier-Transform Infra-Red (FTIR) spectroscopy	41
3.4.4	Raman Spectroscopy	42
3.5	UV-VIS-NIR Hyperspectral Imaging.....	44
3.5.1	Hyperspectral instrument hardware, motion control and data acquisition	44
3.5.2	Characterisation of UV-VIS hyperspectral imaging system	47

3.6	Rust area analysis	57
3.6.1	Red-Blue colour channel subtraction.....	58
3.6.2	Principal component analysis	58
3.6.3	HSV thresholding	58
3.6.4	L*a*b* thresholding.....	59
3.7	Confocal microscopy for pit volume measurement	60
4.	CHARACTERISATION OF CORROSION PRODUCTS OF 304L STAINLESS STEEL USING COLOUR PHOTOGRAPHY AND RAMAN SPECTROSCOPY	61
4.1	Introduction	61
4.2	Results.....	63
4.2.1	Synthesised Iron Oxides and oxide-hydroxides	63
4.2.2	Droplet Experiments.....	70
4.2.3	Exposure conditions for fluctuating ambient droplets	89
4.3	Discussion	93
4.3.1	Identification and assignment of compounds	93
4.3.2	Distribution of compounds by cation.....	95
4.3.3	Distribution of compounds over time	96
4.3.4	Distribution of compounds by chloride deposition density	96
4.4	Conclusions	97
5.	EVALUATION OF HYPERSPECTRAL METHODS.....	99
5.1	Introduction	99
5.2	Results.....	100

5.2.1	UV-VIS-NIR for iron oxide phase identification.....	100
5.2.2	Comparison of techniques for area quantification	116
5.3	Discussion	122
5.3.1	Iron oxide phase identification using UV-VIS-NIR imaging.....	122
5.3.2	Techniques for area quantification/Image analysis.....	126
5.4	Conclusions	129
6.	ASSESSMENT OF PIT VOLUME WITH RESPECT TO VISIBLE RUST AREA	131
6.1	Introduction	131
6.2	Results.....	133
6.2.1	Measurement of Pit Volume via confocal laser scanning microscopy	135
6.2.2	Estimating error in pit volume due to user controlled parameters	143
6.2.3	Determination of threshold for Red-Blue colour channel subtraction method	145
6.2.4	Determination of threshold for principal component analysis method	147
6.2.5	Determination of threshold for HSV thresholding method	149
6.2.6	Determination of threshold for L*a*b* thresholding method.....	151
6.2.7	Rust area vs. pit volume.....	155
6.2.8	Ambient exposure conditions	163
6.3	Discussion	164

6.3.1	Pit volume measurements	164
6.3.2	Rust area measurement	165
6.3.3	Pit volume rust area comparison	167
6.4	Conclusions	169
7.	GENERAL DISCUSSION	171
7.1	Limitations	173
8.	GENERAL CONCLUSIONS	174
9.	FUTURE WORK	176
10.	REFERENCES	178
11.	APPENDIX	187
11.1	Mill certificate – 304L stainless steel	187
11.2	Powdered iron oxide standard synthesis	188
11.3	Matlab script – Raman averaging	191
11.3.1	Main file - Spectral averaging	191
11.3.2	Dependency – import csv spectral from directory	193
11.4	Matlab scripts – Hyperspectral image processing	194
11.4.1	Principal component analysis	194
11.5	Matlab scripts – Image processing	195
11.5.1	Acquire rust area by Red-Blue colour channel subtraction	195
11.5.2	Acquire rust area by principal component analysis	197
11.5.3	Acquire rust area by HSV thresholding	199
11.5.4	Rust area analysis by L*a*b* thresholding	200
11.5.5	Supplemental figures (Chapter 6)	203

TABLE OF SYMBOLS AND ABBREVIATIONS

Abbreviations

AISCC	Atmospherically-induced stress corrosion cracking
ASTM	American society for testing materials
CDD	Chloride deposition density
CCD	Charge coupled device
CMOS	Complementary metal oxide semiconductor
DI	Deionised
DSLR	Digital single lens reflex
GDF	Geological disposal facility
ILW	Intermediate level nuclear waste
NDA	Nuclear decommissioning authority
RH	Relative humidity
UV	Ultraviolet
VIS	Visible
NIR	Near infra-red
XRD	X-Ray diffraction
FTIR	Fourier transform infra red
HSV	Hue saturation value
IAEA	International atomic energy agency

Symbols and units

nm	nanometers
µm	micrometers
cm	centimeters
M	molar

1. INTRODUCTION

The UK's Nuclear Decommissioning Authority (NDA) estimates that it will have to dispose of 286,000m³ of intermediate level nuclear waste.[2] This includes legacy waste from previous nuclear projects as well as a projection of waste produced from future commitments. The current long term disposal plan favoured by both the UK NDA and the International Atomic Energy Agency (IAEA) is internment in a geological disposal in facility (GDF) deep underground. This will require many years to plan and implement.

As no deep GDF yet exists, waste will remain above ground, stored in warehouses for a significant interim period while a site is selected and prepared. During this period the containers housing the waste may be susceptible to atmospheric corrosion. The containers are constructed of stainless steel which displays good resistance to general corrosion, but it is susceptible to localised corrosion known as pitting. Pitting corrosion does not significantly affect the structural integrity of the container, but has been identified as a precursor to atmospherically-induced stress corrosion cracking (AISCC) which might lead to loss of structural integrity when containers are moved to the GDF. It is therefore desirable to monitor the development of pitting corrosion as a precursor to AISCC. As established corrosion detection techniques rely on quantifying material loss, pitting is difficult to detect. Corrosion pitting attack leads to formation of a rust scale on the surface of the container, meaning optical detection methods are of interest.

Hyperspectral imaging is a well-established technique used to detect and quantify similar iron rich compounds in other fields [3-5], Hyperspectral imaging therefore presents a possible avenue for the remote sensing of the corrosion product that forms around pitting on stainless steel.

This project aims to investigate the applicability of hyperspectral imaging and conventional “RGB” colour imaging to monitor atmospheric pitting corrosion in stores. The overall aim of the project is to identify likely corrosion products, determine the optimum imaging method for quantifying visible rust, and then to use this method to determine the relationship between corrosion pit volume and visible rust.

2. LITERATURE REVIEW

2.1 Interim storage of intermediate level nuclear waste

2.1.1 Overview

Nuclear waste is separated into levels based on hazard and heat output as a measure of impact on repository design; the types are low, intermediate and high level waste. Intermediate level waste is radioactive, but does not produce heat in large enough quantities to require additional, specialist cooling. [2, 6]

The UK government's policy for long term disposal of this waste is in a large underground repository called a geological disposal facility (GDF). There will be an interim period of up to 100 years while the site of the GDF is selected, the facility is prepared and the waste is moved. During this time, the waste is to be immobilised in concrete and stored above ground in containers made of 316L and 304L stainless steel[2, 7]

During this period in above-ground storage, the containers will be susceptible to atmospheric pitting corrosion from gradual deposition and deliquescence of chloride salts from the atmosphere. While pitting is the expected mode of corrosion and not likely to affect the structural integrity of the container in itself, it is a known precursor of atmospherically-induced stress corrosion cracking (AISCC) which could compromise container integrity and complicate waste transfer to the GDF.[8]

2.1.2 Conditions within waste stores

The risk of occurrence of atmospheric corrosion is dependent on the local atmospheric conditions. The NDA has commissioned surveys to determine the environment that the waste containers will be exposed to until they are moved to the geological disposal facility.

2.1.3 Temperature and humidity

There are several current ILW stores located around the UK. Encapsulated product stores (EPS) 1 and 2, located at Sellafield are currently subject to environmental control aimed at reducing surface wetting of the containers from condensation, others are passively ventilated[9]. The conditions of stores under passive ventilation will be subject to local weather conditions although the shelter provided by the buildings will slow any rapid variations.

While present in interim storage the surface temperature of the containers expected to follow the trend of the local environment.[10] Temperature and humidity maximum and minimum values for a number of stores fluctuated between near-freezing and high room temperature (Table 1), with more precise time resolved data from Culham (Figure 1) indicating that conditions follow the seasons with higher humidity and lower temperature present in winter months.[9, 11-13]

Table 1 Summary of environmental conditions within some stores and stores analogues.[9, 11, 14]

Store	Monitoring Period		Temperature (°C)		Humidity (% RH)	
	Start	End	Min	Max	Min	Max
Culham[9]	Sep 1990	Aug 2008	1.71	25.3	19.5	100.0
Harwell[9]	Apr 2009	Jun 2010	2.35	18.10	32.03	100.00
Trawsfynydd[11]	Oct 2008	Oct 2009	8	18	55	98
Sellafield[11]	Jul 2001	May 2012	4	20	50	95
Winfrith[14]	May 2008	March 2011	1	24	21	94
Total Range	-	-	1	25.3	21	100

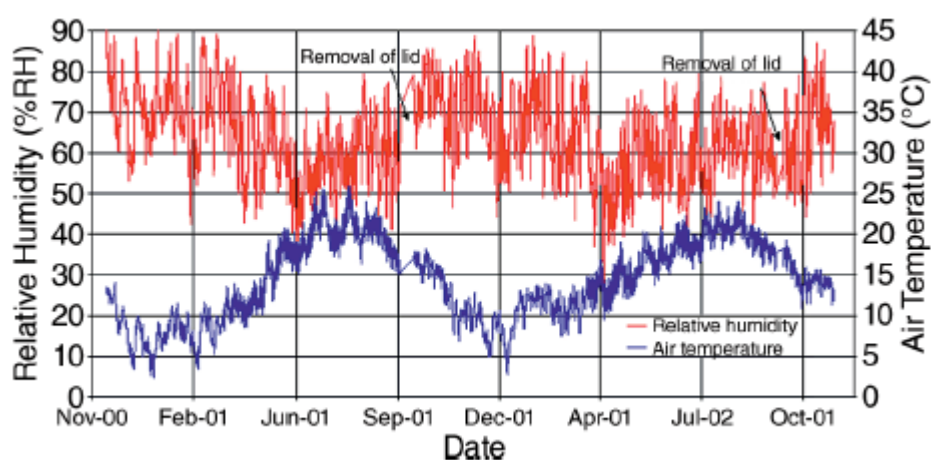


Figure 1 Temperature and humidity data from an inland warehouse in Culham, Oxfordshire for the period Nov '00 to Oct '02.[11]

2.1.4 Aerosol deposition

The composition of aerosol salts deposited on the exterior of containers will play a major role in the initiation and propagation of pitting corrosion as well as the composition and distribution of corrosion product distributed across the container surface. Swab analysis has been carried out on a number of sites in the UK, summarized in Table 2 with values of mass per unit area.[11]

Table 2 Summary of maximum surface concentrations of swab results across stores and a deep store analogue[11]

Anion surface concentration (μgcm^{-2})			Cation surface concentration (μgcm^{-2})		
Species	Surface Store	Deep Store	Species	Surface Store	Deep Store
F ⁻	0.711	2.131	Li ⁺	0.012	3.008
CH ₃ CO ₂ ⁻	3.715	5.553	Na ⁺	16.060	588.963
HCO ₂ ⁻	0.567	1.243	NH ₄ ⁺	0.618	4.794
Cl ⁻	22.296	1024.351	K ⁺	14.426	7.573
NO ₂ ⁻	0.159	0.675	Mg ²⁺	1.947	3.830
Br ⁻	0.030	0.456	Ca ²⁺	23.540	74.734
NO ₃ ⁻	10.819	47.299			
PO ₄ ⁻	0.254	-			
SO ₄ ⁻	25.618	154.342			
C ₂ O ₄ ⁻	1.788	15.803			

During salt swab testing of a 'dummy' container that had been exposed to stores relevant conditions for 12 years at Culham, a similar range and concentration of species were observed to those found in Table 2. [15] It was also observed that the box had a higher than expected concentration of chloride and metal species across the underside of the surface, attributed to road salt and particulate matter deposited during transit. Chloride deposition rates were assessed and estimated to range from 3.8 to 0.14 $\mu\text{g cm}^{-2} \text{yr}^{-1}$. [15, 16]

2.2 Stainless Steel

Table 3 Components of 304L and 316L stainless steel by weight[17, 18]

Type	%C	%Mn	%P	%S	%Si	%Cr	%Ni	%Mo	%N	%Fe
304L	0.03 max	2 max	0.045 max	0.03 max	0.075 max	18-20	8-12	0	0.1 max	balance
316L	0.03 max	2 max	0.045 max	0.03 max	0.075 max	16-18	10-14	2-3	0.1 max	balance

Stainless steel's corrosion resistance stems from the addition of a minimum of 10.5% chromium by weight[19], which forms a Cr-enriched 'passive film' upon

contact with the air[20]. This acts to protect the bulk metal from corrosive environments, increasing the resistance to uniform corrosion.[19] 304L and 316L are common austenitic stainless steel grades have a higher %wt of chromium, as outlined in Table 3. 316L is differentiated from 304L by the addition of 2-4%wt molybdenum which further enhances the resistance to localised corrosion.[21]

304L and 316L stainless steel are both austenitic stainless steels, however some residual ferrite is known to persist throughout the manufacturing process.[22]

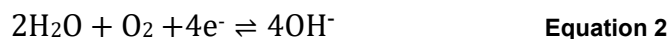
2.3 Corrosion

2.3.1 Overview

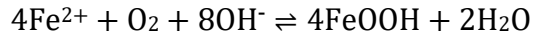
Corrosion is an electrochemical process involving the oxidation and dissolution of a metal, which occurs at an anode. For iron, the anodic (oxidation) reaction is:



For oxidation to take place, it is necessary for the electrons to be consumed in a cathodic (reduction) reaction. The typical cathodic reaction is reduction of oxygen:



When iron corrodes, the soluble ferrous ions may react with the hydroxide ions produced in the cathodic reaction and oxygen from the air to form rust, which is typically an iron oxy-hydroxide with the general formula FeOOH :



Equation 3

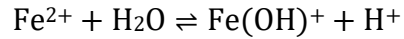
Equation 3 is one example of charge being balanced by combining the metal and hydroxide ions, forming an iron hydroxide which will precipitate out of the solution as corrosion product. The equilibrium point of the reaction in equation 1 and therefore whether a metal is likely to undergo dissolution is governed by the reduction potential and pH of the system. A potential-pH or 'Pourbaix' diagram can be used to indicate graphically whether or not corrosion might be thermodynamically favourable in certain conditions.[23]

2.3.2 Passivity

Passivity occurs when environmental conditions thermodynamically favour the growth of an insoluble metal-oxide layer several atoms thick which prevents the metal underneath from contact with the environment.[24]. On stainless steels this film is enriched in Cr_2O_3 which is stable under a wide range of conditions and strongly adheres to the underlying metal. The addition of a significant %wt of chromium as an alloying element also gives stainless steel the ability to 'heal' this Cr-rich passive film as selective dissolution of Fe will cause the surface layer to rapidly once again become enriched with Cr.[20, 25]

2.3.3 Pitting corrosion of stainless steel

Pitting corrosion of stainless steel usually initiates at MnS or oxide inclusions. Anodic dissolution of the metal forms metal ions which react with water (hydrolysis) forming H^+ ions which lower the local pH, e.g. Equation 4 for iron. This decreases pH and prevents the passive oxide layer from reforming within the pit.[26]



Equation 4

Pitting corrosion of stainless steel is a well-studied phenomenon in full immersion conditions and proceeds in three stages; *initiation*, *meta-stable pitting* and *propagation*. [8, 27].

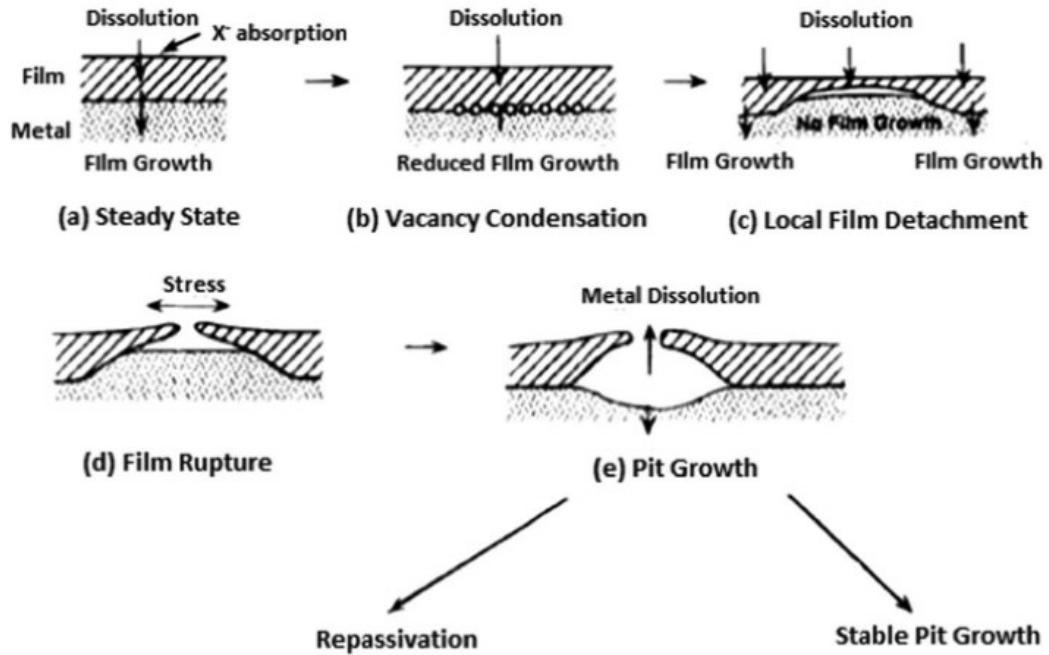


Figure 2 Representation of passive film breakdown via the point defect model [28]

Initiation first requires the breakdown of the protective passive Cr_2O_3 film (Figure 2). This almost always occurs at the site of a metallographic inclusion in stainless steels, usually manganese sulphide in the case of austenitic stainless steels [8, 29-32], but pitting has also been reported to initiate at other inclusions such as multi-element oxides [30, 33-35]. Inclusions which are not thermodynamically stable are then likely to wholly or partially dissolve and leave a cavity or occluded site which can prevent aggressive chemistry from being

diluted by the bulk solution.[29, 31, 36, 37] As a result, the metal continues to dissolve and the pit continues to grow.

While this occluded geometry persists, the pit will go through a period of rapid growth, eventually the passive film above will rupture and the pit solution mixes with the bulk electrolyte. Many pits repassivate at this point as the pH and metal ion concentration inside the pit is no longer low enough to sustain active dissolution. If a young pit repassivates in this manner it's said to have been *meta-stable*. If the rate of diffusion of metal ions out of the pit is equal to or exceeded by the rate of those leaving the metal surface however, the aggressive conditions will be maintained, dissolution will continue and the pit will continue to propagate[26, 38].

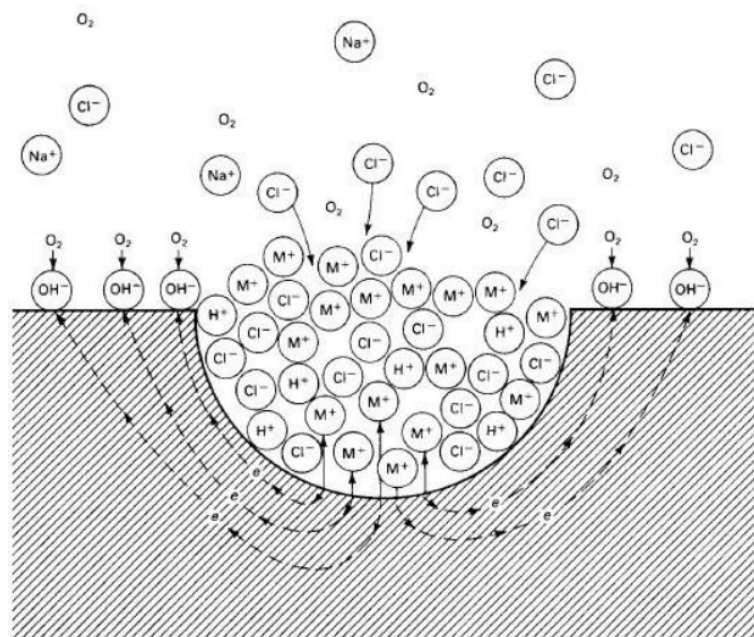


Figure 3 Representation of the key processes involved during propagation of pitting of metal in NaCl solution in non-occluded conditions[39]

The large number of positively charged species in the pit draws anions from the bulk solution to maintain charge balance, Cl^- being of particular note as it remains fully dissociated from H^+ ions, allowing a large concentration of them to remain in the pit and maintain a low pH.

As a result of this occluded geometry and ion exchange with the bulk solution, a concentration gradient of metal ions occurs between the pit mouth and the site of active dissolution, which can super-saturate and cause a layer of salt to form.[40-42] This can act as a reservoir of metal ions and protect the pit against sudden, temporary changes in conditions which could otherwise cause the active surface to repassivate.[43, 44]

2.3.4 Atmospheric pitting corrosion

Atmospheric pitting occurs with deposition of aerosol salts that absorb water from the atmosphere or 'deliquesce' to form a thin, confined layer of solution or 'droplet'. At equilibrium, the water activity is equal to that of the relative humidity the surrounding atmospheric environment. There are several interconnected factors which can affect the severity of this attack: relative humidity of the environment, the density of chloride deposited on the metal surface and the microstructure of the metal.

The relative humidity of the environment controls the solution concentration as any deposited salt will absorb or expel water until it reaches equilibrium with the water activity of the air. As a result, relative humidity (together with the chloride deposition density) governs the total volume of electrolyte as well as the resistivity and diffusivity of the solution. All salt species differ in the minimum

relative humidity at which they absorb enough water from the air (deliquesce) to form a saturated solution. For example, MgCl_2 has a deliquescence humidity of 33% RH at 30°C and so will form a saturated solution above this relative humidity. This will become less concentrated if humidity increases, as shown in Figure 4a.[45]

Due to the confined nature of the solution, a 'three phase boundary' exists between the metal, the solution and the air. This was first explored by Evans in his seminal work where it was observed that the cathodic reactions are most likely to happen towards the droplet edge due to high O_2 availability via diffusion from the surrounding air[46]. The size of the droplet can therefore also affect the corrosion process. A wider droplet area is associated with a larger pit mouth diameter[47] and a higher probability of pitting[45, 48]. Droplet thickness is controlled by a combination of the relative humidity and the salt deposition density (CDD) on the metal surface. An increase in local RH will reduce the solution concentration and therefore increase the diffusivity and conductivity of the droplet (to a point, see Figure 4b), while a higher CDD will give a thicker droplet for a particular RH and therefore increase the overall conductance of the droplet and distance that O_2 needs to travel to reach a cathodic region from the droplet surface. Consequently, both RH and CDD have a significant effect on the growth rate of pits.[47, 49]

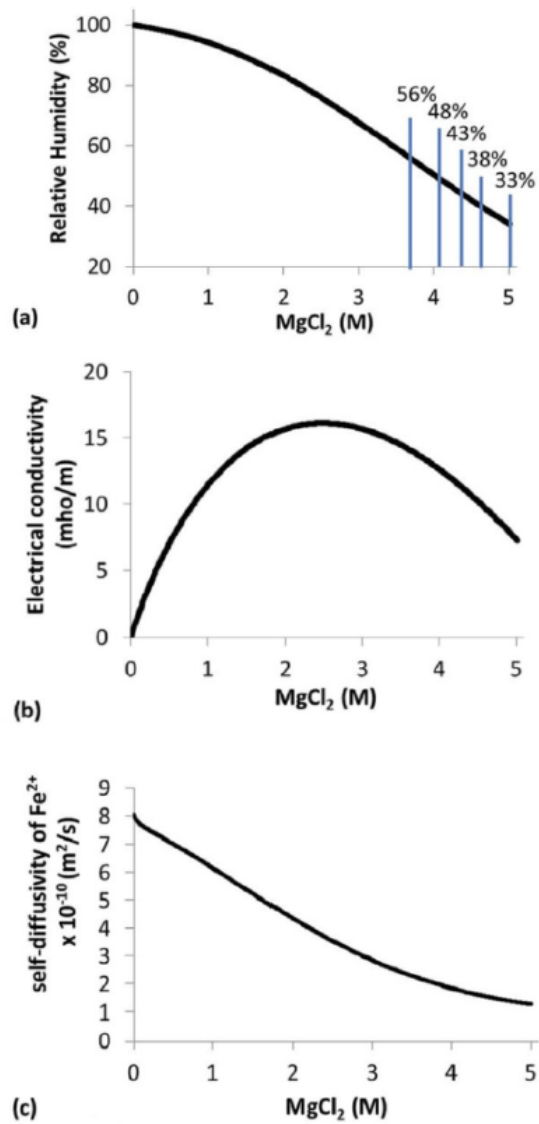


Figure 4 Relationship between the solution concentration (M) of MgCl_2 and (a) equilibrium relative humidity, (b) electrical conductivity (mohmm^{-1}) and (c) self diffusivity of Fe^{2+} (m^2s^{-1}) in MgCl_2 solution at 30°C , calculated using OLI 9, reproduced from Street *et al.* [22]

For pitting to initiate on stainless steel in atmospheric conditions, the relative humidity must be high enough for any deposited salts to deliquesce into a solution, but not so high that the concentration of the solution drops below that needed for pitting to initiate. Prosek *et al.* saw pitting on 304L and 316L at 50% RH, but not at 70% RH where the concentration is lower.[50] Tsutsumi *et al.*

also investigated pitting on 304 stainless steel under MgCl_2 droplets and saw pitting between 65% and 75% RH. [45, 51, 52]

As the relative humidity of the environment rarely stays constant, work has been done to characterise the effects of fluctuating conditions on the pitting process in situations where the electrolyte repeatedly dries out, or 'wet-dry' cycling conditions. It is widely accepted that pits will repassivate during the 'wetting' stage (high RH) while during the 'drying' stage, new pits will initiated and grow.[44, 52-56] Nam *et al.* isolated initiation and repassivation events under MgCl_2 droplets using electrochemical methods. They observed initiation at 47-58% RH for 304 and 48-58% RH for 430 at 298k, and noted repassivation at 56-70% RH for 304 and 67-73% for 430.[57] During wet and dry cycles a droplet's viscosity and conductance vary, which will significantly affect the rate of corrosion. Wet-dry cycling is likely to be more aggressive overall than constant exposure to a thin electrolyte due to multiple initiation events.[58-60]

2.3.4.1 Morphology of pitting

The shape of pits can have a significant effect on how the pit propagates and vary depending on the metallographic structure and on the exposure conditions. In full immersion conditions pits are often hemispherical and require some form of additional occlusion to maintain an aggressive environment. This can be provided by a 'lacy cover' as has been observed over in the initial stages of growth of these pits.[61]

In atmospheric conditions, pits have been shown to grow with different morphologies to full immersion conditions. 'Shallow dish' regions[52, 62, 63] are

prominent on young pits which can either develop into 'spirals' or 'satellites' depending on conditions.[63, 64] It has also been shown that preferential dissolution and therefore pit propagation can occur along bands of residual δ -ferrite in the metal sub-surface.[65]

RH has also been found to significantly influence pit morphology, with Street *et al.* observing 'satellite' morphology at lower RH values (33%) and 'spiral' morphologies at 43-48%RH, along with a shallow dish region. At 56% RH, no shallow dishes were present instead a deeper, rougher morphology was observed[22] This was attributed to differences in solution diffusivity and conductivity producing a higher IR drop for droplets exposed to lower RH conditions. Street also reported that the diameter of the shallow dish region varies with distance from the droplet edge, with smaller diameters seen at locations closer to the droplet edge.

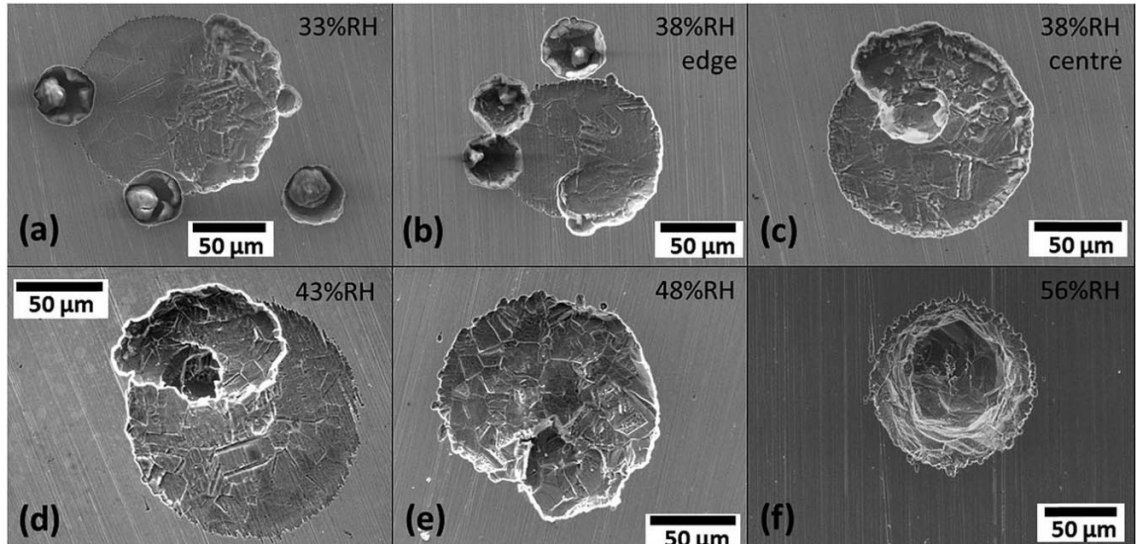


Figure 5 Typical examples of pit morphologies grown under MgCl_2 droplets with CDD of $750 \mu\text{gcm}^{-2}$ after exposure at constant RH for 1 day at 30°C . (a) and (b) show satellite morphologies, (b-e) spiral pits, (f) circular pit [22]

2.3.5 Atmospherically induced stress corrosion cracking

Pitting itself does not significantly affect the structural integrity of the attacked metal, but it is a known precursor of atmospherically induced stress corrosion cracking (AISCC) in high chloride environments. The major contributing factors to risk of AISCC risk that are relevant to this project are temperature (higher temperatures increase risk), solution composition (higher chloride concentrations increase risk) and tensile stress (higher stresses increase risk) with cracks developing perpendicular to the applied stress.[39] It is generally accepted that austenitic stainless steels are resistant to AISCC as long as the temperature remains below $\sim 50^{\circ}\text{C}$, this is due to the fact that stress corrosion cracking can only develop from an active pit if the rate of pit growth is lower than that of the rate of crack growth[66, 67]. There have been high profile exceptions to this, however, where chloride induced AISCC failures of austenitic stainless steels have occurred in swimming pools and coastal areas.[68-70] Austenitic stainless steels such as the 304L and 316L used to fabricate Intermediate level waste containers will be susceptible around the welds used to affix the lids and laser etched identifiers due to residual stress and depletion of chromium increasing susceptibility to corrosion respectively.[71, 72] Stress corrosion cracking can compromise the structural integrity of the container and so identifying sites at risk of AISCC via detecting the development of the pitting precursor is the primary motivation of this project.

2.4 Corrosion products of iron

Rust is the collective name for the mix of iron(II/III) oxide species which form the corrosion product when steel undergoes corrosion. For general surface corrosion it takes the form of a crust that covers the entirety of the metal surface. With localised corrosion, the rust precipitates out of the solution at the intersection between the ions formed by the anode and cathode.

There are many iron oxides; the 9 most likely compounds to form during atmospheric corrosion of stainless steel are outlined in Table 4[73].

Table 4 - Phases of rust, their formula and structure, information collated from Cornell & Schwertmann[73]

Name	Formula	Structure	Colour	Found in:
Goethite	α -FeOOH	Orthorhombic	yellow-brown	rocks, soils
Akaganeite	β -FeOOH	Monoclinic	bright yellow-brown	Chloride rich environments
Lepidocrocite	γ -FeOOH	Orthorhombic	orange	rocks, soil, biota, rust
Feroxyhyte	δ' -FeOOH	Hexagonal	red-brown	'various surface environments'
Hematite	α -Fe ₂ O ₃	Rhombohedral hexagonal	blood-red	soils, rocks
Maghemite	γ -Fe ₂ O ₃	Cubic or tetragonal	red-brown	Soils
Ferrihydrite	Variable - Fe ₂ O ₃ ·XH ₂ O/ Fe ₅ O ₈ H·H ₂ O	Hexagonal	red-brown	streams, rivers, mud, soil, rock, all living things
Magnetite	Fe ₃ O ₄	Cubic	black	rocks, biota
Green rusts	many, contains Fe ^{II} and Fe ^{III} , Cl ⁻ and SO ₄ ²⁻	Layered double hydroxide octahedral	green	corrosion product

2.4.1 Formation and transformation of the iron oxides

Formation of an iron oxide or hydroxide phase is a well understood process and occurs through either direct precipitation from a solution containing ferric (Fe^{3+}) or ferrous (Fe^{2+}) ions or by transformation from another crystal phase, either by dissolution and re-precipitation or by solid state transformation. The formation of a particular species over another is heavily dependent on the pH, temperature, rate of ion supply and presence of other local ions such as chloride or sulphate. [73, 74] Figure 6 shows an overview of major formation pathways of various iron oxides and oxide-hydroxides. Akaganeite ($\beta\text{-FeOOH}$) is of particular interest for the high chloride concentration systems found in atmospheric environments as it forms in acidic solutions above a threshold concentration of chloride ions, which stabilise its 'tunnel' structure in the early stage of formation, despite not being chemically included in compound.[73-75]

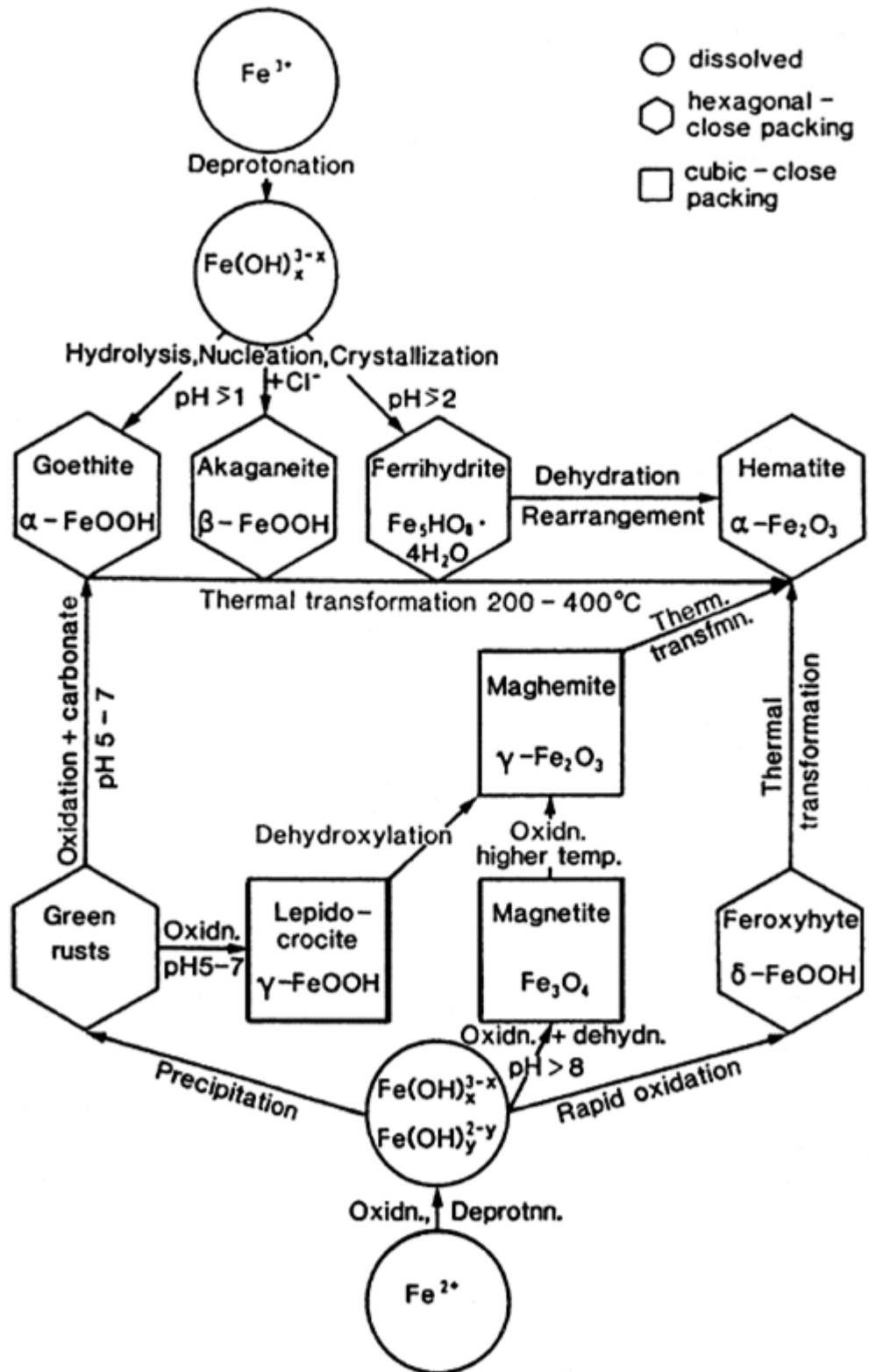


Figure 6 Schematic representation of major formation and transformation pathways of common iron oxides from Cornell & Schwertmann's *The Iron Oxides: Structure, properties, Reactions Occurrences and Uses* [73]

Iron oxides are also well known for their propensity to transform into other oxides and hydroxides[73], care therefore has to be taken to minimise the possibility of transformation when performing characterisation techniques such as Raman spectroscopy which can heat the sample and induce undesired phase transformation, generally to hematite. [76-78]

2.4.2 Characterisation of iron oxides and oxide-hydroxides

Iron oxides and hydroxides have been characterised using various spectroscopic techniques; micro-Raman spectroscopy has been extensively utilised due to the ability to non-destructively discriminate between crystal phases with a small sample volume. [79-84]

The UV-VIS-IR spectral region has been of interest for remote sensing of iron oxides and oxide-hydroxides in earth and space science due the ability to use ambient light to illuminate the sample, thus allowing for spectroscopy to be performed from long distances (i.e. from aircraft or satellites)[85-87].

Sherman[88] *et al.* characterised the UV-VIS-IR diffuse reflectance spectra of iron oxides and oxide-hydroxides from 350 nm-2150 nm for use in identifying Martian minerals and assigns the 400 -1000 nm region as the 'most diagnostic spectral region for delineating the iron oxide phases'.

Mossbauer, XRD and micro-XRD have also been used, but generally in a complementary context to verify sample powder purity, or for assessing physical properties of powders such as size, crystallinity and packing density[77, 87, 89-91]

2.4.3 Atmospheric corrosion products of iron alloys

Extensive work has been performed to characterise the corrosion products of iron, both by controlled laboratory experiment [92, 93] and by evaluation of corrosion products found on archaeological samples [81-83, 90, 94].

Dunnwald *et al.*[92] used Raman spectroscopy to investigate corrosion products of iron after repeated wetting and drying of a 1 μm thin film of iron deposited on gold substrate, they reported a cycle whereby goethite ($\alpha\text{-FeOOH}$) and lepidocrocite ($\gamma\text{-FeOOH}$) were formed, which would transform to Fe(OH)_2 upon rewetting and then Fe(OH)_3 upon partial drying before crystallising to α or $\beta\text{-FeOOH}$ again. This cycle could then be broken by the subsequent reduction of Fe(OH)_2 and FeOOH to magnetite (Fe_3O_4) which would remain as the final product. Dubois *et al.*[95] also observed magnetite, maghemite and goethite under wet-dry cycling of NaCl salt spray in atmospheric conditions, with a gradual transformation to akaganeite observed as more cycles are performed.

Raman spectroscopy has also been extensively used for characterisation of atmospheric corrosion of corrosion products found on archaeological iron samples, Bellot-Gurlet *et al.* and Monnier *et al.* [81, 82] studied samples of iron chain from Amiens cathedral (1497), reporting layered corrosion products with iron oxide-hydroxides goethite, lepidocrocite and akaganeite present. They assign some spectra as 'General poorly crystallised iron(III) oxide or oxide-hydroxide' due to poor signal to noise indicating a lack of crystallinity.

Bellot-Gurlet *et al.* and Neff *et al.* [81, 83] also studied corrosion products in buried samples, seeing different corrosion products based on the level of

aeration of the soil, with Siderite (FeCO_3) and magnetite in anoxic conditions and a mix of goethite, maghemite and magnetite in aerated soils, along with some siderite, iron hydroxychloride ($\beta\text{-Fe}_2(\text{OH})_3\text{Cl}$) and akaganeite associated with increased chloride and carbonate. Similarly, Shengxi *et al.* [90] studying carbon steel samples immersed in seawater for ~60 years found a layer of iron hydroxychloride, Fe_3O_4 and akaganeite covered in a layer of iron and calcium carbonates. Réguer *et al.* [84] also reports increased volumes of akaganeite in chloride rich environments.

“Green rusts” are also potential corrosion products of iron, they are generally short lived and take the form of ‘layered double hydroxides’ in the hydrotalcite super-group of minerals. They are a mix of hydroxide and carbonate groups which include anions such as chloride and sulphate and have been known to include others e.g. halogenides, perchlorate and nitrate.[73]. Legrand identified an electrochemical method of producing chloride ‘GR1’ (green rust 1) and characterised it with Raman spectroscopy.[96] Other, similar minerals exist, such as pyroaurite, iowaite and coalingite within this group and can be distinguished by their ratio of Fe^{3+} to Fe^{2+} [97, 98].

2.4.4 Corrosion products of stainless steel

Some work has been done previously to characterise the product formed from pitting on 304/316 stainless steel in atmospheric conditions. Luo *et al.*[99]., Dong *et al.* [100] and Dhaiveegan *et al.*[101] used a range of techniques including Raman spectroscopy to characterise corrosion products. Luo, Dong and Dhaiveegan studied the development of corrosion of 304L under atmospheric conditions over a time period of several months, the environments were tropical,

marine and urban respectively. Ferreira's samples were under full immersion of 0.15M NaCl. Luo, Dong and Ferreira observed similar Raman spectra; Ferreira assigns goethite, chromium oxides and 'a mixture of oxides and hydroxides formed by atmospheric oxidation' as the main constituents observed, whilst Luo and Dong report a mixture of akaganeite, magnetite, maghemite and hematite. Dhaiveegan was able to take multiple readings over a 36 month period and noted the transformation of corrosion products between magnetite, hematite, lepidocrocite and goethite across rainy seasons, which eventually stabilise to goethite with a low amount of maghemite and akaganeite[101].

2.5 Corrosion detection and monitoring

Many industries routinely inspect for corrosion and so non-destructive techniques have been developed to assess metal attack, some making use of advanced equipment such as millimetre wave radar ultrasound and x ray fluorescence[102] and others using simple visual and percussive-acoustic assessment by a skilled inspector.[103-107] However, these are generally operated manually and require contact or close proximity with the material being tested.

Most remote sensing techniques that have involved image based corrosion detection focused on either texture or colour based analysis [108-110]. These have focused on detection of large areas of rust on carbon steel or for corrosion related deformation of surfaces and will be explored further in the image analysis section.

2.5.1 Principles of imaging and spectroscopy

All characterisation techniques used in this project take advantage of the mechanisms by which light interacts with matter. Light is quantized, which is to say that it behaves as discrete units or *quanta*, each of a specific energy given by:

$$E = h \frac{c}{\lambda} = h \nu$$

Where **E** is the energy of the photon, **h** is planck's constant $6.63 \times 10^{-34} \text{ m}^2\text{kgs}^{-1}$, **c** is the speed of light $3 \times 10^8 \text{ ms}^{-1}$, **λ** is the wavelength and **ν** the frequency of the photon

Each of these units is a photon, which is produced fundamentally by the movement of charge – often via the relaxation of an electron in its atomic or molecular orbital from a high energy or ‘excited’ state to a lower energy state. If this is the case, the photon produced will be of a characteristic energy specific to the atom or molecule that produced it via its internal electronic structure and distribution of possible energy states. For the complex multi-electron, multi-nucleus systems that constitute molecules there are many such states which are further split into sub-states which can be broadly clustered together as ‘*band spectra*’. Specific spectral regions are associated with different excitation modes. For molecules the spectrum can be divided into three spectral ranges corresponding to the different types of transitions between molecular quantum states; the far infrared, characteristic of rotational motion, the near infrared, characteristic of vibration-rotation spectra and the visible and ultraviolet which is characteristic of electronic transitions[111].

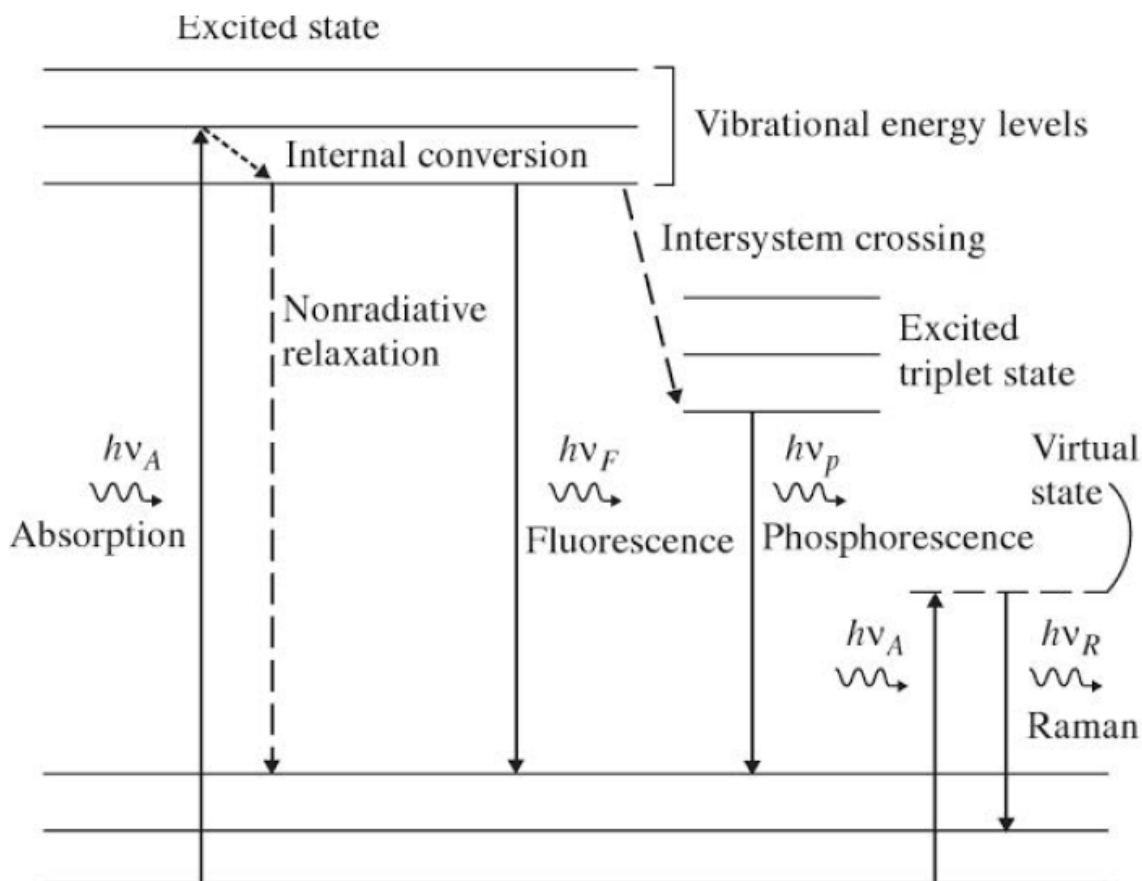


Figure 7 Jablonski Energy level diagram showing modes of emission. Energy of transition is given as $h\nu$ where h is planck's constant 6.63×10^{-34} and ν is the frequency of the photon. The subscripts A, F, p and R represent absorption, fluorescence, phosphorescence and Raman respectively.[112]

Just as an atom or molecule can emit a photon, it can also absorb it, exciting the electron to a higher energy state in the process. This electron might then too relax internally or undergo 'internal conversion' with no radiative emission, transferring some of its energy to kinetic (observable as a temperature increase of the system) meaning a photon of a lower energy will be ultimately re-emitted. Photography, Fourier-Transform Infra-Red spectroscopy (FTIR) and UV-VIS-NIR spectroscopy measure visible to infrared light that has been elastically (Rayleigh) scattered through, absorbed and re-emitted from a sample with a different wavelength, dependent on the compounds present. Raman spectroscopy makes use of the principle of Raman Scattering, which is *inelastic*

scattering of incident light, with no resonant characteristic between incident light and scattering molecule necessary (unlike fluorescence which requires resonant absorption of incident light). For Raman scattering to occur, the incident radiation must be monochromatic (frequency ν). The radiation scattered at right angles to the incident direction will contain not only elastically (Rayleigh) scattered light of frequency ν , but also much weaker radiation of frequency $\nu \pm \nu'$ of which ν' is the Raman scattered component. A resulting spectrum of this scattered light will not only have a strong monochromatic line of the illuminating frequency ν , but weak 'Raman' lines either side of it which will be characteristic of transitions in the scattering molecule.[111]

2.5.2 Hyperspectral imaging

Spectral images are obtained by gathering spectral information for each pixel in an image of a scene, rather than a single intensity value. Hyperspectral imaging is differentiated from multispectral imaging by having a regular spectral interval, usually on the order of 1-10 nm rather than discrete, often irregular wavelength points where intensity information is gathered. Data gathered is arranged in a 'hypercube', with spatial information in the x and y dimensions and spectral in the z.

Hyperspectral imaging sees extensive use in industry and science; for example in earth and extra planetary science for classifying and mapping foliage cover and the extent of urbanisation around the world[113-116], for mineral prospecting [4, 5, 85, 117], for characterising the surface mineralogy of planets and asteroids[86, 118-121], agriculture for large scale assessment of crop state[122], the food industry for assessing product quality[123], in the

preservation and restoration of archives and paintings for characterising inks and paint pigments and also in medicine to diagnose cancers through imaging blood via capillaries in the eye.[124]

Very little work has been done on hyperspectral imaging in a corrosion detection context, but work in prospecting for iron ores using air and space-borne spectral imaging sensors and for characterising the surface of earth and mars are highly relevant as they aim to identify similar iron-bearing mineralogy[3-5, 86, 115, 117-119, 125]. For example the OMEGA instrument aboard the Mars express mission is used for identifying Martian surface mineralogy, atmospheric aerosols and polar CO₂ ice. They are able to generally discriminate iron oxides from other minerals by a broad spectral band centred at 900 nm, but also report useful regions at 1900 nm and 2500 nm for identifying hydration level of goethite [118, 125, 126]. Similarly the Landsat and EO-1 missions have been used for mineral prospecting of iron ores using the multispectral Hyperion and orbital land imager instruments, using band ratios to ascertain hematite-goethite ratio and thus abundance of Fe³⁺ and quality of ore[127].

2.5.3 Image analysis

The process of extracting useful features from an image is critical to the effectiveness of an imaging system, whether hyperspectral or a colour photograph. The simplest method of doing this is *thresholding*, whereby an intensity gradient is identified across the image and a threshold is applied to separate the feature from the background. Due to the aforementioned diffuse UV-VIS-NIR reflectance band at 650-900 nm which gives iron oxides and iron oxide-hydroxides their characteristic red colouring[73, 80, 88], a natural differential exists with which to segment images in a corrosion context.

Colour cameras measure intensity at three wavelength bands centered upon approximately 450, 550 and 650 nm. These correspond to the colours blue, green and red. When overlaid, these three colour 'channels' give an image which is natural to visually interpret, however the raw data is not intuitive to understand outside the representation of an image of a scene. For this reason, *colour-spaces* have been developed to aid and simplify manipulation of colour image data. Used in this project are the '*HSV*' colour space and the '*L*a*b**' colour space.

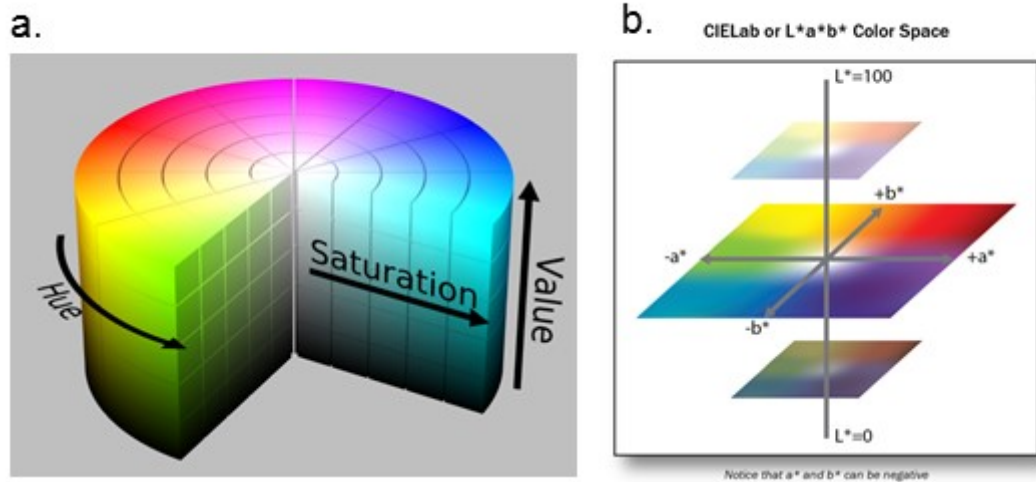


Figure 8 Graphical representation of colour distribution in a. HSV colour space[128] and b. $L^*a^*b^*$ colour space[129]

$L^*a^*b^*$ colour space (Figure 8b), laid out in the 1976 CIELAB standard[130] is based around providing a *device-independent* mathematical description of opposing pairs of primary colours a^* being an axis from green to red, b^* from blue to yellow and L^* representing lightness to darkness. For an image to be reliably represented in $L^*a^*b^*$ colour space it needs to be transformed using a standard reference white.

HSV, or *Hue*, *Saturation*, *Value* (Figure 8a), transforms colour image data into three indices which more closely match human perception of colour mixing attributes via paint mixing or light blending. *Hue* is usually arranged azimuthally and corresponds to major colour group i.e. red, green, blue, yellow. *Saturation* is arranged radially and corresponds to the dominance of a particular Hue in the colour. *Value*, or Intensity is arranged axially and corresponds to the ‘strength’ of the light[131].

Colour segmentation of images is used extensively in industry for machine vision applications such as high throughput produce quality assessment and sorting. [132-134] Some work has been done with the aim of developing image processing based corrosion detection systems: Itzhak *et al.* were first to employ image processing by intensity thresholding greyscale images of pitting on 304 stainless steel in a 10%FeCl₃ solution with the aim of developing statistical analysis tools for evaluating total pitted area of a metal surface. Due to the full immersion conditions producing little rust, segmentation highlighted deformation of the pitted metal surface rather than corrosion products. [135] This is expanded on by Choi *et al.* who combine several texture and colour properties of the pitted metal surface to classify corrosion damage.[136] Medeiros *et al.* use a similar multi-descriptor based approach for corrosion detection on carbon steel, this time imaging the corrosion product rather than the metal surface before performing Fisher linear discriminant analysis (FLDA) [110], similarly Valeti outlined a procedure for colour based corrosion detection in L*a*b* space using *k-means* clustering [137]. Feliciano *et. Al.* have investigated a solely texture based approach on A36 steel to assess the development of corrosion over time.[138]

Principal Component Analysis is extensively made use of as a dimensionality reduction and feature extraction method for hyperspectral imaging due to its ability to easily organize data down lines of maximum variance and quickly optimize a dataset for viewing[139-142]. It has similarly been used for unsupervised feature extraction of colour images with some success[143, 144]

and was also used as a pre-processing step before FLDA during Medeiros *et al*'s corrosion detection work on carbon steel[110] .

2.6 Summary

Atmospheric pitting corrosion of stainless steel is an indicator of risk of AISSC, which could cause failure in containers when they come to be moved to permanent disposal in a GDF. It is caused by the deliquescence of aerosol salt particles to form a concentrated solution. Pitting leaves a deposit of rust which could be used to indicate the presence of a corrosion site.

Hyperspectral imaging is extensively made use of in industry and science for detection and quantification of iron oxide species, but has yet to be applied to corrosion monitoring. Extensive work has been undertaken to characterise iron oxide products of corrosion products using Raman spectroscopy and while some techniques have been developed for detecting corrosion using photography and image processing, little work has specifically targeted pitting corrosion.

The aims of this Thesis are:

- To identify the specific corrosion products present on 304L stainless steel during pitting corrosion
- Evaluate the effect of droplet chemistry on these corrosion products in stores relevant conditions
- Determine the optimum imaging and analysis methods for quantifying visible rust
- Use this method to investigate the relationship between corrosion pit volume and visible rust.

3. Methodology

3.1 Droplet experiments

3.1.1 Materials and sample preparation

All droplet experiments were performed on 3 mm thick 304L stainless steel (Aperam-France, Table 5) which had been cold-rolled and solution treated at 1040-1100°C before undergoing forced air cooling by the manufacturer. The plate was received in 250 x 250 mm plates.

Table 5 - 304L standard vs. forge analysis provided by Aperam (forge reports in appendix 11.1)

Type	%C	%Mn	%P	%S	%Si	%Cr	%Ni	%Co	%N	%Fe
304L standard	0.03 max	2 max	0.045 max	0.015 max	0.075 max	18-19.5	8-10.5	-	0.1 max	balance
304L forge analysis	0.023	1.46	0.032	0.0033	0.44	18.08	8.00	0.171	0.07	balance

Pieces of stainless steel plate were cut to either 25 x 25 mm, 25 x 50 mm or 25 x 75 mm coupons using a Buehler Isomet 4000 saw with a SiC blade and mounted with the surface exposed in VERISET resin (Metprep) in the case of 25x25 and 25x50 mm plates or on clean rubber bungs in the case of 25x75 mm plates. Samples were then wet ground using P400 grit SiC paper parallel to the rolling direction and then finished with P800 grit perpendicular to the rolling direction. They were then ultrasonically cleaned in deionised water (DI) (>15 MΩ·cm, Millipore) for 5 minutes to remove particulates from the grinding process, rinsed in deionised water, dried with the aid of an empty wash bottle and left in a covered container at ambient temperature and humidity for 24 hours to repassivate before deposition.

3.1.2 *Solution preparation*

Bulk 0.044 M MgCl_2 and CaCl_2 solutions were prepared from $\text{MgCl}_2 \cdot 6\text{H}_2\text{O}$ or CaCl_2 salt (Sigma Aldrich) using DI water ($>15 \text{ M}\Omega \cdot \text{cm}$, Millipore), which corresponded to $\sim 100 \mu\text{gcm}^{-2}$ chloride deposition density (CDD) with a $4 \mu\text{L}$ droplet. When a lower chloride deposition density was required, serial dilution was used to create a solution of the appropriate concentration; $0.022 \mu\text{L}$ for a CDD of $50 \mu\text{gcm}^{-2}$ and $0.00088 \mu\text{L}$ for $20 \mu\text{gcm}^{-2}$.

3.1.3 Droplet deposition

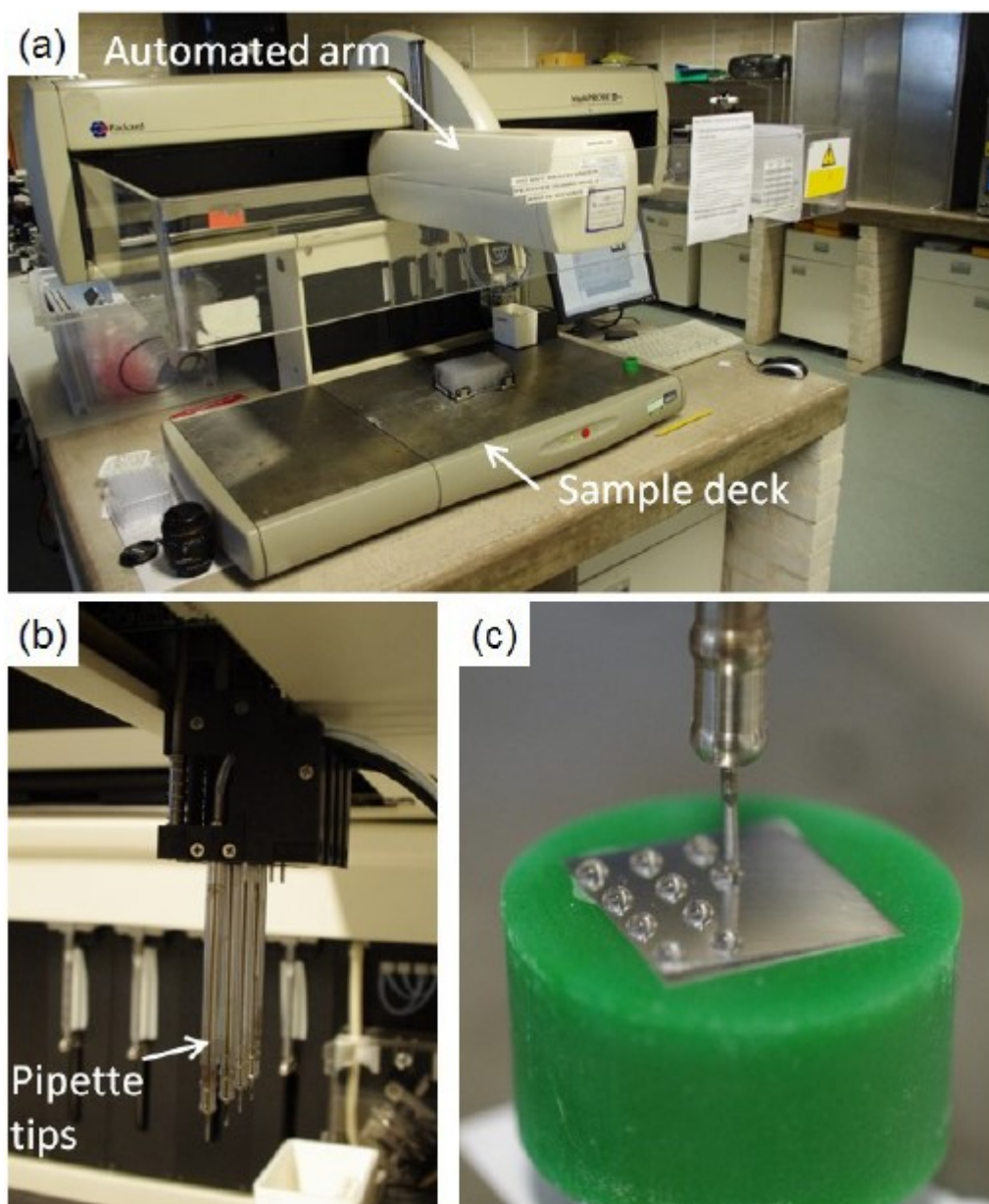


Figure 9 Deposition via MultiPROBE II liquid handling system a) photograph of system showing arm and sample deck b) Pipette tips c) example of droplet deposition procedure, Credit: Dr. A Cook, reproduced with permission[145]

Droplet deposition was performed using MultiPROBE II Ex robotic liquid handling system (Packard Biosciences, Figure 9a.), or by micropipette (Eppendorf, 20 μ L maximum volume) where stated on smaller samples. This

allowed for a large number of droplets of consistent volume and location to be deposited in a short amount of time.[145] The system consists of a robot arm which moves a pipette tip (Figure 9b), fed by an automated syringe. Hydraulic action of 'system liquid' (DI water) is used to aspirate and dispense aqueous solutions. An air gap is kept between the solution and the system liquid at all times and the system is flushed with DI water when switching between solutions.

Droplets were deposited in grids with an interval depending on experimental requirement, but of no less than 2 mm between droplets (Figure 9c).

4 μL droplets were used for all experiments which consistently spread to a radius of approximately 2 mm on the finished sample surface.[63] This allowed chloride deposition density to be controlled by deposition of solution of known concentration alone; 0.044 μL for a CDD of 100 μgcm^{-2} , 0.022 μL for 50 μgcm^{-2} and 0.00088 μL for 20 μgcm^{-2} .

3.1.4 *Exposure to fixed environmental conditions*

Humidity was controlled with sealed desiccators using saturated salt solution to maintain a set humidity based on ASTM standard E104-02(2007)[146]

Temperature was controlled using an oven (Temperature Applied Sciences Ltd.) For the fixed 46% RH and 30°C environment, saturated potassium carbonate (K_2CO_3) solution was added to a quantity of dry K_2CO_3 in the base of a desiccator. The desiccator was sealed and placed in the oven 24 hours prior to the sample in order to allow the environment within the desiccator to reach equilibrium and ensure that the expected conditions were present. Exposure

conditions were verified by EasyLog EL-USB-2-LCD (Lascar Electronics Ltd.) with an accuracy of $\pm 0.5^{\circ}\text{C}$ and $\pm 3\%$ RH.

3.1.5 Exposure to fluctuating ambient environmental conditions

Samples described as exposed to fluctuating ambient conditions were exposed in desiccators which were left covered but not sealed to ensure equilibrium with the environment whilst minimising the chance of unintended additional deposition of atmospheric contaminants. Exposure conditions were recorded and verified by EasyLog EL-USB-2-LCD data logger (Lascar Electronics Ltd. with an accuracy of $\pm 0.5^{\circ}\text{C}$ and $\pm 3\%$ RH.

3.2 Photography

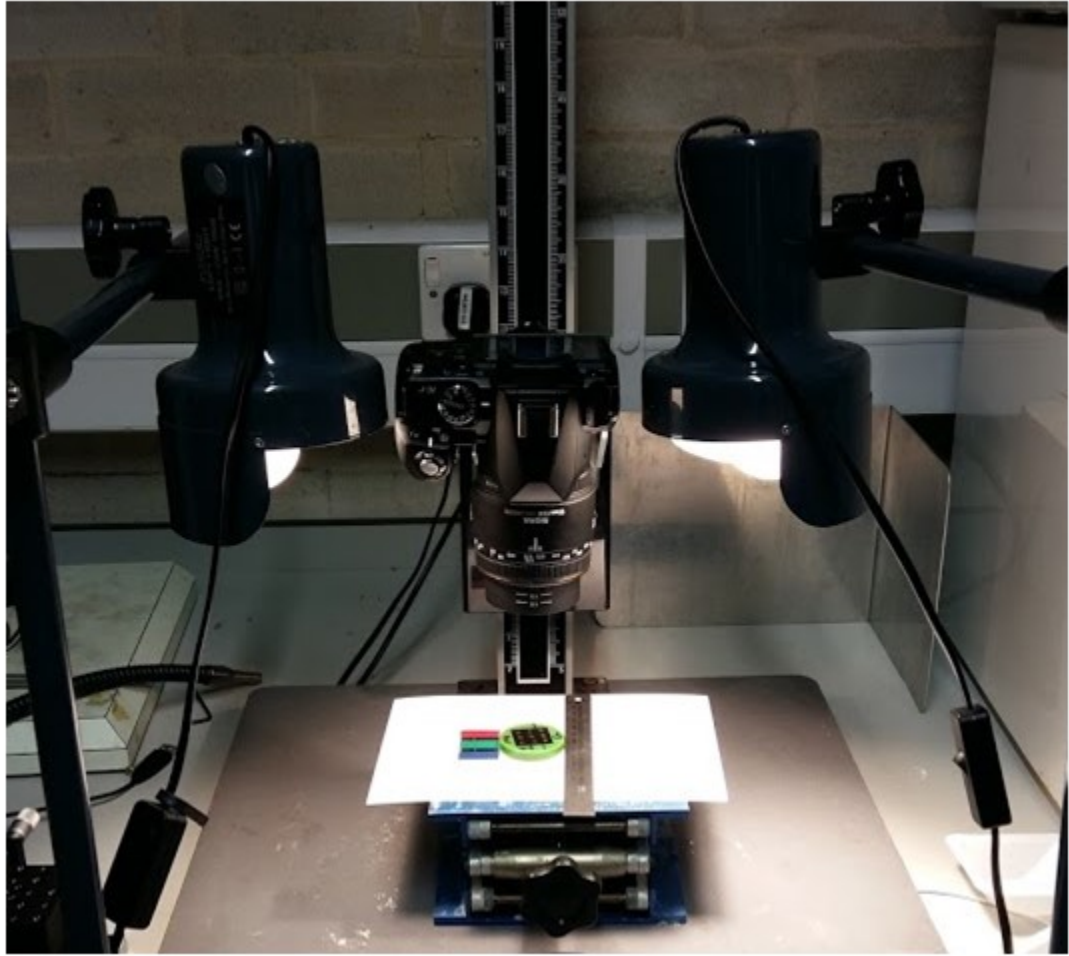


Figure 10 Equipment used for colour photography of samples. Pentax K-r camera with Dx 50 mm macro lens. Lighting was provided by two tungsten lamps.

Colour photographs were taken with a Pentax K-r DSLR utilising a Sigma DG 50 mm f/2.8 macro lens. Images were saved as uncompressed JPEGs using the sRGB colour space. Illumination was provided by two tungsten lamps arrayed either side of the photographic equipment. All images were taken with a steel ruler in frame to provide scale information. Several steps were taken to improve image quality:

1. All images were taken at the minimum focal distance of the lens, maximising the size of the sample area on screen
2. Samples were oriented such that the grinding direction was horizontal on the photograph. This minimised reflection from the light sources from ridges in the grinding pattern and ensured uniformity of lighting in the photograph.
3. Photographs were taken on aperture priority mode with the aperture setting at f/2.8 to maximise sharpness of the image.
4. All additional camera post-processing was disabled

3.3 Iron oxide syntheses

Iron oxides and oxide-hydroxides were synthesised by Dr. Rowena Fletcher-Wood using procedures provided by Cornell and Schwertmann.[73] Individual procedures for each oxide and oxide-hydroxide crystal phase are outlined in Appendix 11.2.

3.4 Characterisation and Spectroscopy

3.4.1 *X-ray diffraction*

A Bruker D2 PHASER was used to gather XRD data, which operates with a Co source, and thus does not cause Fe and Mn to fluoresce. This instrument is run in Lynxeye reflection mode. $\lambda = 1.79026 \text{ \AA}$. The tube operates under 30 kV/10 mA acceleration, producing Co K α -1 radiation. Samples were loaded into a cavity and the surface flattened with a slide and analysed for 1 hour per sample at a range of 5-80°.

3.4.2 *UV-VIS-NIR spectroscopy*

UV-VIS-NIR diffuse reflectance spectra were gathered using an Oceanoptics “Flame” UV-VIS-NIR spectrometer, with an Oceanoptics HL-2000 series tungsten-halogen light source. Spectra were gathered using a probe consisting of two optical fibres which guided light from the source to the sample and reflected light back to the spectrometer. Instrument control and analysis was performed using the “Oceanview” analysis software provided with the instrument. Measurements were taken of the powdered samples deposited on a glass slide with a gently tamped surface. The fibre probe was clamped approximately 2 cm above the sample while measurement was performed. Bright and dark field spectra for correction were taken of SPECTRALON 99% and 2% calibrated reflectance standards. All measurements were taken in a dark room to eliminate visible spectrum interference from lighting,

3.4.3 *Fourier-Transform Infra-Red (FTIR) spectroscopy*

FTIR spectroscopy was performed using a Thermo scientific Nicolet 8700 Model 912A0685. Samples were suspended in KBr, which was dried overnight at 120°C. 300 mg of KBr was used per 3 g of sample.

3.4.4 Raman Spectroscopy

A Renishaw InVia spectrometer with confocal microscope was used to identify corrosion products after exposure. The wavelength of the excitation laser was 488 nm and the maximum estimated power output after optical losses was 20 mW. All spectroscopy was performed through a 20x super long working distance objective, giving a spot size of approximately 10 μm . In order to prevent the thermal transformation of corrosion iron oxide-hydroxide corrosion products laser power was limited to 10% of maximum (~ 2 mW). Each measurement was the product of 30 accumulations of 10 seconds each (unless otherwise specified), giving a total per-measurement acquisition time of 5 minutes. The data range was measured from 50 – 1600 cm^{-1} . The instrument was controlled using Renishaw's WiRE software version 4.0. No sample preparation such as rinsing of salt solution or corrosion product off the sample surface was performed and measurements did not take place under RH or temperature control due to equipment limitations.

3.4.4.1 Raman spectroscopic mapping

Mapping data was collected by automated acquisition of multiple point measurements in a grid across the sample surface with the total number of points and interval between measurements dictated by the size of the sample and instrument time available for acquisition. Each pixel in the final map therefore constitutes an individual spectrum from the acquisition. Due to the long acquisition time necessitated by preventing thermal transformation of corrosion product species, the total acquisition time for a map was the limiting

factor when deciding mapping parameters. Table 6 contains the acquisition dimensions for all droplets mapped in chapters 4 and 5.

Table 6 Mapping dimensions and total number of acquisitions for all mapped droplets (* shorter acquisition time of 6 accumulations x 10seconds for a 1 minute per point exposure time, rather than 5 minutes)

Droplet salt and CDD	Exposure conditions	Exposure time (days)	Mapping dimensions (mm)	Mapping interval (μm)	Total number of points
100 μgcm^{-2} MgCl_2	Fixed	14	3.0x3.2	120	728
100 μgcm^{-2} MgCl_2	Fluctuating	14	3.5x2.1	105	1015
100 μgcm^{-2} CaCl_2	Fixed	14	3.6x2.9	80	1702
100 μgcm^{-2} CaCl_2	Fluctuating	14	3.4x3.9	130	783
100 μgcm^{-2} MgCl_2	Fixed	24	3.1x3.7	50	4725*
50 μgcm^{-2} MgCl_2	Fixed	24	2.3x2.0	60	1326
30 μgcm^{-2} MgCl_2	Fixed	24	1.7x1.7	75	576
30 μgcm^{-2} MgCl_2	Fluctuating	~1275 (42 months)	3.4x3.2	170	420

3.4.4.2 Raman data analysis

Raman data analysis was performed using WiRE 4.0 (Renishaw plc, 2002) and Matlab R2016b. After data acquisition was completed, maps representative of the distribution of chemical compounds present on the sample surface were created by analysing each spectrum in the dataset for a chemical compound with one of two methods:

1. Least squares (“Direct classical least squares (DCLS)” on WiRE 4.0) fitting of an experimental spectrum against a standard spectrum of a known compound. A minimum least squares index threshold of 0.4 was

used for compound assignment. All iron oxide-hydroxide phases were fitted for in this manner.

2. Index thresholding of a wavenumber to find the distribution of a single peak. The threshold intensity was 150 unless otherwise stated. This was performed if an unknown spectrum was observed.

After a map had been created, all spectra associated with said map were averaged to improve the signal to noise ratio using the script provided in Appendix 11.3

3.5 UV-VIS-NIR Hyperspectral Imaging

3.5.1 Hyperspectral instrument hardware, motion control and data acquisition

The hyperspectral imaging apparatus consisted of an Oceanoptics “Flame” UV-VIS-NIR fibre spectrometer with a spectral range of 350-1000 nm, with an Oceanoptics HL-2000 series tungsten-halogen light source focused by a pair of achromatic doublets of focal length 30 mm arranged in opposing directions inside a 60 mm lens tube as described in Figure 11. Both illumination and acquisition were performed through the fibre bundle and the focusing optics. The probe was raster scanned across the sample surface by moving the sample using a pair of Thorlabs motorized translation stages with “K-cube” controllers in an x-y arrangement, allowing 25 x 25 mm range of movement. No sample preparation such as rinsing of salt solution or corrosion product off the sample surface was performed and measurements did not take place under RH or temperature control due to equipment limitations.

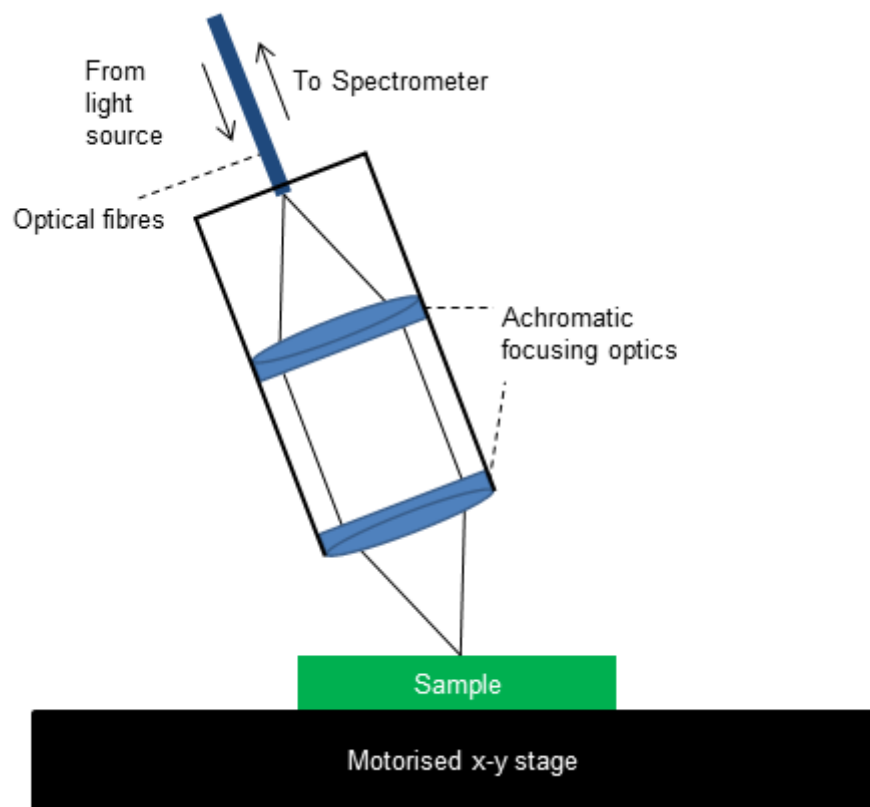


Figure 11 Schematic representation of hyperspectral imaging equipment showing arrangement of focusing optics and light path.

Spectra were acquired at set intervals across the sample surface, forming a hyperspectral image whereby each spectrum constituted a pixel. Integration time was set at 6500 μs for all spectral acquisitions. Focusing was performed to maximise returned signal from the sample surface before acquisition using a Thorlabs PT1B manual z stage mounted vertically.

The instrument was controlled by laptop via USB. Labview was used to integrate motion control with spectral acquisition, the program is provided with supplemental data attached to this document. Each hyperspectral image was output as a comma separated text file and processed using Matlab R2017b. Scripts for processing can be found in Appendix 11.4.

3.5.1.1 Flat field correction

Flat field correction was performed on all experimental and standard acquisitions unless otherwise stated. This was done for an x by y (*spatial*) by n (spectral) hyperspectral image matrix I using:

$$I_{corrected} = \frac{I_{raw} - I_{dark}}{I_{bright} - I_{dark}}$$

Equation 1 Where $I_{corrected}$ is the final hyperspectral image, I_{raw} is the raw hyperspectral image, I_{dark} and I_{bright} are single spectra of 2% and 99% spectralon reflectance standards respectively as the dark and bright field

I_{bright} and I_{dark} were $1 \times n$ spectra averaged from hyperspectral images of 2x2 mm areas of 99% and 2% spectralon calibrated reflectance tiles (Figure 13). The spectra were reacquired at the beginning of every experimental session.

3.5.2 Characterisation of UV-VIS hyperspectral imaging system

3.5.2.1 Resolution characterisation

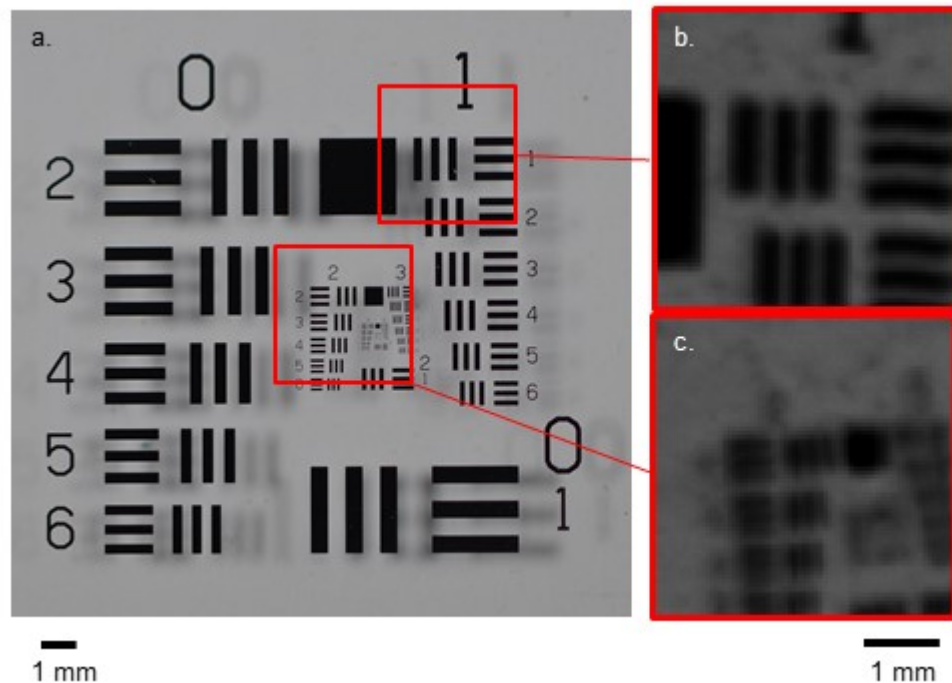


Figure 12 a. USAF standard 1951 image of test pattern taken with Pentax DSLR camera placed upon a white card background b. HS image slice at 535 nm of test pattern's 1-1 region showing 2 cycles per mm c. HS image slice at 535 nm of the central test patterns second group, showing 2-2 (top, shown clearly in a.) 2-3 (second from top) and 2-4 (second from bottom) along with well as the 3 group on the right [147]

Figure 12 a. shows an image taken with a DSLR camera of the USAF 1951 resolution test pattern printed on a glass slide, placed upon a white card background. The insets b. and c. are greyscale images of the 535 nm slice of a hyperspectral acquisition of the highlighted 4 x 4 mm areas of the standard taken at a 0.05 mm per pixel sampling resolution in order to test the resolving power of the instrument. Observable in inset a. is the test pattern's 1-1 and 1-2 region which consist of the triplets of horizontal and vertical lines with 2.00 and 2.24 lines per mm respectively. Observable in inset b. is the central region of

the test pattern with regions 2-1 to 2-4 present on the left hand side of the image at 4.00 to 5.66 cycles per mm. 3-1 to 3-6 are present on the right hand side (partially obscured by image edge) with 8.00 - 14.3 lines per mm. Regions 4 to 7 are present in the lower half of the image between regions 2 and 4, but are unresolvable. A full list of cyclic resolution values can be found in Table 7.

Table 7 Reproduction of table included with 1951 USAF test pattern showing the resolution values for markings present[147]

RESOLUTION VALUES FOR STANDARD USAF 1951 RESOLUTION TEST PATTERN (All values in Cycles Per Millimeter)										
	GROUPS									
ELEMENTS	-2	-1	0	1	2	3	4	5	6	7
1	.250	.500	1.00	2.00	4.00	8.00	16.0	32.0	64.0	128
2	.281	.561	1.12	2.24	4.49	8.98	17.9	35.9	71.8	143
3	.315	.629	1.26	2.52	5.04	10.1	20.1	40.3	80.6	161
4	.354	.707	1.41	2.83	5.66	11.3	22.6	45.3	90.5	181
5	.397	.794	1.59	3.17	6.35	12.7	25.4	50.8	101	203
6	.445	.891	1.78	3.56	7.13	14.3	28.5	57.0	114	228

3.5.2.2 Instrument response function characterisation

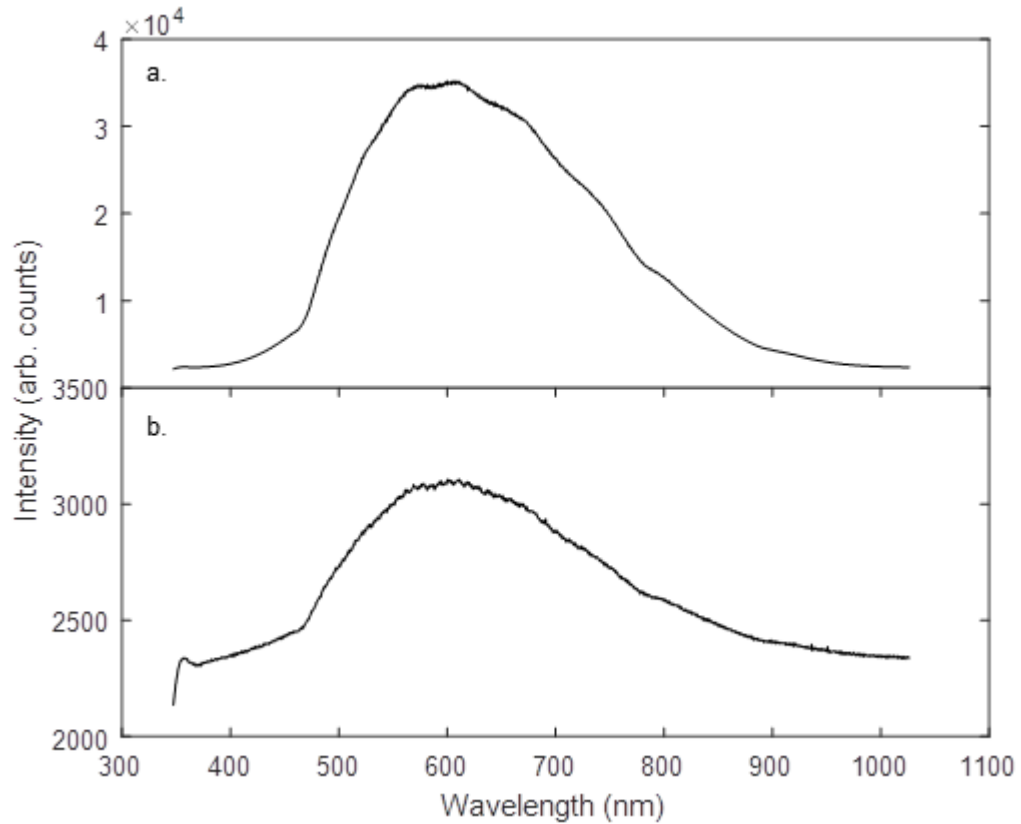


Figure 13 Spectral responses used for flat field correction, taken using a. 99% SPECTRALON diffuse reflectance standard and b. 2% SPECTRALON diffuse reflectance standard. No flat field correction was applied

Figure 13 shows averages of a 2 x 2 mm area of a. 99% and b. 2% calibrated reflectance standards taken at a sampling resolution of 0.2 mm per pixel, showing combined spectral responses of the light source, fibre, focusing optics and spectrometer. These spectra were used for flat field correction of all other images in this chapter using Equation 1. The highest intensity is in the 450 nm-850 nm wavelength interval, which is where the light source is brightest and the optics most transmissive. This is therefore where the signal to noise ratio will be highest. Subsequent spectral acquisitions will be trimmed to this wavelength interval.

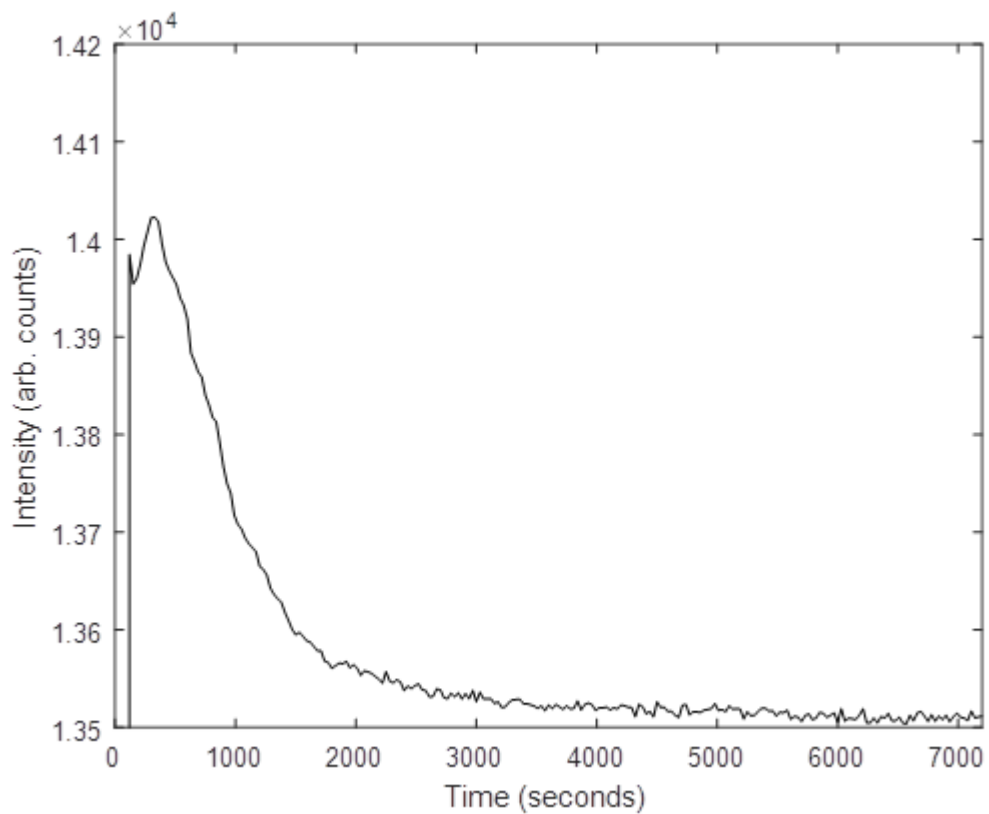


Figure 14 Average value of light source intensity over 240 minutes as measured using a 99% SPECTRALON reflectance standard

Figure 14 shows the average light source intensity over time as measured from the diffuse reflectance of a 99% calibrated reflectance standard. A spectrum was taken every 30 seconds and averaged and no flat field correction was applied. The first two minutes of acquisition give an approximate intensity of 2500 counts before the intensity rapidly increases to approximately 14,000 counts, dropping to 13500 counts over the following 50 minutes where it remains stable. As a result, apparatus was left for an hour after the light source was switched on in order to reduce error from light source instability.

3.5.2.3 Characterisation of wavelength specific intensity drift with distance from focal point

It was found that addition of optics to focus light to and from the fibre introduced significant chromatic aberration into the system.

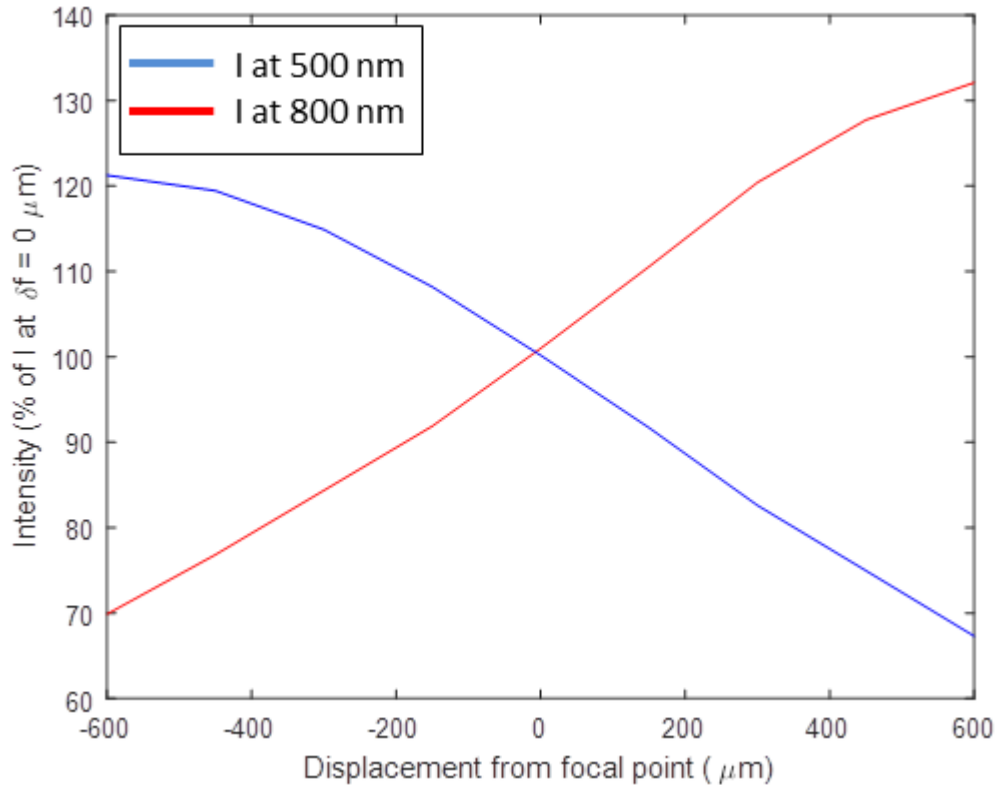


Figure 15 Intensity drift with respect to target distance away from focal point using non-achromatic lenses.

As axial distance from the focal point increased, so did the intensity recorded at 800 nm with a corresponding drop in intensity at 500 nm, as shown in Figure 15. As focal distance was reduced, the effect was reversed. This would prevent useful spectra from being acquired as the sample surface on a droplet experiment can vary significantly on this scale over the course of a droplet. To

combat this chromatic aberration in the instrument, the lenses present in the focusing optics were replaced with achromatic lenses.

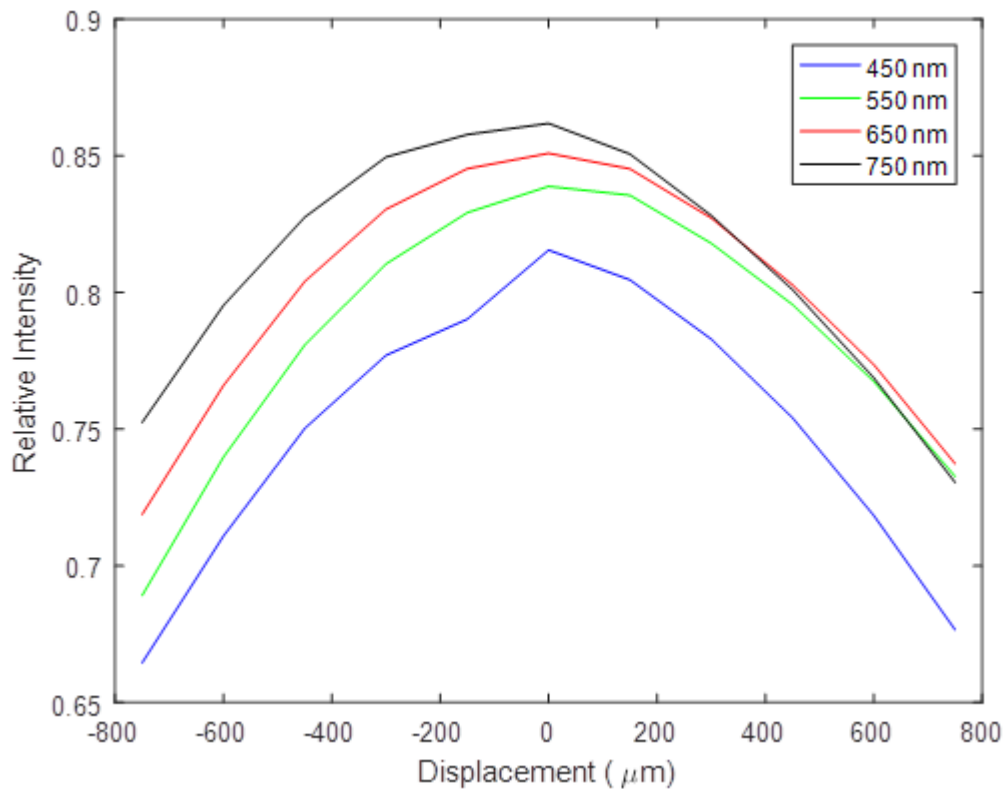


Figure 16 Intensity drift relative to a calibrated 75% reflectance standard as distance from focal point increases by wavelength after focusing optics were replaced with achromatic lenses.

Figure 16 shows chromatic intensity drift relative to a maximum at 0 displacement, indicating that intensity drops uniformly with axial displacement from the focal point. The system was focused by shifting the assembly such that the absolute intensity reflected from a 99% reflectance tile was maximized. Reference spectra of 99% and 2% standards were then taken before and used to correct subsequent spectra. Spectra were taken of a 75% reflectance standard at displacements away from the focal point ranging from -750 μm to +750 μm in increments of 150 μm . Spectra were the average of a 2 x 2 mm

area taken at an interval of 0.2 mm per acquisition. Intensity values are shown for several wavelengths as a decimal of the intensity of the 99% reflectance standard used for calibration. It should be noted that the corrected 75% reflectance standard consistently produces a spectrum of 80 - 85% reflectance rather than the expected 75%. Slight chromatic aberration is present above +200 μm , seen as converging lines, but this is not significant enough to compromise the ability to gather spectra on rough surfaces. Of note is ~5% lower than expected intensity at -150 μm displacement, this does not compromise the spectral response as a whole.

3.5.2.4 Characterisation of intensity with imaging angle relative to target surface

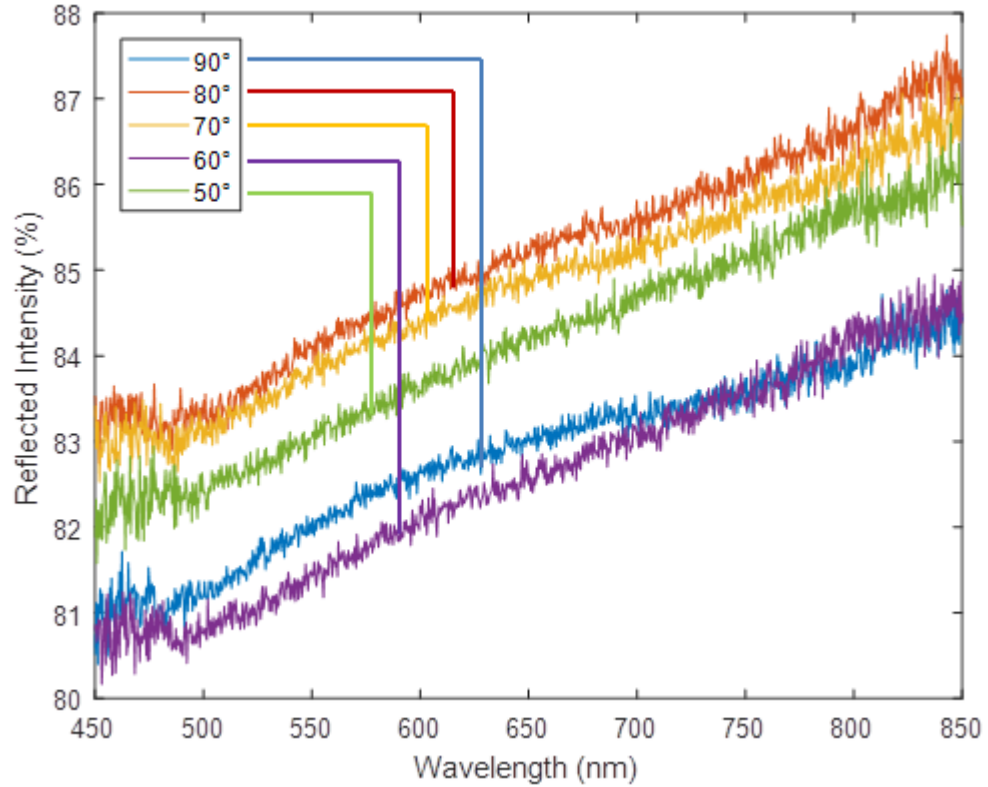


Figure 17 Averaged spectra from a 2x2 cm patch of a 75% reflectance standard taken at different acquisition angles at a resolution of 0.2 mm per acquisition

As the application requires imaging against a shiny metal surface, it is necessary to take measures to ensure that the reflectance spectra gathered are diffuse rather than specular in nature. This was done by taking spectra at an angle away from normal to the plane of the surface of the metal. Figure 17 shows the effect of varying this angle on a 75% diffuse reflectance phantom. No overall trend is present in average intensity is, but a slight relative rise in intensity is visible on the 90° acquisition, relative to a linear baseline, this could be contribution from specular reflection as it is across the wavelength interval

where the light source is at its most intense and the effect becomes less pronounced as imaging angle decreases. An angle of 80° was deemed sufficient to avoid most of the effects of specular reflection and as a result is the acquisition angle used for all subsequent droplet and standard acquisitions, unless stated otherwise.

3.5.2.5 Spectroscopic validation

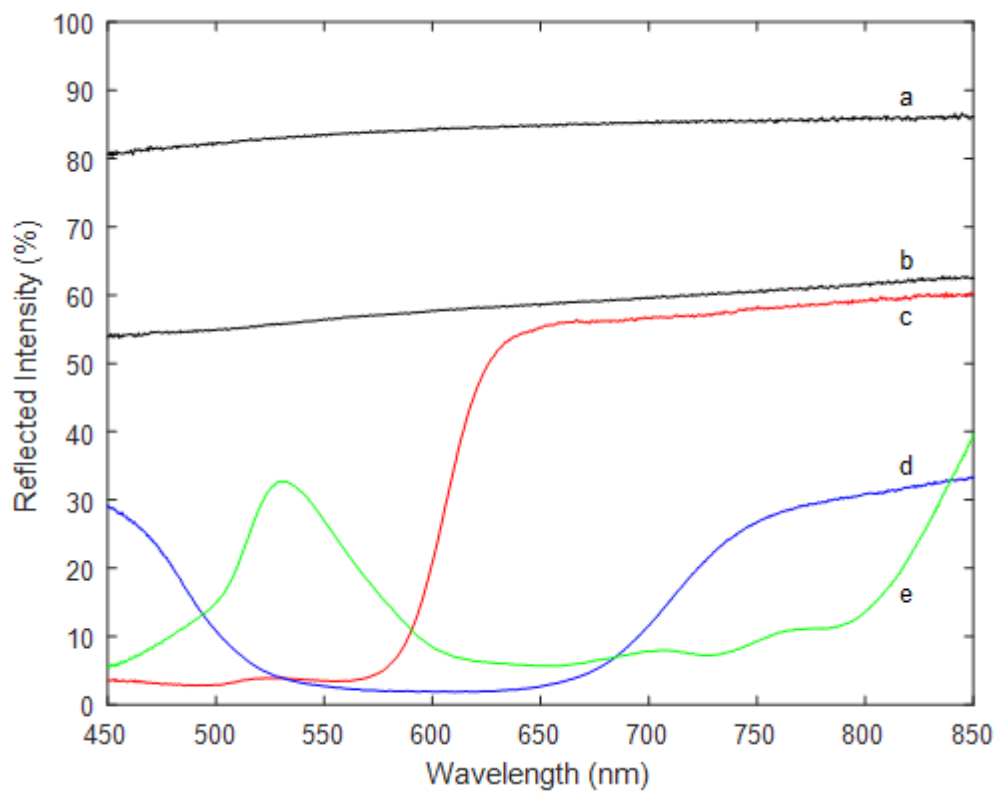


Figure 18. a. 75% calibrated diffuse reflectance standard, b. 50% calibrated diffuse reflectance standard, c. red d. blue and e. green standard colour tiles

Figure 18 shows a series of spectra from both “SPECTRALON” calibrated spectrally flat reflectance tiles and “X-RITE” colour characterisation tiles. Spectra a. and b. are of calibrated 75% and 50% diffuse reflectance tiles, but display slight chromatic asymmetry favouring the NIR, as well as a 5-10% larger

relative intensity than expected. If the 99% standard is not spectrally flat and reflects lower intensity than desired, it could produce similar results to those observed after flat field correction is performed. As the drift is on the order of 5-10% and is a known quantity, this does not compromise the ability to gather subsequent spectra c, d and e are red, blue and green X-RITE colour checker tiles which behave as expected with maxima in the 430-470 nm, 530-550 nm and 630-650 nm regions respectively. It should be noted that X-RITE does not provide absolute reflected intensity standardisation, nor make any claims about the performance in the NIR region and so only the relative intensities particular to the colour are guaranteed. All spectra were gathered at 90° to the surface and are the average of a 2x2 cm area of the target, taken at a resolution of 0.2 mm per pixel.

3.6 Rust area analysis

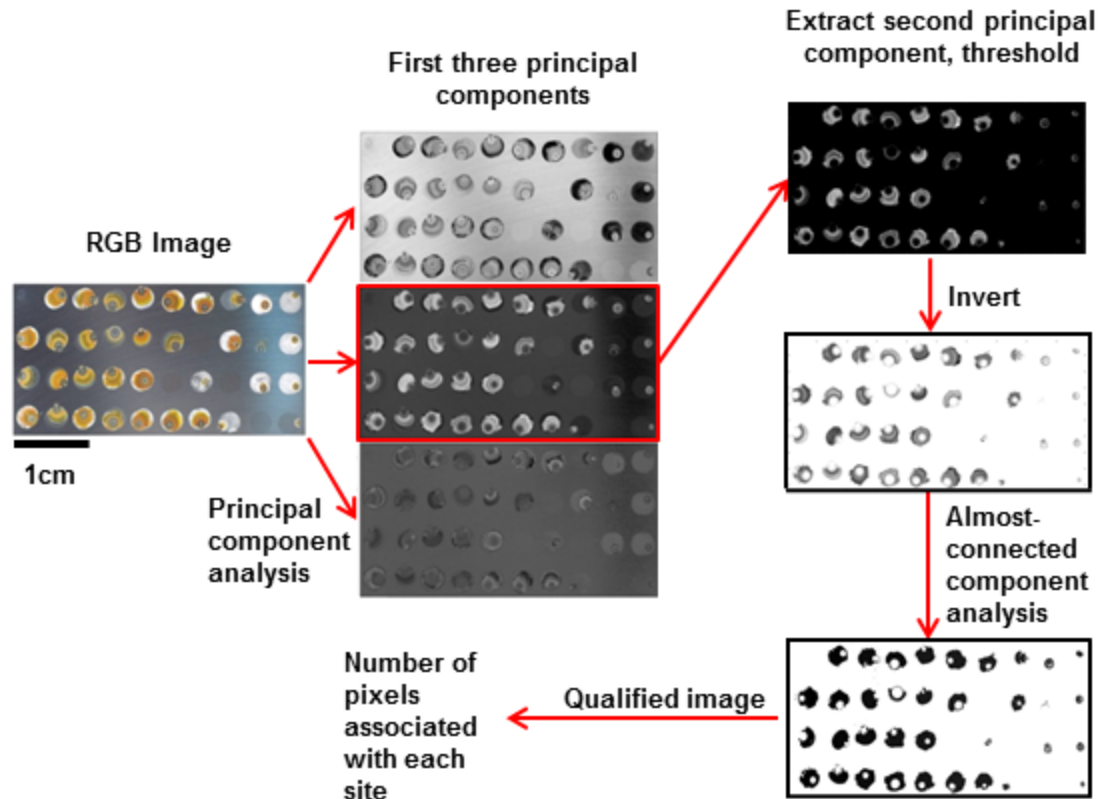


Figure 19 Flowchart of the procedure for extracting rust areas associated with individual corrosion sites from a colour photograph using the principal component analysis method

Semi-automated high-throughput rust area analysis was performed on colour photographs using Matlab R2017b[148]. Scripts used can be found in Appendices 11.4 and 11.5. Figure 19 shows the process for extracting rust areas from corrosion sites using the principal component analysis (PCA) segmentation technique, the full procedure is as follows:

1. Images were segmented using one of four techniques outlined below in sections 3.6.1 to 3.6.4 in order to separate 'rust' pixels from 'non-rust' pixels (Figure 19 shows segmentation via the 2nd principal component).

2. Connected component analysis was performed to group neighbouring pixels into individual 'sites', using the 'bwconncomp' function[148]
3. Sites with less than 100 pixels were discarded.
4. Almost-connected component analysis was used to group neighbouring sites (distance of less than 50 pixels from its nearest neighbour) and label individual corrosion sites.
5. The number of pixels associated with each corrosion site was then extracted and converted to an area by multiplication by the average pixel dimensions as determined from the scale photographed alongside the sample.

3.6.1 Red-Blue colour channel subtraction

The RGB colour image is separated into its constituent colour channels and the red channel is subtracted from the blue, before thresholding to produce the segmented image. Matlab code for this procedure can be found in Appendix 11.5.1

3.6.2 Principal component analysis

Principal component analysis was performed on the data; the second principal component is then thresholded to produce the segmented image. Matlab code for this procedure can be found in appendix 11.5.2

3.6.3 HSV thresholding

The image is converted to HSV colour space from sRGB using the Matlab standard "rgb2hsv" function before thresholds are then applied in hue and saturation. Matlab code for this procedure can be found in Appendix 11.5.3

3.6.4 $L^*a^*b^*$ thresholding

The image is converted to $L^*a^*b^*$ colour space from sRGB using the Matlab standard “rgb2lab” function with the ‘d65’ standard white point. A threshold is then applied in b^* . Matlab code for this procedure can be found in appendix 11.5.4

3.7 Confocal microscopy for pit volume measurement

Pit volumes measurements were performed using an Olympus LEXT OLS-4000 confocal laser scanning microscope. 3D measurements were taken by sequentially scanning vertical sections of the sample which were reconstructed by the software to a 3D volume. The upper and lower limits of each 3D measurement were chosen by focusing on the metal surface and the lowest visible point in the pit respectively. Each cross section measurement was the average of 16 repeated scans of each horizontal slice of the sample.

Each measurement was then tilt corrected using the software to compensate for any uneven surface present from the mounting process. Volumes were then taken by defining a bounding box around the horizontal extent of the pit and integrating the volume using the software.

4. CHARACTERISATION OF CORROSION PRODUCTS OF 304L STAINLESS STEEL USING COLOUR PHOTOGRAPHY AND RAMAN SPECTROSCOPY

4.1 Introduction

Intermediate level nuclear waste (ILW) will be packaged in containers made of 304L and 316L stainless steel and stored above ground in warehouses for up to 100 years while a geological disposal facility (GDF) is prepared to accept them for permanent disposal.[2] During this period the containers will be open to the atmosphere and therefore susceptible to deposition and deliquescence of aerosol salts which can cause atmospheric pitting corrosion to take place.

While there have been investigations into the corrosion products of stainless steels, they are either for full immersion conditions and/or at high temperatures[149-151] or in atmospheric conditions but in urban or tropical marine environments[99, 101] which do not reflect the relatively still, covered conditions present in temporary waste stores where the majority of salt encountered is calcium chloride and carbonate from concrete dust.[9, 11, 16]

The aim of this chapter is to assess the difference in corrosion products deposited during atmospheric corrosion of 304L stainless steel in stores relevant conditions. This will be done by comparison of synthesised iron oxide and oxide-hydroxide powder samples with controlled atmospheric corrosion droplet experiments on stainless steel using Raman spectroscopic mapping. This will be done by comparing:

- Effects of salt – MgCl_2 and CaCl_2 .

- Effects of atmospheric conditions – fixed 46% RH, 30°C and fluctuating ambient temperature and humidity on 100 μgcm^{-2} droplets exposed for 14 days
- Effects of chloride deposition density (CDD) – 100 μgcm^{-2} , 50 μgcm^{-2} and 20 μgcm^{-2} on MgCl_2 droplets exposed for 24 days
- Effects of exposure time – 100 μgcm^{-2} MgCl_2 droplets exposed to fixed 46% RH, 30°C for 14 days and 24 days.

4.2 Results

4.2.1 Synthesised Iron Oxides and oxide-hydroxides

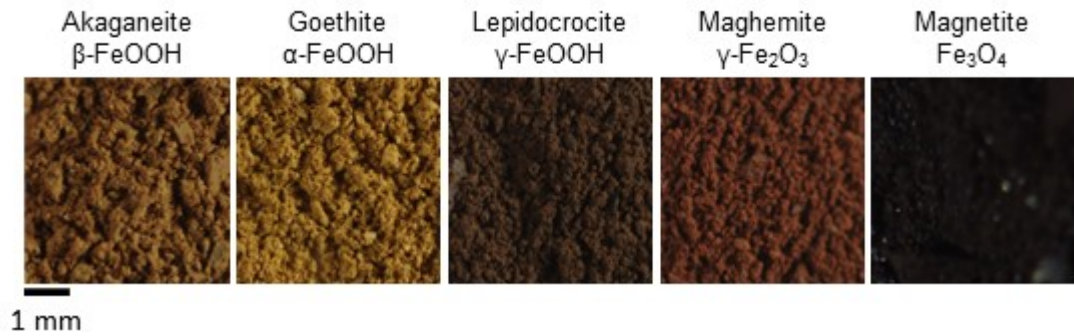


Figure 20 Colour images of powdered akaganeite (β -FeOOH), goethite (α -FeOOH), lepidocrocite (γ -FeOOH), maghemite (γ -Fe₂O₃) and magnetite (Fe₃O₄)

Figure 20 shows colour images of iron oxides and oxide-hydroxides that were synthesised using methods outlined by Cornell & Schwertmann[73], (Appendix 11.2) to provide standards for imaging and spectroscopy. Powdered akaganeite (β -FeOOH), goethite (α -FeOOH), lepidocrocite (γ -FeOOH), maghemite (γ -Fe₂O₃) and magnetite (Fe₃O₄) are shown from left to right.

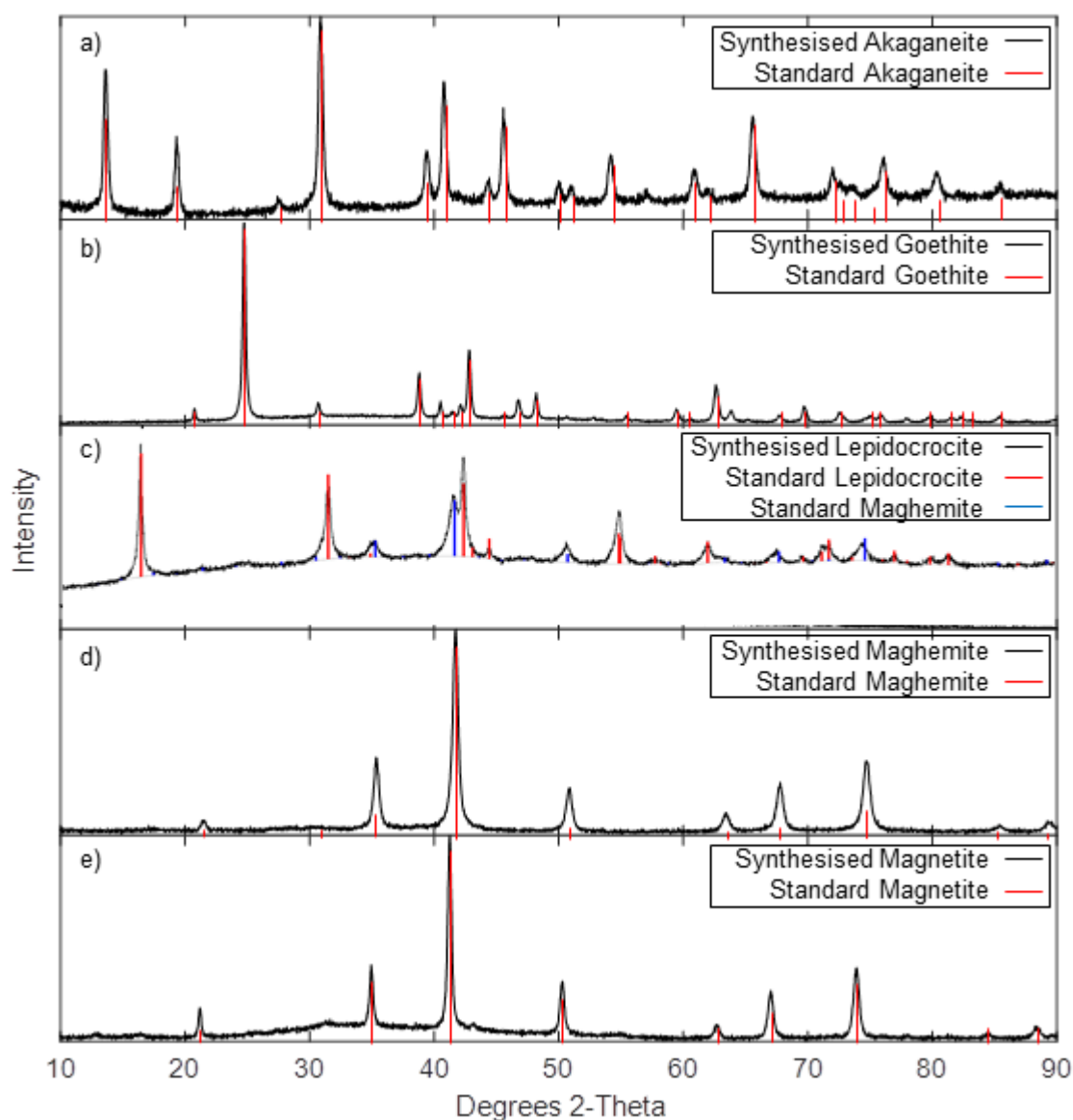


Figure 21 X-ray diffraction spectra of synthesised iron oxides and oxide-hydroxides, overlaid with coloured bars showing suggested fit from ICDD PDF2 standards database[152] a) akaganeite (β -FeOOH), b) Goethite (α -FeOOH), c) Lepidocrocite with some maghemite (γ -FeOOH), d) Maghemite (γ -Fe₂O₃), e) Magnetite (Fe₃O₄)

X-ray diffraction spectroscopy was performed on the synthesised standards in order to verify the presence of desired crystal phase via comparison with the ICDD PDF2 standards database[152]. Figure 21 shows the results of this spectroscopy. All syntheses show good agreement with their expected phase,

apart from lepidocrocite which contains a significant fraction of maghemite. A significant baseline is also present for lepidocrocite and to a lesser degree akaganeite and magnetite.

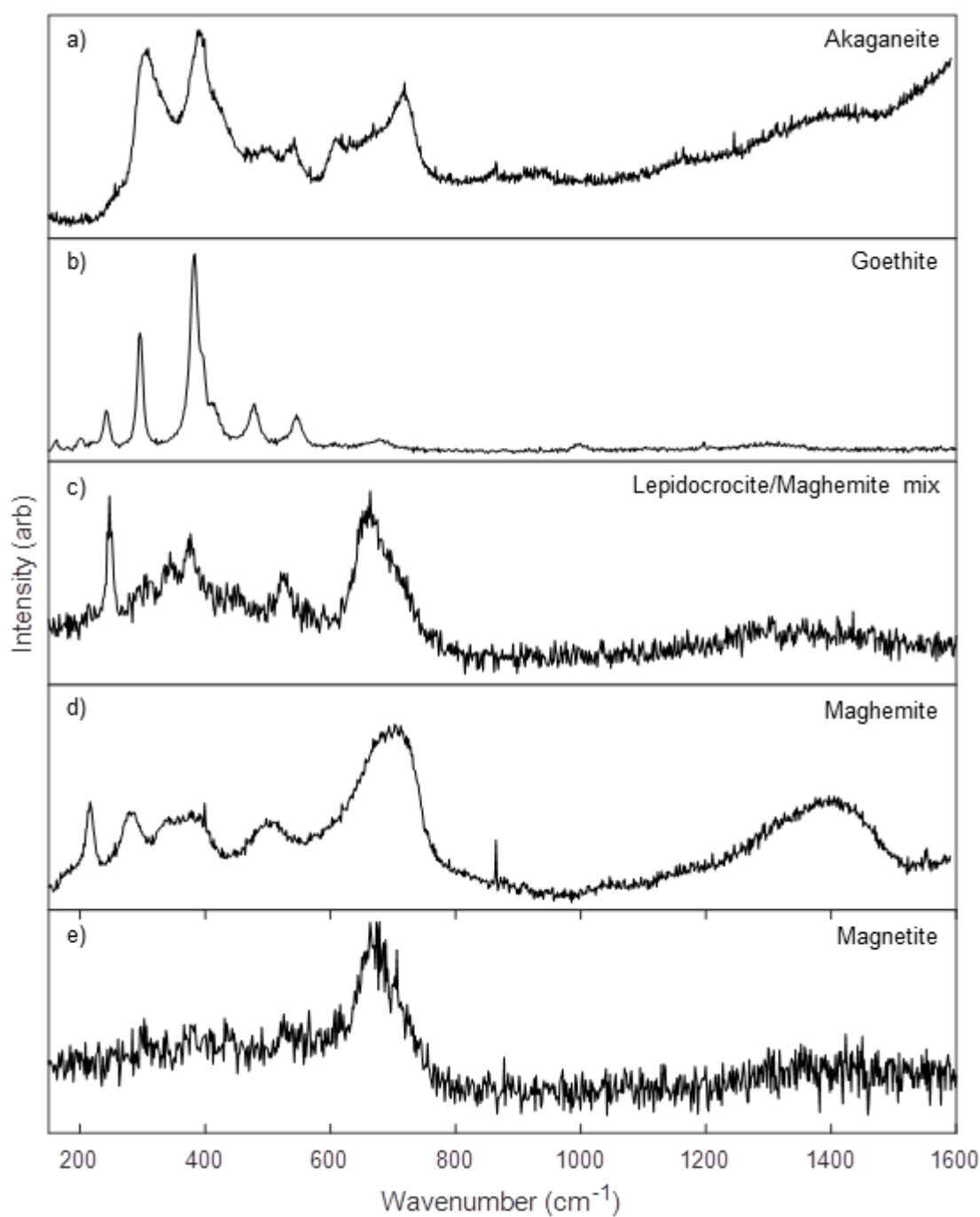


Figure 22 Raman spectra of synthesised iron oxides and oxide-hydroxides a) akaganeite (β -FeOOH), b) Goethite (α -FeOOH), c) Lepidocrocite with some maghemite (γ -FeOOH), d) Maghemite (γ -Fe₂O₃), e) Magnetite (Fe₃O₄)

Raman spectroscopy was performed on the synthesised powders, shown in Figure 22. a) Akaganeite has peaks at 300, 390, 520, 610 and 720 cm⁻¹. b)

Goethite has peaks at 160, 200, 240, 300, 380, 480, 550, 680 and 1300 cm^{-1} . c) Lepidocrocite (with maghemite) had peaks at 250, 340, 370, 530, 670 cm^{-1} . d) Maghemite has peaks at 180, 365, 500, 650-720 and 1300 cm^{-1} . e) Magnetite has a single visible peak at 650 cm^{-1} .

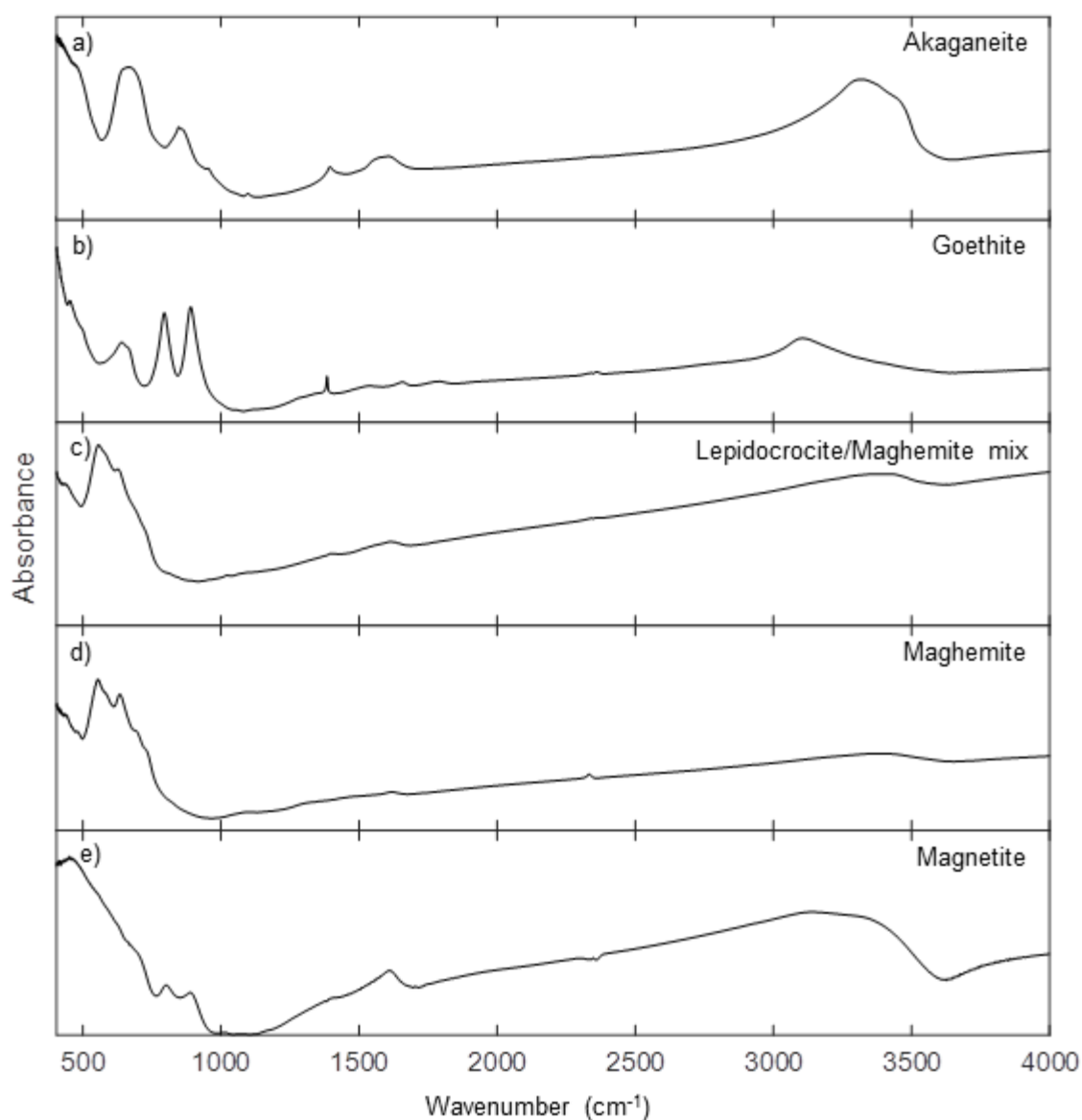


Figure 23 Fourier-Transform Infra-red spectroscopy of synthesised iron oxides and oxide-hydroxides a) akaganeite ($\beta\text{-FeOOH}$), b) Goethite ($\alpha\text{-FeOOH}$), c) Lepidocrocite with some maghemite ($\gamma\text{-FeOOH}$), d) Maghemite ($\gamma\text{-Fe}_2\text{O}_3$), e) Magnetite (Fe_3O_4)

Figure 23 shows Fourier-transform infra-red spectroscopy of synthesised powder samples. All samples have a region of characteristic features from 500-1000 cm^{-1} and a maximum absorbance from 1000-1200 cm^{-1} .

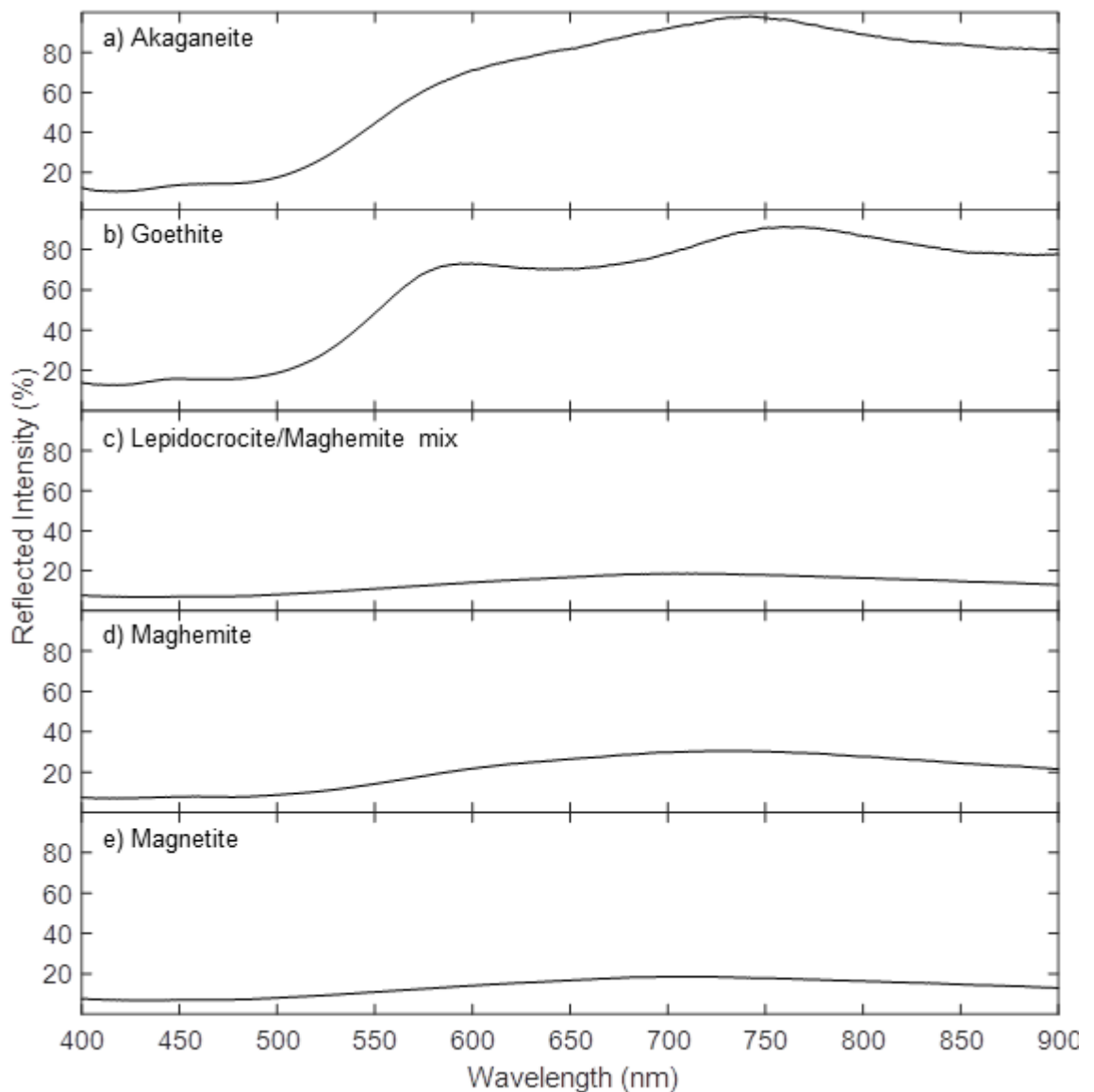


Figure 24 UV-VIS-NIR spectroscopy of synthesised iron oxides and oxide-hydroxides a) akaganeite (β -FeOOH), b) Goethite (α -FeOOH), c) Lepidocrocite with some maghemite (γ -FeOOH), d) Maghemite (γ -Fe₂O₃), e) Magnetite (Fe₃O₄)

Figure 24 shows UV-VIS-NIR spectroscopy of the synthesised iron oxide and oxide-hydroxide standards. All spectra have a minimum at 420-500 nm. a)

Akaganeite (β -FeOOH) and b) Goethite (α -FeOOH) both show similar double peaks at 575 and 775 nm and have the highest overall reflectance with a maximum at 850 nm. The c) Lepidocrocite (γ -FeOOH)-maghemite mix, d) Maghemite (γ -Fe₂O₃), e) Magnetite (Fe₃O₄) all reflect a much less light and have a maximum reflectance at 700-750 nm of 20-30%.

4.2.2 Droplet Experiments

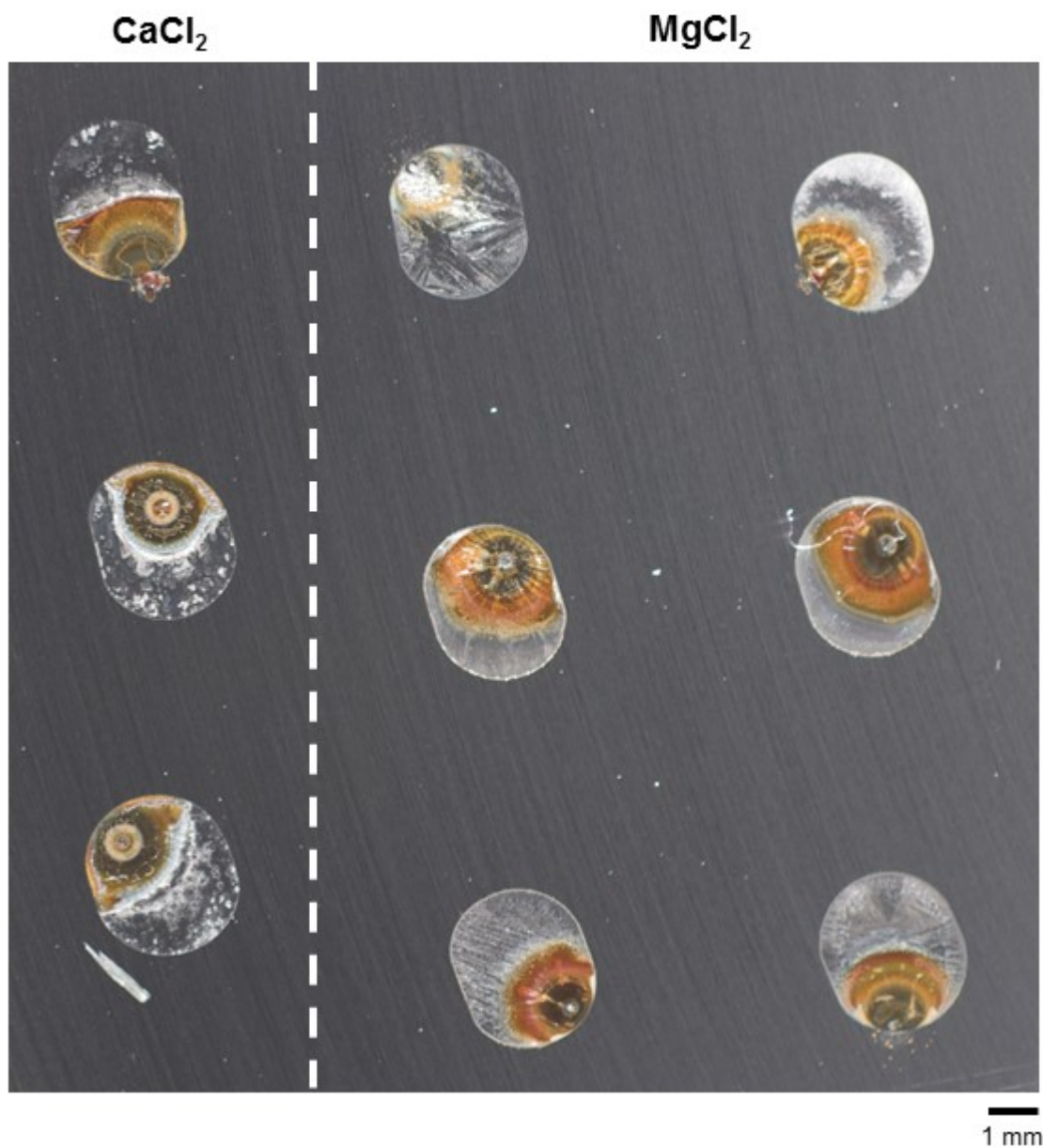


Figure 25 CaCl_2 and MgCl_2 droplets deposited on 304L stainless steel with a chloride deposition density of $100 \mu\text{gcm}^{-2}$ and exposed for 14 days at 46% relative humidity and 30°C .

Arrays of droplets of MgCl_2 and CaCl_2 were deposited on 304L steel and exposed in either fixed 46% RH and 30°C or fluctuating ambient conditions. Figure 25 is an example of one sample plate of 304L steel after 14 days

exposed to fixed 46% RH and 30°C with CaCl₂ and MgCl₂ droplets of chloride deposition density 100µgcm⁻². All droplets contain pits. MgCl₂ droplets exposed to fixed conditions all have a dark ring of corrosion product directly around the pit mouth, surrounded by a lighter ring of red-brown rust. This in turn is surrounded by a white precipitate which occupies the rest of the droplet to the edge. CaCl₂ droplets exposed to fixed conditions similarly have a dark ring directly around the pit surrounded by lighter red-brown rust. There is an additional thick band of white precipitate immediately at the edge of the red-brown rust and further small areas of white precipitate throughout the remainder of the droplet. CaCl₂ droplets that were exposed to fluctuating ambient conditions have a similar red-brown ring of corrosion product surrounded by white precipitated salt as the MgCl₂ droplets exposed to fixed conditions. The major difference is in a deep red corrosion product which has precipitated directly over the pit mouth. MgCl₂ droplet exposed to fluctuating conditions had a thinner band of corrosion product and no precipitate. After 14 days a single, representative droplet for each salt species and exposure condition was selected for Raman mapping by similarity to other members of its set and consistency of features. No sample preparation such as rinsing of salt solution or corrosion product off the sample surface was performed for any photography or Raman spectroscopy in this chapter. Measurements did not take place under RH or temperature control, however, due to equipment limitations.

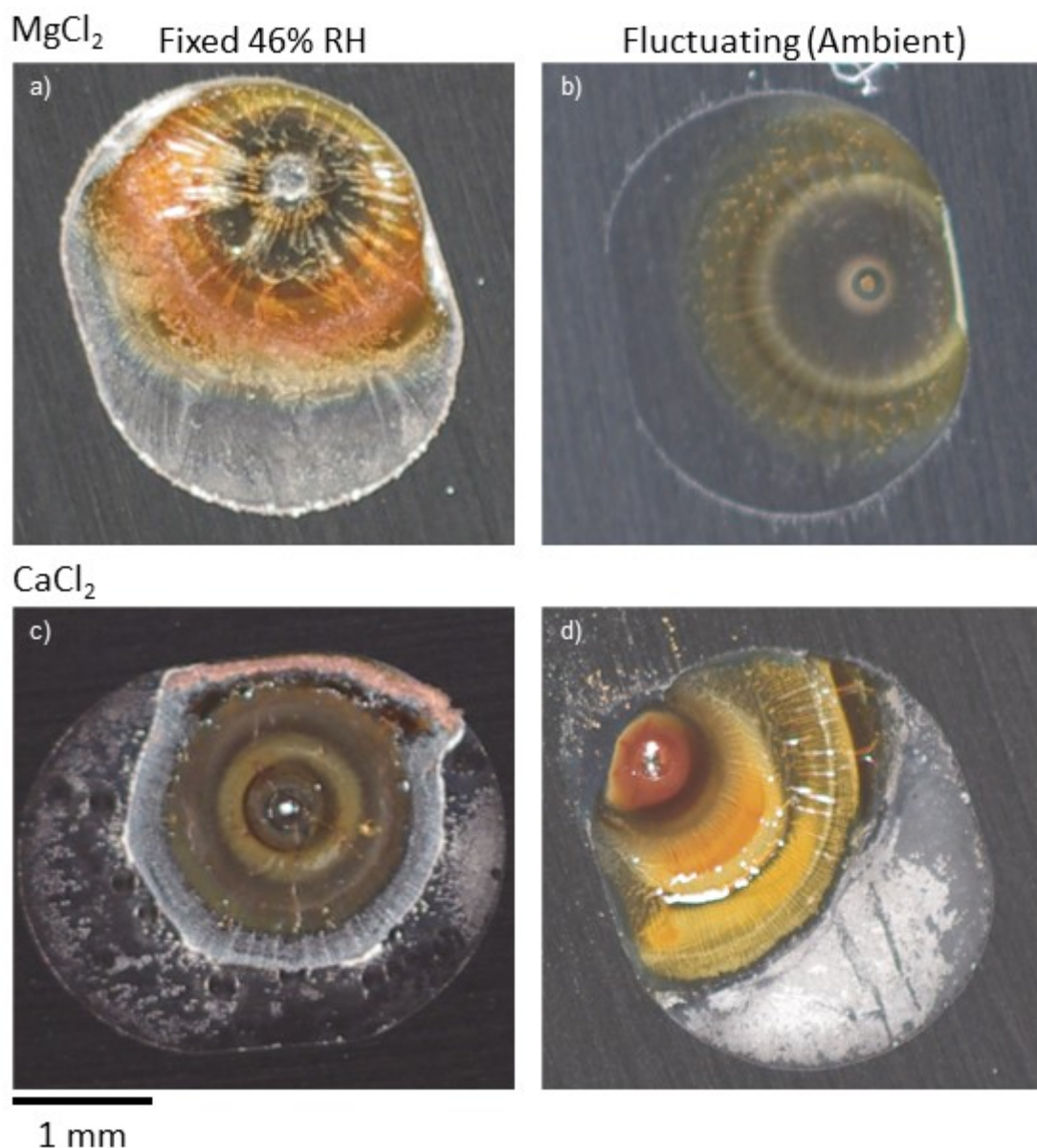
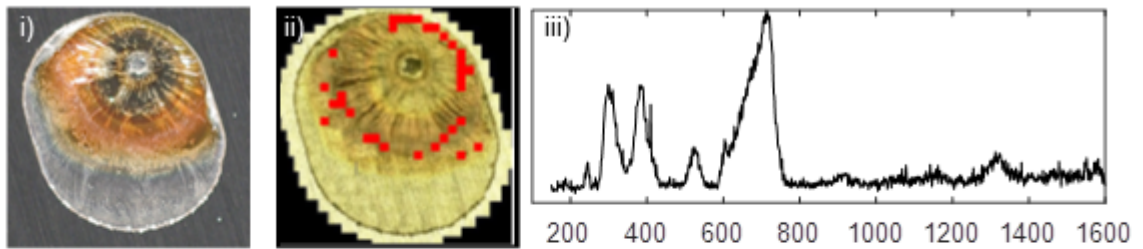


Figure 26 Colour photography of the 100 μgcm^2 droplets selected for Raman mapping after being exposed for 14 days. a) MgCl_2 and c) CaCl_2 were exposed to fixed 46% RH and 30°C b) MgCl_2 was exposed to ambient conditions which fluctuated between 26 and 55% relative humidity and 19 and 31°C and d) CaCl_2 was exposed to conditions which fluctuated between 24 and 46% relative humidity and 17 and 24°C

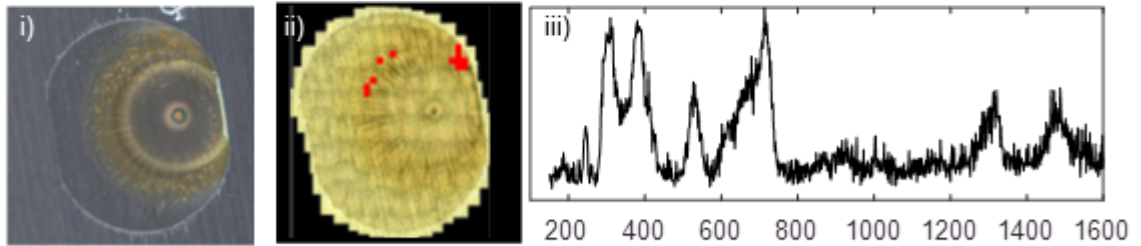
Figure 26 compares colour photography of 100 μgcm^{-2} MgCl_2 and CaCl_2 droplets on which Raman mapping was performed. a) and c) were exposed at fixed 46% RH and 30°C while b) MgCl_2 was exposed to ambient conditions which fluctuated between 26 and 55% relative humidity and 19 and 31°C

(shown in detail in Figure 35) and d) CaCl_2 was exposed to conditions which fluctuated between 24 and 46% relative humidity and 17 and 27°C (Shown in detail in Figure 36) a), b) and c) precipitated rust in a ring around the pit mouth, which remains clear of corrosion product itself. d) had deeper, red rust directly over the pit mouth. All droplets then had a region of white precipitate outside the main rust region. This precipitate was dense immediately around the rust on droplet c) while other droplets it was either evenly spread across the non-rusty regions of the droplet or at denser the droplet edge.

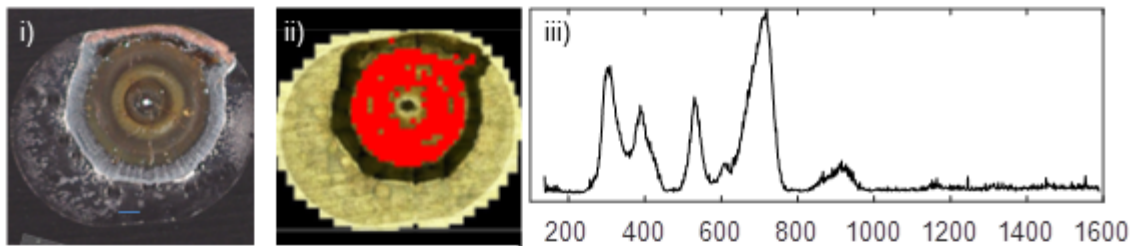
a) MgCl_2 , fixed conditions



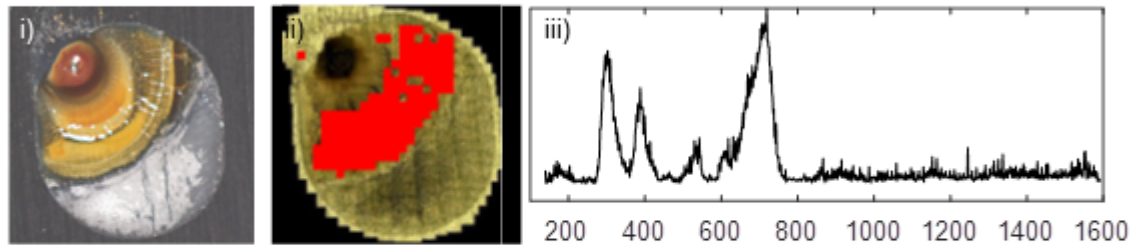
b) MgCl_2 , fluctuating conditions



c) CaCl_2 , fixed conditions



d) CaCl_2 , fluctuating conditions



1 mm

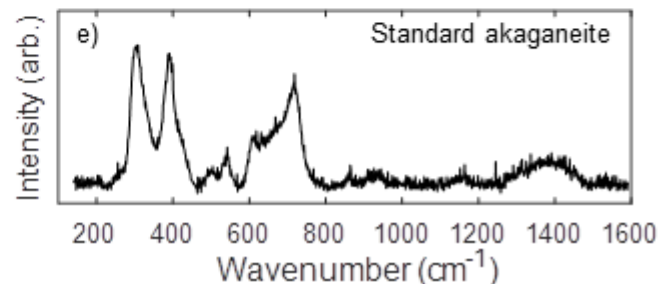


Figure 27 i) Colour photography of $100 \mu\text{gcm}^{-2}$ droplets of a) MgCl_2 exposed to fixed 46% RH and 30°C , b) MgCl_2 exposed to fluctuating 26-55% RH and $19\text{--}31^\circ\text{C}$, c) CaCl_2 exposed to fixed 46% RH and 30°C and d) CaCl_2 exposed to 24-46% RH and $17\text{--}27^\circ\text{C}$. ii) Distribution of akaganeite on droplets as determined by least squares mapping using WiRE 4.0 software iii) the average of all spectra highlighted by the mapping process. e) Standard akaganeite spectrum used for least squares fitting.

Raman mapping was performed by raster scanning across the sample surface, acquiring spectra at set intervals. Each spectrum was assessed for the presence of a compound via either least squares (DCLS) fitting against a known standard spectrum or by taking the intensity at a particular wavenumber and thresholding using the WiRE 4.0 software provided with the Raman spectrometer. Figure 27 shows the results of this process for akaganeite. For all droplets a)-d), i) shows a colour image of the droplet, ii) shows the distribution of akaganeite in red of the droplets as assessed by direct classical least squares (DCLS) fitting against e) synthesised standard akaganeite from Figure 22 with a minimum least squares index threshold of 0.4. iii) shows the averaged spectrum of all points associated with a compound in this manner.

The akaganeite in a) MgCl_2 exposed to fixed 46% RH and 30°C was predominantly found at the intersection between the main rust band and the droplet edge, with a smaller amount distributed in a ring throughout the main rust ring. In b) MgCl_2 exposed in fluctuating ambient conditions which varied between 26-55% RH and 19-31°C, a small amount of akaganeite was present in the main rust band but most was concentrated at the droplet edge adjacent to the white salt precipitate. There were also two peaks present at 1350 cm^{-1} and 1480 cm^{-1} rather than the broad 1400 cm^{-1} present in the standard and the other droplets. In c) CaCl_2 exposed to fixed 46% RH and 30°C, the akaganeite was present across the entire central region of the droplet above the pit, extending to the boundary with the white precipitate. There was an additional peak present on these spectra at 900 cm^{-1} . In d) CaCl_2 exposed to fluctuating ambient

conditions which varied between 24-46% RH and 17-27°C the akaganeite was concentrated in a band across the droplet away from the pit mouth.

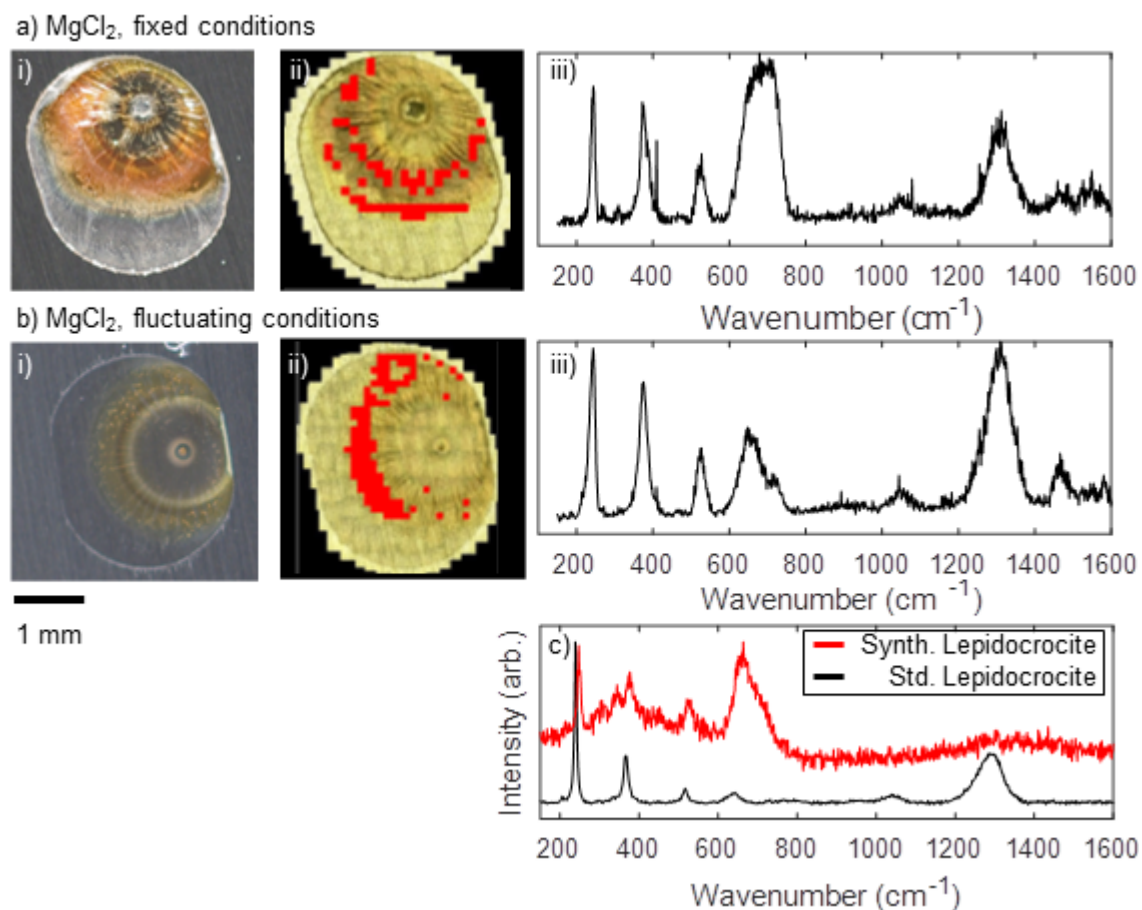


Figure 28 i) Colour photography of $100 \mu\text{gcm}^{-2}$ droplets of a) MgCl_2 exposed to fixed 46% RH and 30°C, b) MgCl_2 exposed to fluctuating 26-55% RH and 19-31°C. ii) Distribution of lepidocrocite on droplets as determined by least squares mapping using WiRE 4.0 software iii) the average of all spectra highlighted by the mapping process. c) Standard lepidocrocite taken from a weathering steel sample spectrum used for least squares fitting along with the spectrum from the synthesised lepidocrocite.

Figure 28 shows the distribution of lepidocrocite as determined by least squares fitting of a lepidocrocite spectrum taken from a weathering steel sample (chosen for similarity to literature spectra[81-83]). a,b) i) shows a colour image of the droplet, ii) shows the distribution of akaganeite in red of the droplets as assessed by direct classical least squares (DCLS) fitting with a minimum least

squares index threshold of 0.4. c) shows the standard lepidocrocite Raman spectrum acquired on a weathering steel sample that was used for fitting alongside the spectrum of the mixed lepidocrocite/maghemite spectrum from the synthesised powder sample. iii) shows the averaged spectrum of all points associated with a compound in this manner. The lepidocrocite in a) MgCl_2 exposed to fixed 46% RH and 30°C was predominantly found in two bands at the centre and edge of the main rust area away from the droplet edge. In b) MgCl_2 exposed in fluctuating ambient conditions which varied between 26-55% RH and 19-31°C, lepidocrocite constituted a large band across the majority towards the outer edge of the main rust area in relation to the pit. No lepidocrocite was present on either CaCl_2 droplet.

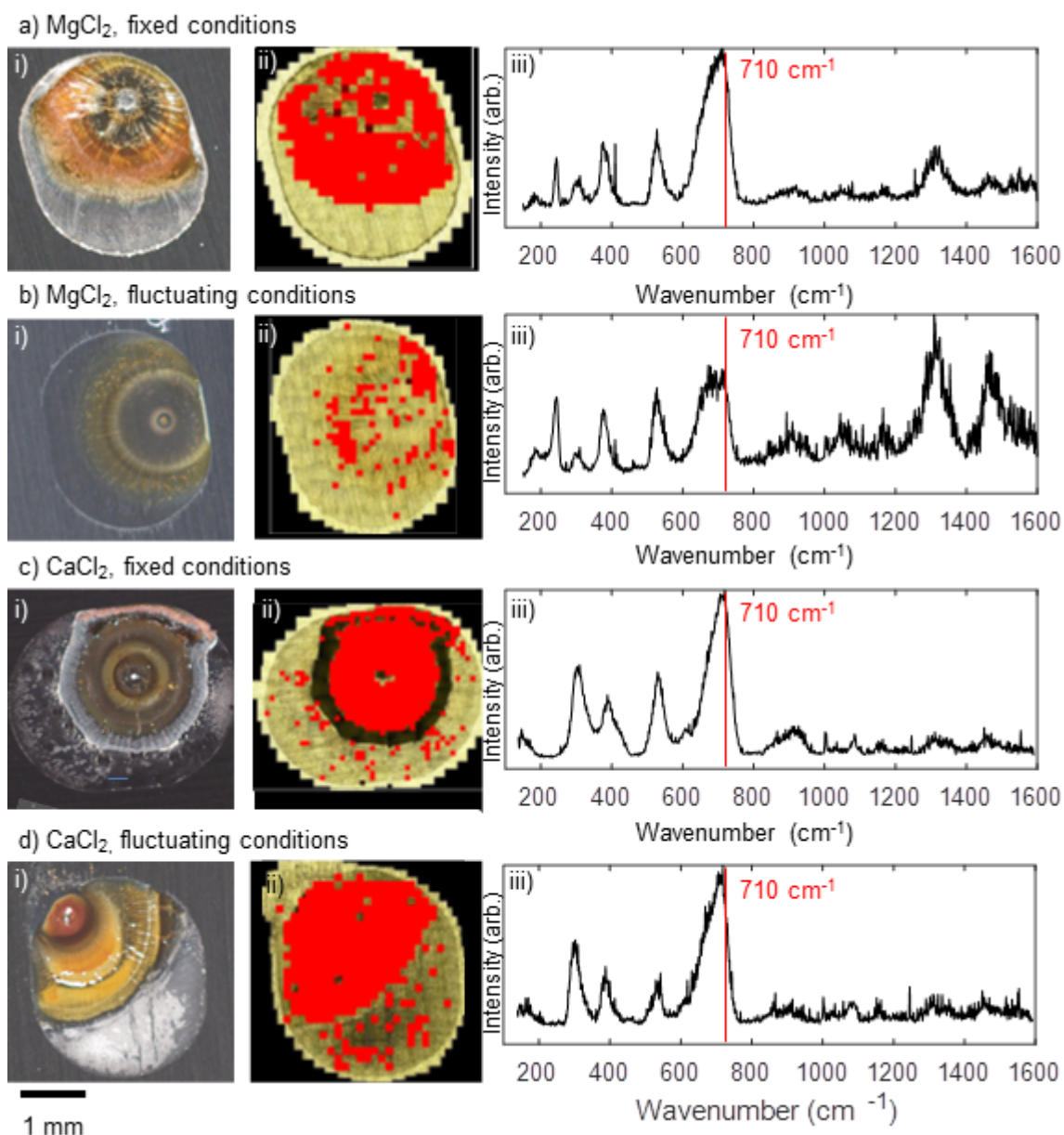


Figure 29 i) Colour photography of $100 \mu\text{gcm}^{-2}$ droplets of a) MgCl_2 exposed to fixed 46% RH and 30°C , b) MgCl_2 exposed to fluctuating 26-55% RH and $19\text{--}31^\circ\text{C}$, c) CaCl_2 exposed to fixed 46% RH and 30°C and d) CaCl_2 exposed to 24-46% RH and $17\text{--}27^\circ\text{C}$. ii) Distribution of 710cm^{-1} peak on droplets as determined by peak mapping using WiRE 4.0 software iii) the average of all spectra highlighted by the mapping process.

A large number of spectra had no discernible lower wavenumber peaks for specific phase assignment due to poor signal to noise, but did contain a broad peak at 710 cm^{-1} . Figure 29 shows the distribution of this peak across all

droplets a-d). i) shows colour photographs of the droplet, a-d) ii) shows maps created by highlighting all spectra with an intensity about 150 at a wavenumber 710 cm^{-1} a-d) iii) are the average spectrum of all highlighted pixels in an associated droplet.

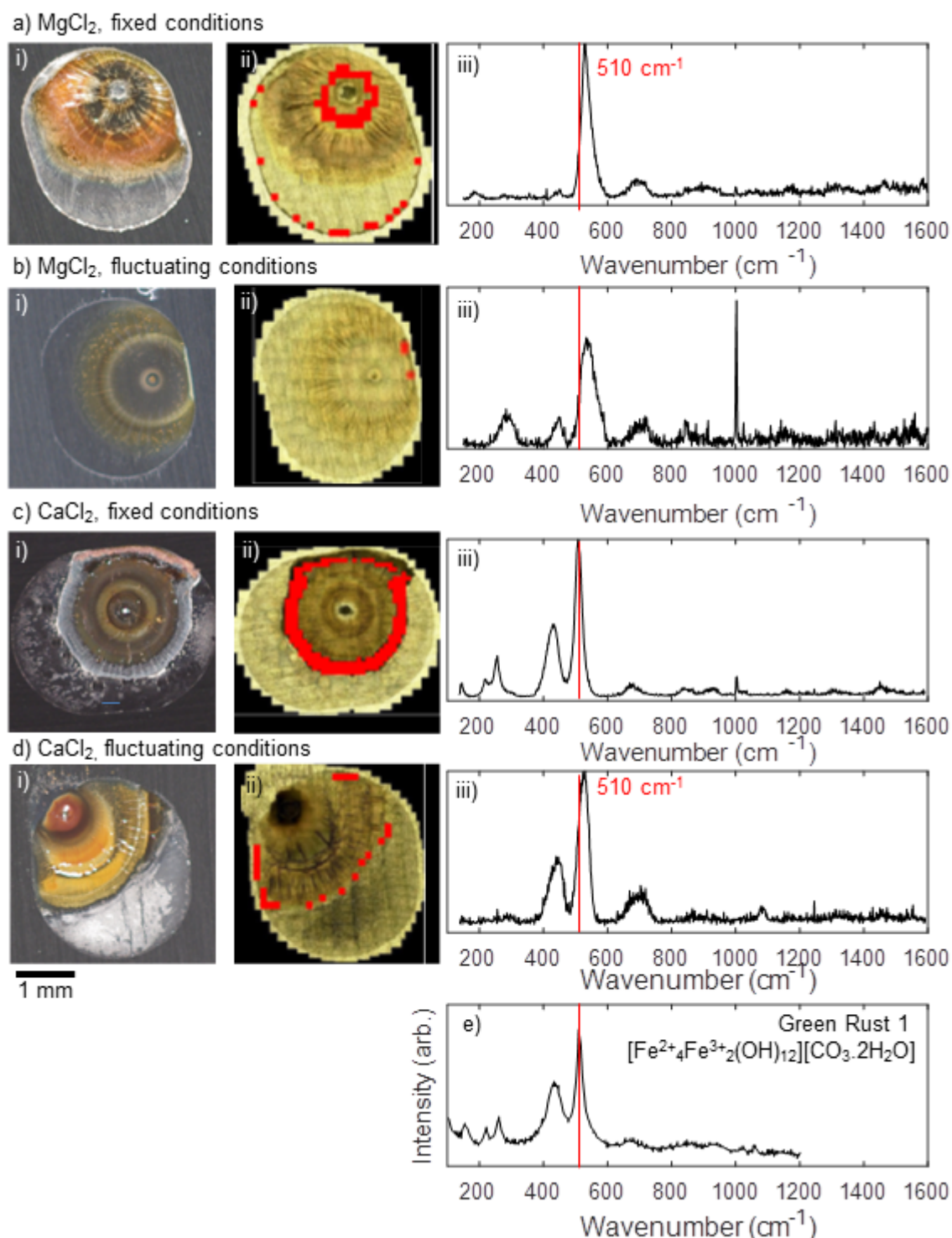


Figure 30 i) Colour photography of $100 \mu\text{gcm}^{-2}$ droplets of a) MgCl_2 exposed to fixed 46% RH and 30°C , b) MgCl_2 exposed to fluctuating 26-55% RH and $19\text{--}31^\circ\text{C}$, c) CaCl_2 exposed to fixed 46% RH and 30°C and d) CaCl_2 exposed to 24-46% RH and $17\text{--}27^\circ\text{C}$. ii) Distribution of 510cm^{-1} peak on droplets as determined by peak mapping using WIRE 4.0 software iii) the average of all spectra highlighted by the mapping process. e) Standard green rust spectrum for comparison[96]

Figure 30 shows the distribution of the peak at 510cm^{-1} . For all droplets a)-d), i) shows a colour image of the droplet, ii) shows all points with a 510cm^{-1} peak with an intensity of over 150 counts in red iii) shows the averaged spectrum of all points associated with this peak. e) is a published spectrum of green rust 1[96]

In a) MgCl_2 exposed to fixed 46% RH and 30°C this peak is distributed in two locations. The first band is directly around the pit mouth and the second is around the droplet edge, the peak itself is slightly shifted to $530\text{-}540\text{ cm}^{-1}$. There are smaller peaks present at 180 cm^{-1} , 440 cm^{-1} and 900 cm^{-1} . In b) MgCl_2 exposed in fluctuating ambient conditions which varied between 26-55% RH and $19\text{-}31^\circ\text{C}$, a small number of pixels with the $530\text{-}540\text{ cm}^{-1}$ peak the droplet edge adjacent to the white salt precipitate. There are secondary peaks at 280 cm^{-1} , 440 cm^{-1} and 900 cm^{-1} . In c) CaCl_2 exposed to fixed 46% RH and 30°C , the 510 cm^{-1} peak was present across the white precipitate at the edge of the rust. The secondary peaks are present at 210 cm^{-1} , 240 cm^{-1} , 440 cm^{-1} , 900 cm^{-1} and 1000 cm^{-1} . In d) CaCl_2 exposed to fluctuating ambient conditions which varied between 24-46% RH and $17\text{-}27^\circ\text{C}$, the 510 cm^{-1} peak is present at the edge of the rust area. The peak is also slightly shifted to $520\text{-}530\text{ cm}^{-1}$. There is a small carbonate peak present at 1080 cm^{-1}

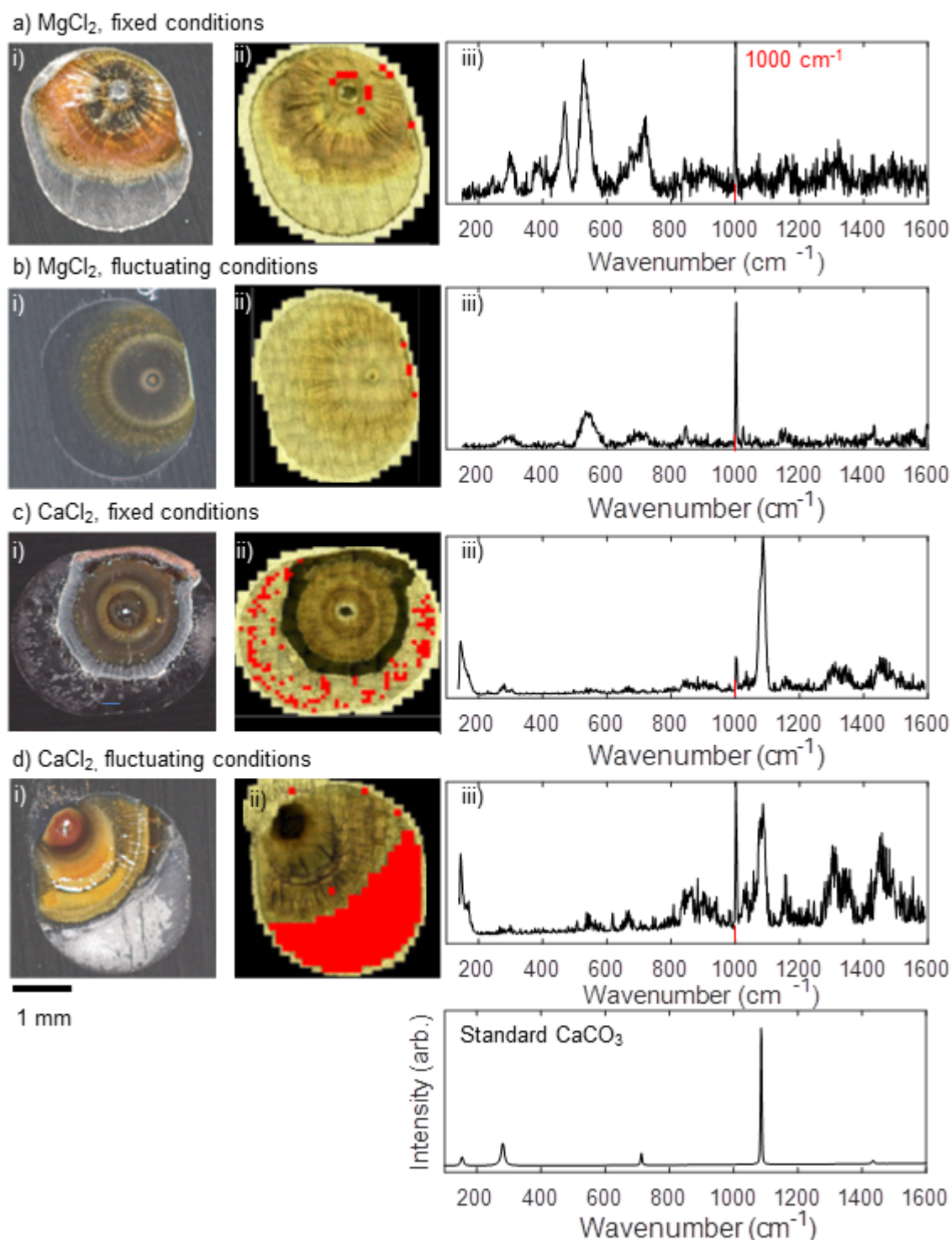


Figure 31 i) colour photography of $100 \mu\text{gcm}^{-2}$ droplets of a) MgCl_2 exposed to fixed 46% RH and 30°C , b) MgCl_2 exposed to fluctuating 26-55% RH and $19\text{--}31^\circ\text{C}$, c) CaCl_2 exposed to fixed 46% RH and 30°C and d) CaCl_2 exposed to 24-46% RH and $17\text{--}27^\circ\text{C}$. ii) Distribution of 1000cm^{-1} peak on droplets as determined by peak mapping using WIRE 4.0 software iii) the average of all spectra highlighted by the mapping process. e) Standard calcium carbonate spectrum for comparison

Figure 31 shows the distribution of the peak at 1000 cm^{-1} , associated with the bicarbonate anion. For all droplets a)-d), i) shows a colour image of the droplet, ii) shows all points with a 1000 cm^{-1} peak with an intensity of over 150 counts in red iii) shows the averaged spectrum of all points associated with this peak. e) is a standard spectrum of calcium carbonate (CaCO_3)[153] with a major peak at 1080 cm^{-1}

a) CaCl_2 , Fluctuating conditions

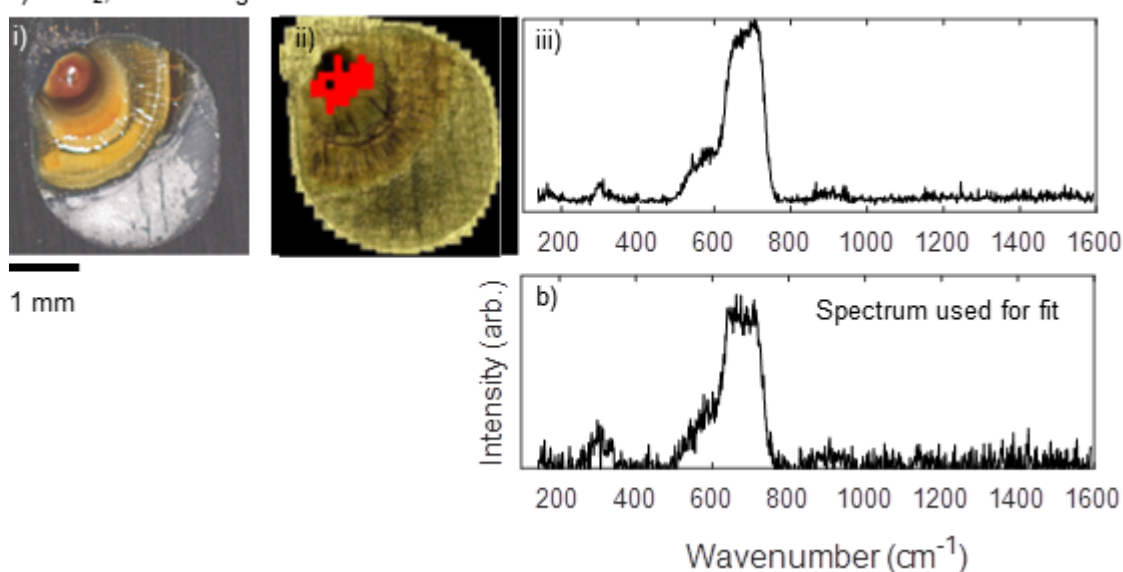
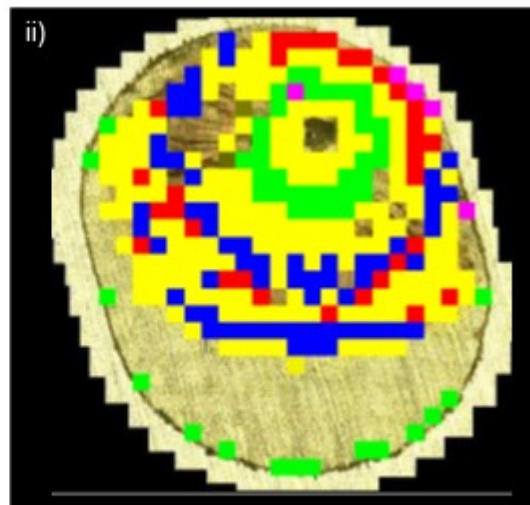


Figure 32 a)i) CaCl_2 exposed to 24-46% RH and 17-27°C. ii) Distribution of 650cm^{-1} peak on droplets as determined by least squares mapping using WiRE 4.0 software iii) the average of all spectra highlighted by the mapping process. b) single spectrum from region used for fitting.

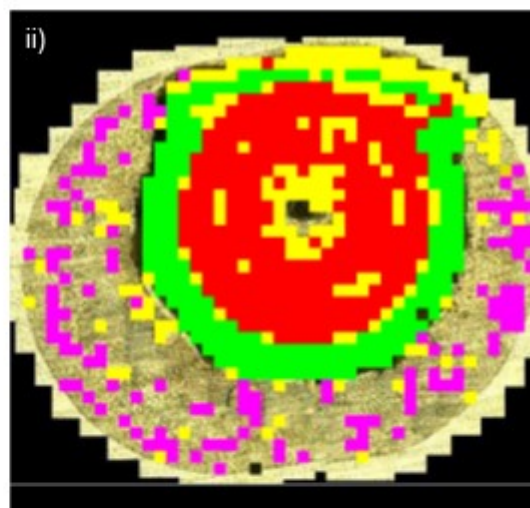
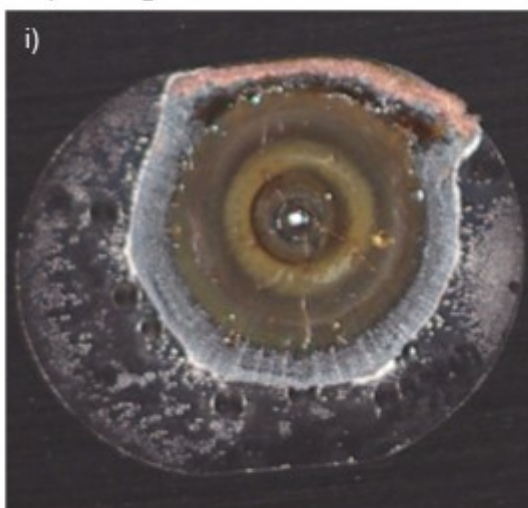
Figure 32 shows the spectrum associated with the red/brown region directly over the pit mouth on the CaCl_2 droplet exposed to fluctuating ambient conditions 24-46% RH and 17-27°C for 14 days (Figure 36). i) colour photography of the droplet. ii) shows the distribution of the spectra as determined by least squares fitting of b) a sample spectrum from the region in

question. iii) shows the average of the 30 spectra associated with the region by least squares fitting with a threshold of 0.8 least squares index.

a) MgCl_2



b) CaCl_2



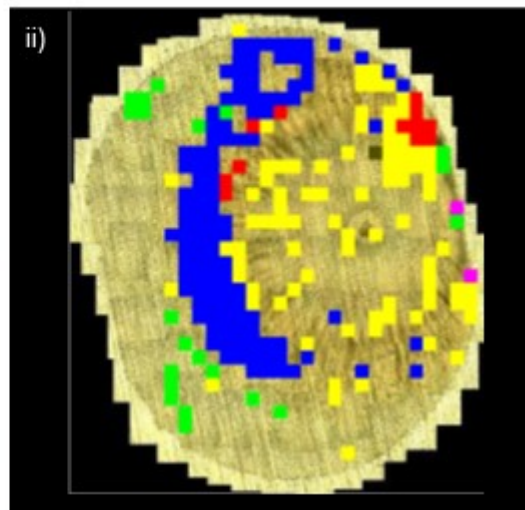
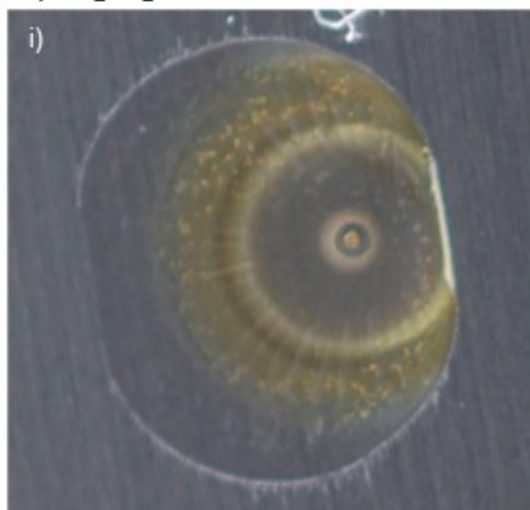
1 mm



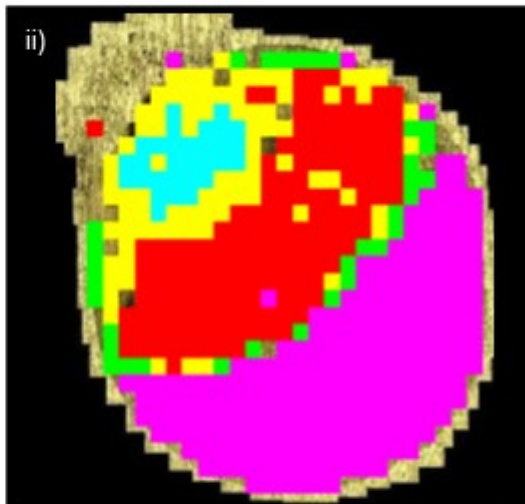
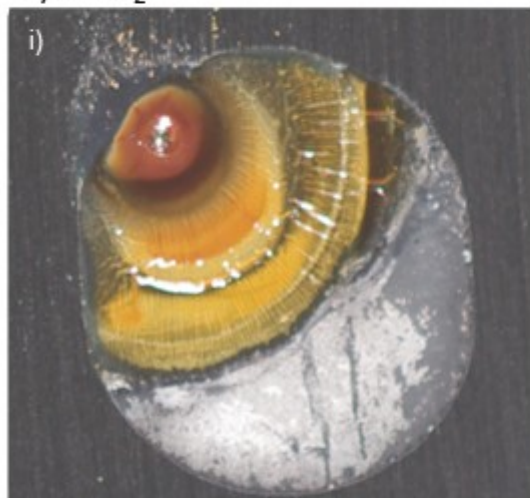
Figure 33 Overview of corrosion product species identified by Raman spectroscopy on i) colour photography and ii) Raman mapping of $100\text{ }\mu\text{gcm}^{-2}$ a) MgCl_2 and b) CaCl_2 exposed to fixed 46% RH and 30°C for 14 days.

Figure 33 shows the distribution of all compounds as determined by Raman spectroscopic mapping under a) MgCl_2 and b) CaCl_2 droplets exposed for 14 days at fixed 46% relative humidity and 30°C . The majority of rust present under the a) MgCl_2 droplet is highlighted as 'poorly formed iron(III) oxide-oxide-hydroxide' due to lack of identifying peaks in the spectra. Where phase assignment was possible two bands of lepidocrocite ($\beta\text{-FeOOH}$) were observed throughout the centre of the rust ring, away from the droplet edge while akaganeite ($\alpha\text{-Fe-OOH}$) was observed primarily at the droplet edge, with smaller amounts concentrated throughout the main rust area. The rust under the b) CaCl_2 droplet was predominantly akaganeite ($\alpha\text{-FeOOH}$), surrounded by a band of green rust 1, identified by a peak at 510 cm^{-1} which in turn was surrounded by general carbonate salt identified by a peak at 1000 cm^{-1} .

a) MgCl_2



b) CaCl_2



1 mm

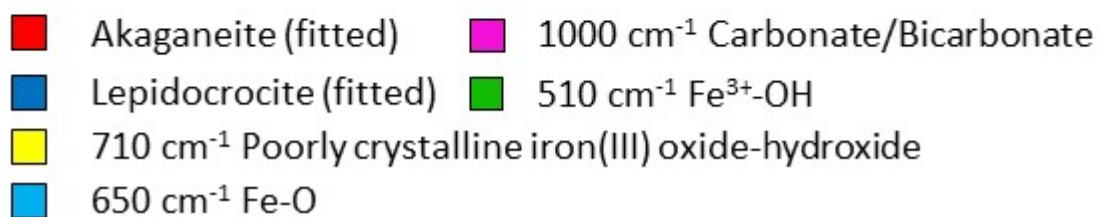


Figure 34 Overview of corrosion product species identified by Raman spectroscopy on i) colour photography and ii) Raman mapping of $100\text{ }\mu\text{gcm}^{-2}$ a) MgCl_2 exposed to fluctuating conditions between 26-55% RH and 19-31°C and b) CaCl_2 exposed to fluctuating conditions between 24-46% RH and 17-27°C droplets. Both droplets were exposed for 14 days.

Figure 34 shows the distribution of compounds as determined by Raman spectroscopic mapping for a) a MgCl_2 droplet exposed to ambient conditions which fluctuated between 26 and 55% relative humidity and 19 and 31°C (shown in detail in Figure 35) and b) a CaCl_2 droplet which was exposed to conditions which fluctuated between 24 and 46% relative humidity and 17 and 27°C (Shown in detail in Figure 36).

The predominant phase present in the a) MgCl_2 droplet was lepidocrocite, with a small amount of akaganeite present at the droplet edge. A small amount of non-phase specific iron(III) oxide-oxide-hydroxide is present across the rest of the rust area identified by a 710 cm^{-1} peak and no phase specific lower wavenumber peaks. Small amounts of green rust, identified by a peak at 510 cm^{-1} are present towards the edge of the rust area and the droplet edge and two pixels of salt spectrum, identified by a peak at 1000 cm^{-1} are present along a line of white precipitate along the right hand edge of the droplet.

The predominant phase in the b) CaCl_2 droplet is akaganeite which forms a large band across the centre of the droplet, surrounded by non-phase specific iron (III) oxide-oxide-hydroxide. This is surrounded by a band of green rust identified by a peak at 510 cm^{-1} which is in turn surrounded by carbonate/bicarbonate. There is also a spectrum identified by a strong peak at 650 cm^{-1} in addition to the one at 710 cm^{-1} associated with the deep red rust directly over the pit.

4.2.3 Exposure conditions for fluctuating ambient droplets

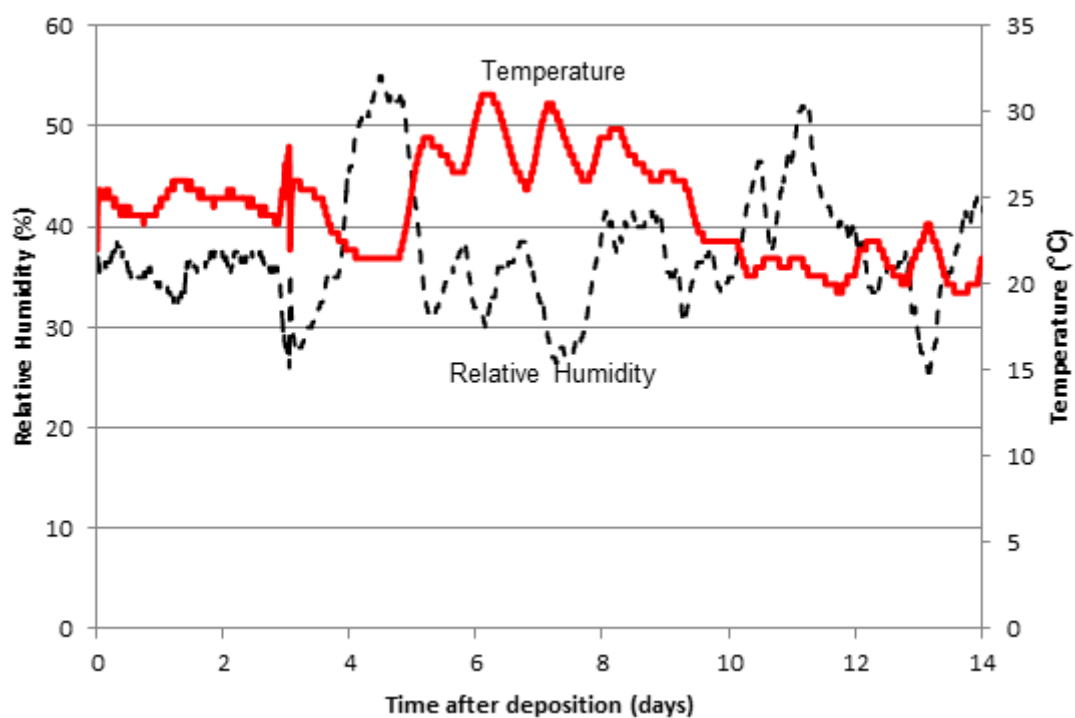


Figure 35 Variation in atmospheric temperature and relative humidity that the $100 \mu\text{gcm}^{-2}$ MgCl_2 droplet underwent over 14 days.

Figure 35 shows the atmospheric temperature and relative humidity for the 14 days that the $100 \mu\text{gcm}^{-2}$ “fluctuating ambient” MgCl_2 droplet was exposed to. The range was 26-55% RH and 19-31°C, with most of the experiment occurring below 40% RH and 30°C.

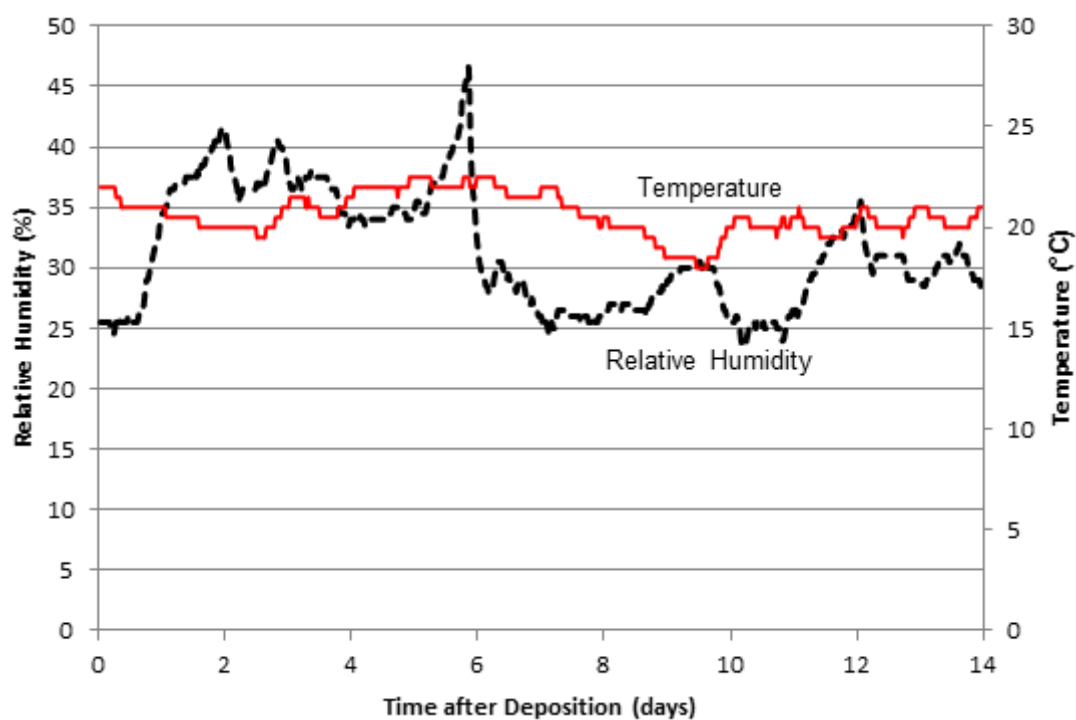


Figure 36 Variation in atmospheric temperature and relative humidity that the $100 \mu\text{gcm}^{-2}$ CaCl_2 droplet underwent over 14 days. .

Figure 36 shows the atmospheric temperature and relative humidity for the 14 days that the $100 \mu\text{gcm}^{-2}$ “fluctuating ambient” MgCl_2 droplet was exposed to. The range was 24-46% RH and 17-24°C with most of the experiment occurring below 40% RH and 25°C.

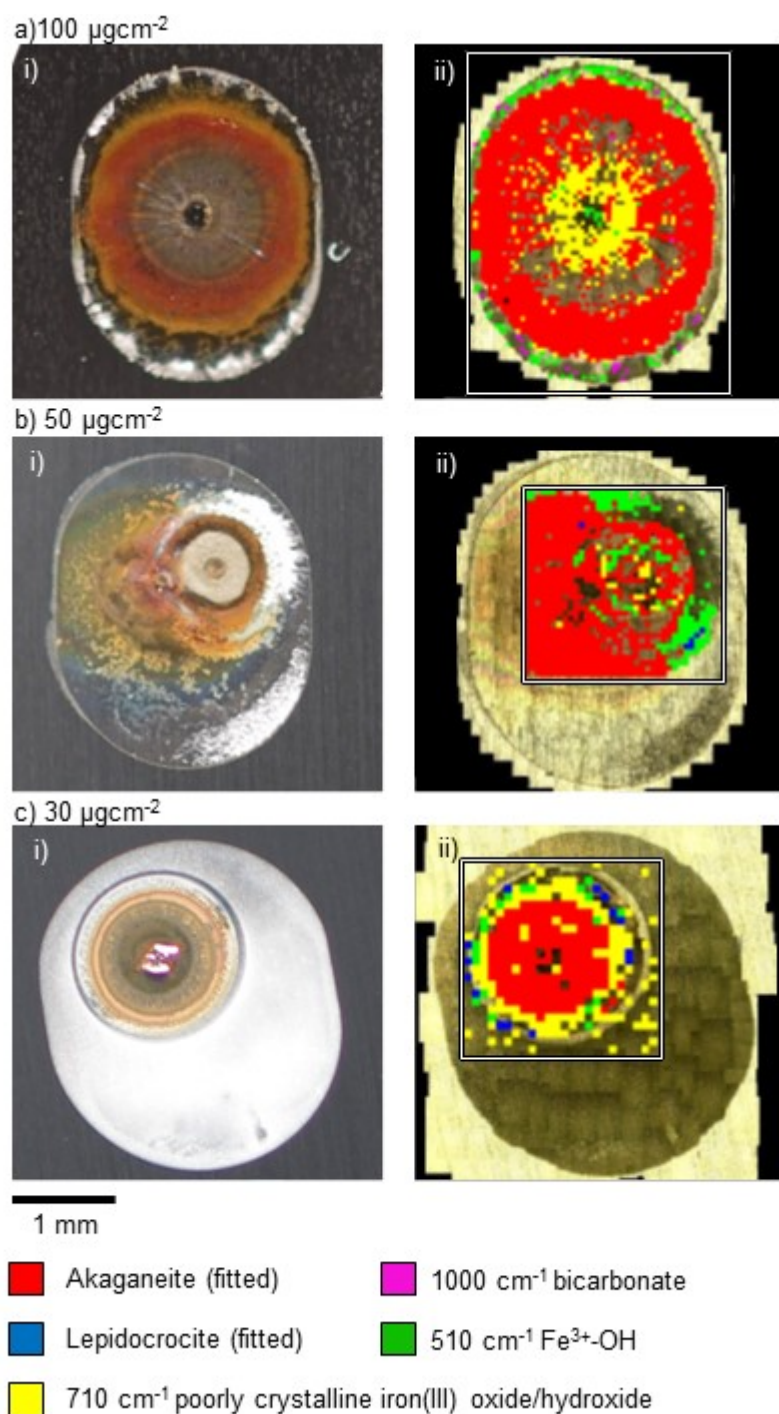


Figure 37 Variation in corrosion product distribution for chloride deposition densities of a) $100 \mu\text{gcm}^{-2}$ b) $50 \mu\text{gcm}^{-2}$ and c) $30 \mu\text{gcm}^{-2}$ MgCl_2 droplets after 24 days exposure at fixed 46% RH and 30°C . a-c i) colour photograph of the droplets in question while ii) compound distribution as determined by either least squares fitting (fitted) or by individual peak fitting (peak number). Bounding boxes signify the extent of mapping.

Figure 37 shows the distribution of corrosion products as determined by Raman spectroscopic mapping under a) $100 \mu\text{gcm}^{-2}$, b) $50 \mu\text{gcm}^{-2}$ and c) $30 \mu\text{gcm}^{-2}$ MgCl_2 droplets exposed for 14 days at fixed 46% relative humidity and 30°C . Raman spectra were taken at intervals across the sample surface and analysed to determine the presence of a particular compound. Akaganeite and lepidocrocite presence was determined by 'direct classical least squares' (DCLS) fitting experimentally acquired spectra against synthesised standards using WiRE 4.0. Carbonate, green rust and poorly crystalline iron(III) oxide-oxide-hydroxide were determined by mapping the presence of a single characteristic peak. These were at 1000 cm^{-1} for carbonate/bicarbonate, 510 cm^{-1} for green rust and 710 cm^{-1} for poorly crystalline iron(III) oxide-oxide-hydroxide. Minimum thresholds for assigning a compound to a pixel were 0.4 for the DCLS method or an intensity of 150 counts for the peak presence method. The predominant phase of iron oxide-hydroxide on all droplets in Figure 37 is akaganeite, with minor regions consisting of lepidocrocite only present on the b) $50 \mu\text{gcm}^{-2}$ and c) $30 \mu\text{gcm}^{-2}$ droplets along the outer edge of the rust area. All pixels with the presence of an iron oxide-hydroxide specific peak at 710 cm^{-1} but no minor phase specific peaks at lower wavenumbers were assigned as poorly formed iron(III) oxide-oxide-hydroxide. Outside the iron oxide-hydroxide region, spectra with a strong peak at 510 cm^{-1} associated with $\text{Fe}^{3+}\text{-OH}$ are present. Bicarbonate, identified by a peak at 1000 cm^{-1} was only observed on the a) $100 \mu\text{gcm}^{-2}$ droplet.

4.3 Discussion

The distribution of corrosion products of 304L stainless steel was assessed by Raman spectroscopy for multiple chloride deposition densities (CDDs) of MgCl_2 and CaCl_2 droplets exposed for 14 and 24 days in both fixed and fluctuating ambient conditions. Iron oxide-hydroxide phase assignment was performed by direct classical least squares (DCLS) fitting against synthesised iron oxide-hydroxide standards, remaining compounds were identified by fitting of individual characteristic peaks and comparing them to spectra found in literature.

4.3.1 Identification and assignment of compounds

Iron(III) oxide-hydroxides, identified by a broad peak from $650\text{--}710\text{ cm}^{-1}$ constituted the majority of corrosion product identified. Significant numbers of spectra had poor signal to noise and no discernable peaks at lower wavenumber characteristic which would identify it as a specific phase, and so fitting was performed by presence of the main peak at 710 cm^{-1} for these regions (Figure 29). This lack of identifying spectral features is associated with poor crystallinity[81, 82] and as such these points likely have a highly hydrated mix of ferrihydrite (2-line and 6 line) [77] which have a similar broad peak at $360\text{--}400\text{ cm}^{-1}$ and 710 cm^{-1} . This is supported by the higher incidence of more regular crystalline akaganeite on the MgCl_2 exposed to fixed conditions for 24 days (Figure 37) when compared to the one exposed for 14 days (Figure 33).

Akaganeite and lepidocrocite were the only specific iron oxide-hydroxide phases identified. Their presence was determined by least squares fitting against synthesized iron oxide-hydroxide powders (Figure 20) which had purity

verified by XRD spectroscopy (Figure 21). Due to the maghemite present in the lepidocrocite standard, a lepidocrocite spectrum from weathering steel was used which better agreed with lepidocrocite spectra present in the literature [76-83, 91, 92, 96, 99-101, 149, 151, 154-158]

The formation of akaganeite is known to be favoured in the acidic, high chloride concentration environments[73] which are present under droplets during atmospheric corrosion. Without such a high chloride concentration environment, it's likely that goethite would form instead. The formation of lepidocrocite is also pH dependent, but occurs in less acidic conditions (pH5-7) and is known to form via a green rust intermediary as well as by direct precipitation from Fe^{3+} species[73] suggesting that former green rust regions could be tracked via lepidocrocite presence.

“Green rusts” (Figure 30) were identified by their large 510 cm^{-1} peak which is attributed to the Fe^{3+} -OH stretching mode.[159] Legrand demonstrated that the ratio of 450 cm^{-1} (Fe^{2+} -OH) peak area to that of the 510 cm^{-1} (Fe^{3+} -OH) peak allows us to infer chemistry of the green rust.[96] As such, the reduced peak ratios in MgCl_2 droplets suggest that we might instead be looking at a similar double layered hydroxide (LDH) of the hydrotalcite supergroup such as Coalingite ($\text{Mg}_{10}\text{Fe}^{3+}_2(\text{CO}_3)(\text{OH})_{24}\cdot 2\text{H}_2\text{O}$) or Iowaite ($\text{Mg}_6\text{Fe}^{3+}_2(\text{OH})_{16}\text{Cl}_2\cdot 4\text{H}_2\text{O}$) for MgCl_2 droplets. The spectrum present on CaCl_2 droplets agrees with the one described by Legrand, with additional peaks at 280 cm^{-1} , 1000 cm^{-1} and 1080 cm^{-1} .

Many spectra present a peak at 900 cm^{-1} which was attributed to perchlorate.[160, 161] Bicarbonate peaks were also present on all droplets at 1000 cm^{-1} , CaCl_2 droplets also had carbonate peaks at 1080 cm^{-1} . [160]

4.3.2 *Distribution of compounds by cation*

A broad peak at 710 cm^{-1} indicating iron(III) oxide-hydroxide was present across all red-brown rusty regions on all droplets (Figure 29), in many places this peak was present without additional peaks that would denote a particular crystal phase such as lepidocrocite (Figure 28) or akaganeite (Figure 27). Where better crystallinity is observed i.e. the spectrum has a greater signal to noise ratio and peaks are more easily discernable, akaganeite favours CaCl_2 droplets while lepidocrocite favours MgCl_2 and is not present on CaCl_2 droplets. It is known that a major pathway for the formation of lepidocrocite is via a green rust intermediary[73] and as such the lack of lepidocrocite on CaCl_2 droplets could be due to a longer lived GR species which does not transform to lepidocrocite as readily. This is supported by the lack of a well matching GR spectrum with peaks at 280 cm^{-1} and 450 cm^{-1} on the MgCl_2 droplet exposed in fixed conditions and that the distribution of lepidocrocite on this droplet occupies a similar location to the green rust on the CaCl_2 droplets, along the edge of the rust area.

All droplets have a region outside the main rust area where a white substance precipitates. On MgCl_2 droplets this was found to be solely bicarbonate, while in CaCl_2 it was a mix of carbonate and bicarbonate.

4.3.3 Distribution of compounds over time

Two $100 \mu\text{gcm}^{-2}$ MgCl_2 droplets exposed to fixed conditions were analysed, one after 14 days exposure (Figure 33), the other after 24 days (Figure 37). The proportion of well crystallised iron oxide-hydroxide phases is much larger on the 24 day droplet compared to the 14 day as crystallinity improves over time. It's also worth noting that the 14 day droplet shows a mix of lepidocrocite and akaganeite when a phase could be assigned while the 24 day droplet solely presents akaganeite.

4.3.4 Distribution of compounds by chloride deposition density

Figure 37 shows $100 \mu\text{gcm}^{-2}$, 50 cm^{-2} and $20 \mu\text{gcm}^{-2}$ MgCl_2 droplets that were exposed for 24 days to fixed 46% RH and 30°C conditions before Raman mapping was performed to assess how corrosion product distribution varied with chloride deposition density. The distribution of species was similar across all CDDs, with iron oxide-hydroxide deposited over and around the pit mouth, surrounded by a band of $\text{Fe}^{3+}\text{-OH}$ indicating presence of green rust or green rust-like layered double hydroxide. The predominant iron oxide-hydroxide phase on all droplets was akaganeite, with only small amounts of lepidocrocite present at the interface between the iron oxide-hydroxide rust area and points bearing green rust. The green rust-like region was in turn surrounded by regions of white precipitate which were likely bicarbonate, but fluoresced too heavily for specific peaks to be identifiable. The main difference between CDDs was the extent of the rust area, with a higher CDD having a larger extent of iron oxide-hydroxide. This could be due to the electrolyte layer being thicker for higher chloride deposition densities, meaning that more charge carriers are available

and the 'wire' is thicker. This would give a smaller I-R drop between anode and cathode and therefore allowing for a larger current of iron hydroxide ions further away from the pit .[63]

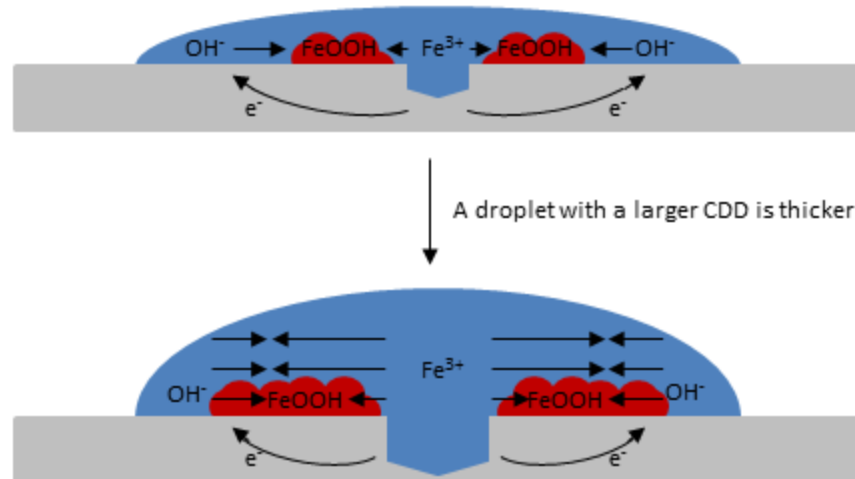


Figure 38 A thicker droplet has a lower I-R drop and can facilitate a higher current of metal ions further away the pit

4.4 Conclusions

The corrosion products formed during the atmospheric corrosion of 304L stainless steel were investigated using Raman spectroscopic mapping and colour photography. The distribution of corrosion products was recorded after two weeks exposure for MgCl₂ and CaCl₂ droplets under both fixed and fluctuating atmospheric conditions:

1. Iron oxide-hydroxides were formed in a ring around the pit mouth on all droplets. When crystal phase was identifiable, it was either akaganeite (β -FeOOH) or lepidocrocite (γ -FeOOH)
2. Akaganeite was present on all droplets and was the predominant phase on most droplets after 14 days, the exception being the MgCl₂ droplet exposed to fluctuating ambient conditions

3. Lepidocrocite was only observed on MgCl_2 droplets and was the predominant phase on the MgCl_2 droplet exposed to ambient conditions after 14 days.
4. Layered double iron oxide-hydroxides were formed on all droplets. On CaCl_2 this was green rust 1 (Carbonate, fougérite group) and was present in a ring around the main iron oxide-hydroxide region. Specific mineral allocation was difficult for similar spectra on MgCl_2 droplets.
5. The white precipitate which surrounded the iron oxide-hydroxide was comprised of carbonate and bicarbonate.

The distribution of corrosion products of 304L under different chloride deposition densities was also investigated by Raman mapping of MgCl_2 droplets after a 24 day exposure to fixed 46% RH and 30°C where a larger region of iron oxide-hydroxide was associated with a higher chloride deposition density. Additionally, when a 100 μgcm^{-2} MgCl_2 droplet that was exposed for 14 days in fixed conditions was compared with one exposed for 24 days, proportionally more of the iron oxide-hydroxide species was akaganeite, indicating that crystallinity improves over time

5. EVALUATION OF HYPERSPECTRAL METHODS

5.1 Introduction

Hyperspectral imaging has been extensively studied for remote sensing of iron oxides in earth, space and medical science[3, 118, 124, 162, 163] as well as for assessment of food quality for retail, soil quality and plant health in agriculture and in recovering text and detecting forgeries in historical conservation[122, 123, 164]It has yet to be applied to corrosion detection in any significant capacity.

This chapter evaluates applicability of hyperspectral imaging as a detection and monitoring technique for pitting on stainless steel via the rust that precipitates around the pit mouth. This was done by taking hyperspectral images of mature corrosion sites present on 304L stainless steel in the UV-VIS-NIR region (450 nm – 850 nm) and comparing spectra to compound distribution information acquired via Raman spectroscopic mapping. For this purpose, a hyperspectral imager was constructed which operates by raster scanning a UV-VIS-NIR fibre optic probe across the target surface, recording diffuse UV-VIS-NIR reflectance spectra at set intervals. The first section of this chapter concerns the imaging and analysis of a mature corrosion site and the second section consists of an overview of some methods which could be used to segment an image for decision making based on observed rust area.

5.2 Results

5.2.1 UV-VIS-NIR for iron oxide phase identification

A typical corrosion site on a mature sample was imaged optically with a Leica DMLM microscope to provide RGB images and with the UV-VIS-NIR hyperspectral imaging apparatus. The spectra gathered by the HS imaging apparatus were compared to Raman spectroscopic mapping (as utilized in chapter 4) which allowed the determination of crystal phase of the iron oxide-hydroxide compounds as well as the identification of other compounds present in the droplet.

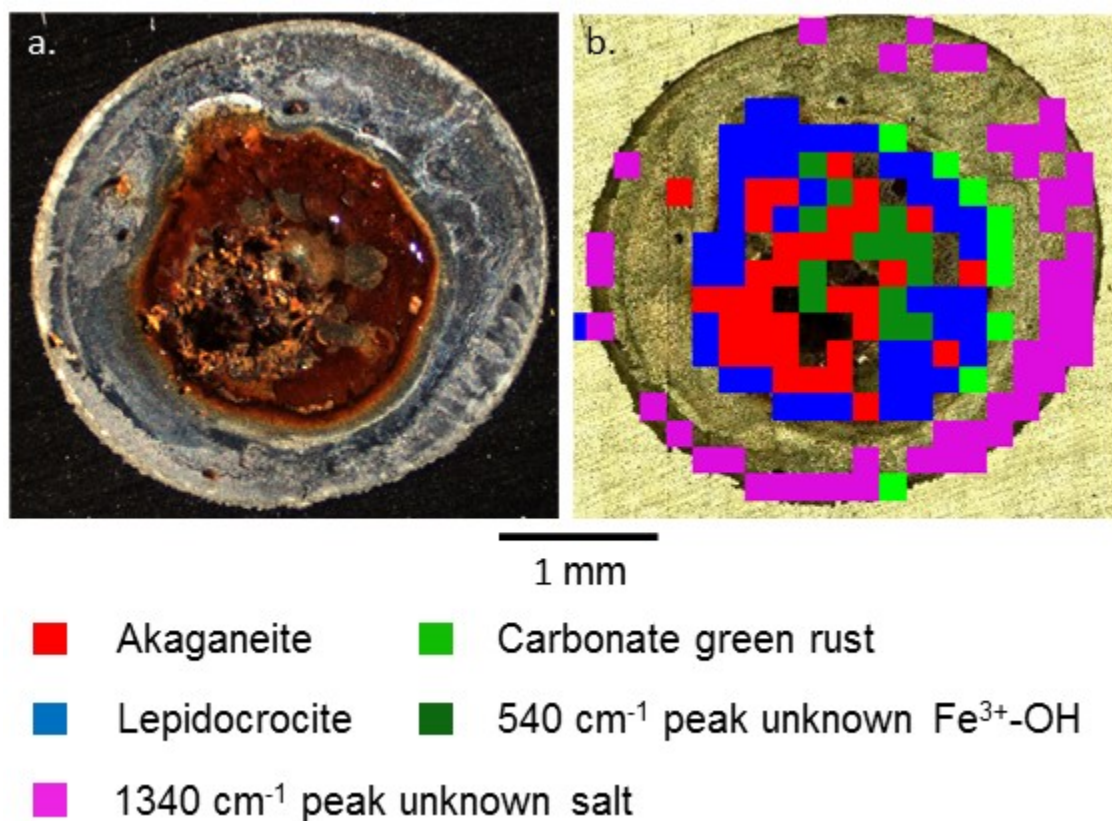


Figure 39 a. Microscopy of 30 μgcm^{-2} MgCl_2 droplet exposed for 42 months in ambient conditions
b. Raman DCLS map of the droplet showing distribution of compounds

Figure 39 shows the distribution of compounds across the droplet surface. The sample was a MgCl_2 droplet with chloride deposition density (CDD) of $30 \mu\text{gcm}^{-2}$ which had been exposed for 2 weeks at 46% R.H. and 30°C then a further 42 months in fluctuating ambient conditions. The central rust spot is primarily akaganeite ($\beta\text{-FeOOH}$), surrounded by a ring of lepidocrocite ($\gamma\text{-FeOOH}$). This is in turn surrounded by a region of carbonate green rust (GR1) as described by Legrand[96]. There is a similar but distinct compound with a 540 cm^{-1} peak interspersed in regions throughout the main body of red/brown rust which remains unassigned. The remaining droplet area is an unassigned 'salt', characterised by a peak at 1370 cm^{-1} which was not observed on droplets in chapter 4.

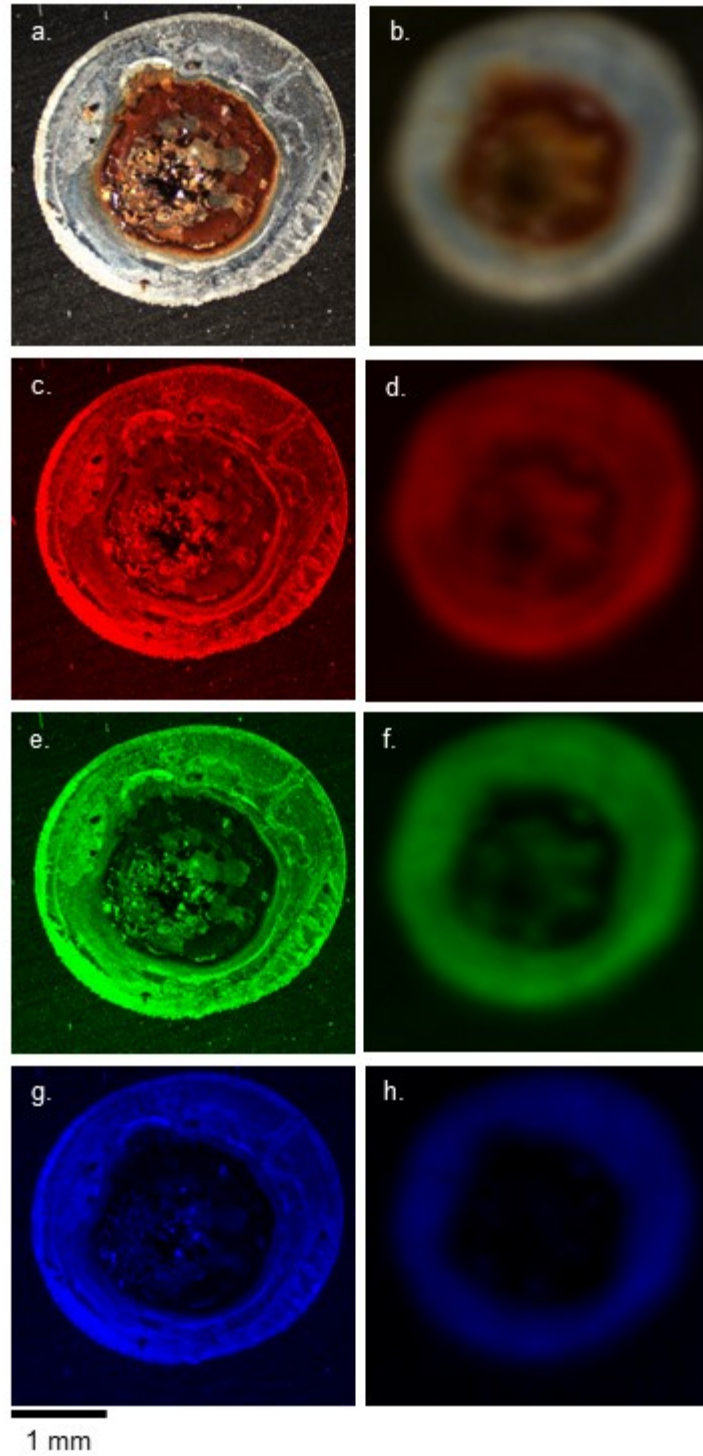


Figure 40 a. RGB Colour microscopy of $30\mu\text{gcm}^{-2}$ droplet b. 81×81 pixel pseudo-RGB image of droplet taken by combining d. 450 nm, f. 550nm, h.650 nm wavelength slices of HS image to make pseudoRGB image c,e,g. red, green and blue channels of RGB microscope image.

Figure 40 shows colour microscopy compared to 'pseudoRGB' images constructed using 450 nm, 550 nm and 650 nm wavelength slices of an 81x81 pixel HS image to visualize the hyperspectral data cube for point data correlation. a and b consist of the combined 'full colour' images while c, e, g correspond to red, green and blue colour channels of the RGB colour microscopy and d, f, h correspond to the 450 nm, 550 nm and 650 nm wavelength slices taken from a HS image. The hyperspectral image of the droplet was of a 4 x 4 mm area, taken at a resolution of 0.05 mm per pixel. Visible on both composite images are the central rust region, surrounding white 'salt' and bare steel background.

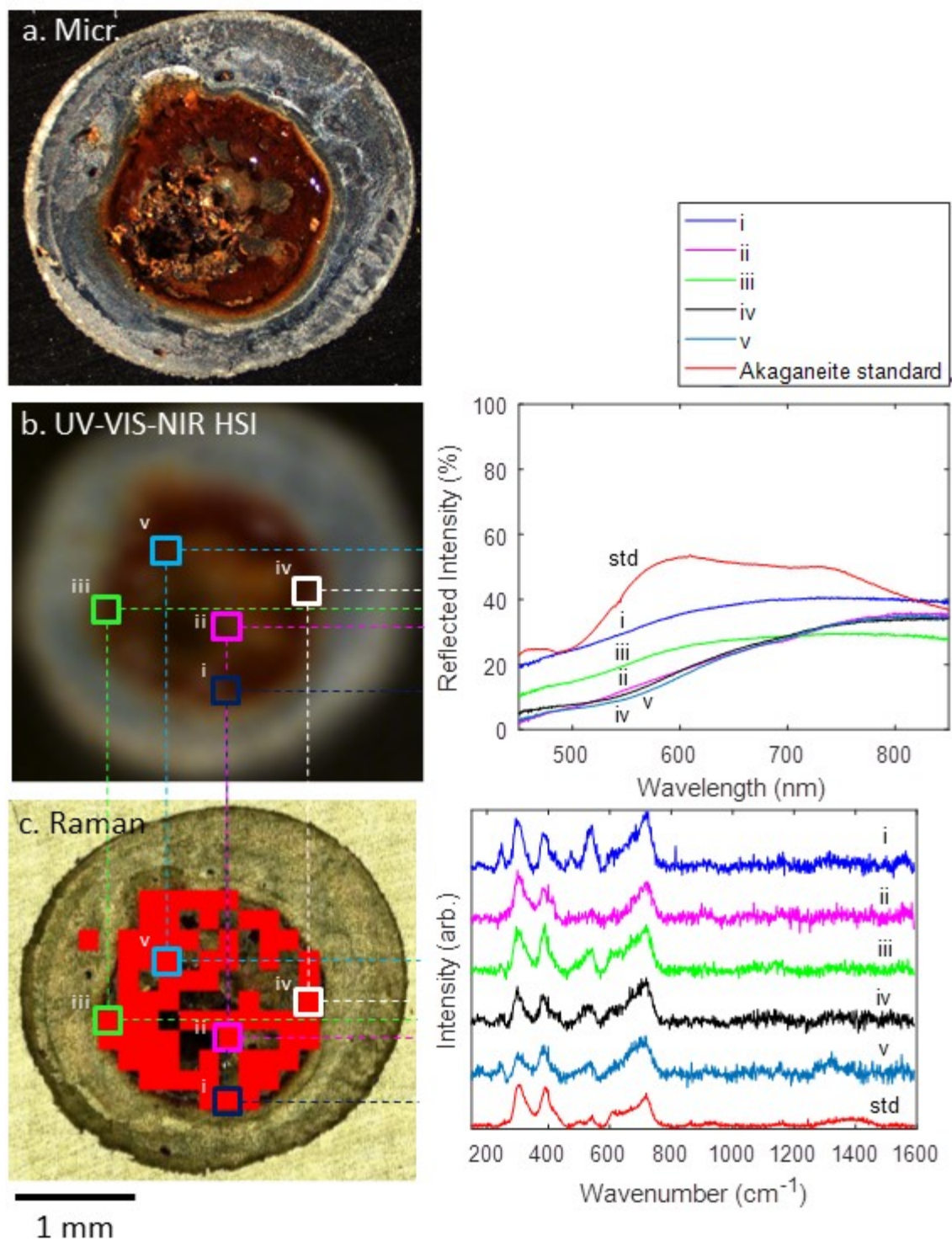


Figure 41 Comparison of Raman spectra and spectra taken from HS image for akaganeite regions. a. Microscopy of $30\mu\text{gcm}^{-2}$ CDD MgCl_2 droplet, exposed for 42 months in ambient conditions b.) PseudoRGB image constructed from hyperspectral image (left) and UV-VIS-NIR spectra associated with regions i-iv (right) c. Raman DCLS map showing the distribution of akaganeite (left) alongside Raman spectra associated with regions i-iv (right)

In Figure 41, akaganeite regions are identified using Raman spectroscopic mapping and UV-VIS-NIR spectra are extracted from a HS image and compared. Points i-v were selected as representative akaganeite regions and their UV-VIS-NIR spectra were compared with that of a synthesised akaganeite standard (Figure 24, chapter 4). a. is microscopy of 30 μgcm^{-2} MgCl_2 droplet corroded for 2 weeks at 46% RH and 30°C before a further 42 months in fluctuation ambient conditions. b. 81 x 81 pixel PseudoRGB image of same, constructed from hyperspectral image with 4 x 4 mm area with sampling resolution of 0.05 mm per acquisition. c. DCLS map of binary akaganeite presence overlaid on microscopy of droplet. Raman spectra are consistent with the standard, with major peaks at 300 cm^{-1} , 390 cm^{-1} , 540 cm^{-1} and 710 cm^{-1} accounted for in all spectra. UV-VIS-NIR spectra are lower in intensity than the standard and do not present the same distinctive double peak. Spectra from regions ii, iv and v in the interior of the rust region are similar to each other, while those associated with i and iii towards the droplet edge have more variation.

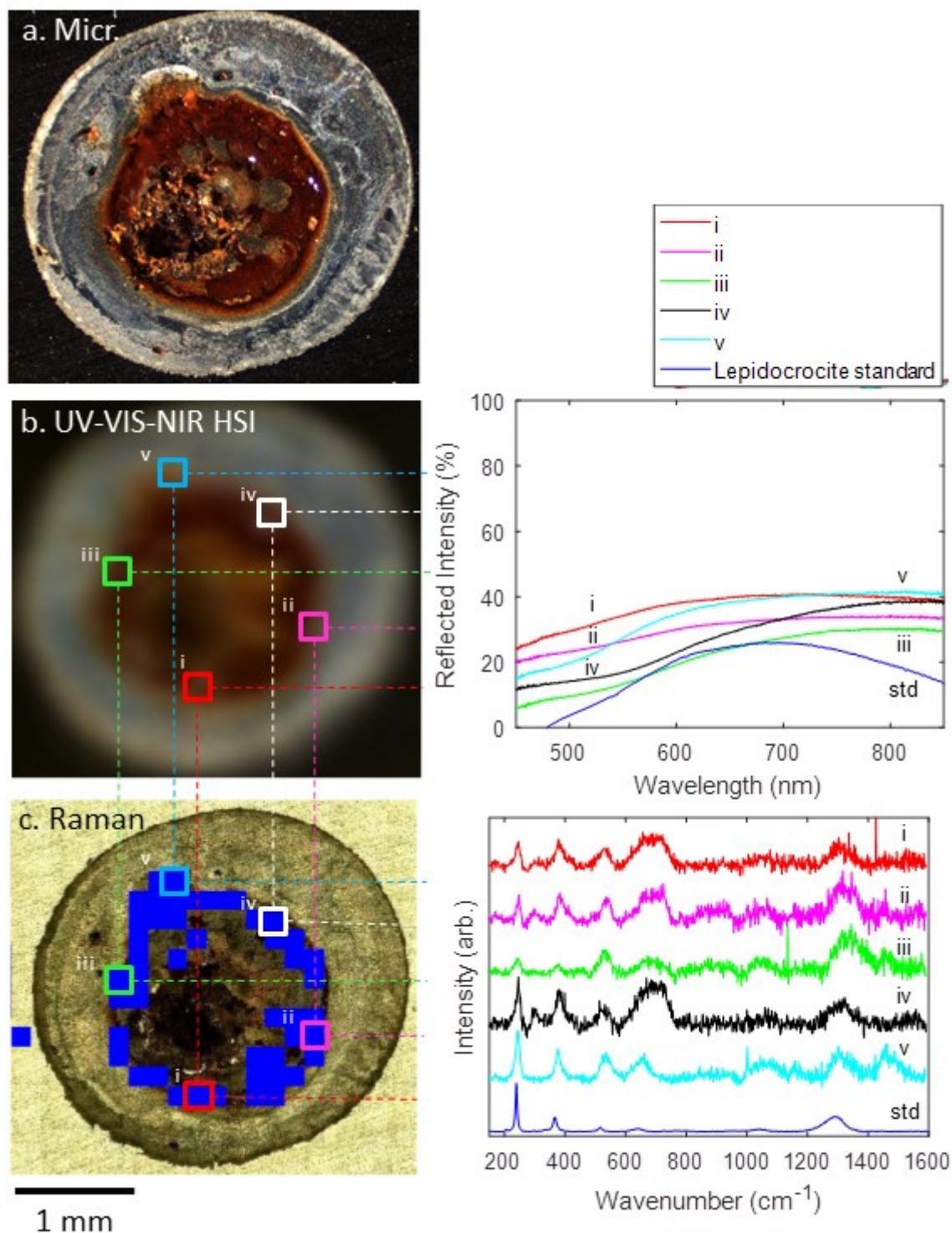


Figure 42 Comparison of Raman spectra and spectra taken from HS image for lepidocrocite regions. a. Microscopy of $30\mu\text{gcm}^{-2}$ MgCl_2 droplet, exposed for 42 months in ambient conditions b.) PseudoRGB image constructed from hyperspectral image (left) and UV-VIS-NIR spectra associated with regions i-iv (right) c. Raman DCLS map showing the distribution of lepidocrocite (left) alongside Raman spectra associated with regions i-iv (right)

In Figure 42, lepidocrocite regions are identified as points i-v and their UV-VIS-NIR spectra are compared with that of a representative lepidocrocite spectrum taken from weathering steel due to its similarity to literature spectra[81-84] . a. is microscopy of $30 \mu\text{gcm}^{-2}$ MgCl_2 droplet corroded for 2 weeks at 46% RH and 30°C before a further 42 months in fluctuation ambient conditions. b. 81×81 pixel PseudoRGB image of same, constructed from hyperspectral image with 4×4 mm area with sampling resolution of 0.05 mm per acquisition. c. DCLS map of binary lepidocrocite presence, overlaid on microscopy of droplet. Raman spectra are mostly consistent with the standard, with major peaks at 240 cm^{-1} , 370 cm^{-1} , 515 cm^{-1} , 640 cm^{-1} , and 1300 cm^{-1} accounted for in all spectra. Spectra i-iv have an additional peak which extends the 640 cm^{-1} peak to 720 cm^{-1} . UV-VIS-NIR spectra are higher in overall intensity than the standard, particularly in the UV-blue (below 500 nm) and red-NIR regions (over 700 nm).

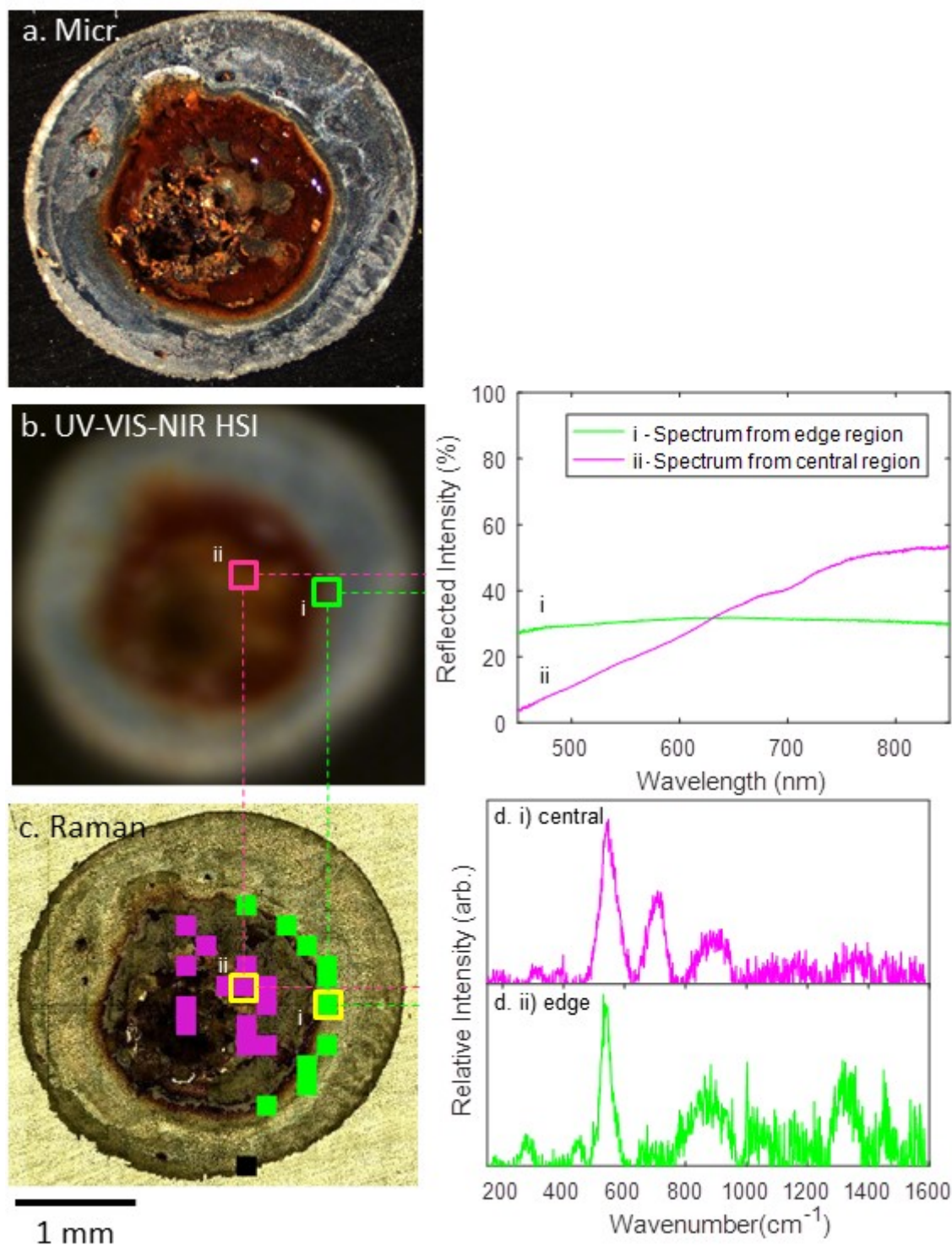


Figure 43 a. Microscopy of 30 $\mu\text{g cm}^{-2}$ MgCl_2 droplet, exposed for 42 months in ambient conditions b.) PseudoRGB image constructed from hyperspectral image (left) and UV-VIS-NIR spectra associated with i) central and ii) edge regions c. Raman DCLS map showing the distribution of fitted GR-like species(left) alongside Raman spectra associated with central and edge regions(right)

Figure 43 shows regions which are characterised by their large 540 cm^{-1} peak in Raman spectroscopy. a. is microscopy of $30\text{ }\mu\text{gcm}^{-2}$ MgCl_2 droplet corroded for 2 weeks at 46% RH and 30°C before a further 42 months in fluctuation ambient conditions. b. 81×81 pixel PseudoRGB image of same, constructed from hyperspectral image with $4 \times 4\text{ mm}$ area with sampling resolution of 0.05 mm per acquisition. c. DCLS map of 540 cm^{-1} peak presence, overlaid on microscopy of droplet. Two similar but distinct spectra are present. Spectra associated with the edge of the rust area are characterised by additional peaks at 290 cm^{-1} and 450 cm^{-1} . The compound towards the centre has no significant peaks below 540 cm^{-1} and has a large additional peak at 700 cm^{-1} . The rough, broad peaks at 900 cm^{-1} are unassigned. The compounds present at the edge of the rust region are spectrally flat in the UV-VIS-NIR. The spectra present towards the centre of the rust region display the same red/brown 'cliff' as is present in the previous spectra associated with iron oxide-hydroxide.

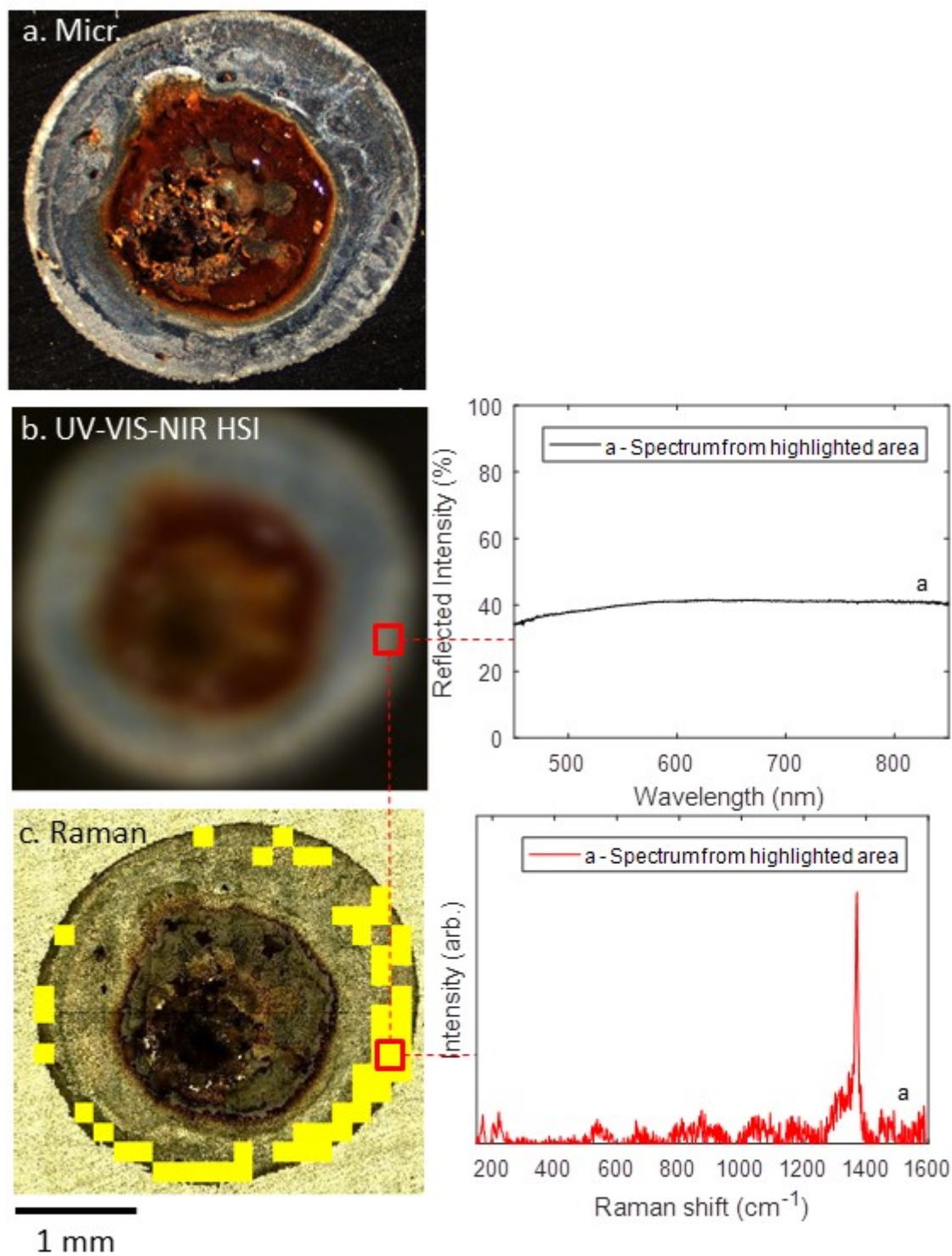


Figure 44 a. Microscopy of $30\mu\text{gcm}^{-2}$ MgCl_2 droplet, exposed for 42 months in ambient conditions
b.) PseudoRGB image constructed from hyperspectral image (left) and UV-VIS-NIR spectra associated with highlighted region c. Raman DCLS map showing the distribution of fitted 'salt' spectrum (left) alongside example Raman spectrum used for fitting (right)

Figure 44 shows the UV-VIS-NIR spectra associated with the white compound which surrounds the central rust spot. It is spectrally flat with a reflectance of approximately 40% of the calibrated 99% reflectance standard. The Raman spectrum shows a strong peak at 1370 cm^{-1} , with a smaller shoulder at 1340 cm^{-1} .

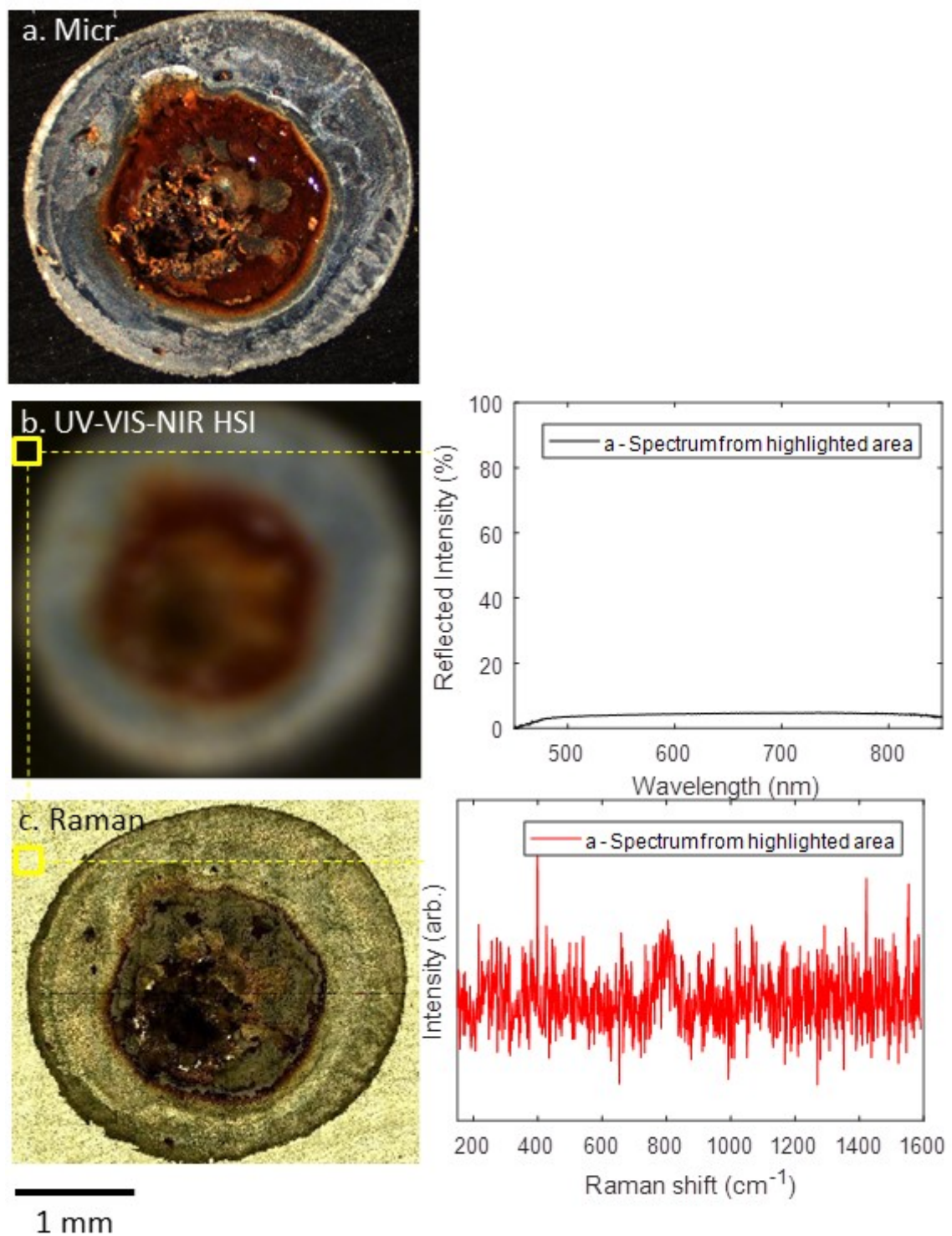


Figure 45 a. Microscopy of $30\mu\text{gcm}^{-2}$ MgCl_2 droplet, exposed for 42 months in ambient conditions b.) PseudoRGB image constructed from hyperspectral image (left) and UV-VIS-NIR spectra associated with highlighted region c. Microscopy showing region where example background steel was taken from.

Figure 45 shows UV-VIS-NIR spectra associated with the bare stainless steel surrounding the droplet. It is spectrally flat with a reflectance of approximately 5% of the 99% calibrated reflectance standard. The Raman spectrum is that of a typical area of the steel.

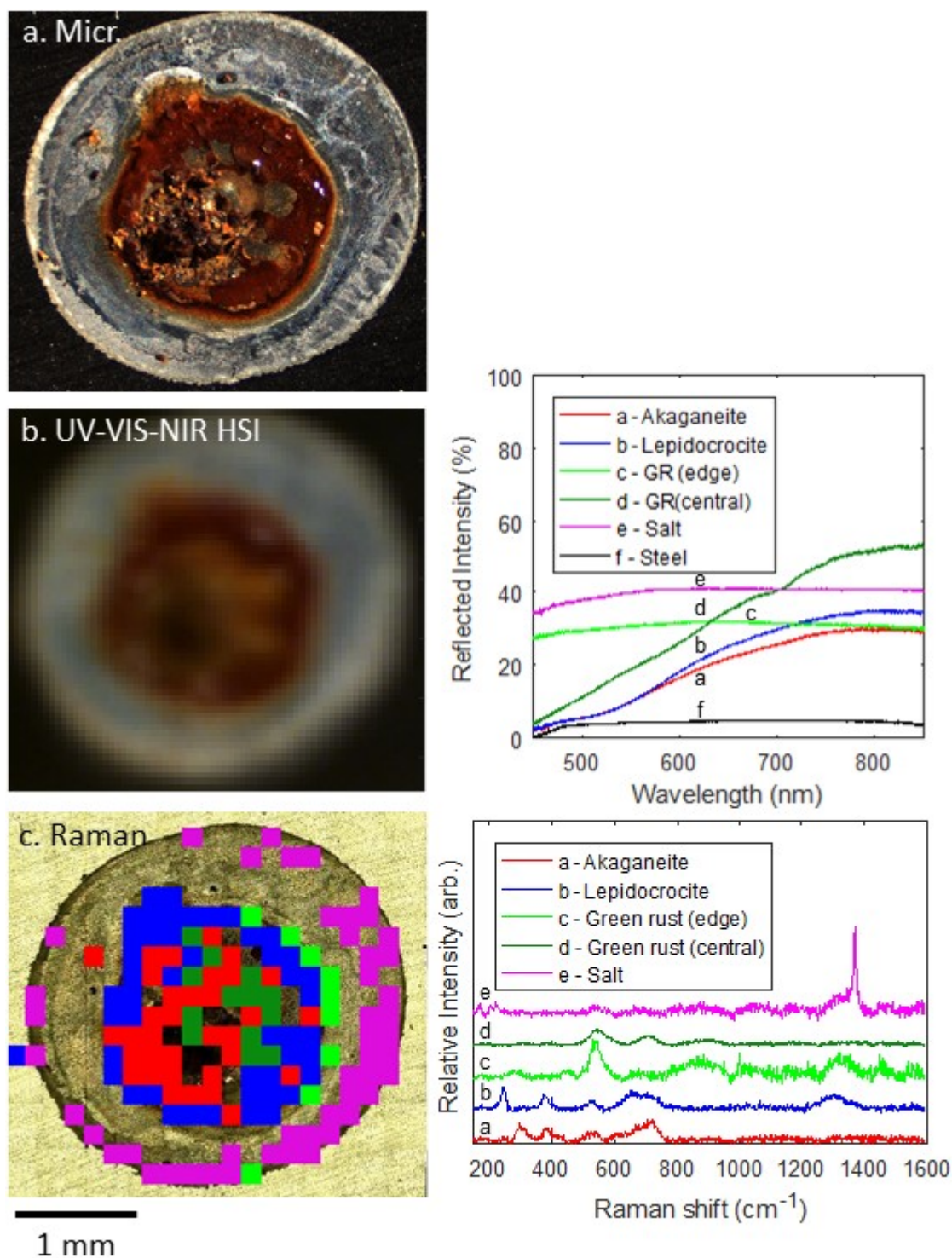


Figure 46 a. 30 $\mu\text{g cm}^{-2}$ CDD MgCl_2 droplet exposed for 42 months in ambient conditions, image taken with microscope b. composite RGB image made from hyperspectral image by combining 450 nm, 550nm, 650 nm wavelength slices alongside representative UV-VIS-NIR spectra for each region. c. Raman map showing overall distribution of spectra appearing in accompanying stacked plot.

Figure 46 consists of representative examples of all spectra associated with all measured species. Of note is that the spectra from regions assigned as central 'green rust', lepidocrocite and akaganeite spectra are point iv on Figure 42 and point iii on Figure 41. Spectra are either flat (Figure 46 e,d,f) or have a positive gradient with a maximum at 800 - 850 nm (Figure 46 a,b,c)

5.2.2 Comparison of techniques for area quantification

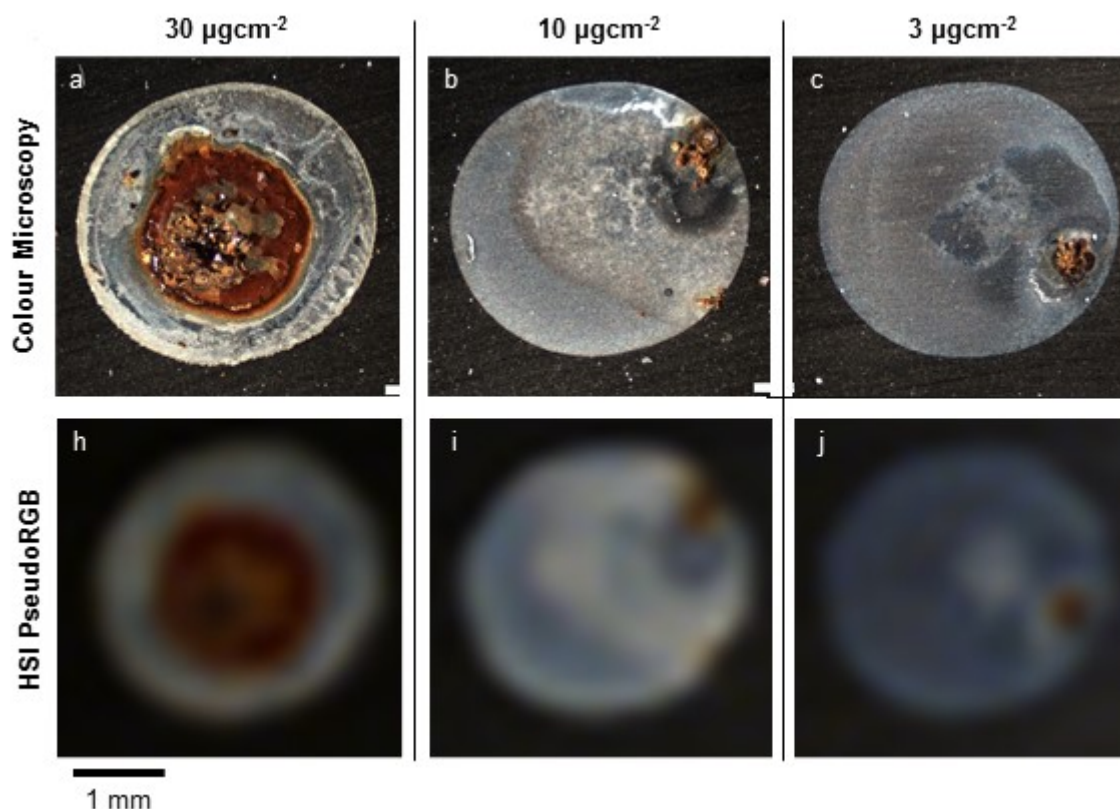


Figure 47 a, b, c colour microscopy of 3 droplets with CDD of 30, 10 and 3 μgcm^{-2} , exposed for 42 months in fluctuating ambient conditions. d, e, f. pseudoRGB images of the above droplets made by combining the 450 nm, 550 nm and 650 nm wavelength slices from a hyperspectral acquisition with a resolution of 0.2 mm per acquisition and a sample area of 4 x 4 cm.

Three HS images were acquired of droplets with chloride deposition densities of 30, 10 and 3 μgcm^{-2} , exposed for 2 weeks at 46% RH and 30°C and then for a further 42 months at ambient RH and temperature. Figure 47 shows a,b,c colour microscopy of droplets. (d, e, f) Pseudo-RGB images of each, constructed with 450 nm, 550nm and 650 nm wavelength slices of HS images for broad comparison. Each HS image consists of a 4 x 4 acquisition area with a sampling resolution of 0.2 mm per acquisition.

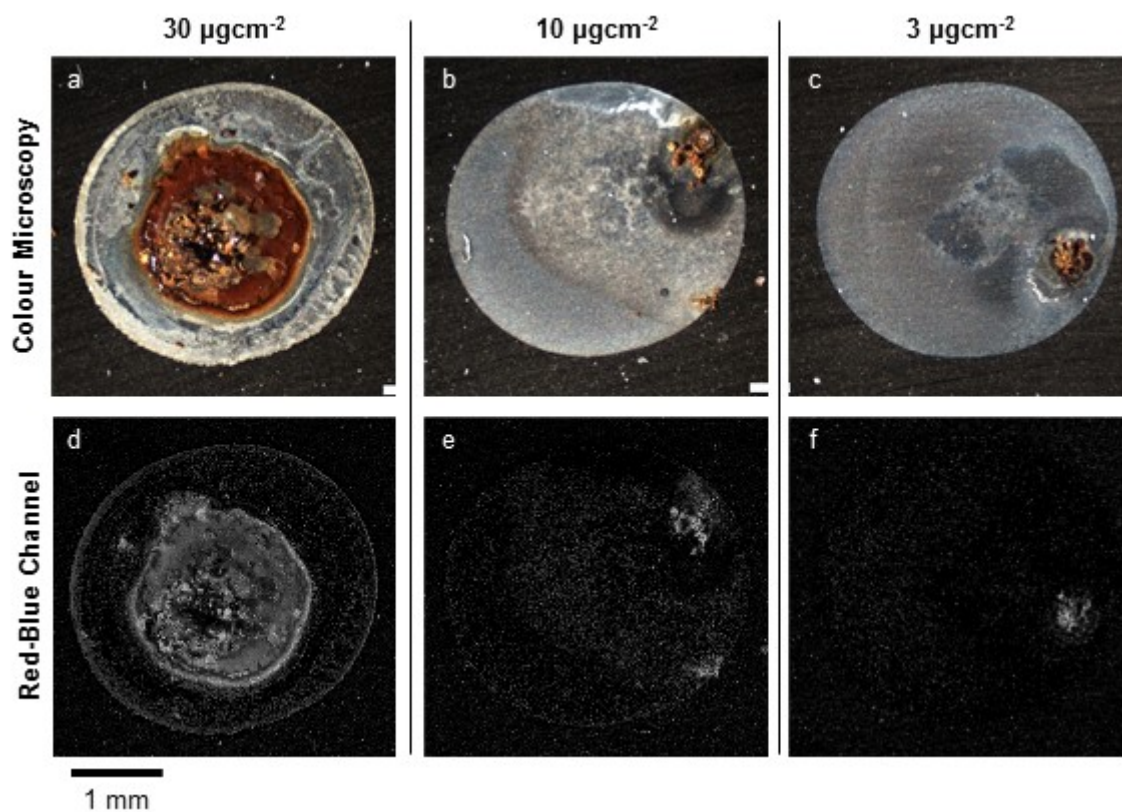


Figure 48 a, b, c. colour microscopy of 3 droplets with CDD of 30, 10 and 3 μgcm^{-2} , exposed for 42 months in fluctuating ambient conditions d, e, f greyscale images of remaining intensity after the blue colour channel is subtracted from the red.

Figure 48 shows the colour microscopy (a,b,c) compared to the intensity values remaining when the blue channel is subtracted from the red as a technique for segmenting 'red' areas of the image.

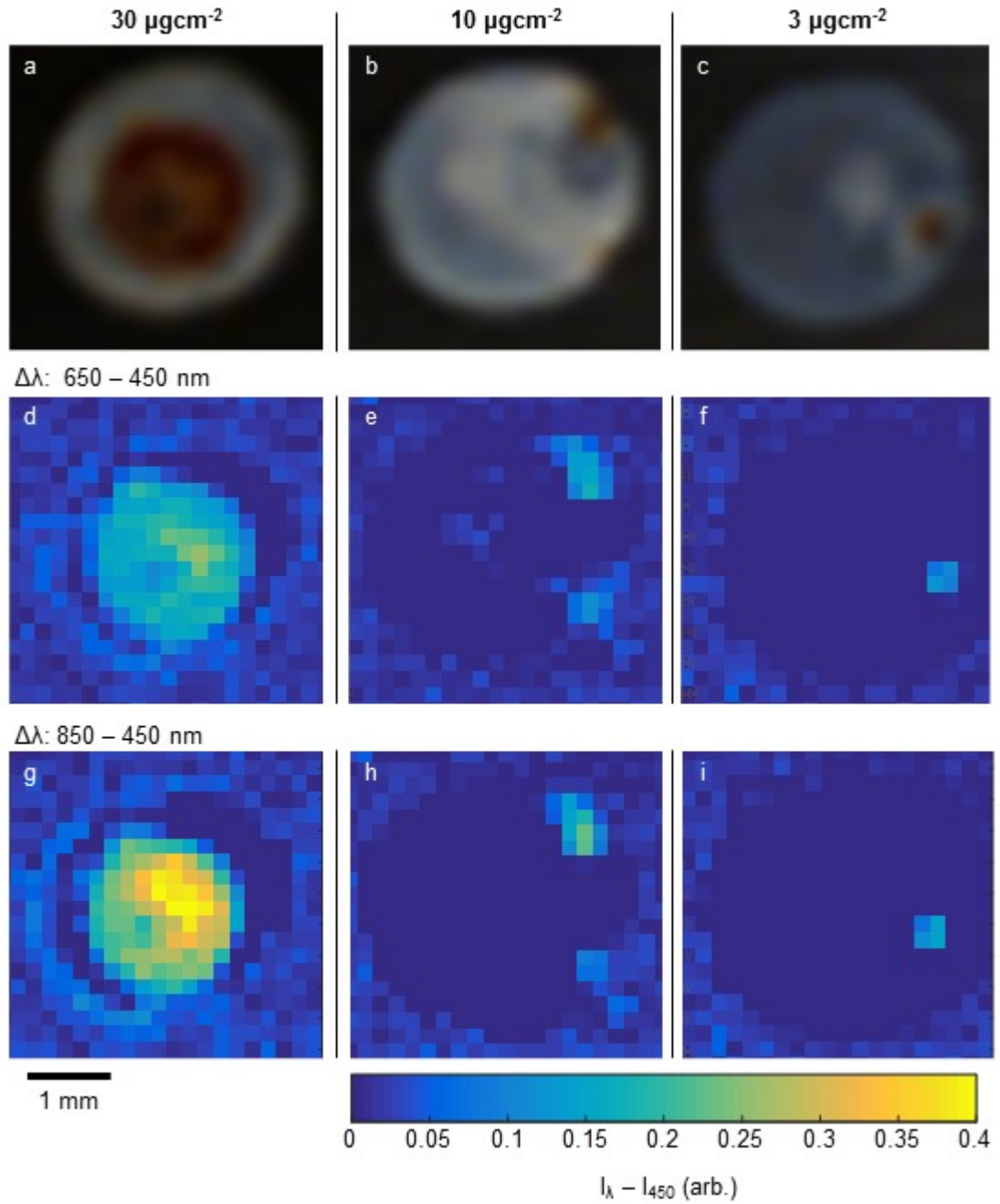


Figure 49 a, b, c. pseudoRGB images of 3 droplets with CDD of 30, 10 and 3 μgcm^{-2} made by combining the 450 nm, 550 nm and 650 nm wavelength slices from a hyperspectral acquisition d, e, f. Images of intensity remaining after subtracting the 450 nm wavelength slice from the 650 nm wavelength slice. g, h, i. Images created by subtracting the 450 nm slice from the 850 nm slice.

Figure 49 shows the HS pseudoRGB images (a,b,c) and the contrast between 450 nm and 650 nm wavelength slices (d,e,f) against the contrast between 450 nm and 850 nm slices (g,h,i), showing that a higher residual intensity and

therefore better contrast is present for the 850 nm-450 nm subtraction than for the 650 nm -450 nm subtraction.

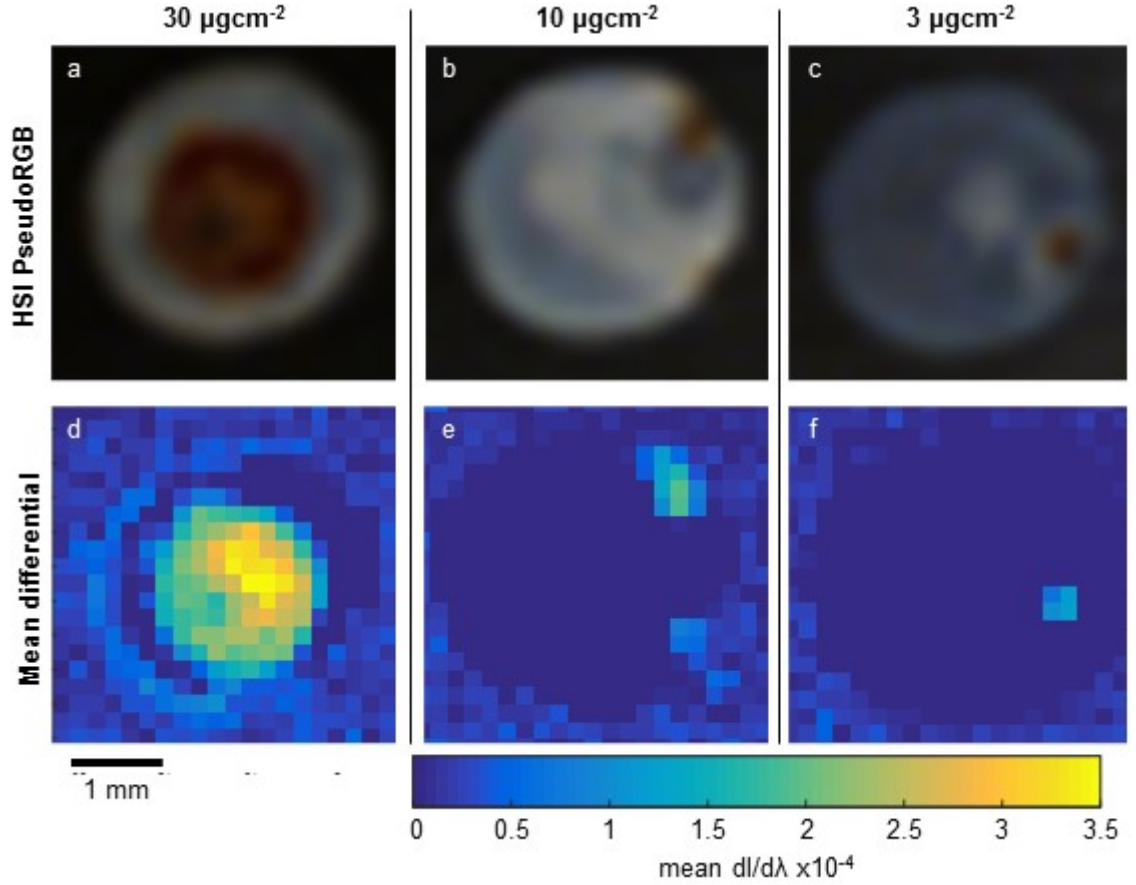


Figure 50 a, b, c PseudoRGB images of 30 , 10 and $3 \mu\text{gcm}^{-2}$ MgCl_2 droplets. d, e, f images derived from hyperspectral images by taking the mean differential of the spectrum associated with each pixel.

Figure 50 shows a comparison between the pseudoRGB and the mean differential of the spectrum associated with each pixel. Red/brown coloured regions are associated with a higher mean differential.

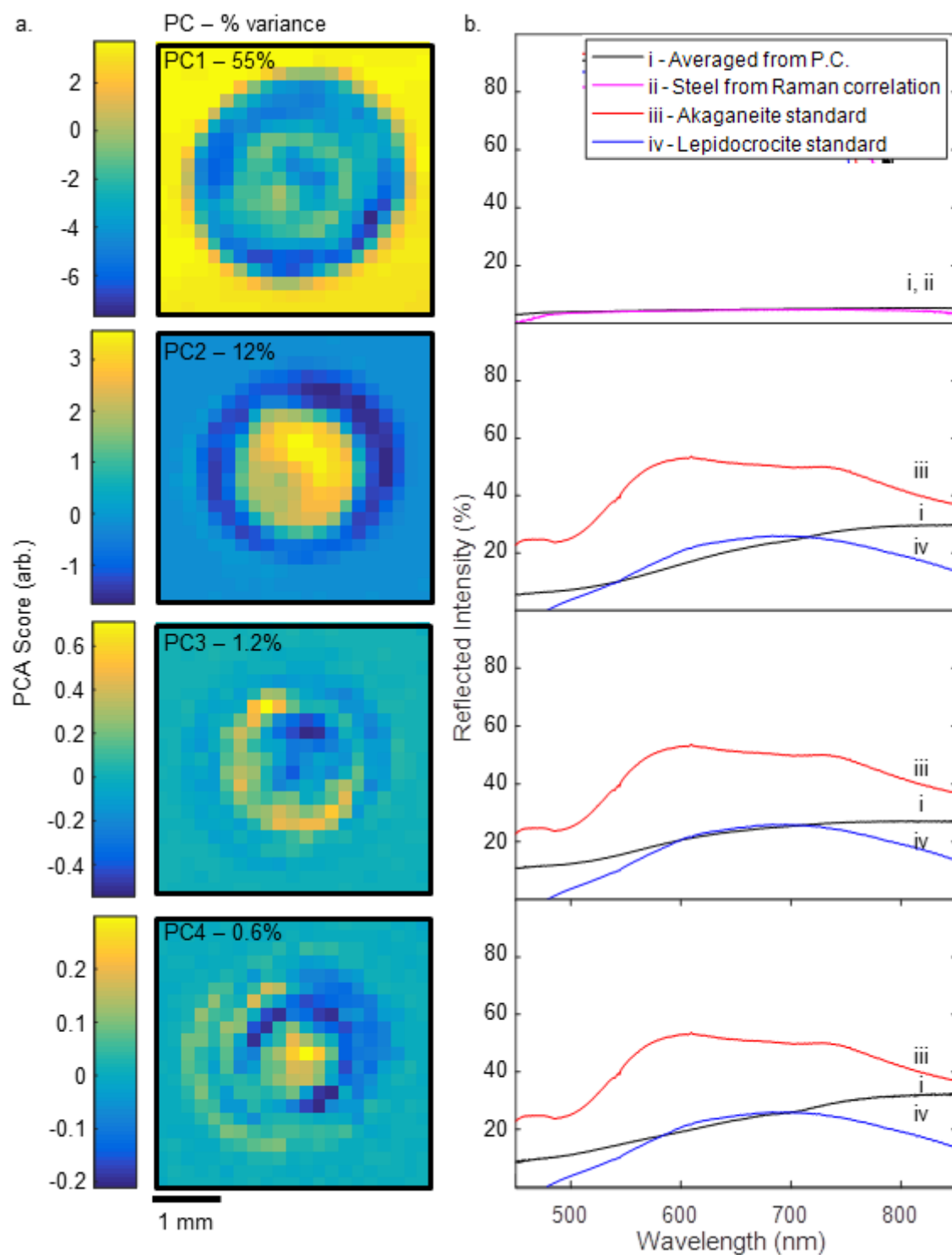


Figure 51 a, PC1-4 images reconstructed from scores generated from principal component analysis of a hyperspectral image of a corrosion site under a $30 \mu\text{gcm}^{-2}$ MgCl_2 droplet. b i. spectra associated with bright regions in accompanying images, generated by averaging the spectra from all pixels with a P.C. score exceeding 0.1. ii,iii,iv are standard spectra provided for comparison.

Principal component analysis was performed on the HS image in order to assess its viability for fast analysis of HS images in a corrosion context. Figure 51 shows the results of principal component analysis of a 21 x 21 pixel hyperspectral image of a corrosion site under a 30 μgcm^{-2} MgCl_2 droplet, corroded for 2 weeks at 43% RH and 30°C, followed by 42 months in fluctuating ambient conditions. The hyperspectral image is of a 4 x 4 mm area taken at a sampling resolution of 0.2 mm per acquisition. A. PC1-4 are images constructed with per pixel scores for each of the first 4 principal components, accounting for 55% (PC1), 12% (PC2), 1.2% (PC3) and 0.6% (PC4) of the variance in the dataset. Their corresponding spectra are displayed in b, gathered by averaging all spectra associated with relevant P.C. and with a score greater than 0.1. P.C.1 highlights bare steel surrounding the droplet, P.C.2 highlights the red/brown 'rust' region in the central droplet. P.C.3 highlights the yellow tinted region immediately surrounding the main rust region. P.C.4 highlights the thicker rust layer to the bottom left of the circumference of the droplet as well as an area of rust at the centre.

5.3 Discussion

Apparatus for taking hyperspectral images of droplet sized targets was assembled and characterised (Section 3.5.2). This apparatus was then used to take hyperspectral images of mature corrosion sites exposed for 42 months. The gathered spectra were compared to Raman spectroscopic mapping for compound identification and phase assignment. Some techniques for preliminary hyperspectral image analysis were explored.

5.3.1 *Iron oxide phase identification using UV-VIS-NIR imaging*

Spectra of a mature corrosion site gathered using the hyperspectral apparatus were compared to Raman spectroscopic mapping for phase analysis. This distribution can be seen in Figure 39. The corrosion site was under a $30\ \mu\text{gcm}^{-1}$ CDD MgCl_2 droplet, exposed for 2 weeks at 30°C and 46% RH and a further 42 months in fluctuating ambient conditions. An exposure of greater than a month was desired to ensure relevance to corrosion sites that will be found in temporary waste stores.

The major constituents of the rust region as seen in Figure 39 were identified as akaganeite ($\beta\text{-FeOOH}$) towards the centre of the rust area and lepidocrocite ($\gamma\text{-FeOOH}$) around the edge of the rust area, which is typical of MgCl_2 droplets over short term exposures (as seen in Chapter 4). Raman spectra matching green rust 1 (GR1) as described by Legrand were also observed in the vicinity immediately surrounding the droplet (Figure 43c)[96]. Some central regions with a strong $540\ \text{cm}^{-1}$ peak which corresponds to $\text{Fe}^{3+}\text{-OH}$ [159] and $700\ \text{cm}^{-1}$ peak corresponding to Fe-O [77, 81, 82] were also observed. The absence of a peak at $290\ \text{cm}^{-1}$ and $450\ \text{cm}^{-1}$ prevents these central spectra from being assigned as

GR1. There was also a strong 1370cm^{-1} peak associated with the white compound surrounding the rust region that remains unassigned (Figure 44 c). This 'salt' spectrum was stronger near the droplet edge, indicating that the crystals were larger and better formed. This likely due to the droplet edge being first to dry and crystallize during wet-dry cycles as it is where the electrolyte is thinnest.

In order to aid visualization and correlation between HS images and Raman maps 'pseudo-RGB' images were created by combining 450 nm, 550 nm and 650 nm wavelength slices of the HS image as the red, green and blue photographs in a colour image. These were then used for matching and validation of the regions used for correlation with the Raman mapping.

UV-VIS-NIR spectra were then extracted from HS images for regions of each compound identified by Raman mapping. For points identified as bearing akaganeite by Raman spectroscopy in Figure 41, no UV-VIS-NIR spectra present the same intensity distribution as the akaganeite standard (Figure 24), which has reflectance of 40-60% in the 550-600 nm region, giving it a yellow hue. Instead the 'akaganeite' spectra in the HS image have a reflectance in the 10-30% range. Similarly in Figure 42, no regions of the HS image associated with lepidocrocite via Raman spectroscopy present UV-VIS-NIR spectra that match the standard powdered lepidocrocite. There could be several reasons for this disparity; Synthesized standards were dry and ground into powder whilst lepidocrocite and akaganeite present in the droplet are precipitated from and still present alongside the droplet solution meaning particle size, wetting and arrangement were different for standards and droplet spectra, meaning differing

scattering effects between the two. Additionally, the large ($\sim 50\text{-}100\text{ }\mu\text{m}^2$) acquisition area of the UV-VIS-NIR illumination makes it likely that several compounds are illuminated at once, as opposed to the very small region ($\sim 10\text{ }\mu\text{m}^2$) gathered during Raman mapping, which would mean that spectra would be acquired as a mixture.

There are minor regional differences in UV-VIS-NIR spectrum observed for both crystal phases of iron oxide. For akaganeite in Figure 41, regions ii, iv and v are consistent with each other despite being from different areas of the droplet, though all three regions are located towards the interior of the rust region. Regions i and iii are closer to the edge of the rust region and have a higher reflectance in the blue-green (450 -550 nm) wavelength interval and a shallower slope overall. This could be due to spectral blending with light reflected from outside the rust region due to the large circle of confusion of the illumination.

Regional comparison of lepidocrocite is shown in Figure 42. Significantly more variation is present in the spectra extracted from HS images due to the regions of lepidocrocite present on the droplet occurring towards the outer area of the rust region and so some spectral blending with the surrounding 'salt' has occurred in the HS image. It should be noted that regions i, ii and iv also have an additional Raman peak at 700 cm^{-1} usually attributed to Fe-O[157] and an additional unknown peak at 1500 cm^{-1} . The addition of this Fe-O peak doesn't have a reliable effect on the UV-VIS-NIR spectrum however as all measured display the broad 450-850 nm red/brown slope the same degree.

On the edge of the rust region and in the central region there are spectra characterised by a strong 540 cm^{-1} peak corresponding to $\text{Fe}^{3+}\text{-OH}$ [96]. The spectra around the edge of the rust region match a carbonate green rust that Legrand describes[96], with an additional sharp peak at 1000 cm^{-1} which corresponds to bicarbonate[160] and weaker peaks at 450 cm^{-1} ($\text{Fe}^{2+}\text{-OH}$) and at 290 cm^{-1} . The UV-VIS-NIR spectrum associated with this region differs very little from the surrounding salt and does not present a green hue that is usually associated with green rust. The spectrum associated with the central region is characterised by an additional peak at 700 cm^{-1} and significantly reduced 450 cm^{-1} and 290 cm^{-1} peaks. The presence of a 700 cm^{-1} Fe-O band suggests that this is a distinct but similar double layered iron oxide-hydroxide in the fougurite group rather than Legrand's green rust 1. This is further supported by the observed UV-VIS-NIR spectrum presenting the red/brown cliff associated with akaganeite and lepidocrocite regions across the rest of the droplet. Similar spectra presenting large 540 cm^{-1} peaks and small 450 cm^{-1} peaks are reported in a paper by Gomez and suggest that it could be due to the uptake of Mg to form MgFeCO_3 or MgFeSO_4 , but neither carbonate or sulphate peaks are present between 950 and 1100 cm^{-1} for central regions[165].

The UV-VIS-NIR salt spectra in Figure 45 are distinct from the surrounding steel (Figure 46) by virtue of a significantly higher overall reflectance – 30-40% as opposed to 5-10%, but neither have major spectral features. The Raman spectrum associated with this 'salt' has a single major peak at 1370 cm^{-1} which remains unassigned. This suggests that despite lack of spectral features the

surface contaminants can be discerned from background steel solely by reflected intensity rather than any particular spectral band.

5.3.2 *Techniques for area quantification/Image analysis*

Due to the high dimensionality of the data gathered with a hyperspectral acquisition, it is necessary to find efficient techniques to both analyse and visualize the data in an intuitive manner.

Figure 47 shows a comparison between microscopy and 'pseudoRGB' images of three droplets of CDD $30 \mu\text{gcm}^{-1}$, $10 \mu\text{gcm}^{-1}$ and $3 \mu\text{gcm}^{-1}$, chosen for having significantly different rust areas. The rust regions are clearly visible as red/brown pixels. A simple way of segmenting these images for rust area feature extraction is to highlight red pixels by subtracting the blue channel from the red, as has been demonstrated in Figure 48 on the colour microscopy images, and as is commonly utilized as a spectral identifier for iron oxide[5, 117, 166, 167]. This technique is applied to HS images in Figure 49 by subtracting the 450 nm channel from the 650 nm, with similar results to the microscopy. Precise area comparison is difficult due to the low spatial resolution of the HS imager but rusty regions of interest are similarly highlighted. When the same technique is applied to the 850 nm channel in the near infra-red (Figure 49c) an average of 65% better contrast is seen over pixels associated with rust region, suggesting that NIR could significantly improve detectability of small rust regions. As the peaks are broad, this could be performed with filters i.e. a multispectral system rather than needing the full spectral range of a HS imaging system.

Another feature extraction technique explored in the Figure 50 is the use of the mean differential of the spectrum. Higher order differentials are routinely used for industrial applications[168], but the fact that no sharp features are present in droplet spectra suggest that higher orders are unnecessary. This is further supported by the differential method not showing any improvement over colour channel subtraction for highlighting rusty areas.

Principal component analysis is a method which has been used heavily in hyperspectral imaging applications for dimensionality reduction as well as for supervised feature extraction of data due to the technique's ability to self-order data along lines of maximum variance, essentially grouping together like spectra[5, 121, 166, 169, 170]. PCA has been performed on a HS image of a corrosion site in Figure 51. The first P.C. contrasts the bare metal and the droplet area as a whole, likely due to bulk reflected intensity differences. The second P.C. specifically highlights the red/brown rust region due to the positive intensity gradient associated with the iron oxides present. The majority of the variance (67%) in the dataset is explained by these first two principal components, but the third is potentially of note despite the low variance fraction (1.2%) as it highlights the thinner yellow/orange rust around the exterior of the rust region, co-incident with the lepidocrocite Raman map. However, the UV-VIS-NIR spectrum associated with these pixels does not match that of the standard lepidocrocite. The fourth P.C. corresponds to only 0.6% of the loading and has no easily discernable spectral features, suggesting that it is not useful despite it highlighting areas to the edge of the rust ring and centre of the rust region.

In summary, the distinctive red/brown spectrum associated with rust is a powerful indicator for use in corrosion site detection. The differential in intensity between the red/NIR (650/850 nm) and the blue (450 nm) allows for simple feature detection with minimal hardware and software complexity. Hyperspectral imaging has an advantage in that it provides more reliable intensity information with a larger spectral range and so could aid with detecting and classifying unknown non-corrosion related compounds. Unsupervised analysis techniques such as PCA could also be employed to make use of this increased volume of data and efficiently segment images with unknown spectra. If complete automation is the goal, significant attention should be paid to variance fractions so as to avoid false positives. If a pure corrosion detector is desired, however, it is not clear that HS + PCA would be any more effective than an arithmetic colour channel subtraction performed on high resolution colour photography. While there was a 65% increase in contrast observed by utilizing the 850 nm wavelength channel over the 650 nm, this would be at the cost of significant increases in complexity and acquisition time for little gain as all rust was still detected on the three sites by using colour photography. Single wavelength optical filters could also be used to take advantage of the extra contrast given by utilizing the near infra-red without having to invest in HS hardware.

5.4 Conclusions

Methods for remote sensing of corrosion products were assessed for their viability for long term monitoring of corrosion on stainless steel. The expected corrosion products contain spectral features present in the UV-VIS-NIR region which are suited for hyperspectral imaging. A system was constructed which images in the 450 - 850 nm wavelength interval was characterised and compared to colour photography for detecting corrosion. corrosion product phase information was verified by Raman spectroscopic mapping.

1. Both UV-VIS-NIR hyperspectral imaging and colour photography were effective at detecting corrosion site presence from the deposition of rust around the pit mouth
2. Iron oxide phase identification was not possible using the UV-VIS-NIR hyperspectral imager, but a positive intensity gradient from 450 nm to 850 nm was associated with the presence of iron oxides and hydroxides.
3. Subtraction of the 450 nm (blue) channel from the 650 nm (red) channel of RGB colour imagery is adequate for rust region detection, but utilizing the intensity at 850 nm (NIR), present in the HS image, instead of 650 nm (red) provided 65% better contrast for imaging.
4. HSI has the potential to provide higher contrast for detection of rust, but at the cost of significantly increased complexity and acquisition time as colour photography provides the ability to acquire 650 nm and 450 nm colour channels using off the shelf hardware.
5. Principal component analysis was demonstrated to segment hyperspectral data of a corrosion site, with PC1 contrasting the

background metal with anomalies due to bulk intensity variation and PC2
contrasting rust regions by the red/brown intensity gradient.

6. ASSESSMENT OF PIT VOLUME WITH RESPECT TO VISIBLE RUST AREA

6.1 Introduction

Corrosion attack is usually quantified by metal loss, either by weight or by volume, but metal loss for pitting is small which presents a challenge for inspection efforts. Standard methodology for assessing pitting attack is based on labour intensive individual close inspection of the attack sites, with surfaces being cleaned of corrosion product before inspection[171]. During atmospheric pitting all rust generated will be retained in the immediate vicinity of the corrosion site, suggesting that quantifying metal attack by measuring visible rust is possible. To date there has been no quantification of visible rust with respect to a metric for metal loss.

In this chapter, this relationship is investigated for salts relevant nuclear waste stores (MgCl_2 , CaCl_2), chloride deposition density (CDD) ($<100 \mu\text{gcm}^{-2}$) and conditions (fluctuating, $20\text{-}30^\circ\text{C}$ and $20\text{-}50\%$ RH)[9] by comparing rust area measurements from colour photography to pit volume information gathered by confocal laser scanning microscopy.

Colour based image segmentation techniques are widespread in industry and has been previously proposed for corrosion detection[110, 136, 137]. Four colour based image processing techniques (outlined in sections 3.6.1 to 3.6.4) are compared for their efficacy at rust detection:

- Red-Blue colour channel subtraction of the RGB image, followed by thresholding of the remaining intensity. This was chosen due to its

simplicity of application, requiring only two matrix operations to fully segment the image.

- Principal component analysis (PCA) of the RGB image, followed by thresholding of the score of the second principal component. PCA is an unsupervised technique in wide use for anomaly detection and semi-automated segmentation of RGB colour and hyperspectral images in industry[141, 144, 170, 172, 173].
- Conversion to HSV colour space followed by thresholding of the hue and saturation indices. Use of HSV colour space allows for thresholding to be performed using criteria which are more intuitive to a user. Chroma (Hue) is separated from saturation(S) and brightness (Value), allowing for the selection of colour independent of lighting condition.
- Conversion 1976 CIELAB ($L^*a^*b^*$) colour space, followed by thresholding of the b^* (green-yellow) index. $L^*a^*b^*$ colour space was designed to be both device independent and perceptually uniform, meaning that the technique should be more robust when using data gathered using different instruments and that the supervised thresholding process should be more consistent.

6.2 Results

MgCl₂ and CaCl₂ droplets of 100, 50 and 20 µgcm⁻² chloride deposition density were deposited on 304L stainless steel and exposed for 14 days in either fixed 46% RH and 30°C conditions or fluctuating ambient conditions between 19-49% RH and 19-24°C to provide a range of rust areas and pit volumes. 73 MgCl₂ and 74 CaCl₂ droplets with pits were analysed. After exposure, colour photographs were taken before the corrosion product was removed and confocal laser scanning microscopy was performed to measure pit volume.

Four segmentation techniques were used to separate rust area from other surface features in the colour photographs:

- Red-Blue colour channel subtraction of the RGB image, followed by thresholding of the remaining intensity
- Principal component analysis (PCA) of the RGB image, followed by thresholding of the score of the second principal component
- Conversion to HSV colour space, followed by thresholding of the hue and saturation indices
- Conversion to L*a*b* colour space, followed by thresholding of the b* (green-yellow) index.

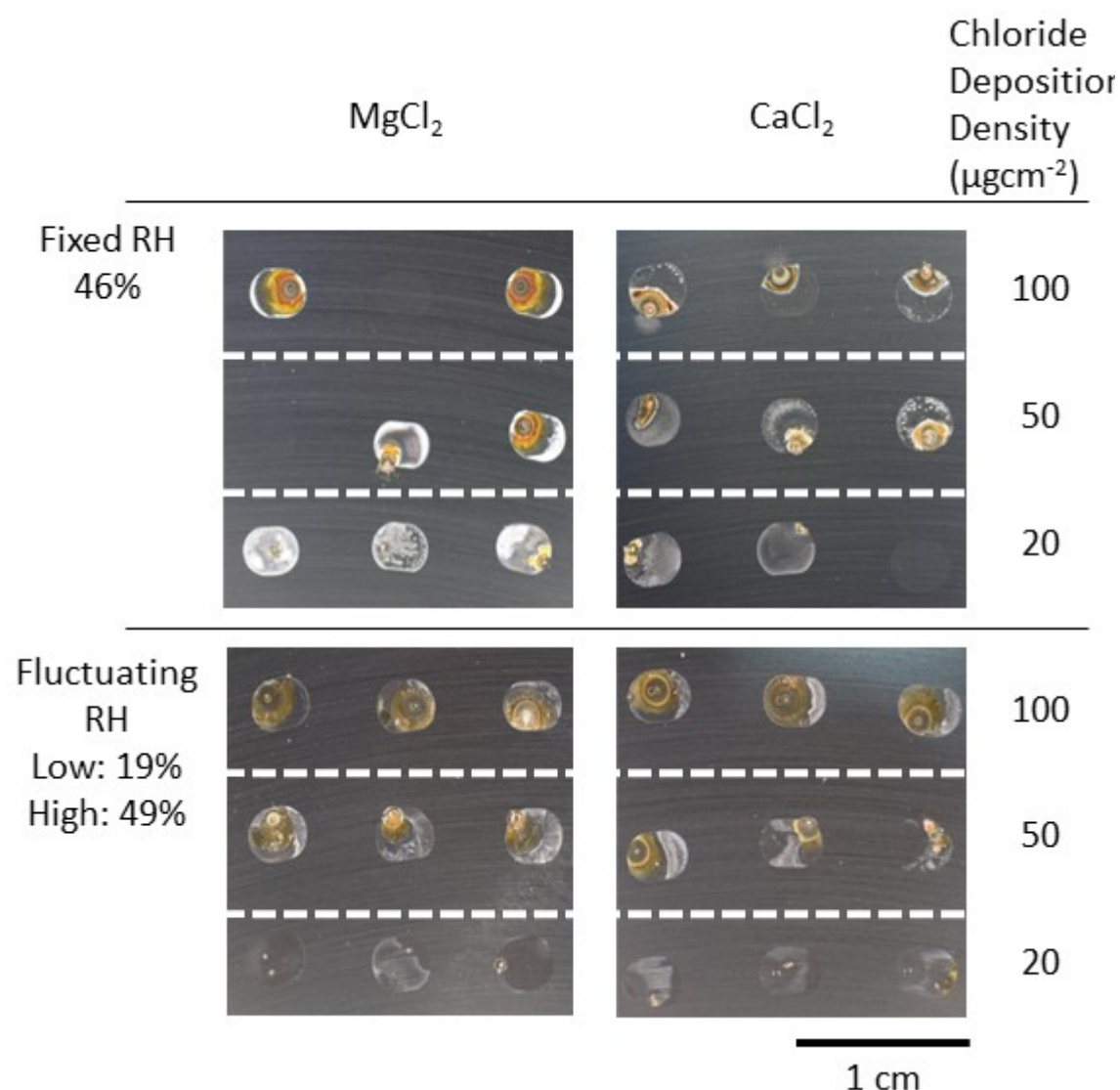


Figure 52 Representative corrosion product morphology for all tested conditions; 20, 50 100 µgcm⁻² chloride deposition densities, fluctuating and fixed RH and temperature and both MgCl₂ and CaCl₂ droplets.

Figure 52 shows colour photography of representative examples of corrosion product morphologies observed under all tested conditions at point of extraction, before corrosion products were washed off. 100, 50 and 20 µgcm⁻² MgCl₂ and CaCl₂ droplets were exposed in both fixed 43% RH and 30°C and fluctuating ambient conditions with a range of 19% - 49% RH and 19-24°C. All droplets with pits show red/brown rust directly around the pit mouth and a white salt precipitate outside the rust area, concentrated at the droplet edge. In CaCl₂

droplets exposed in fixed conditions there is a thick, white band of salt precipitate present at the edge of the rust area.

6.2.1 Measurement of Pit Volume via confocal laser scanning microscopy

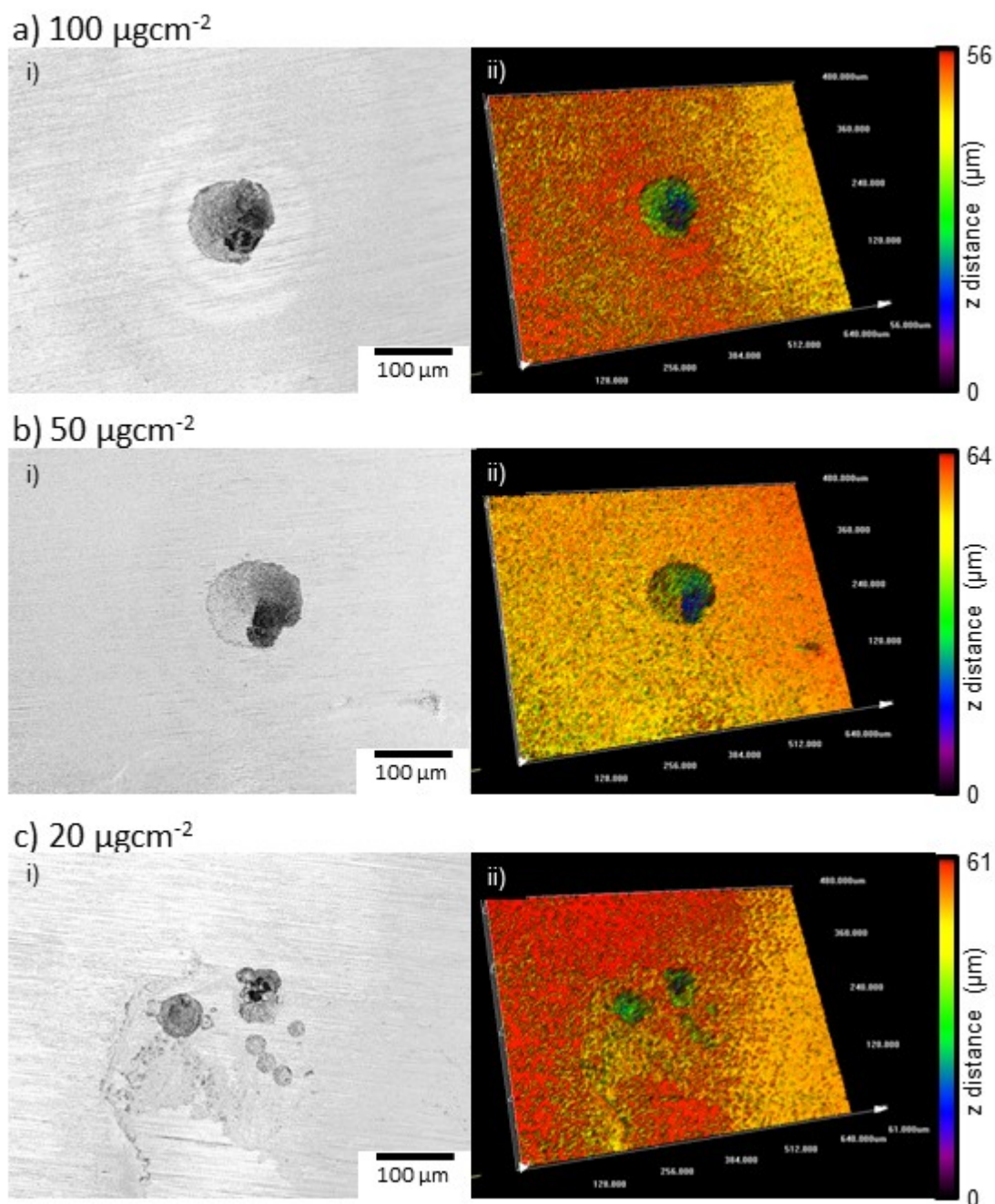


Figure 53 a)b)c) i) Height maps generated by the confocal laser microscope are compared to ii) unprocessed 3D heat-maps for 3 representative pits from CaCl₂ droplets exposed in fluctuating ambient conditions of CDD a) 100 b) 50 and c) 20 μgcm^{-2}

After exposure, the samples were photographed, rinsed and ultrasonically cleaned in deionized water to remove corrosion products. Laser scanning confocal microscopy was then used to measure pit volumes. Figure 53 shows a) i, b) i, c) i intensity height map produced by the confocal microscopy in relation to the raw 3D heat map produced by the software. a), b), c) ii.

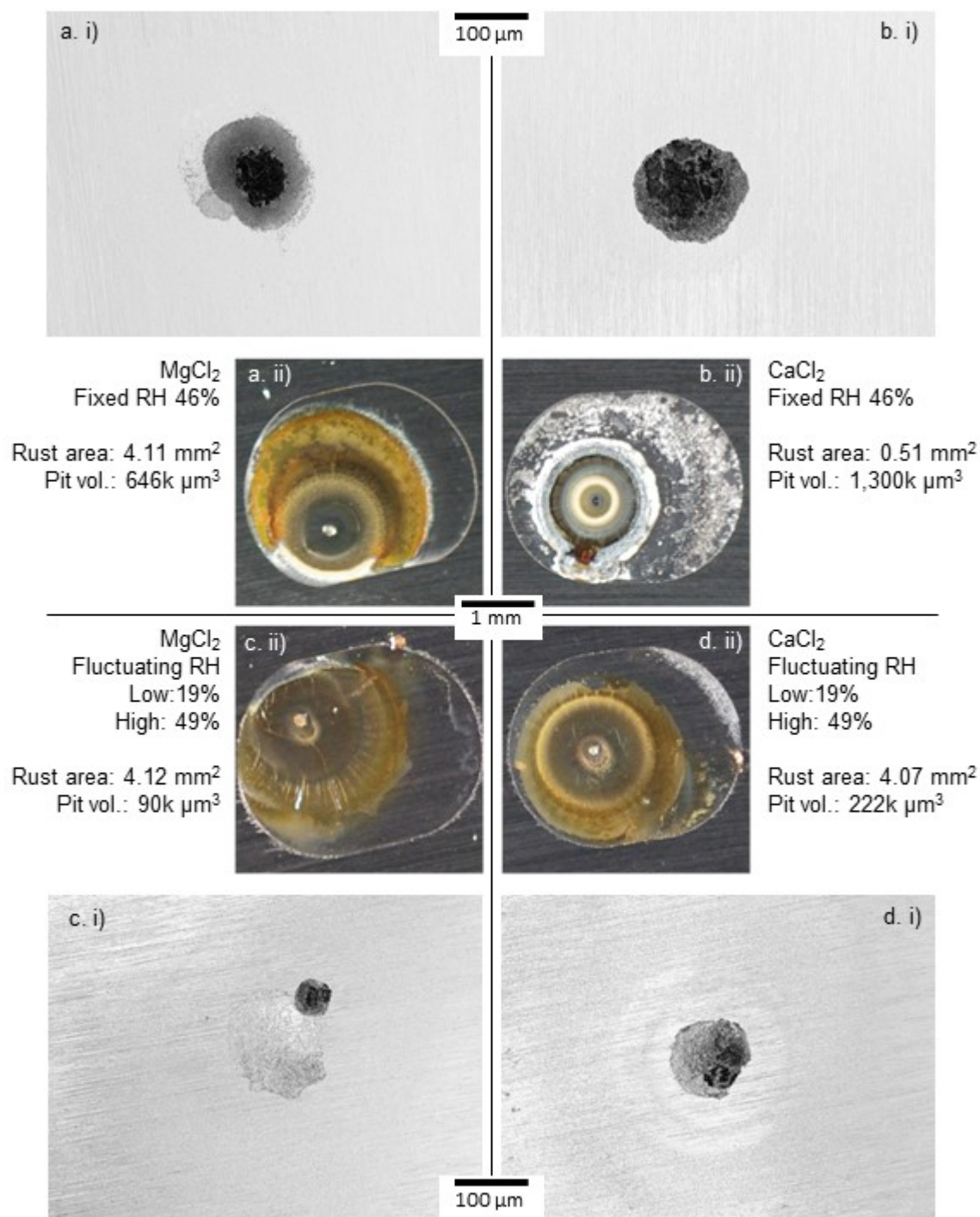


Figure 54 Comparison between photography of droplets of similar rust area and intensity height maps of their pits, gathered by confocal microscopy. All droplets have a CDD of $100 \mu\text{gcm}^{-2}$. a i), ii) MgCl_2 droplet in fixed conditions b i), ii) CaCl_2 droplet in fixed conditions c i), ii) MgCl_2 droplet in fluctuating ambient conditions d i), ii) CaCl_2 in fluctuating ambient conditions.

Figure 54 shows photography of a representative set of $100 \mu\text{gcm}^{-2}$ CDD droplets of similar rust area for all tested conditions and associated confocal microscopy images showing pit morphology. In the case of the CaCl_2 droplet (b), a site was chosen with a large pit volume as no valid droplet was available with similar rust area to the other sites. All other droplets have different pit volumes, despite having near identical rust area. Several pit morphologies are present. a and b i) showing hemispherical morphology while c and d i) show a shallow dish with a spiral morphology.

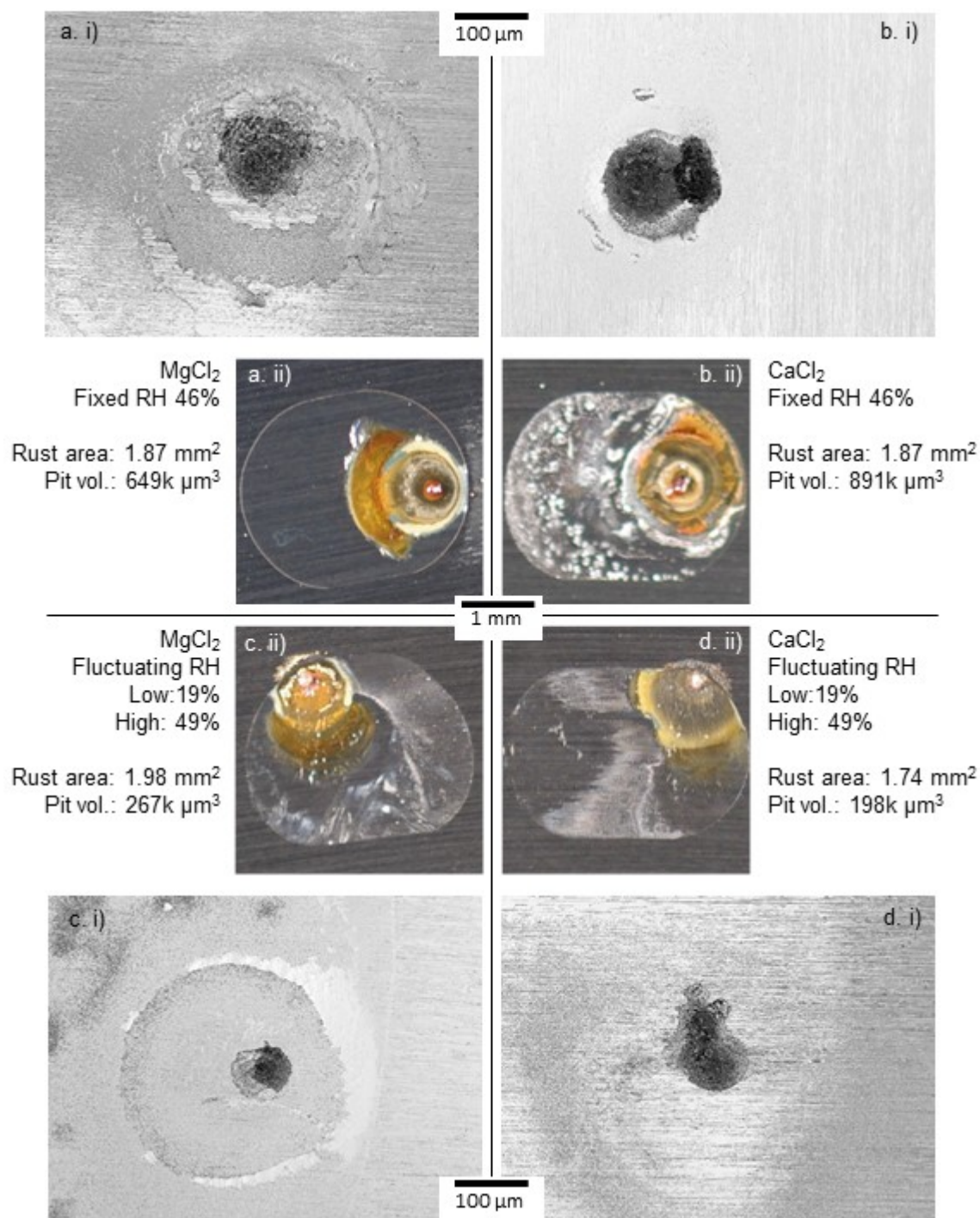


Figure 55 Comparison between photography of droplets of similar rust area and confocal microscopy of their pits. All droplets have a CDD of $50 \mu\text{gcm}^{-2}$. a i), ii) MgCl_2 droplet in fixed conditions b i), ii) CaCl_2 droplet in fixed conditions c i), ii) MgCl_2 droplet in fluctuating ambient conditions d i), ii) CaCl_2 in fluctuating ambient conditions.

Figure 55 shows photography of a representative set of $50 \mu\text{gcm}^{-2}$ CDD droplets of similar rust area for all tested conditions and associated confocal microscopy images showing pit morphology. All pits show a hemispherical morphology.

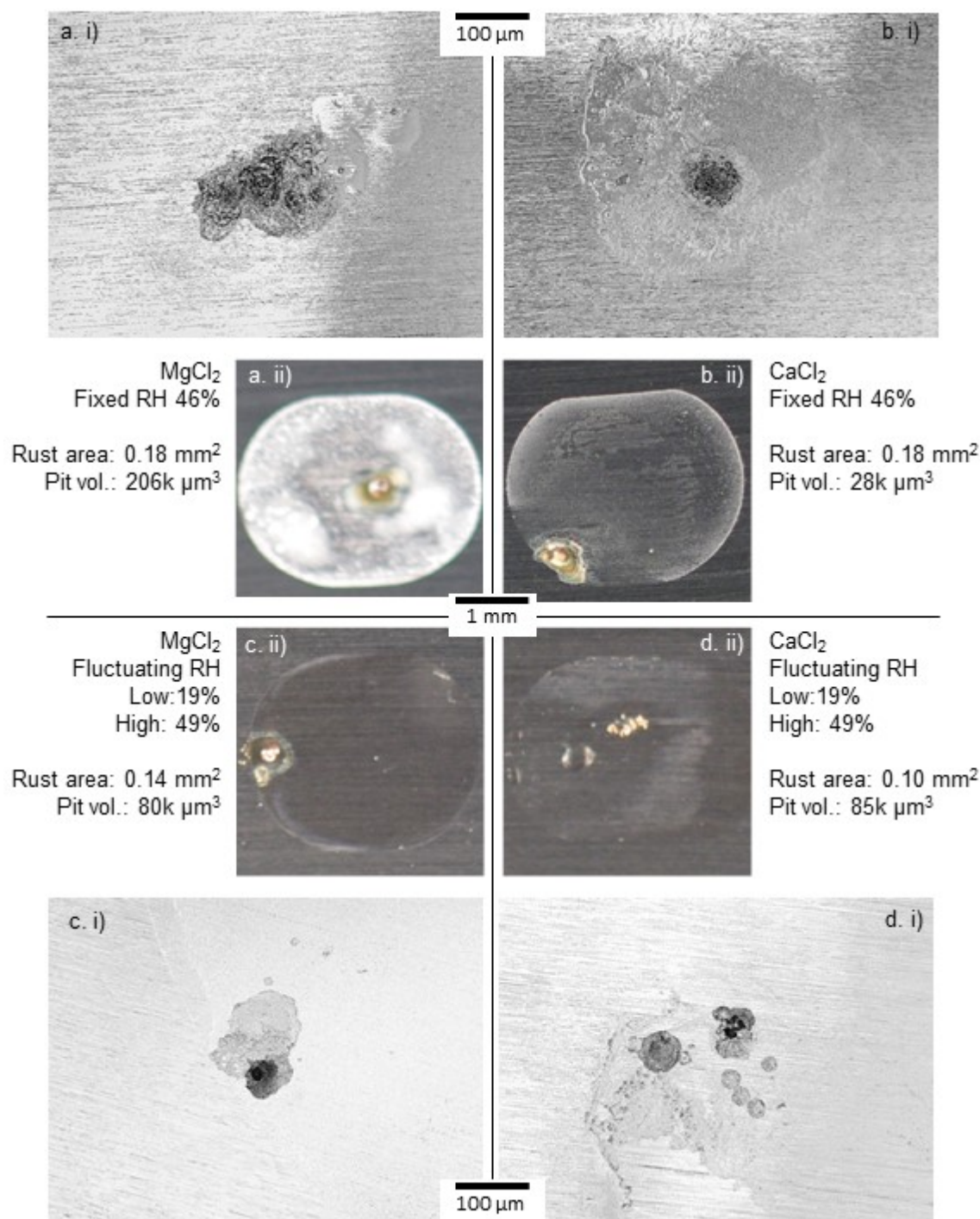


Figure 56 Comparison between photography of droplets of similar rust area and confocal microscopy of their pits. All droplets have a CDD of $20 \mu\text{gcm}^{-2}$. a i), ii) MgCl_2 droplet in fixed conditions b i), ii) CaCl_2 droplet in fixed conditions c i), ii) MgCl_2 droplet in fluctuating ambient conditions d i), ii) CaCl_2 in fluctuating ambient conditions.

Figure 56 shows photography of a representative set of $20 \mu\text{gcm}^{-2}$ CDD droplets of similar rust area for all tested conditions and associated confocal

microscopy images showing pit morphology. a) and b) show hemispherical morphology while c) and d) show spiral and satellite morphologies respectively.

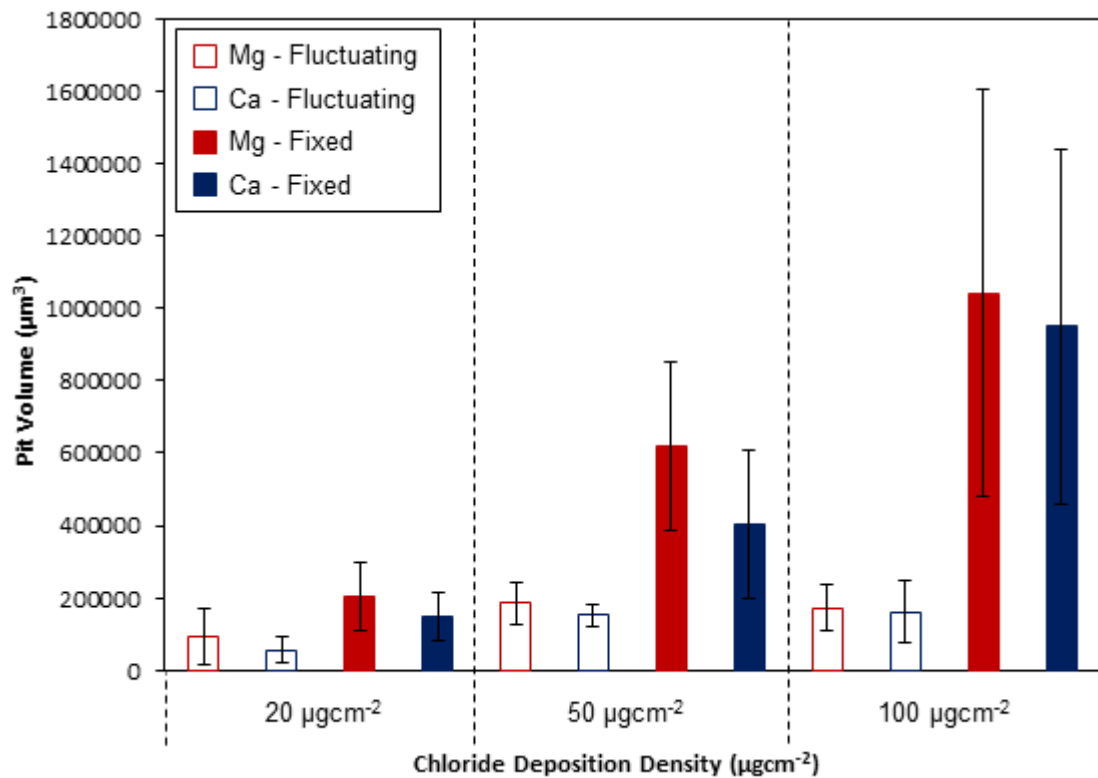


Figure 57 Pit volumes of all droplets compared to their CDD as measured by confocal laser microscopy, with error bars showing standard deviation of the measurements.

Figure 57 shows the pit volumes of all droplets as measured by confocal laser microscopy, arranged by chloride deposition density and by condition. Larger volumes are recorded for droplets exposed to fixed conditions than to fluctuating. At corrosion sites where multiple pits were present, the volume of all pits was summed to give a single value per site. A larger pit volume is also associated with a larger variability in volume. Error bars were applied as the standard deviation of all pits exposed to a particular condition and CDD.

6.2.2 Estimating error in pit volume due to user controlled parameters

The process for pit volume measurement had opportunities for the introduction of random error due to user set parameters in tilt correction of the sample surface, upper and lower vertical limits during acquisition and manual region allocation for volume assessment. In order to estimate the error introduced by user input during the measurement process, acquisition of pit volume was repeated 6 times on 34 pits from MgCl_2 and CaCl_2 droplets in fixed conditions.

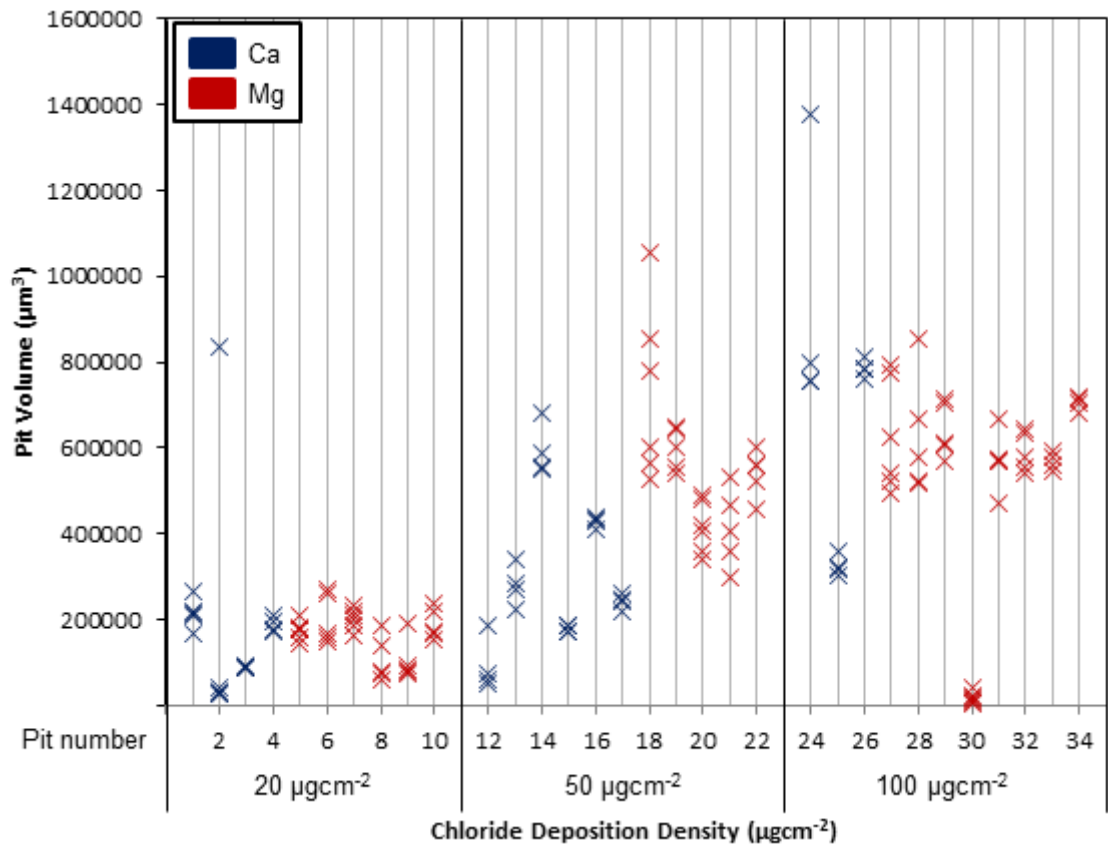


Figure 58 Volumes for 6 repeat measurements of pit volume for 34 pits using laser scanning confocal microscopy for 100, 50 and 20 μgcm^{-2} CDDs exposed to fixed 46% RH and 30°C. Each vertical line represents an individual pit, crosses are volumes given by each repeat measurement of said pit.

Figure 58 shows the variation of repeated measurements of pit volume due to user error for 34 droplets exposed to fixed 46% RH and 30°C conditions.

Table 8 Breakdown of standard deviation as averaged percentage of the mean associated pit measurement by salt cation and chloride deposition density for all 34 pits present in Figure 58

Salt Cation	Chloride Deposition density (μgcm^{-2})			All CDDs
	100	50	20	
Mg	16%	12%	23%	18%
Ca	8%	16%	14%	17%

Table 8 shows the averaged percentage standard deviation present in the measurement of pit volume for 34 pits exposed to fixed conditions. Standard deviations are shown as an averaged percentage of the mean of all measurements for a particular chloride deposition density, salt cation or combination of the two.

6.2.3 Determination of threshold for Red-Blue colour channel subtraction method

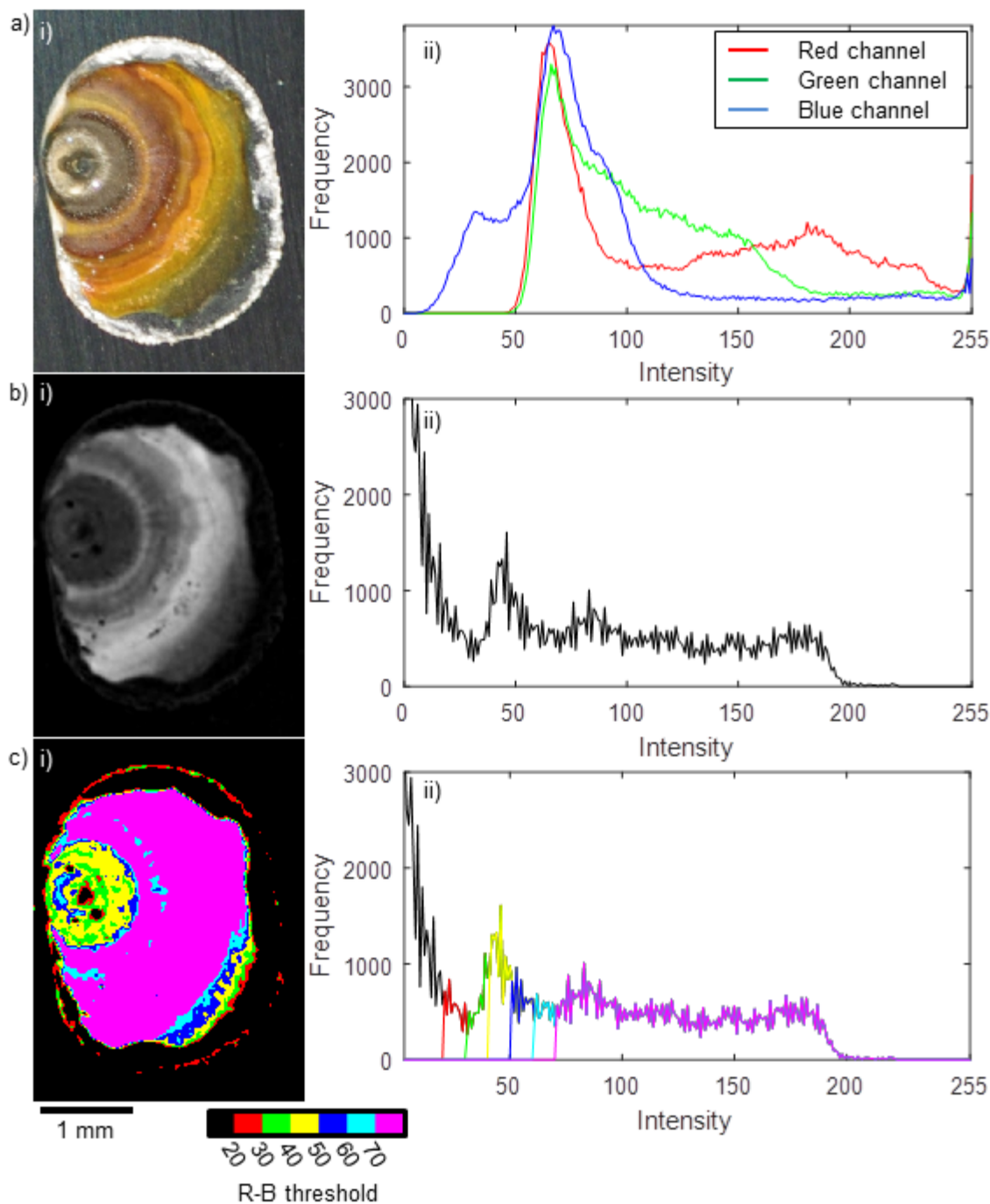


Figure 59 a) i) Colour photograph of 100 μgcm^{-2} CDD MgCl_2 droplet exposed in fixed conditions and ii) Distribution of intensities associated with each colour channel in a) i). b) i) Grayscale image of remaining intensity when the blue channel of a) i) is subtracted from the red. b) ii) Distribution of residual intensities after colour channel subtraction c) i) Area segmented when an intensity threshold of 20, 30, 40, 50, 60 or 70 is applied to b) i). c) ii) Distribution of residual intensities after colour channel subtraction with thresholds highlighted.

Figure 59 consists of a i) a colour photograph of a $100 \mu\text{gcm}^{-2}$ MgCl_2 droplet. Visible in the image is the red/brown rust area showing the range and area distribution of red rust. The associated histogram a ii) shows all three intensity distributions peaking at 70, indicating that most of the brightness is centred around this value. The red channel has an additional broad peak at 190, and blue a low shoulder at 30-40 indicating that there are a significant number of pixels with a red hue. Finally all three distributions show a sharp peak at 255, indicating the presence of white pixels.

Inset b i) consists of the intensity remaining when the blue channel from a) is subtracted from the red as a method for separating all pixels with a red hue. The central rust area remains visible along with a small amount of the white salt at the droplet edge. The associated histogram b ii) shows the intensity distribution of the remaining pixels. The highest frequency is near zero, with a secondary peak at 50. Frequencies are then equally represented until 200, where frequency drops to zero.

Inset c) shows the areas of the image segmented when thresholding is applied to b), with each colour corresponding to extra area acquired when a lower threshold is applied. The associated histogram has the same colours overlaid showing intensity intervals accounted for by a particular threshold. An Intensity threshold of 70 segments the smallest area, a threshold of 20 segments the highest.

6.2.4 Determination of threshold for principal component analysis method

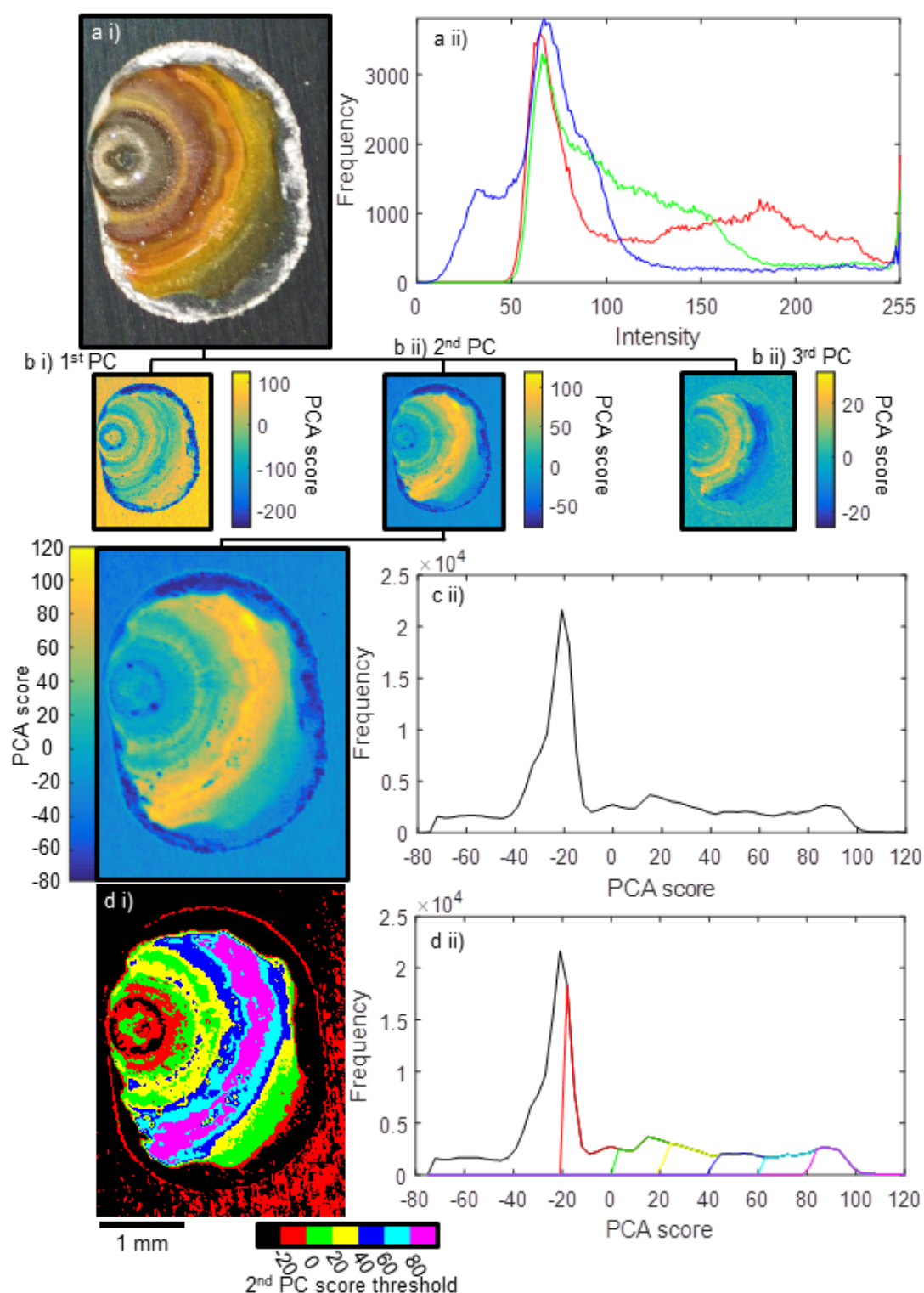


Figure 60 a) i) Colour photograph of 100 μgcm^{-2} CDD MgCl_2 droplet exposed in fixed conditions and ii) Distribution of intensities associated with each colour channel in a) i). b) i-iii) 1st, 2nd and 3rd principal components of a) i). c) i) Distribution of scores in the 2nd principal component c) ii) histogram of scores of the 2nd principal component. d) i) Areas segmented when score threshold is applied to the second principal component d) ii) distribution of intensities segmented with a particular threshold.

Figure 60 consists of a i) a colour photograph of a $100 \mu\text{gcm}^{-2}$ MgCl_2 droplet. Visible in the image is the red/brown rust area showing the range and area distribution of red rust. The associated histogram a ii) shows all three intensity distributions peaking at 70. The red channel has an additional broad peak at 190, the green channel has a large shoulder from 70 to 170 and the blue channel has two shoulders at 40 and 100 either side of the main peak at 70. Finally all three distributions show a sharp peak at 255.

b i-iii) shows heat maps of the 1st, 2nd and 3rd principal components of the image in a) The first principal component highlights the variation in overall intensity with the bright white salt around the droplet being given a low score and the rest of the image approximately equal. In the second principal component the rusty region is highlighted with a lighter yellow rust colour associated with a higher score. The third principal component highlights visible rust with a deeper red-brown rust colour associated with a higher score. c i) shows a zoom of the 2nd principal component and the associated histogram cii) shows the score distribution. It has a large peak in score at -20 with the rest of the distribution being approximately equal in frequency up to a score of 80, where it drops to zero.

The image d i) and associated histogram d ii) are the product of score thresholding of the second principal component showing the regions contained within each score interval. A threshold of -20 includes significant non-rusty pixels, a threshold of zero maximizes segmentation of rusty area.

6.2.5 Determination of threshold for HSV thresholding method

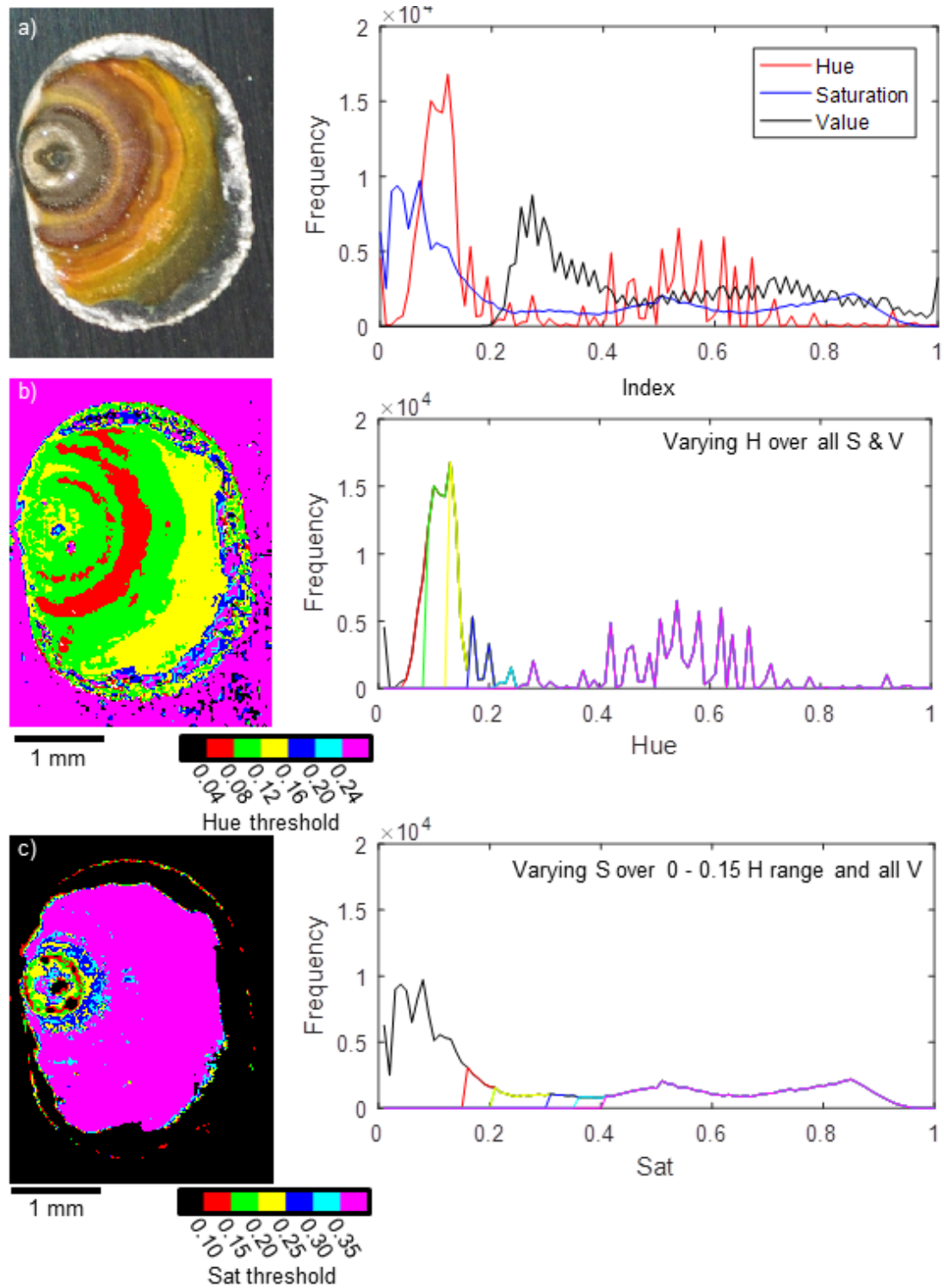


Figure 61 Comparison of rust areas gathered by applying different thresholds to photography in HSV colour space alongside histograms of the pixel distribution of the images. a) Initial colour photograph showing corrosion product morphology of a $100 \mu\text{gcm}^{-2}$ MgCl_2 droplet alongside histogram of the intensity distribution of its colour channels taken using DSLR camera b) map of areas generated when a minimum hue threshold was applied to a. c) map of areas generated when a minimum saturation threshold was applied to a as well as limiting hue to 0-0.15.

Figure 61 consists of a) colour photograph of a $100 \mu\text{gcm}^{-2}$ MgCl_2 droplet alongside the histogram of the hue, saturation and value distributions. The major feature in hue is a large peak at 0-0.15. Saturation is largest close to 0 with minor peaks at 0.5 and 0.8. Value is zero below 0.2, peaks at 0.3 and has a very broad peak centred at 0.7. Inset b) shows the areas associated with different values of hue. All areas are included with a value over 0.2, while progressively smaller regions of the total rusty area are included with lower thresholds. Inset c) shows the areas gathered when saturation thresholds are applied to an image trimmed to 0-0.15 in hue. All thresholds include the rust area but saturations below 0.3 also include parts of the white salt at the edge of the droplet.

6.2.6 Determination of threshold for $L^*a^*b^*$ thresholding method

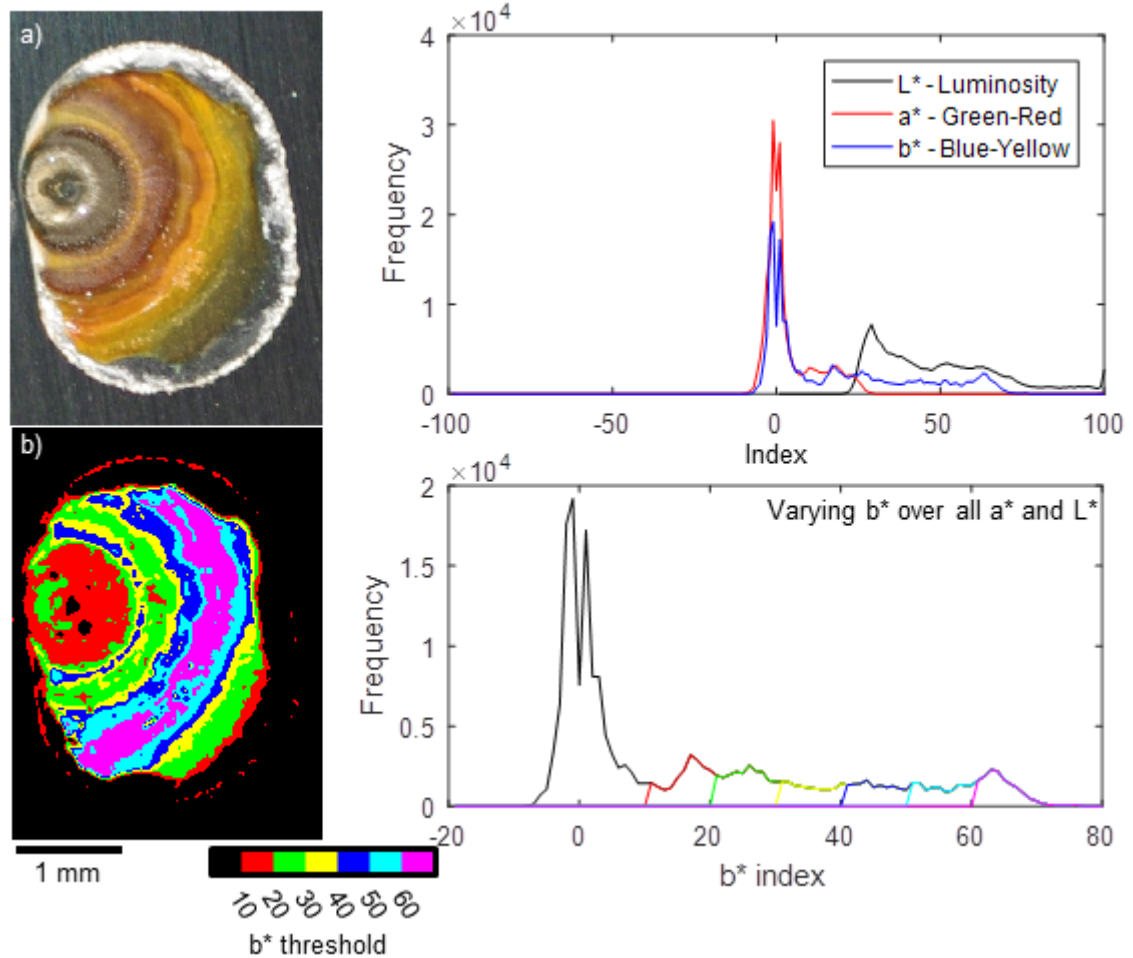


Figure 62 Comparison of rust areas gathered by applying different thresholds to photography in $L^*a^*b^*$ colour space alongside histograms of the pixel distribution of the images. a) Initial colour photograph showing corrosion product morphology of a 100 μgcm^{-2} MgCl_2 droplet alongside histogram of the intensity distribution of its colour channels b) map of areas generated when a minimum b^* threshold was applied to a).

Figure 62 shows a) colour photograph of a 100 μgcm^{-2} MgCl_2 droplet alongside a histogram of the Luminance (L^*), green-red (a^*) and blue-yellow (b^*) distributions of the image when converted to the 1976 CIELAB colour space. b) consists of the area distributions associated with different thresholds in (b^*). A threshold of 20 is associated with the difference between getting purely rust area and including elements of the white salt at the edge of the droplet.

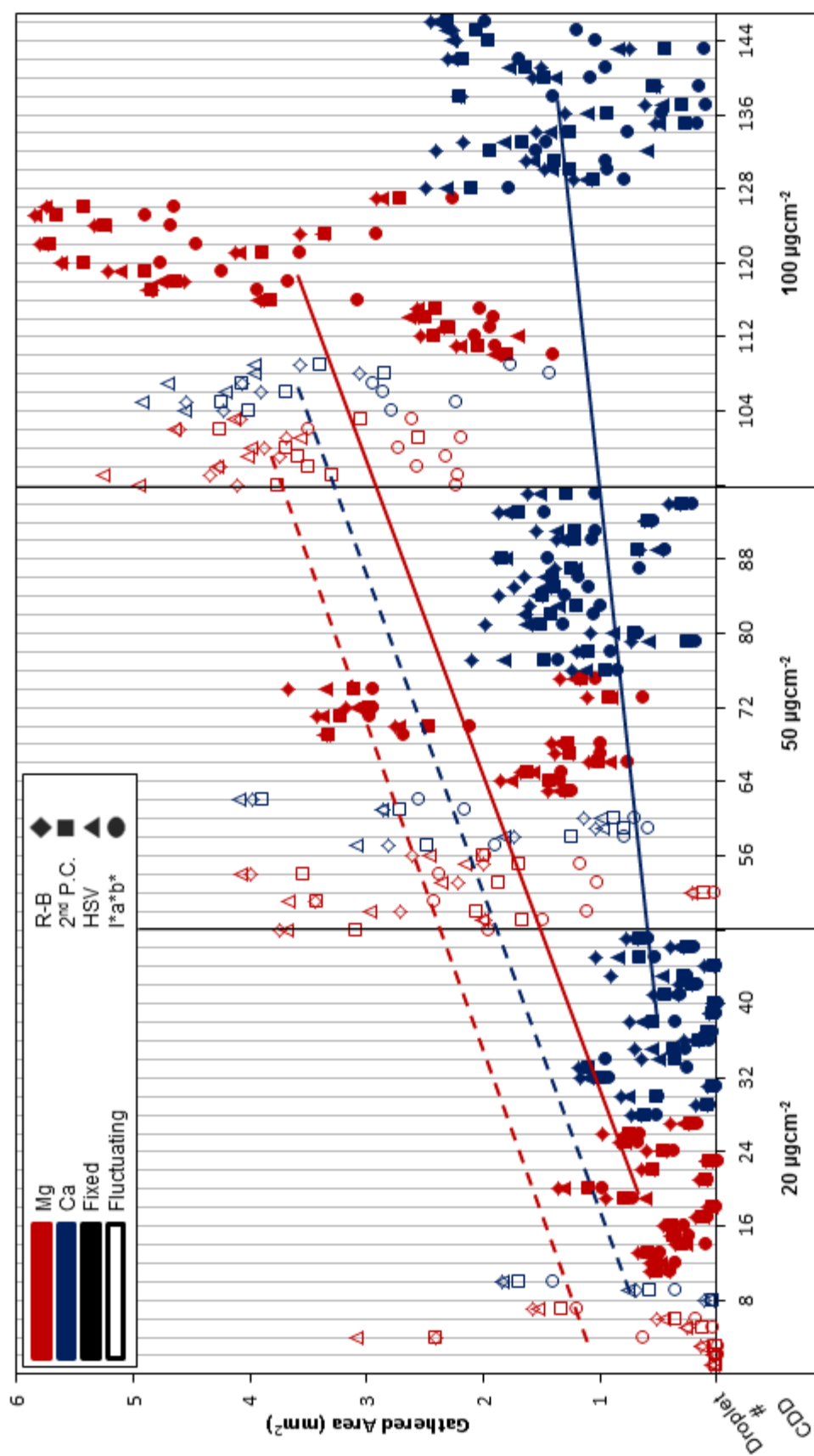


Figure 63 Comparison of rust areas gathered by different segmentation methods for all tested droplets (labelled individually as Droplet #). Segmentation methods are differentiated by shape, conditions and salt cation by colour and fill. Thresholds for each technique were: 20 for R-B colour channel subtraction, 30 for principal component analyses 0-0.15H, 20S for HSV and 20b* for L*a*b*. Line annotations show general trend in gathered area with increasing CDD.

Figure 63 shows a per droplet comparison of different rust area acquisition segmentation techniques for MgCl_2 (red) and CaCl_2 (blue) droplets in fixed 46% RH and 30°C (no fill) and fluctuating ambient conditions between 19% and 49% RH and 19-24°C (filled). Thresholds were determined by visual inspection of rust area with respect to the extent of pixel areas segmented by a particular threshold and technique for a small sample of the dataset. Thresholds used for each technique were:

- 20 for R-B colour channel subtraction,
- 30 for principal component analysis
- 0-0.15H, 20S for HSV
- 20b* for $L^*a^*b^*$

Chloride deposition densities of 20, 50 and 100 μgcm^{-2} were tested. There is a general trend where rust area increases with CDD, except for CaCl_2 droplets exposed in fixed conditions which have low rust areas compared to other droplets.

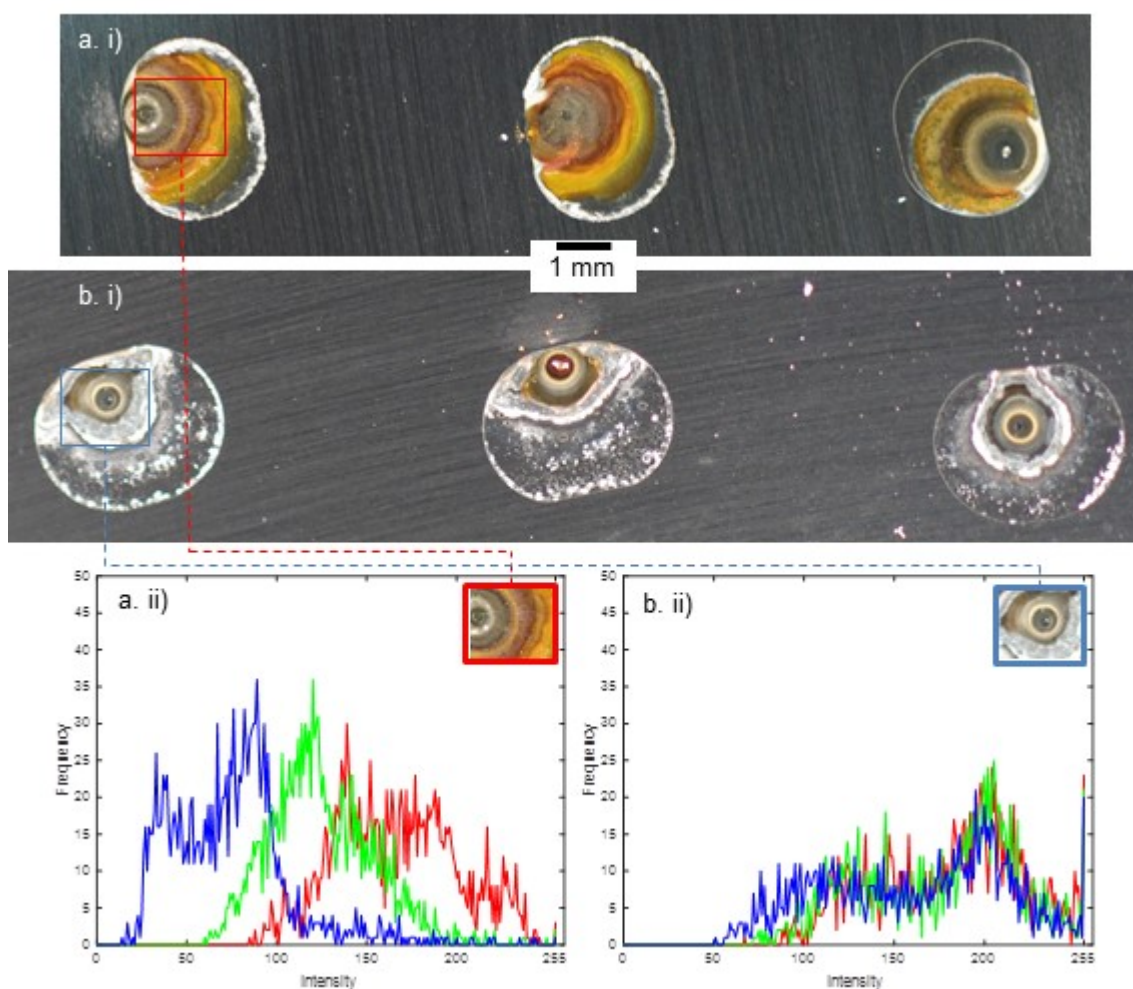


Figure 64 Comparison of colour intensity values by histogram of highlighted region of interest of a i), ii) MgCl_2 and b i), ii) CaCl_2 droplets corroded for 2 weeks at 46% RH and 30°C.

Figure 64 shows an example of the central region directly over the pit of a) a MgCl_2 droplet compared to that of a b) CaCl_2 droplet in the same conditions, with the histograms a,b) ii) showing this lack of colour gradient for use in colour based segmentation.

6.2.7 Rust area vs. pit volume

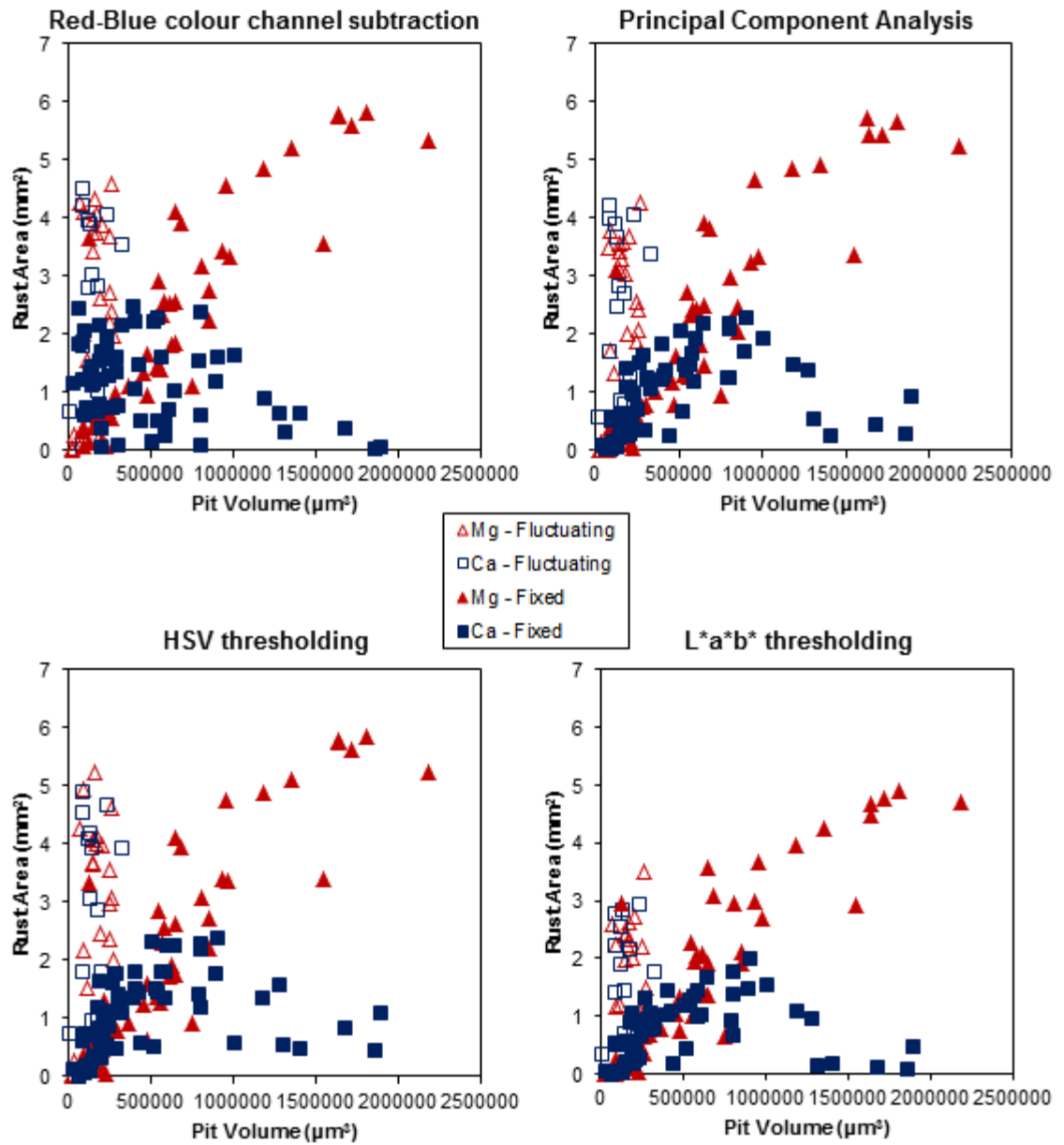


Figure 65 Comparison of pit volume vs. rust area for all rust area segmentation methods for both MgCl_2 and CaCl_2 droplets exposed for 2 weeks under either fixed conditions (46% RH and 30°C) or fluctuating ambient conditions (19-49% RH and 10-24°C)

Figure 65 shows a comparison between rust area and pit volume for the four rust area segmentation methods. Thresholds used were:

- Red-Blue colour channel subtraction with a residual intensity threshold of

- 2nd principal component score of 30 for the PCA method.
- HSV threshold of 0.15 hue and 0.2 saturation
- b* threshold of 20 for L*a*b* thresholding

All four methods present a broadly linear relationship for droplets exposed in fixed 46% RH and 30°C, while droplets exposed in fluctuating ambient conditions (19-49% RH and 10-24°C) are limited to pit volumes of less than 400,000 μm^3 despite having a similar spread of rust areas to the droplets exposed to fixed conditions. CaCl_2 droplets with pit volumes over 1,000,000 μm^3 had significantly lower rust areas than would be expected from a linear relationship.

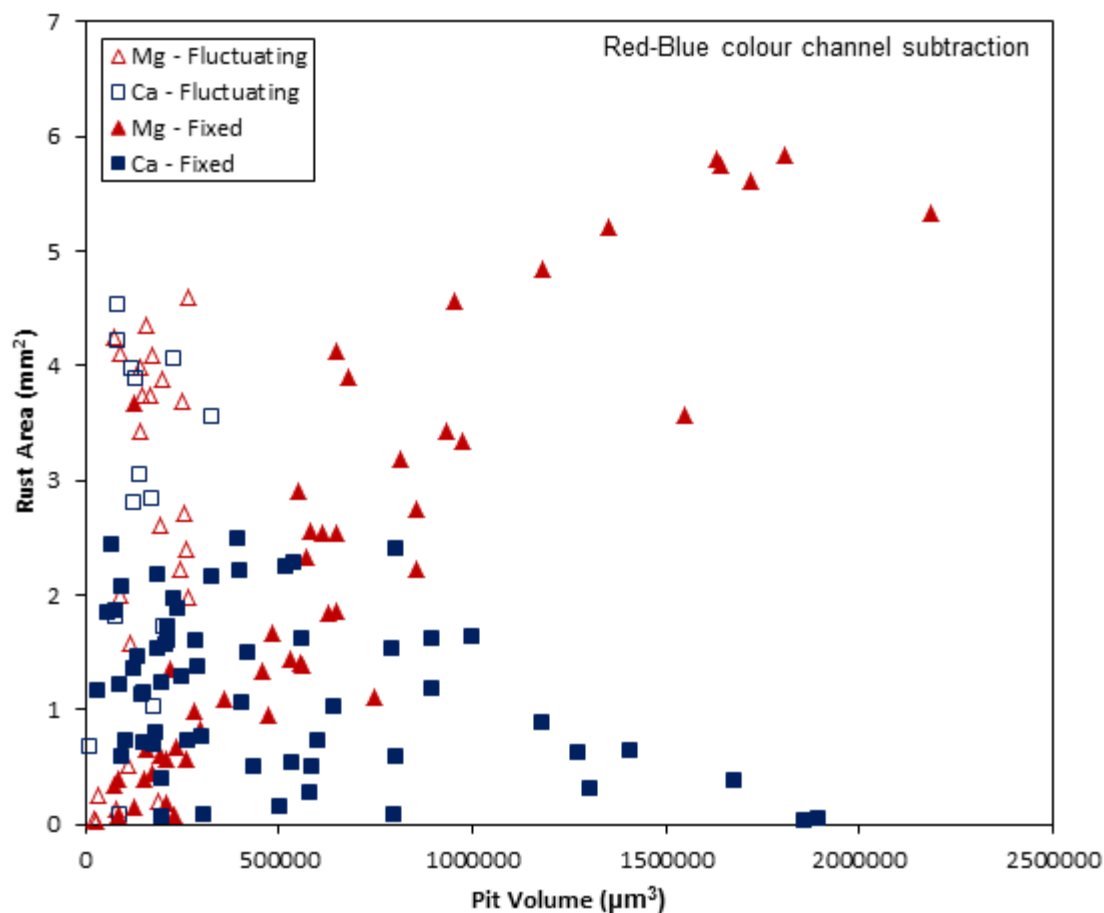


Figure 66 Comparison of pit volume vs rust area gathered by Red-Blue colour channel subtraction and thresholding (as in figure 62) for both MgCl_2 and CaCl_2 droplets exposed for 2 weeks under either fixed conditions (46% RH and 30°C) or fluctuating ambient conditions (19-49% RH and 19-24°C).

Figure 66 shows a comparison of pit volume vs rust area as gathered by Red-blue colour channel subtraction and thresholding to above a residual intensity of 20 for both MgCl_2 and CaCl_2 droplets exposed for 2 weeks under either fixed conditions (46% RH and 30°C) or fluctuating ambient (19-49% RH and 19-24°C) conditions. MgCl_2 droplets exposed in fixed conditions display a linear relationship between pit volume and rust area whilst CaCl_2 droplets show a much larger variation in pit volumes and rust areas. Droplets exposed in fluctuating ambient conditions have a maximum pit volume of 400,000 μm^3 .

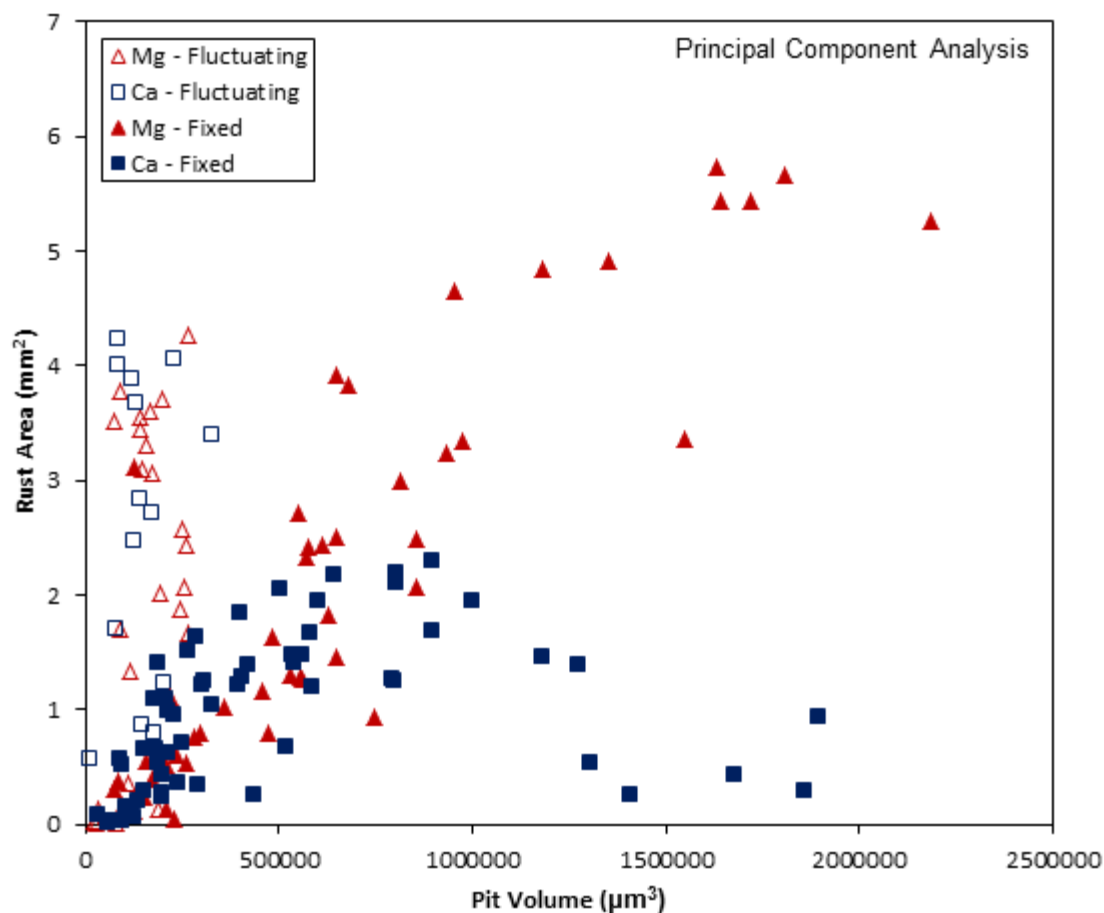


Figure 67 Comparison of pit volume vs rust area gathered by thresholding of the second principal component (as in figure 62) for both MgCl_2 and CaCl_2 droplets exposed for 2 weeks under either fixed conditions (46% RH and 30°C) or fluctuating ambient conditions (19-49% RH and 19-24°C).

Figure 67 shows a comparison of pit volume vs rust area as gathered by thresholding of the second principal component score to above 30 for both MgCl_2 and CaCl_2 droplets exposed for 2 weeks under either fixed conditions (46% RH and 30°C) or fluctuating ambient (19-49% RH and 19-24°C) conditions. MgCl_2 droplets exposed in fixed conditions display a linear relationship between pit volume and rust area whilst CaCl_2 droplets in fixed conditions have a similar relationship below 1,000,000 μm^3 . Above this

threshold observed rust area is reduced to below 1.5 mm^2 . Droplets exposed in fluctuating ambient conditions have a maximum pit volume of $400,000 \text{ }\mu\text{m}^3$.

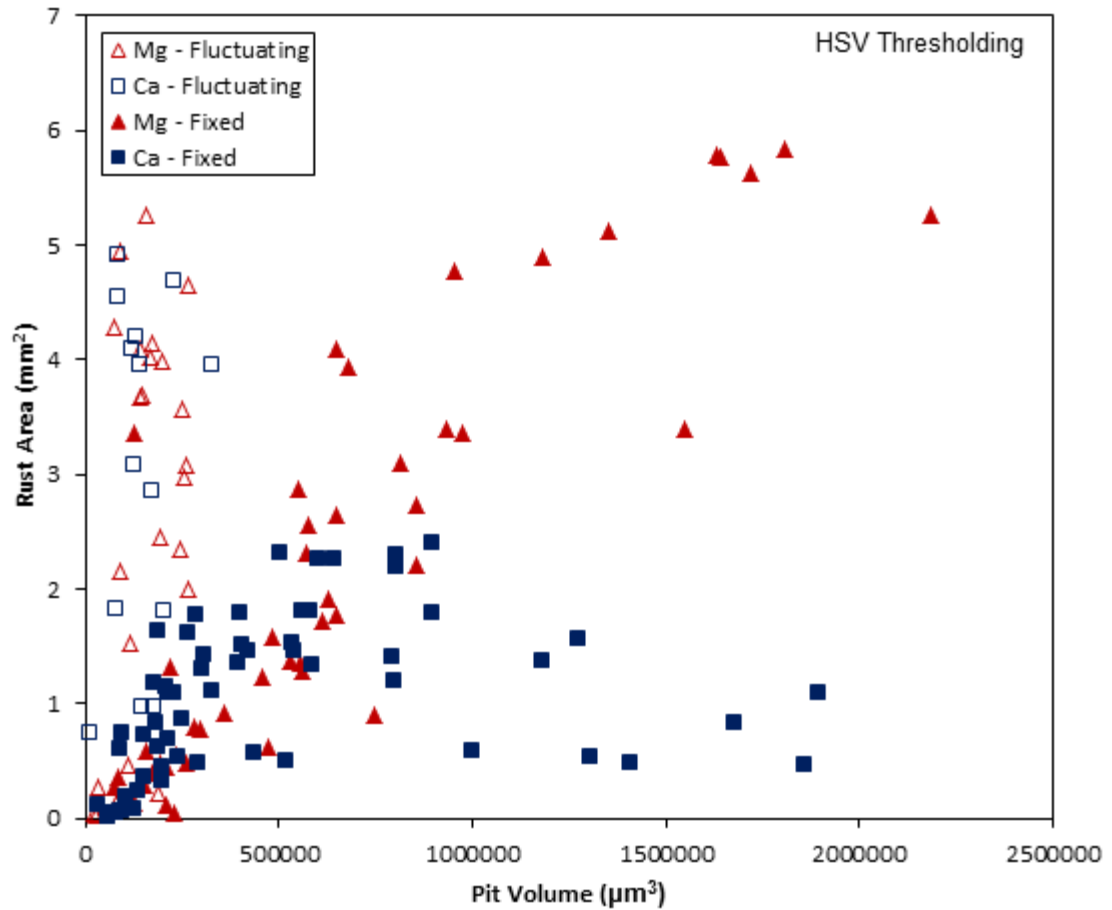


Figure 68 Comparison of pit volume vs rust area gathered by thresholding in HSV colour space (as in figure 62) for both MgCl_2 and CaCl_2 droplets exposed for 2 weeks under either fixed conditions (46% RH and 30°C) or fluctuating ambient conditions (19-49% RH and $19\text{-}24^\circ\text{C}$).

Figure 68 shows a comparison of pit volume vs rust area as gathered by thresholding in HSV colour space to 0.15 in hue and 0.2 in saturation for both MgCl_2 and CaCl_2 droplets exposed for 2 weeks under either fixed conditions (46% RH and 30°C) or fluctuating ambient (19-49% RH and $19\text{-}24^\circ\text{C}$) conditions. MgCl_2 droplets exposed in fixed conditions display a linear relationship between pit volume and rust area whilst CaCl_2 droplets in fixed

conditions have a similar relationship below $1,000,000 \mu\text{m}^3$. Above this threshold observed rust area is reduced to below 1.5 mm^2 . Droplets exposed in fluctuating ambient conditions have a maximum pit volume of $400,000 \mu\text{m}^3$.

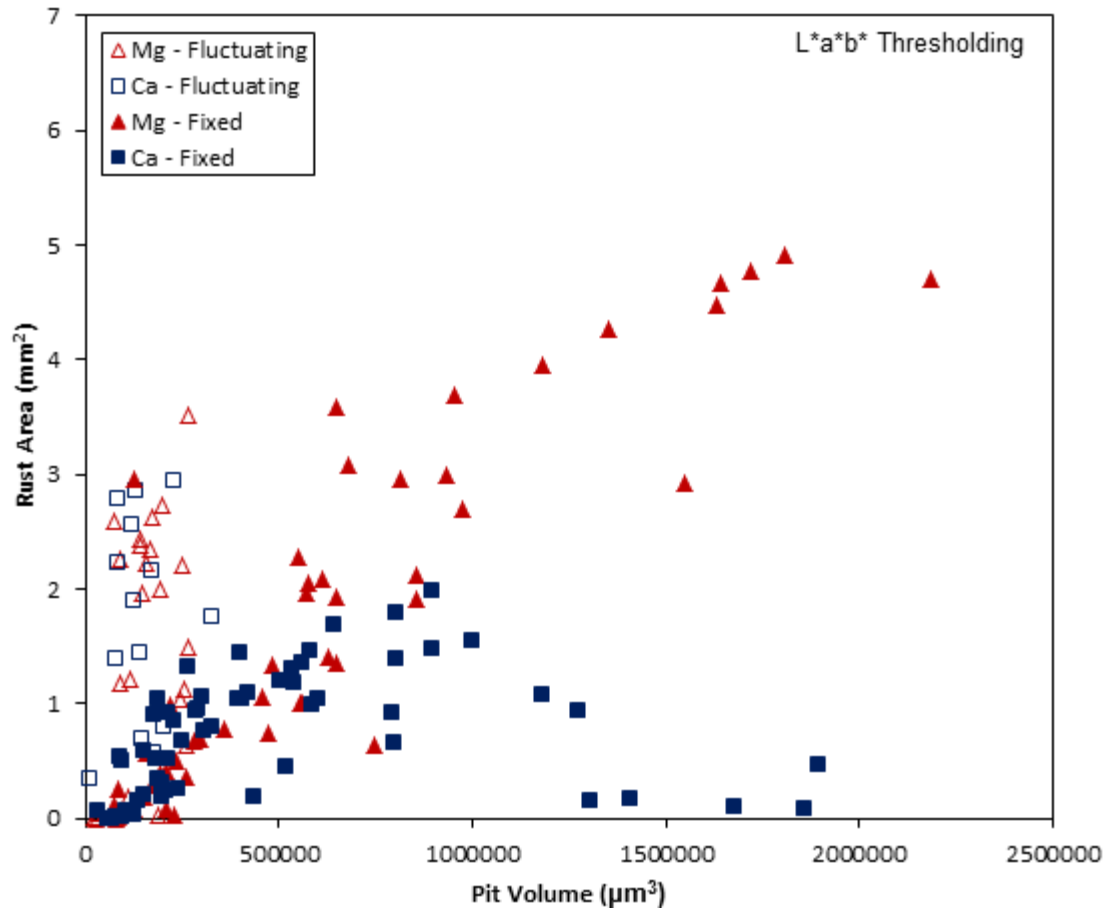


Figure 69 Comparison of pit volume vs rust area gathered by thresholding in L*a*b* colour space (as in figure 62) for both MgCl_2 and CaCl_2 droplets exposed for 2 weeks under either fixed conditions (46% RH and 30°C) or fluctuating ambient conditions (19-49% RH and $19-24^\circ\text{C}$).

Figure 69 shows a comparison of pit volume vs rust area as gathered by thresholding to a b^* index of 20 in 1976 CIELAB ($L^*a^*b^*$) colour space for both MgCl_2 and CaCl_2 droplets exposed for 2 weeks under either fixed conditions (46% RH and 30°C) or fluctuating ambient (19-49% RH and $19-24^\circ\text{C}$) conditions. MgCl_2 droplets exposed in fixed conditions display a linear

relationship between pit volume and rust area whilst CaCl_2 droplets in fixed conditions have a similar relationship below $1,000,000 \mu\text{m}^3$. Above this threshold observed rust area is reduced to below 1.5 mm^2 . Droplets exposed in fluctuating ambient conditions have a maximum pit volume of $400,000 \mu\text{m}^3$.

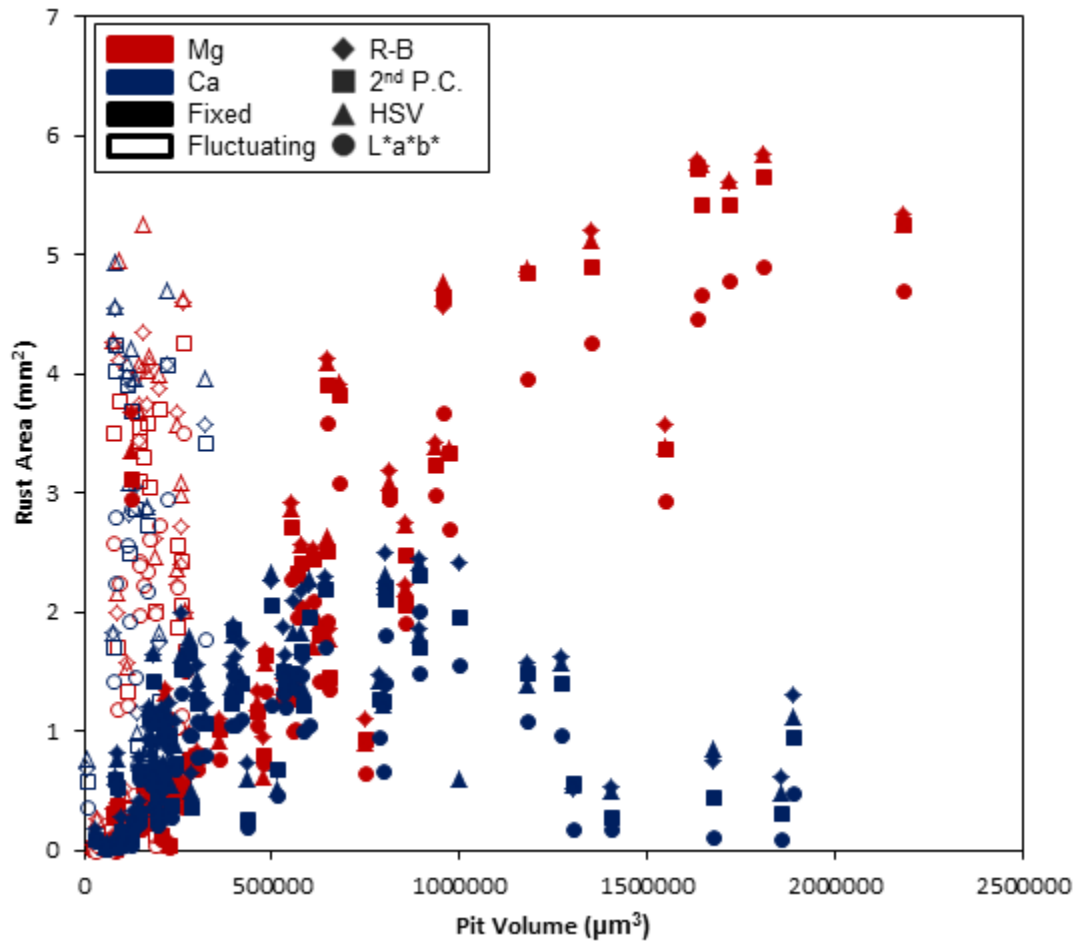


Figure 70 Comparison of pit volume vs rust area gathered by four image processing techniques (as in figures 62-66) for both MgCl_2 and CaCl_2 droplets exposed for 2 weeks under either fixed conditions (46% RH and 30°C) or fluctuating ambient conditions (19-49% RH and $19-24^\circ\text{C}$).

Figure 70 shows data on pit volume gathered by confocal laser microscopy compared to rust area data gathered by the four colour based segmentation techniques described in section 3.6. MgCl_2 and CaCl_2 droplets exposed for 2

weeks under either fixed conditions (46% RH and 30°C) or fluctuating ambient (19-49% RH and 19-24°C) conditions. MgCl₂ droplets exposed in fixed conditions display a linear relationship between pit volume and rust area whilst CaCl₂ droplets in fixed conditions have a similar relationship below 1,000,000 µm³. Above this threshold observed rust area is reduced to below 1.5 mm². Droplets exposed in fluctuating ambient conditions have a maximum pit volume of 400,000 µm³.

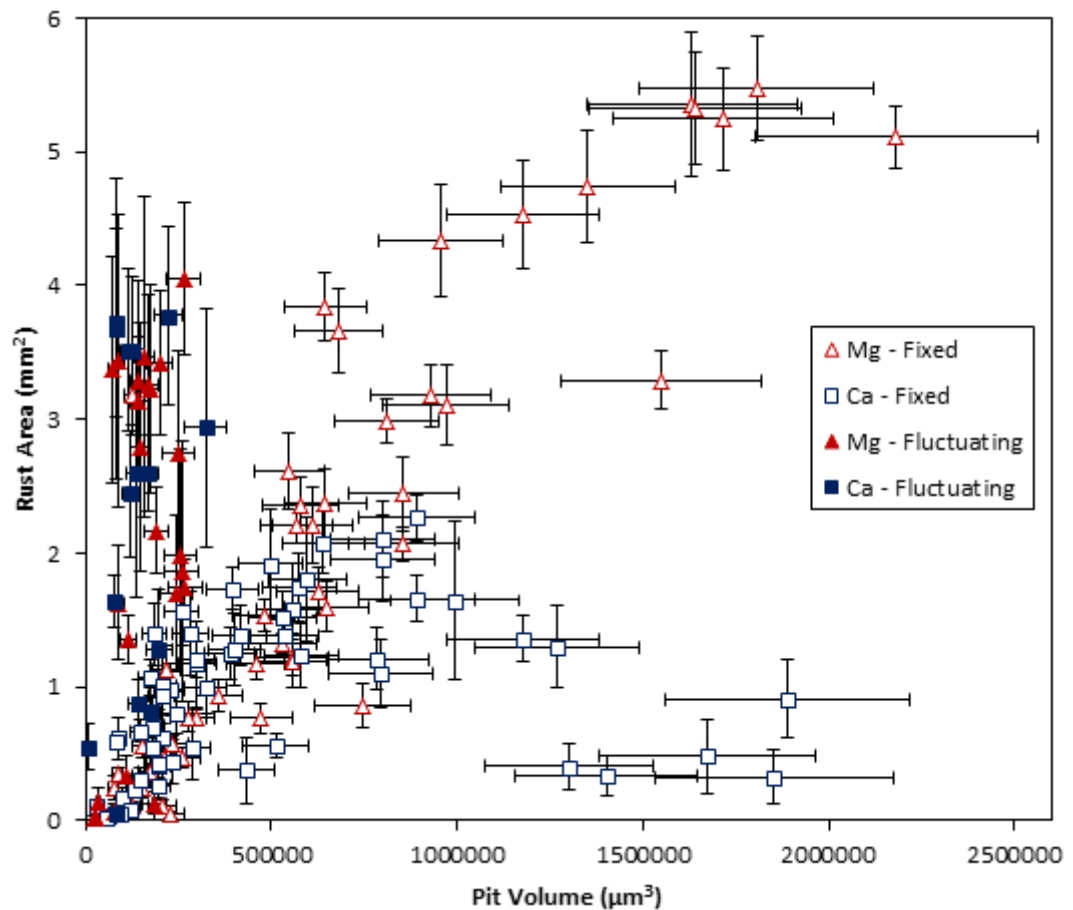


Figure 71 Comparison of pit volume vs rust area for both MgCl₂ and CaCl₂ droplets exposed for 2 weeks under either fixed conditions (46% RH and 30°C) or fluctuating ambient (19-49% RH and 19-24°C). Error bars show standard deviation of pit volume measurements (x) and standard deviation of area measurements acquired through different threshold-based techniques (y).

Figure 71 shows data on pit volume gathered by confocal laser microscopy compared to averaged rust area data gathered by the four colour based segmentation techniques described in section 3.6. Vertical error bars (variable) were drawn by calculating the standard deviation of areas across all four techniques for each individual droplet whilst horizontal error bars (17.4%) were drawn by taking the average standard deviation of 6 volume measurements of 34 representative pits and extrapolating to the full population as described in section

6.2.8 Ambient exposure conditions

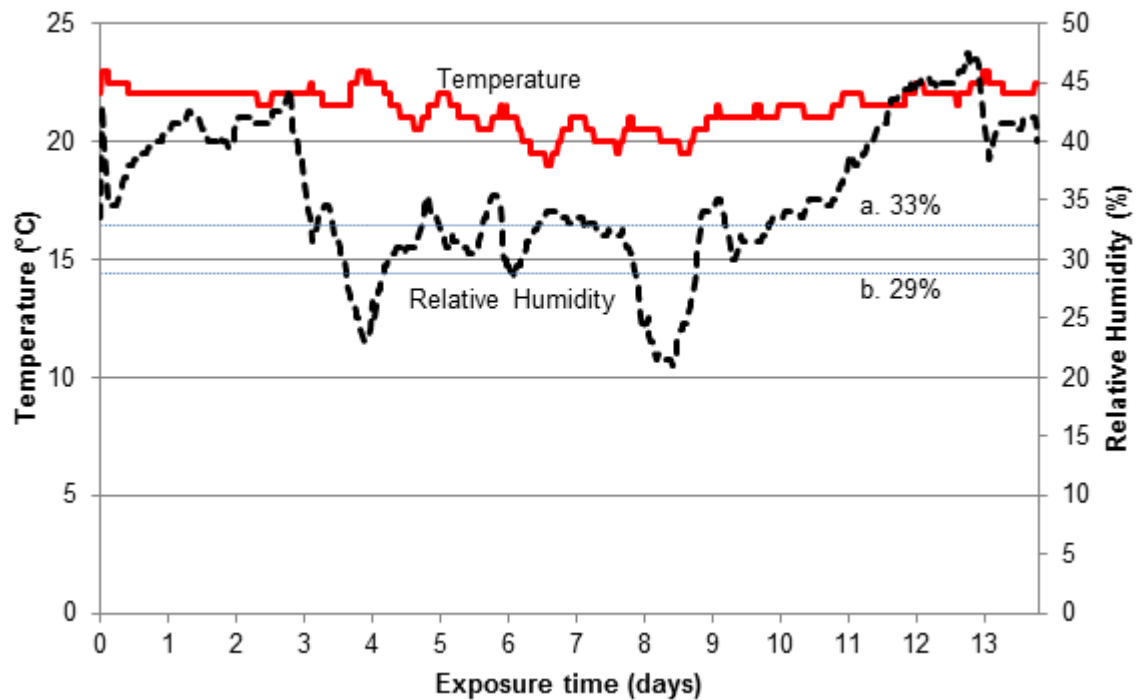


Figure 72 Data from temperature and humidity logger placed alongside fluctuating ambient samples during exposure with a 30 minute interval between acquisitions. a and b show deliquescence points for CaCl_2 (29% RH) and MgCl_2 (33% RH) respectively at this temperature range [174]

Figure 72 shows the exposure conditions as recorded from a data logger placed alongside the samples left open to fluctuating ambient conditions. The temperature remains steady between 19°C and 23°C whilst the relative humidity fluctuated between 20% and 43%. Deliquescence points of a. $\text{MgCl}_2 \cdot 6\text{H}_2\text{O}$ at 33% RH and b. $\text{CaCl}_2 \cdot 6\text{H}_2\text{O}$ at 29% RH are marked.[174]

6.3 Discussion

6.3.1 Pit volume measurements

A general increase in pit volume with chloride deposition density (CDD) was observed for droplets exposed to fixed conditions, but this relationship was not present for droplets in fluctuating conditions (Figure 57), where pit volumes were consistently very low compared to those in fixed conditions.

It is well understood that pit morphology is heavily dependent on atmospheric conditions via solution concentration[175, 176] and during this experiment the droplets exposed to fluctuating ambient conditions spent significant amounts of time at a lower relative humidity and temperature than the ones in fixed conditions (Figure 72).

This would have a number of effects. Firstly a lower temperature would mean a lower overall growth rate and a longer initiation time[63, 145] and secondly a generally lower relative humidity would mean a more concentrated solution and a thinner electrolyte layer, meaning a higher I-R drop limiting cathodic area. As pit growth rate is cathodically controlled[8, 27, 55] this would manifest as lower gross metal loss after a set time. This is likely to be in combination with a change in morphology to a spiral or satellite mode rather than hemispherical, as

seen in Figure 54, Figure 55 and Figure 56. Significant volume of the pit could be undercut and therefore unobserved by confocal microscopy.[64, 65] It's also worth noting that a larger number of small pits such as in a satellite pitting regime might correspond to a lower risk of stress corrosion cracking for similar total metal loss in a hemispherical pit[22, 177]. Additionally, preferential dissolution of delta ferrite in 304L stainless steel could account for significant 'lost' volume as almost all of this growth could be undercut along the rolling direction of the steel.[64] This makes volume assessment difficult without vertical sectioning or sequential tomographic grinding of the sample, which should be performed in future experiments. Finally, the relative humidity dropped below the efflorescence point of the electrolyte salts twice during the experiment, meaning that there was a risk that some or all of the droplets left in fluctuating ambient conditions underwent wet-dry cycling. This drop was less than a day in both cases however (Figure 72) and it has been previously observed that this is not enough time for the occluded environment within the pit to dry and repassivate.[44]

6.3.2 *Rust area measurement*

Rust area was assessed by image processing of colour photography through four techniques: Red-Blue colour channel subtraction and thresholding (Figure 59), Principal component analysis (PCA) followed by thresholding of the 2nd principal component (Figure 60), thresholding of hue and saturation in HSV colour space (Figure 61) and thresholding of b* (blue-yellow channel) in L*a*b* colour space (Figure 62). **Error! Reference source not found.** shows the variation in area measurement for each droplet in the dataset). Final thresholds for rust area

determination of the full dataset were determined by visual inspection of rust area with respect to the extent segmented area by a particular threshold and technique for a single droplet. i.e. The threshold which extracted the greatest rust area without assigning any of the surrounding steel or salt was the one used for rust area extraction for the full dataset.

Thresholds used for each technique were:

- Residual intensity of 20 for R-B colour channel subtraction,
- Score of 30 for principal component analysis
- 0.15 hue and 20 saturation for HSV
- b^* index of 20 for $L^*a^*b^*$

After segmentation with appropriate thresholds (**Error! Reference source not found.**), a general increase in rust area associated with chloride deposition density was present for all four techniques on all droplets except CaCl_2 droplets exposed under fixed conditions. The low rust area gathered for CaCl_2 droplets with pits above $1,000,000 \mu\text{m}^3$ in fixed conditions was due to all techniques requiring a colour gradient to be detected, which was minimal for these droplets due to the dominant precipitation of a white corrosion product, determined as green rust 1 in chapter 4. Figure 64 shows this in detail, the MgCl_2 droplet's red colouration manifests as a clear difference in the distribution of red and blue channels, allowing the red area to be segmented while the CaCl_2 droplets distributions are equal, preventing segmentation.

All four segmentation techniques were able to separate rusty pixels from non-rusty by colour. R-B colour channel subtraction gave consistently higher area

measurements than the mean of the 4 techniques, followed by HSV thresholding, then 2nd P.C. and finally L*a*b* produced the lowest area measurements. The average single droplet standard deviation from the mean for all area measurement techniques was 24%, meaning results were reasonably consistent.

6.3.3 *Pit volume rust area comparison*

Figure 66 - Figure 69 compare pit volume and rust area measured by each rust area segmentation technique and Figure 70 shows all techniques in a single plot for comparison. For all techniques, pit volume and rust area have a linear relationship for droplets exposed to fixed conditions, excepting CaCl₂ droplets with a pit volume greater than 1,000,000 μm^3 . Above this volume threshold, segmented rust area is much lower than would be expected from similar pits under MgCl₂ droplets.

Red-Blue colour channel subtraction (Figure 66) shows a generally higher area of rust gathered, but a larger spread in the rust areas, while the principal component analysis based technique (Figure 67) has a more consistent relationship between pit volume and rust area as do the comparisons with HSV (Figure 68) and L*a*b (Figure 69) techniques. It should be noted that the principal component analysis based technique is unsupervised for the non-thresholded portion of the process, meaning that the 2nd principal component used for area allocation will show different pixels depending on the properties of the data. i.e. if no rust is present in the image (red-blue variance axis), the second principal component will show the next highest axis of variance in the image. The other 3 techniques are all supervised for the whole process,

meaning that they require user input to set the thresholds which segment the rust area. Under different lighting conditions or if a different camera is used, these thresholds would need to be reassessed. As the 1976 CIELAB colour space used for the L^*a^*b area measurement was designed to be device independent, this need would be minimized for that technique.

Droplets exposed in fluctuating conditions have a similar spread of rust areas to those in fixed, but due to their lower pit volumes, no correlation is present between pit volume and rust area. Figure 71 shows the pit volume data against averaged rust area data with error bars. The average standard deviation for the rust area by the four techniques in Figure 54-Figure 57 was 24%, while the average standard deviation of pit volume of a representative sample of pits was 17.4%. These are not large enough to significantly affect the confidence in the trends in the data and no rust area segmentation technique proved decisively more effective than any other.

Both pit volume and rust area were observed to increase with CDD for the majority of droplets in fixed conditions (Figure 57, **Error! Reference source not found.**), but only rust area was seen to increase for fluctuating ambient conditions. This manifested as a linear relationship between pit volume and rust area for $MgCl_2$ droplets in fixed conditions and for $CaCl_2$ droplets with pit volumes of less than $1,000,000 \mu m^3$ (Figure 70, Figure 71), while no relationship was present between pit volume and rust area for droplets exposed to fluctuating ambient conditions.

In summary, rust area gathered by image processing of photography is a good indicator of corrosion site presence, but preliminary attempts at quantification are inconclusive due to unresolved questions with undercutting potentially disrupting pit volume measurement and non-red corrosion product disrupting area measurement. Future work should endeavour to improve reliability of measurements by taking other corrosion products into account as well as total rust volume or density into account instead of solely rust area. A tomographic technique such as sequential grinding should also be utilized to measure pit volume in order to resolve the question of unmeasured volume due to undercut pit morphology.

6.4 Conclusions

The relationship between rust deposition area and pit volume on 304L stainless steel after two weeks of exposure was assessed for fixed 46% relative humidity and 30°C and ambient conditions which fluctuated between 20% - 46% RH and 19-23°C. Four colour-threshold based segmentation techniques were compared for assessing rust area via colour photography and pit volume was measured using confocal laser scanning microscopy.

1. Visible rust area increased with chloride deposition density for all segmentation techniques, but no rust area segmentation technique proved decisively more effective than any other.
2. In fixed conditions a linear relationship between pit volume and rust areas was present for MgCl_2 droplets and for all CaCl_2 droplets with pits of volume less than $1,000,000 \mu\text{m}^3$.

3. No relationship was observed between rust area and pit volume in fluctuating conditions due to low observed pit volumes for a given rust area.
4. CaCl_2 droplets with pit volumes of greater than $1,000,000 \mu\text{m}^3$ generated a band of green rust 1 which confounded rust area assessment by colour analysis.

7. GENERAL DISCUSSION

Hyperspectral imaging and image processing of colour photography were investigated with the aim of assessing their applicability to long term monitoring of intermediate level waste containers. Corrosion product species that could be expected to be present in waste stores were first identified using Raman spectroscopic mapping for relevant salts and conditions. RGB colour and hyperspectral images were then acquired and compared to Raman spectroscopic mapping of a mature corrosion site in order to assess the viability of different imaging techniques. Finally rust area was compared to pit volume in order to investigate the relationship between visible surface rust and extent of metal attack.

The corrosion products of 304L stainless steel were found to consist of the iron oxide-hydroxide akaganeite (β -FeOOH), lepidocrocite (γ -FeOOH) and layered double hydroxide (green rust) also present on some droplets. Akaganeite was the majority phase present on most droplets, with a notable exception being MgCl_2 exposed to fluctuating ambient conditions which mainly consisted of lepidocrocite. The 'mature' droplet utilised in chapter 5 had a mix of akaganeite, lepidocrocite and green rust which made it viable for broad comparison between HS imaging and colour photography.

When UV-VIS-NIR hyperspectral imaging was performed on a mature droplet with a corrosion site containing all common corrosion products it was found that specific phase identification was not possible with HS imaging i.e. only the general presence of iron oxide-hydroxide could be distinguished from the background steel. This was because the iron oxide-hydroxide spectra gathered

from droplet experiments have no significant features besides the broad band at 700-900 nm and as such the high spectral resolution (~ 1 nm) afforded by the hyperspectral imaging apparatus is not utilised.

As a result, corrosion product detection can be performed by comparing just two wavelength points – the maximum at 700-900 nm and the minimum at 500 nm. High resolution colour photography was able to provide good rust area assessment, with the red (~ 650 nm) and blue (~ 450 nm) colour channels of a standard RGB colour camera providing an ‘off-the-shelf’ solution as sensors, optics and software techniques designed for use with colour photography are well understood and widely available. This did come at the cost of lower contrast for corrosion detection, however, as the reflectivity of iron oxide-hydroxide is lower at 650 nm (red) than 850 nm (near infra-red) as explored in chapter 5.

Colour photography was used to assess rust area by way of this intensity differential in chapter 6 and while there was no clear correlation drawn between rust area and pit volume, rust was detected by using colour photography in every droplet that pitted. It is worth noting that for CaCl_2 droplets exposed to fixed 46% RH for two weeks (Figure 34, Figure 64), the thick band of LDH-green rust that was associated with large pits did not prevent detection of the corrosion site entirely in any case.

A system might therefore be implemented whereby high resolution colour photography provides fast, broad scale assessment of container surfaces to highlight regions of interest for closer inspection and chemical analysis using

Raman spectroscopy, which would be able to better determine the chemical composition of a particular region of interest.

7.1 Limitations

It should be noted that the investigations undertaken during the course of this project had a number of potential limitations. Firstly, most droplets were exposed for less than a month and therefore their corrosion products may not be representative of those found in stores which could have been present for years or even decades. However, comparing the distribution of corrosion products of 30 μgcm^{-2} droplets present in Figure 37 (24 days exposure, fixed 46% RH and 30°C) and Figure 39 (14 days at fixed 46% RH and 30°C followed by 42 months in fluctuating ambient conditions) suggests that the distribution and species of corrosion product does not significantly change with additional exposure time, only that species become better crystallised due to the lack spectra with poor signal to noise and a single identifying peak at 710 cm^{-1} . This is further supported by Cornell and Schwertmann that suggest that significant heating or pH change is required to undergo phase transformation[73]

Secondly, all experiments were performed on 304L stainless steel, when containers will be made out of both 304L and 316L.[178] This is unlikely to significantly affect the results as other alloying elements such as nickel and chromium were not incorporated into corrosion products and so it's not expected that molybdenum would change the distribution or composition of corrosion products. Boucherit *et al*/ discuss incorporation of molybdates into goethite macrostructure, however [159] and so it is not out of the realm of possibility that similar incorporation occurs with other iron oxide-hydroxides.

8. GENERAL CONCLUSIONS

Corrosion products of 304L stainless steel exposed to ILW stores relevant atmospheric corrosion conditions were characterised using Raman spectroscopic mapping. A hyperspectral imager was then assembled, characterised and used to image a mature corrosion site in the 450-850 nm wavelength interval, with iron oxide-hydroxide phase information being verified by Raman spectroscopic mapping. Finally surface rust area assessed by colour photography was compared to metal loss from pitting by volume gathered by laser scanning confocal microscopy.

1. The major visible corrosion products were the iron oxide-hydroxides akaganeite and lepidocrocite with a major secondary presence of layered double hydroxide (green rust).
2. Colour based image segmentation was effective at detecting the presence of pitting corrosion by the ring of iron oxide-hydroxide deposited around the pit mouth
3. Iron oxide-hydroxide phase assignment on corrosion product from droplet experiments was not possible using UV-VIS-NIR hyperspectral imaging with a spectral range of 450 – 850 nm due to a lack of identifying features in spectra acquired from precipitated rust.
4. Image segmentation of corrosion product species was more effective when utilising the near infra-red (850 nm) rather than the red (650 nm), producing up to 65% greater contrast with the blue (450 nm) due to iron oxide-hydroxides' reflectance being larger in this band.

5. The additional spectral resolution afforded by hyperspectral imaging is not utilised due to the feature-poor UV-VIS-NIR spectrum of corrosion products that precipitate in droplets and while there was the benefit of additional image contrast from using hyperspectral imaging, the additional complexity and acquisition time is significant. Colour photography could instead be implemented as an off-the-shelf solution, but would sacrifice the improved contrast of the NIR spectral region.
6. Visible surface rust was useful for indicating the presence of a corrosion site, however no general correlation could be drawn between visible surface rust and sub-surface attack in all circumstances. A relationship was present for droplets exposed in fixed conditions, but there was no correlation observed for those exposed to fluctuating ambient conditions.

9. FUTURE WORK

Tomographic techniques for improved pit volume measurement

A major confounding element in chapter 6 was the possibility of undercutting pit morphology preventing accurate pit volume assessment, more accurate methods of assessing pit volume such as vertical sectioning could be used in the future.

The effects of relative humidity and temperature

The range of atmospheric conditions tested for was limited; a single RH and temperature point for fixed conditions and poorly controlled fluctuating conditions via ambient exposure. As it was found that corrosion product morphology was significantly affected by atmospheric conditions, a larger range of fixed conditions should be investigated, as well as a better controlled study into what effects varying the atmospheric conditions have on the formation of corrosion product.

The effects of salt accumulation over time

All droplet experiments were the result of a single deposition of salt, whereas atmospheric corrosion in the real world involves the accumulation of salt over time. This could have a significant effect on droplet formation and therefore on final corrosion product distribution. Further investigation is needed into the effects of droplet size and salt accumulation over time

Effects of other salt anions, cations as well as real-world compounds

All experiments were carried out using single salt depositions. Real world conditions not only involve the simultaneous deposition of multiple different

chloride salts, but also multiple anions such as carbonates, nitrates and sulphates. Combinatorial studies of these as well as standard mixes such as concrete dust and ocean water would be useful for understanding the potential effects of deposition mixtures on corrosion product formation.

Investigate corrosion product spectra in the SWIR region

No work was undertaken in the short wave infrared (SWIR) spectral region from 1000 nm to 2500nm. This is a region is made use of in industry and science and while it is not as strongly diagnostic as the 400-1000 nm it has been reported to be useful for assessment of hydration level of iron oxide-hydroxide[126]

Photography and hyperspectral imaging

A more detailed assessment comparing hyperspectral imaging to colour photography is necessary as no investigation of false positive/negative detection rate was performed and no possible confounding variables were introduced such as non-corrosion related substances which might trigger detection, such as paints, tape or dust.

10. REFERENCES

1. Frost R. The Road Not Taken. 1916.
2. Nuclear Decommissioning Authority, Geological Disposal: An overview of the generic Disposal System Safety Case. Radioactive Waste Management Limited. 2010.
3. Ramanaidou E, Wells M. Hyperspectral Imaging of Iron Ores. In: Broekmans MATM, editor. Proceedings of the 10th International Congress for Applied Mineralogy (ICAM): Springer Berlin Heidelberg; 2012. p. 575-80.
4. Sabins FF. Remote sensing for mineral exploration. *Ore Geol Rev.* 1999;14(3-4):157-83.
5. van der Meer FD, van der Werff HMA, van Ruitenbeek FJA, Hecker CA, Bakker WH, Noomen MF, et al. Multi- and hyperspectral geologic remote sensing: A review. *Int J Appl Earth Obs Geoinf.* 2012;14(1):112-28.
6. 2013 UK Radioactive Waste Inventory: Waste Quantities from all sources.
7. T.W. Hicks TDBaJMS, Galson Sciences Ltd, D.G. Bennett TL. Likelihood of Criticality: The Likelihood of Criticality Following Disposal of LLW/ILW/DNLEU. 2014.
8. Frankel GS. Pitting corrosion of metals. A review of the critical factors. *Journal of the Electrochemical Society.* 1998;145(8):2970-.
9. Harris C. Current Environmental Conditions Within Interim Stores and GDF Analogues. AMEC. 2012.
10. Authority ND. UK Radioactive Higher Activity Waste Storage Review, March 2009. 2009.
11. Harris C. A Survey of Current Environmental Conditions Within ILW Interim Stores and Potential GDF analogues. AMEC. 2015.
12. Drew N. Analysis of Chloride Deposition rates relevant to ILW stores. 2005.
13. P.A.H. Fennel NRS, M. Izzo, N.A. Turner. Characterisation of Environmental Conditions in an ILW Store. AMEC, 2012.
14. Fennell PAH. Characterisation of Environmental Conditions in an ILW store. AMEC. 2012.
15. R.J. Winsley NRS, B. Reddy, A.P. Rance, P.A.H. Fennell,. 4 metre Box Monitoring Programme - Final Report for the Period 2007-2010. Serco. 2011.
16. Padovani C, R.J. Winsley, N.R. Smart, P.A.H. Fennell, C Harris and K. Christie. Corrosion Control of Stainless Steels in Indoor Atmospheres - Practical Experience (Part 2). Corrosion. 2015.
17. Steel A. Product data sheet 304/304L Stainless steel. 2007.
18. Steel A. Product data sheet 316/316L stainless steel. 2007.
19. Bhadeshia. Steels - Microstructure and Properties. 3rd Ed. Oxford: Butterworth-Heinemann. 2006.
20. Olsson COA, Landolt D. Passive films on stainless steels—chemistry, structure and growth. *Electrochim Acta.* 2003;48(9):1093-104.
21. Marcus P, Moscatelli M. THE ROLE OF ALLOYED MOLYBDENUM IN THE DISSOLUTION AND THE PASSIVATION OF NICKEL-MOLYBDENUM ALLOYS IN THE PRESENCE OF ADSORBED SULFUR. *Journal of the Electrochemical Society.* 1989;136(6):1634-7.
22. Street SR, Mi N, Cook AJMC, Mohammed-Ali HB, Guo L, Rayment T, et al. Atmospheric pitting corrosion of 304L stainless steel: the role of highly concentrated chloride solutions. *Faraday discussions.* 2015;180:251-65.
23. Pourbaix MJN. Thermodynamique des solutions aqueuses diluées: Représentation graphique du rôle du pH et du potentiel [PhD Thesis]. Delft: Delft Technical University. 1945.

24. Barry MaM, G. . Growth and Stability of Passive Films in Corrosion Mechanisms in Theory and Practice. CRC Press. 2002:189-216.
25. Asami K, Hashimoto K, Shimodaira S. XPS STUDY OF PASSIVITY OF A SERIES OF IRON-CHROMIUM ALLOYS IN SULFURIC-ACID. Corrosion Science. 1978;18(2):151-60.
26. Galvele JR. TRANSPORT PROCESSES AND MECHANISM OF PITTING OF METALS. Journal of the Electrochemical Society. 1976;123(4):464-74.
27. Newman RC. 2001 W.R. Whitney Award Lecture: Understanding the corrosion of stainless steel. Corrosion. 2002;58(3):292-.
28. Macdonald DD. THE POINT-DEFECT MODEL FOR THE PASSIVE STATE. Journal of the Electrochemical Society. 1992;139(12):3434-49.
29. Wranglen G. Pitting and sulphide inclusions in steel. Corrosion Science. 1974;14(5):331-49.
30. Jun J, Holguin K, Frankel GS. Pitting Corrosion of Very Clean Type 304 Stainless Steel. Corrosion. 2014;70(2):146-55.
31. Eklund GS. INITIATION OF PITTING AT SULFIDE INCLUSIONS IN STAINLESS-STEEL. Journal of the Electrochemical Society. 1974;121(4):467-73.
32. Baker MA, Castle JE. THE INITIATION OF PITTING CORROSION AT MNS INCLUSIONS. Corrosion Science. 1993;34(4):667-82.
33. Ke R, Alkire R. SURFACE-ANALYSIS OF CORROSION PITS INITIATED AT MNS INCLUSIONS IN 304 STAINLESS-STEEL. Journal of the Electrochemical Society. 1992;139(6):1573-80.
34. Ke RR, Alkire R. Initiation of corrosion pits at inclusions on 304 stainless steel. Journal of the Electrochemical Society. 1995;142(12):4056-62.
35. Wijesinghe T, Blackwood DJ. Real time pit initiation studies on stainless steels: The effect of sulphide inclusions. Corrosion Science. 2007;49(4):1755-64.
36. Galvele J. Transport processes in passivity breakdown—II. Full hydrolysis of the metal ions. Corrosion Science. 1981;21(8):551-79.
37. Williams DE, Kilburn MR, Cliff J, Waterhouse GIN. Composition changes around sulphide inclusions in stainless steels, and implications for the initiation of pitting corrosion. Corrosion Science. 2010;52(11):3702-16.
38. Isaacs HS. The localized breakdown and repair of passive surfaces during pitting. Corrosion Science. 1989;29(2):313-23.
39. Fontana M. Corrosion Engineering. New York: McGraw-Hill Book Company. 1986.
40. Isaacs HS. BEHAVIOR OF RESISTIVE LAYERS IN LOCALIZED CORROSION OF STAINLESS-STEEL. Journal of the Electrochemical Society. 1973;120(11):1456-62.
41. Beck TR, Alkire RC. OCCURRENCE OF SALT FILMS DURING INITIATION AND GROWTH OF CORROSION PITS. Journal of the Electrochemical Society. 1979;126(10):1662-6.
42. Alkire RC, Wong KP. THE CORROSION OF SINGLE PITS ON STAINLESS-STEEL IN ACIDIC CHLORIDE SOLUTION. Corrosion Science. 1988;28(4):411-&.
43. Laycock NJ, Newman RC. Localised dissolution kinetics, salt films and pitting potentials. Corrosion Science. 1997;39(10-11):1771-90.
44. Guo L. Atmospheric Localised corrosion of type 304 austenitic stainless steels [PHD thesis] University of Birmingham. 2016.
45. Tsutsumi Y, Nishikata A, Tsuru T. Pitting corrosion mechanism of Type 304 stainless steel under a droplet of chloride solutions. Corrosion Science. 2007;49(3):1394-407.
46. Evans UR. The Ferroxyl Indicator in Corrosion Research With special

Reference to the Controversy Regarding the Cause of Pitting. The Metal Industry. 1926;11.

47. Mi N, Ghahari M, Rayment T, Davenport AJ. Use of inkjet printing to deposit magnesium chloride salt patterns for investigation of atmospheric corrosion of 304 stainless steel. *Corrosion Science*. 2011;53(10):3114-21.
48. Wang YH, Wang W, Liu YY, Zhong L, Wang J. Study of localized corrosion of 304 stainless steel under chloride solution droplets using the wire beam electrode. *Corrosion Science*. 2011;53(9):2963-8.
49. Chen ZY, Kelly RG. Computational Modeling of Bounding Conditions for Pit Size on Stainless Steel in Atmospheric Environments. *Journal of the Electrochemical Society*. 2010;157(2):C69-C78.
50. Prosek T, Iversen A, Taxen C, Thierry D. Low-Temperature Stress Corrosion Cracking of Stainless Steels in the Atmosphere in the Presence of Chloride Deposits. *Corrosion*. 2009;65(2):105-17.
51. Tsutsumi Y, Nishikata A, Tsuru T. Initial stage of pitting corrosion of type 304 stainless steel under thin electrolyte layers containing chloride ions. *Journal of the Electrochemical Society*. 2005;152(9):B358-B63.
52. Hastuty S, Nishikata A, Tsuru T. Pitting corrosion of Type 430 stainless steel under chloride solution droplet. *Corrosion Science*. 2010;52(6):2035-43.
53. Chen A, Cao F, Liao X, Liu W, Zheng L, Zhang J, et al. Study of pitting corrosion on mild steel during wet-dry cycles by electrochemical noise analysis based on chaos theory. *Corrosion Science*. 2013;66:183-95.
54. Yadav AP, Nishikata A, Tsuru T. Electrochemical impedance study on galvanized steel corrosion under cyclic wet-dry conditions—influence of time of wetness. *Corrosion Science*. 2004;46(1):169-81.
55. Cruz RPV, Nishikata A, Tsuru T. Pitting corrosion mechanism of stainless steels under wet-dry exposure in chloride-containing environments. *Corrosion Science*. 1998;40(1):125-39.
56. Cruz RPV, Nishikata A, Tsuru T. AC impedance monitoring of pitting corrosion of stainless steel under a wet-dry cyclic condition in chloride-containing environment. *Corrosion Science*. 1996;38(8):1397-406.
57. Tran Van N, Tada E, Nishikata A. Pit Initiation and Repassivation of Stainless Steels Exposed to Cyclic Relative Humidity Changes. *Journal of the Electrochemical Society*. 2015;162(9):C419-C25.
58. Shi YY, Zhang Z, Su JX, Zhang JQ. EIS study on 2024-T3 aluminum alloy corrosion in simulated acid rain under cyclic wet-dry conditions. *Mater Corros*. 2005;56(10):701-6.
59. El-Mahdy G, Kim KB. AC impedance study on the atmospheric corrosion of aluminum under periodic wet-dry conditions. *Electrochim Acta*. 2004;49(12):1937-48.
60. Li CL, Ma YT, Li Y, Wang FH. EIS monitoring study of atmospheric corrosion under variable relative humidity. *Corrosion Science*. 2010;52(11):3677-86.
61. Schwenk W. THEORY OF STAINLESS STEEL PITTING. *Corrosion*. 1964;20(4):T129-8.
62. Maier B, Frankel GS. Pitting Corrosion of Bare Stainless Steel 304 under Chloride Solution Droplets. *Journal of the Electrochemical Society*. 2010;157(10):C302-C12.
63. Street SR. Atmospheric corrosion of austenitic stainless steels[PhD Thesis]. University of Birmingham. 2016.
64. Ali HBM. Atmospheric Pitting Corrosion of Stainless Steel [PhD Thesis]. University of Birmingham. 2016.
65. Davenport AJ, Guo L, Mi N, Mohammed-Ali H, Ghahari M, Street SR, et al. Mechanistic studies of atmospheric pitting corrosion of stainless steel for ILW containers. *Corros Eng Sci Technol*. 2014;49(6):514-20.

66. Albores-Silva OE. Atmospheric stress corrosion cracking and pitting of austenitic stainless steel: Newcastle University; 2011.
67. Albores-Silva OE, Charles EA, Padovani C. Effect of chloride deposition on stress corrosion cracking of 316L stainless steel used for intermediate level radioactive waste containers. *Corros Eng Sci Technol*. 2011;46(2):124-8.
68. Nurnberger U. STRESS-CORROSION CRACKING OF STAINLESS-STEEL STRUCTURAL COMPONENTS IN INDOOR SWIMMING POOLS. *Stahl Und Eisen*. 1990;110(6):141-8.
69. Faller M, Richner P. Material selection of safety-relevant components in indoor swimming pools. *Mater Corros*. 2003;54(5):331-8.
70. Gnanamoorthy JB. Stress corrosion cracking of unsensitized stainless steels in ambient-temperature coastal atmosphere 1990. 63-5 p.
71. Christie K. The Examination and Reporting of Atmospheric Stress Corrosion Cracking Tests. NNC report C6125/TR/006. 2002(3).
72. Smart NRS. Literature Review of Atmospheric Stress Corrosion Cracking of Stainless Steels Report to NIREX. 2007.
73. R. M. Cornell US. The Iron Oxides: Structure, Properties, Reactions, Occurrences and uses.
74. Misawa T, Hashimoto K, Shimodaira S. MECHANISM OF FORMATION OF IRON-OXIDE AND OXYHYDROXIDES IN AQUEOUS-SOLUTIONS AT ROOM-TEMPERATURE. *Corrosion Science*. 1974;14(2):131-49.
75. Scheck J, Lemke T, Gebauer D. The Role of Chloride Ions during the Formation of Akaganeite Revisited. *Minerals*. 2015;5(4):778-87.
76. Shebanova ON, Lazor P. Raman study of magnetite (Fe₃O₄): laser-induced thermal effects and oxidation. *J Raman Spectrosc*. 2003;34(11):845-52.
77. Hanesch M. Raman spectroscopy of iron oxides and (oxy)hydroxides at low laser power and possible applications in environmental magnetic studies. *Geophys J Int*. 2009;177(3):941-8.
78. Mazzetti L, Thistlethwaite PJ. Raman spectra and thermal transformations of ferrihydrite and schwertmannite. *J Raman Spectrosc*. 2002;33(2):104-11.
79. deFaria DLA, Silva SV, deOliveira MT. Raman microspectroscopy of some iron oxides and oxyhydroxides. *J Raman Spectrosc*. 1997;28(11):873-8.
80. Froment F, Tournie A, Colomban P. Raman identification of natural red to yellow pigments: ochre and iron-containing ores. *J Raman Spectrosc*. 2008;39(5):560-8.
81. Bellot-Gurlet L, Neff D, Reguer S, Monnier J, Saheb M, Dillmann P. Raman Studies of Corrosion Layers Formed on Archaeological Irons in Various Media. *J Nano Res*. 2009;8:147-56.
82. Monnier J, Bellot-Gurlet L, Baron D, Neff D, Guillot I, Dillmann P. A methodology for Raman structural quantification imaging and its application to iron indoor atmospheric corrosion products. *J Raman Spectrosc*. 2011;42(4):773-81.
83. Neff D, Bellot-Gurlet L, Dillmann P, Reguer S, Legrand L. Raman imaging of ancient rust scales on archaeological iron artefacts for long-term atmospheric corrosion mechanisms study. *J Raman Spectrosc*. 2006;37(10):1228-37.
84. Reguer S, Neff D, Bellot-Gurlet L, Dillmann P. Deterioration of iron archaeological artefacts: micro-Raman investigation on Cl-containing corrosion products. *J Raman Spectrosc*. 2007;38(4):389-97.
85. Haest M, Cudahy T, Laukamp C, Gregory S. Quantitative Mineralogy from Infrared Spectroscopic Data. II. Three-Dimensional Mineralogical Characterization of the Rocklea Channel Iron Deposit, Western Australia. *Econ Geol*. 2012;107(2):229-49.
86. Morris RV, Golden DC, Bell JF, Shaffer TD, Scheinost AC, Hinman NW, et al. Mineralogy, composition, and alteration of Mars Pathfinder rocks and soils: Evidence

- from multispectral, elemental, and magnetic data on terrestrial analogue, SNC meteorite, and Pathfinder samples. *J Geophys Res-Planets*. 2000;105(E1):1757-817.
87. Morris RV, Lauer HV, Lawson CA, Gibson EK, Nace GA, Stewart C. SPECTRAL AND OTHER PHYSICOCHEMICAL PROPERTIES OF SUBMICRON POWDERS OF HEMATITE (ALPHA- Fe_2O_3), MAGHEMITE (GAMMA- Fe_2O_3), MAGNETITE (Fe_3O_4), GOETHITE (ALPHA- FeOOH), AND LEPIDOCROCITE (GAMMA- FeOOH). *Journal of Geophysical Research-Solid Earth and Planets*. 1985;90(NB4):3126-44.
 88. Sherman DM, Waite TD. ELECTRONIC-SPECTRA OF Fe^{3+} OXIDES AND OXIDE HYDROXIDES IN THE NEAR IR TO NEAR UV. *Am Miner*. 1985;70(11-12):1262-9.
 89. Rancourt DG, Fortin D, Pichler T, Thibault PJ, Lamarche G, Morris RV, et al. Mineralogy of a natural As-rich hydrous ferric oxide coprecipitate formed by mixing of hydrothermal fluid and seawater: Implications regarding surface complexation and color banding in ferrihydrite deposits. *Am Miner*. 2001;86(7-8):834-51.
 90. Li SX, George RD, Hihara LH. Corrosion analysis and characteristics of discarded military munitions in ocean waters. *Corrosion Science*. 2016;102:36-43.
 91. Rout K, Mohapatra M, Anand S. 2-Line ferrihydrite: synthesis, characterization and its adsorption behaviour for removal of $\text{Pb}(\text{II})$, $\text{Cd}(\text{II})$, $\text{Cu}(\text{II})$ and $\text{Zn}(\text{II})$ from aqueous solutions. *Dalton Trans*. 2012;41(11):3302-12.
 92. Dunnwald J, Otto A. AN INVESTIGATION OF PHASE-TRANSITIONS IN RUST LAYERS USING RAMAN-SPECTROSCOPY. *Corrosion Science*. 1989;29(9):1167-76.
 93. Antony H, Legrand L, Marechal L, Perrin S, Dillmann P, Chausse A. Study of lepidocrocite gamma- FeOOH electrochemical reduction in neutral and slightly alkaline solutions at 25 degrees C. *Electrochim Acta*. 2005;51(4):745-53.
 94. Antony H, Perrin S, Dillmann P, Legrand L, Chausse A. Electrochemical study of indoor atmospheric corrosion layers formed on ancient iron artefacts. *Electrochim Acta*. 2007;52(27):7754-9.
 95. Dubois F, Mendibide C, Pagnier T, Perrard F, Duret C. Raman mapping of corrosion products formed onto spring steels during salt spray experiments. A correlation between the scale composition and the corrosion resistance. *Corrosion Science*. 2008;50(12):3401-9.
 96. Legrand L, Sagon G, Lecomte S, Chausse A, Messina R. A Raman and infrared study of a new carbonate green rust obtained by electrochemical way. *Corrosion Science*. 2001;43(9):1739-49.
 97. Genin JMR, Refait P, Bourrie G, Abdelmoula M, Trolard F. Structure and stability of the $\text{Fe}(\text{II})$ - $\text{Fe}(\text{III})$ green rust "fougerite" mineral and its potential for reducing pollutants in soil solutions. *Applied Geochemistry*. 2001;16(5):559-70.
 98. Trolard F, Genin JMR, Abdelmoula M, Bourrie G, Humbert B, Herbillon A. Identification of a green rust mineral in a reductomorphic soil by Mossbauer and Raman spectroscopies. *Geochimica Et Cosmochimica Acta*. 1997;61(5):1107-11.
 99. Luo H, Li XG, Dong CF, Xiao K. Degradation of austenite stainless steel by atmospheric exposure in tropical marine environment. *Corros Eng Sci Technol*. 2013;48(3):221-9.
 100. Dong CF, Luo H, Xiao K, Ding Y, Li PH, Li XG. Electrochemical Behavior of 304 Stainless Steel in Marine Atmosphere and Its Simulated Solution. *Anal Lett*. 2013;46(1):142-55.
 101. Dhaiveegan P, Elangovan N, Nishimura T, Rajendran N. Corrosion behavior of 316L and 304 stainless steels exposed to industrial-marine-urban environment: field study. *RSC Adv*. 2016;6(53):47314-24.
 102. Tanaka S, Soc I, Control E. Non-destructive inspection of concrete structures using an electromagnetic wave radar. Tokyo: Soc Instrument Control Engineers Japan; 2004. 1493-7 p.

103. BDM Federal I. Corrosion Detection Technologies: A sector study. North American Technology and Industrial Base Organisation.
104. Agarwala VS, Reed PL, Ahmad S. Corrosion Detection and Monitoring - A Review. 2000/1/1/. NACE: NACE International.
105. N. Fuse TF. Evaluation of Applicability of Noncontact Analysis Methods to Detect Rust Regions in Coated Steel Plates. Transactions on terahertz science and technolu. 2012;2(2):242-9.
106. Rodriguez C, Biezma MV. Pitting corrosion detection in stainless steels using ultrasounds. Rev Metal. 2014;50(1):11.
107. V. Sharma TT. Techniques for detection of rusting od metals using image processing: a survey. Internation journal of emerging science and engineering. 2013;1(4).
108. Acosta MRG, Diaz JCV, Castro NS. An innovative image-processing model for rust detection using Perlin Noise to simulate oxide textures. Corrosion Science. 2014;88:141-51.
109. Ahuja SK, Shukla MK, Ravulakollu KK. Surface Corrosion Detection and Classification for Steel Alloy using Image Processing and Machine Learning. Helix. 2018;8(5):3822-7.
110. Medeiros FNS, Ramalho GLB, Bento MP, Medeiros LCL. On the Evaluation of Texture and Color Features for Nondestructive Corrosion Detection. Eurasip Journal on Advances in Signal Processing. 2010.
111. Eisberg RaR, R. Quantum Physics of Atoms, Molecules, Solids, Nuclei and Particles (Second Edition).
112. Wu. LVWaH-i. Biomedical optics: principles and imaging. John Wiley & Sons. 2012.
113. Blaschke T. Object based image analysis for remote sensing. ISPRS-J Photogramm Remote Sens. 2010;65(1):2-16.
114. Weng QH. Remote sensing of impervious surfaces in the urban areas: Requirements, methods, and trends. Remote Sens Environ. 2012;117:34-49.
115. Mulder VL, de Bruin S, Schaepman ME, Mayr TR. The use of remote sensing in soil and terrain mapping - A review. Geoderma. 2011;162(1-2):1-19.
116. Pal M, Mather PM. An assessment of the effectiveness of decision tree methods for land cover classification. Remote Sens Environ. 2003;86(4):554-65.
117. Mielke C, Boesche NK, Rogass C, Kaufmann H, Gauert C, de Wit M. Spaceborne Mine Waste Mineralogy Monitoring in South Africa, Applications for Modern Push-Broom Missions: Hyperion/OLI and EnMAP/Sentinel-2. Remote Sens. 2014;6(8):6790-816.
118. Bibring JP, Langevin Y, Gendrin A, Gondet B, Poulet F, Berthe M, et al. Mars surface diversity as revealed by the OMEGA/Mars Express observations. Science. 2005;307(5715):1576-81.
119. Goudge TA, Mustard JF, Head JW, Salvatore MR, Wiseman SM. Integrating CRISM and TES hyperspectral data to characterize a halloysite-bearing deposit in Kashira crater, Mars. Icarus. 2015;250:165-87.
120. Khelifi R, Adel M, Bourennane S. Segmentation of multispectral images based on band selection by including texture and mutual information. Biomed Signal Process Control. 2015;20:16-23.
121. Zabalza J, Ren JC, Zheng JB, Han JW, Zhao HM, Li ST, et al. Novel Two-Dimensional Singular Spectrum Analysis for Effective Feature Extraction and Data Classification in Hyperspectral Imaging. IEEE Trans Geosci Remote Sensing. 2015;53(8):4418-33.
122. Nansen C, Zhao GP, Dakin N, Zhao CH, Turner SR. Using hyperspectral imaging to determine germination of native Australian plant seeds. J Photochem Photobiol B-Biol. 2015;145:19-24.

123. Kamruzzaman M, ElMasry G, Sun DW, Allen P. Prediction of some quality attributes of lamb meat using near-infrared hyperspectral imaging and multivariate analysis. *Anal Chim Acta*. 2012;714:57-67.
124. Provoost J. Hyperspectral Imager Opens Options for Consumer, Medical and Industrial Uses. *Photon Spectr*. 2015;49(4):46-50.
125. Bibring JP, Langevin Y, Mustard JF, Poulet F, Arvidson R, Gendrin A, et al. Global mineralogical and aqueous mars history derived from OMEGA/Mars express data. *Science*. 2006;312(5772):400-4.
126. Combe JP, Le Mouelic S, Sotin C, Gendrin A, Mustard JF, Le Deit L, et al. Analysis of OMEGA/Mars express data hyperspectral data using a Multiple-Endmember Linear Spectral Unmixing Model (MELSUM): Methodology and first results. *Planet Space Sci*. 2008;56(7):951-75.
127. Ducart DF, Silva AM, Bemfica Toledo CL, de Assis LM. Mapping iron oxides with Landsat-8/OLI and EO-1/Hyperion imagery from the Serra Norte iron deposits in the Carajas Mineral Province, Brazil. *Brazilian Journal of Geology*. 2016;46(3):331-49.
128. SharkD. By HSV_color_solid_cylinder.png: SharkDderivative work: SharkD Talk - HSV_color_solid_cylinder.png, CC BY-SA 3.0, <https://commons.wikimedia.org/w/index.php?curid=9801673>.
129. Jeffrey K. <https://opentextbc.ca/graphicdesign/wp-content/uploads/sites/42/2015/04/Lab-colour-space.png>, <https://opentextbc.ca/graphicdesign/lab-colour-space/>. License: Creative Commons 4.0 <https://creativecommons.org/licenses/by/4.0/>.
130. Consortium IC. Specification ICC.1:2004-10 (Profile version 4.2.0.0) [REVISION of ICC.1:2003-09]. Image technology colour management — Architecture, profile format, and data structure. 2004.
131. Joblove GH, Greenberg D. Color spaces for computer graphics. *SIGGRAPH Comput Graph*. 1978;12(3):20-5.
132. E. Rehkugler G, A. Throop J. Apple Sorting with Machine Vision. *Transactions of the ASAE*. 29(5):1388-97.
133. Cubero S, Aleixos N, Molto E, Gomez-Sanchis J, Blasco J. Advances in Machine Vision Applications for Automatic Inspection and Quality Evaluation of Fruits and Vegetables. *Food and Bioprocess Technology*. 2011;4(4):487-504.
134. Zhuang JJ, Luo SM, Hou CJ, Tang Y, He Y, Xue XY. Detection of orchard citrus fruits using a monocular machine vision-based method for automatic fruit picking applications. *Computers and Electronics in Agriculture*. 2018;152:64-73.
135. Itzhak D, Dinstein I, Zilberberg T. PITTING CORROSION EVALUATION BY COMPUTER IMAGE-PROCESSING. *Corrosion Science*. 1981;21(1):17-22.
136. Choi KY, Kim SS. Morphological analysis and classification of types of surface corrosion damage by digital image processing. *Corrosion Science*. 2005;47(1):1-15.
137. Valeti B, Pakzad S. Automated Detection of Corrosion Damage in Power Transmission Lattice Towers Using Image Processing. Soules JG, editor 2017. 474-82 p.
138. Feliciano FF, Leta FR, Mainier FB. Texture digital analysis for corrosion monitoring. *Corrosion Science*. 2015;93:138-47.
139. Du Q, Fowler JE. Hyperspectral image compression using JPEG2000 and principal component analysis. *Ieee Geoscience and Remote Sensing Letters*. 2007;4(2):201-5.
140. Jia XP, Richards JA. Segmented principal components transformation for efficient hyperspectral remote-sensing image display and classification. *IEEE Trans Geosci Remote Sensing*. 1999;37(1):538-42.


141. Cheriyyadat A, Bruce LM, leee, leee, leee. Why principal component analysis is not an appropriate feature extraction method for hyperspectral data. New York: leee; 2003. 3420-2 p.
142. Prasad S, Bruce LM. Limitations of Principal Components Analysis for Hyperspectral Target Recognition. *leee Geoscience and Remote Sensing Letters*. 2008;5(4):625-9.
143. Hancock PJB, Baddeley RJ, Smith LS. THE PRINCIPAL COMPONENTS OF NATURAL IMAGES. *Netw-Comput Neural Syst*. 1992;3(1):61-70.
144. Wang R, Nie FP, Yang XJ, Gao FF, Yao ML. Robust 2DPCA With Non-greedy l(1)-Norm Maximization for Image Analysis. *IEEE T Cybern*. 2015;45(5):1108-12.
145. Cook AJMC. The Atmospheric Corrosion of 304L and 316L stainless steels under conditions relevant to the itnerim storage of intermediate level nuclear waste [PhD Thesis]. University of Birmingham. 2017.
146. ASTM. E104-02(2007) "Standard Practice for maintaining constant relative humidity by means of aqueous solutions". 2007.
147. USAF MIL-STD-150A. US Defense Logistics Agency. 1951.
148. Matlab R2017b and Image Processing toolbox. Mathworks, Inc. ; 2017.
149. Ferreira MGS, Silva TME, Catarino A, Pankuch M, Melendres CA. ELECTROCHEMICAL AND LASER RAMAN-SPECTROSCOPY STUDIES OF STAINLESS-STEEL IN 0.15M NACL SOLUTION. *Journal of the Electrochemical Society*. 1992;139(11):3146-51.
150. Maslar JE, Hurst WS, Bowers WJ, Hendricks JH, Windsor ES. Alloy 600 Aqueous Corrosion at Elevated Temperatures and Pressures: An In Situ Raman Spectroscopic Investigation. *Journal of the Electrochemical Society*. 2009;156(3):C103-C13.
151. Ningshen S, Mudali UK, Ramya S, Raj B. Corrosion behaviour of AISI type 304L stainless steel in nitric acid media containing oxidizing species. *Corrosion Science*. 2011;53(1):64-70.
152. Kabekkodu DS. ICDD PDF-4+ 20xx (Database), available at: <http://www.icdd.com/index.htm>.
153. Glanvill S. ATMOSPHERIC CORROSION OF AA2024 IN OCEAN WATER ENVIRONMENTS [PHD THESIS]. University of Birmingham. 2018.
154. Belo MD, Walls M, Hakiki NE, Corset J, Picquenard E, Sagon G, et al. Composition, structure and properties of the oxide films formed on the stainless steel 316L in a primary type PWR environment. *Corrosion Science*. 1998;40(2-3):447-63.
155. Oblonsky LJ, Devine TM. Corrosion of carbon steels in CO₂-saturated brine a surface enhanced Raman spectroscopic. *Journal of the Electrochemical Society*. 1997;144(4):1252-60.
156. Ramya S, Anita T, Shaikh H, Dayal RK. Laser Raman microscopic studies of passive films formed on type 316LN stainless steels during pitting in chloride solution. *Corrosion Science*. 2010;52(6):2114-21.
157. Shebanova ON, Lazor P. Raman spectroscopic study of magnetite (FeFe₂O₄): a new assignment for the vibrational spectrum. *J Solid State Chem*. 2003;174(2):424-30.
158. Thibeau RJ, Brown CW, Heidersbach RH. RAMAN-SPECTRA OF POSSIBLE CORROSION PRODUCTS OF IRON. *Appl Spectrosc*. 1978;32(6):532-5.
159. Boucherit N, Hugotlegoff A, Joiret S. INFLUENCE OF NI, MO, AND CR ON PITTING CORROSION OF STEELS STUDIED BY RAMAN-SPECTROSCOPY. *Corrosion*. 1992;48(7):569-79.
160. Socrates G. Infrared and Raman Characteristic Group Frequencies. Wiley. 2004.
161. Gu BH, Tio J, Wang W, Ku YK, Dai S. Raman spectroscopic detection for perchlorate at low concentrations. *Appl Spectrosc*. 2004;58(6):741-4.

162. Gomez RB. Hyperspectral imaging: a useful technology for transportation analysis. *Opt Eng.* 2002;41(9):2137-43.
163. Lagacherie P, Sneepe AR, Gomez C, Bacha S, Coulouma G, Hamrouni MH, et al. Combining Vis-NIR hyperspectral imagery and legacy measured soil profiles to map subsurface soil properties in a Mediterranean area (Cap-Bon, Tunisia). *Geoderma.* 2013;209:168-76.
164. Padoan S, Klein, Aalderink, de Bruin. Quantitative Hyperspectral Imaging of historical documents: technique and applications. 9th international conference on NDT of Art, Jerusalem.
165. Gomez MA, Hendry MJ, Elouatik S, Essilfie-Dughan J, Paikaray S. Fe(II)((aq)) uptake of Mg(II)-Al(III)/Fe(III)-SO₄/CO₃ HTLCs under alkaline conditions: adsorption and solid state transformation mechanisms. *RSC Adv.* 2014;4(98):54973-88.
166. Folkman M, Pearlman J, Liao L, Jarecke P. EO-1/Hyperion hyperspectral imager design, development, characterization, and calibration. In: Smith WL, Yasuoka Y, editors. *Hyperspectral Remote Sensing of the Land and Atmosphere. Proceedings of the Society of Photo-Optical Instrumentation Engineers (Spie).* 4151. Bellingham: Spie-Int Soc Optical Engineering; 2001. p. 40-51.
167. Henrich V, Krauss G, Götze C, Sandow C. The IndexDatabase Bonn2011 [updated 2011]. Available from: <https://www.indexdatabase.de/>.
168. Tsai F, Philpot W. Derivative Analysis of Hyperspectral Data. *Remote Sens Environ.* 1998;66(1):41-51.
169. Leone AP, Sommer S. Multivariate analysis of laboratory spectra for the assessment of soil development and soil degradation in the southern Apennines (Italy). *Remote Sens Environ.* 2000;72(3):346-59.
170. Yang J, Zhang D, Frangi AF, Yang JY. Two-dimensional PCA: A new approach to appearance-based face representation and recognition. *IEEE Trans Pattern Anal Mach Intell.* 2004;26(1):131-7.
171. ASTM. G46 - 94 (2013) "Standard Guide for Examination and Evaluation of Pitting Corrosion". 2013.
172. Chen G, Qian S-E. Denoising of Hyperspectral Imagery Using Principal Component Analysis and Wavelet Shrinkage. *IEEE Trans Geosci Remote Sensing.* 2011;49(3):973-80.
173. Taguchi YH, Iwadate M, Umeyama H. Principal component analysis-based unsupervised feature extraction applied to in silico drug discovery for posttraumatic stress disorder-mediated heart disease. *BMC Bioinformatics.* 2015;16:26.
174. Lide D, and Cleveland. *Handbook of Chemistry and Physics.* 1994.
175. Street SR, Cook A, Mohammed-Ali HB, Rayment T, Davenport AJ. The Effect of Deposition Conditions on Atmospheric Pitting Corrosion Location Under Evans Droplets on Type 304L Stainless Steel. *Corrosion.* 2018;74(5):520-9.
176. Szklarska-Smialowska Z. *Pitting Corrosion of Metals.* Houston, Texas: National Association of Corrosion Engineers. 1986.
177. Jones RHaR, R.E. *Stress-Corrosion Cracking Materials Performance and Evaluation.* 1992.
178. King F. *Container Materials for the Storage and Disposal of Nuclear Waste.* *Corrosion.* 2013;69(10).

11.APPENDIX

11.1 Mill certificate – 304L stainless steel

GM 106218-01-09

 Aperam - Stainless France Aperam Isbergues 62330 Isbergues FRANCE		MILL CERTIFICATE BS EN 10204/3.1 CERTIFICAT DE RECEPTION NF EN 10204/3.1 ABNAHMEPRUEFZEUGNIS DIN EN 10204/3.1		N-Nr-N 1210198868-02 V01																																																																																	
		Ausgestellt im Einvernehmen mit dem TÜV SÜD - Auf Gegenzeichnung wird verzichtet Issued in accordance with TÜV SÜD - Verification is not required Etabli en accord avec le TÜV SÜD - Dispense de contresignature A.D.2000 Merkblatt W0 - W2 - PED 97/23 EC		ISO 9001 V2008 - ISO TS 16949 V2009 - ISO 14001 V 2004																																																																																	
Manufacturer's works order number N° de la commande usine productrice Werksauftragsnummer 80091691 /01-66508/1		Surveyor's mark Cachet de l'expert Stempel des Werksachverständigen UI2		Purchaser and/or consignee Client et/ou destinataire Besteller und/oder Empfänger THE METAL CENTRE WESTERN WAY WEDNESBURY WS10 7 WEST MIDLANDS GR.BRETAGNE																																																																																	
Product - Produit - Erzeugnis COLD-ROLLED SHEET TOLE LAMINEE A FROID KALTGEWALZTES BLECH		Steelmaking process Mode d'élaboration de l'acier - Stahlherstellungsverfahren Prod.proces: Electric arc furnace - VOD/AOD - Continuous casting Proc.fabric: Four à arc - VOD/AOD - Coulée continue Fertigungsablauf: Elektro-Ofen - VOD/AOD - Stranggussanlage		Purchaser's order number N° de commande client Kundenbestellnummer 80790 June																																																																																	
Steel designation Désignation de l'acier Stahlbezeichnung EN 10028-7 / 08 - 1.4307 - 1.4301 ASTM A 240 / 10 - TYPE 304L - TYPE 304 ASME SA 240 / 10 - TYPE 304L - TYPE 304 EN 10088-2 / 05 - 1.4307 - 1.4301		Finish Présentation Auslieferung 2B 2B 2B		Product delivery condition Etat de livraison du produit - Lieferzustand Solution treated Hypertrempe : 1040-1100 C Loesungsgeglühtescheckert Forced Air Air forcé - Gebläse Luft																																																																																	
ATTESTATION PED 97/23/EC PAR TÜV SÜD WACE MR 0175/ISO 15156-1 ASO 15156-3																																																																																					
Identification of the product Identification du produit - Identifizierung des Erzeugnisses MELTED IN BELGIUM, MADE IN FRANCE		Dimensions Dimensions - Abmessungen Thickness Epaisseur - Dicke 3,000 mm		Number of pieces Nb de pièces - Stückzahl 138																																																																																	
Coil n. N.Bobine - Band Nr. 69052		Heat n. N.Coulée - Schmelz Nr. 714800		Net weight Poids net - netto Gewicht 10208 KGS																																																																																	
CHEMICAL ANALYSIS - ANALYSE CHIMIQUE - CHEMISCHE ZUSAMMENSETZUNG																																																																																					
<table border="1"> <thead> <tr> <th></th> <th>C</th> <th>Si</th> <th>Mn</th> <th>Ni</th> <th>Cr</th> <th>Mo</th> <th>Ti</th> <th>N</th> <th>S</th> <th>P</th> <th>Co</th> <th></th> <th></th> <th></th> <th></th> </tr> </thead> <tbody> <tr> <td>Required - Exigé %mini</td> <td>0,030</td> <td>0,75</td> <td>2,00</td> <td>8,00</td> <td>18,00</td> <td></td> <td></td> <td>0,100</td> <td>0,0150</td> <td>0,045</td> <td></td> <td></td> <td></td> <td></td> <td></td> </tr> <tr> <td>Cast Analysis</td> <td>0,023</td> <td>0,44</td> <td>1,46</td> <td>8,00</td> <td>18,08</td> <td></td> <td></td> <td>0,072</td> <td>0,0033</td> <td>0,032</td> <td>0,171</td> <td></td> <td></td> <td></td> <td></td> </tr> <tr> <td>Analysis coulée</td> <td>C71</td> <td>C72</td> <td>C73</td> <td>C74</td> <td>C75</td> <td>C76</td> <td>C77</td> <td>C78</td> <td>C79</td> <td>C80</td> <td>C81</td> <td>C82</td> <td>C83</td> <td>C84</td> <td>C85</td> </tr> <tr> <td>Analysis Schmelze</td> <td></td> <td></td> <td></td> <td></td> <td></td> <td></td> <td></td> <td></td> <td></td> <td></td> <td></td> <td></td> <td></td> <td></td> <td></td> </tr> </tbody> </table>							C	Si	Mn	Ni	Cr	Mo	Ti	N	S	P	Co					Required - Exigé %mini	0,030	0,75	2,00	8,00	18,00			0,100	0,0150	0,045						Cast Analysis	0,023	0,44	1,46	8,00	18,08			0,072	0,0033	0,032	0,171					Analysis coulée	C71	C72	C73	C74	C75	C76	C77	C78	C79	C80	C81	C82	C83	C84	C85	Analysis Schmelze															
	C	Si	Mn	Ni	Cr	Mo	Ti	N	S	P	Co																																																																										
Required - Exigé %mini	0,030	0,75	2,00	8,00	18,00			0,100	0,0150	0,045																																																																											
Cast Analysis	0,023	0,44	1,46	8,00	18,08			0,072	0,0033	0,032	0,171																																																																										
Analysis coulée	C71	C72	C73	C74	C75	C76	C77	C78	C79	C80	C81	C82	C83	C84	C85																																																																						
Analysis Schmelze																																																																																					
Tests to verify batch and quality have been carried out : OK Tests de vérification de la conformité de la nuance fournie : OK Verwechslungsprüfung wurde durchgeführt : OK																																																																																					
Location (1)																																																																																					
MECHANICAL PROPERTIES - PROPRIETES MECANQUES - MECHANISCHE WERTE																																																																																					
Room temperature - Température ambiante - Raumtemperatur																																																																																					
Test temperature (°C) :																																																																																					
<table border="1"> <thead> <tr> <th rowspan="2">Direction (2)</th> <th rowspan="2">Required Exigé Anforderung</th> <th colspan="2">Yield or proof strength Limite d'élasticité Dehngrenze MPa</th> <th colspan="2">Tensile strength Résistance à la traction Zugfestigkeit MPa</th> <th colspan="2">Elongation after fracture Allongement après rupt. Bruchdehnung %</th> <th rowspan="2">Hardness Dureté Haerte</th> <th colspan="2">Yield or proof strength Limite d'élasticité Dehngrenze MPa</th> <th colspan="2">Tensile str. Résist. MPa Zugfestigkeit</th> <th rowspan="2">Elongation % Allongement. Bruchdehnung</th> </tr> <tr> <th>Rp0.2%</th> <th>Rp1%</th> <th>Rm</th> <th>A50mm</th> <th>HRB C30</th> <th>Rp0.2%</th> <th>Rp1%</th> <th>Rm</th> </tr> </thead> <tbody> <tr> <td rowspan="2">1 T</td> <td>mini</td> <td>230</td> <td>260</td> <td>540</td> <td>45</td> <td>40</td> <td>92</td> <td></td> <td></td> <td></td> <td></td> <td></td> <td></td> </tr> <tr> <td>maxi</td> <td>313</td> <td>359</td> <td>708</td> <td>59</td> <td>55</td> <td>86</td> <td></td> <td></td> <td></td> <td></td> <td></td> <td></td> </tr> <tr> <td rowspan="2">2 T</td> <td>Obtained Obtenu Ergebnisse</td> <td></td> <td></td> <td>629</td> <td></td> <td></td> <td>87</td> <td></td> <td></td> <td></td> <td></td> <td></td> <td></td> </tr> <tr> <td></td> <td>C11</td> <td></td> <td>C14</td> <td></td> <td>C12</td> <td>C13</td> <td>C15</td> <td>C31</td> <td>C16</td> <td>C17</td> <td>C18</td> <td>C19</td> </tr> </tbody> </table>						Direction (2)	Required Exigé Anforderung	Yield or proof strength Limite d'élasticité Dehngrenze MPa		Tensile strength Résistance à la traction Zugfestigkeit MPa		Elongation after fracture Allongement après rupt. Bruchdehnung %		Hardness Dureté Haerte	Yield or proof strength Limite d'élasticité Dehngrenze MPa		Tensile str. Résist. MPa Zugfestigkeit		Elongation % Allongement. Bruchdehnung	Rp0.2%	Rp1%	Rm	A50mm	HRB C30	Rp0.2%	Rp1%	Rm	1 T	mini	230	260	540	45	40	92							maxi	313	359	708	59	55	86							2 T	Obtained Obtenu Ergebnisse			629			87								C11		C14		C12	C13	C15	C31	C16	C17	C18	C19				
Direction (2)	Required Exigé Anforderung	Yield or proof strength Limite d'élasticité Dehngrenze MPa		Tensile strength Résistance à la traction Zugfestigkeit MPa				Elongation after fracture Allongement après rupt. Bruchdehnung %		Hardness Dureté Haerte	Yield or proof strength Limite d'élasticité Dehngrenze MPa		Tensile str. Résist. MPa Zugfestigkeit		Elongation % Allongement. Bruchdehnung																																																																						
		Rp0.2%	Rp1%	Rm	A50mm	HRB C30	Rp0.2%	Rp1%	Rm																																																																												
1 T	mini	230	260	540	45	40	92																																																																														
	maxi	313	359	708	59	55	86																																																																														
2 T	Obtained Obtenu Ergebnisse			629			87																																																																														
		C11		C14		C12	C13	C15	C31	C16	C17	C18	C19																																																																								
Impact strength test Essai de résilience Kerbschlagzähigkeitstest																																																																																					
Corrosion test Test de corrosion Korrosionstest																																																																																					
EN ISO 3651-2 :OK																																																																																					
Internal cleanliness:																																																																																					
A: B: C: D:																																																																																					
Location of the sample (1) Emplacement de l'échantillon Lage des Probenabschnittes 1. Front - Début - Anfang 2. Back - Fin - Ende 3. Middle - Milieu - Mitte		The delivery is in accordance with the order La fourniture est conforme aux exigences de la commande Die Lieferung entspricht den Bestellbedingungen		Organisation inspection Organisme et/ou service contrôle Überwachungsabteilung																																																																																	
Direction of the test pieces (2) Orientation des éprouvettes Probenrichtung T. Transverse - Travers - Quer L. Longitudinal - Long - Längs		Packing list Avis d'expédition Lieferscheinnummer 120601100078-5731		Service Métallurgique 01/06/2012 M. THOMAS The inspector Le responsable Der Werksachverständige																																																																																	

Test Cert - Your Ref. K9360 Our Ref. 0462407

Figure 73 mill certificate of 304L austenitic stainless steel provided by Aperam, France.

11.2 Powdered iron oxide standard synthesis

Powdered iron oxides were prepared by Dr. Rowena Fletcher-Wood using the following procedures:

Akaganeite was precipitated from a solution consisting of 5.37 g of $\text{FeCl}_3 \cdot 6\text{H}_2\text{O}$ (Sigma Aldrich 97%) dissolved in 200 ml deionised water, mixed in a polypropylene flask and held at 70 °C in a preheated oven for 48 hours before being immediately removed to cool to room temperature. An orange brown grainy powder was produced that penetrated filter paper when filtered with a Buchner funnel under suction filtration. To separate the solid from the liquid, the sample was left to settle and water pipetted off to leave a dense suspension. The remainder of the solution was left upon a warm oven for 5 days to dry, before being scraped from the bottom of the flask.

Goethite was prepared by dissolving 25.24 g of KOH (Sigma Aldrich 90%) in 90 ml deionised water to get 5 M KOH solution which was subsequently combined with 1 M $\text{Fe}(\text{NO}_3)_3 \cdot 9\text{H}_2\text{O}$ (Aldrich 98+%) solution, itself prepared by first dissolving 20.20 g of the solid in 50 ml deionised water. The solution was diluted to 500 ml with deionised water and poured into a polypropylene flask, sealed, then held at 70 °C in a preheated oven for 60 hours before turning off the oven to allow the sample to cool to room temperature. The solution was filtered with a Buchner funnel whilst still warm (~ 40 °C). The goethite precipitate was a pale orange brown colour and crystals were shape flaky and block-like.

Lepidocrocite and **magnetite** were prepared from identical starting solutions. 5.93 g of $\text{FeCl}_2 \cdot 4\text{H}_2\text{O}$ (Sigma Aldrich $\geq 99.0\%$) was dissolved in 500 ml deionised water. A concentrated solution of NaOH (Sigma Aldrich $\geq 98\%$) was also prepared by dissolving flakes in deionised water. The pH of the iron chloride solution was monitored with a HANNA Instruments pH211 Microprocessor pH Meter calibrated using buffer solutions at $\sim\text{pH}9$ and $\text{pH}6$. NaOH solution was administered dropwise using a squeezey pipette to maintain a pH of 7 ± 0.20 . As pH varied, the reaction colour differed from orange (low pH) to misty green (high pH). Simultaneously, air was bubbled through the solution via a cannula attached to the exhaust of a vacuum pump. The pump was first flushed for ~ 10 minutes by pumping on and into air to eliminate contaminants. An empty flask was placed between the pump and cannula to prevent suck back. A round bottomed flask fitted with a Young's tap was introduced at a T junction control the flow rate by turning the tap to create a second exhaust, thus limiting the pressure that passed directly through the cannula. A measurement of flow rate could not be obtained, but was approx. 1-5 bubbles per second.

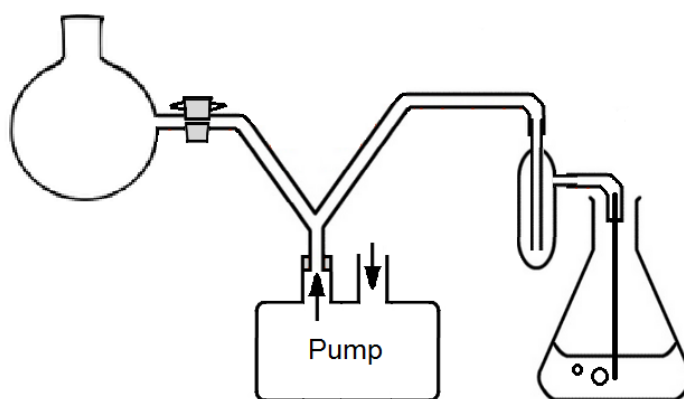


Diagram of bubble set up from the vacuum pump exhaust.

Lepidocrocite was obtained after bubbling and holding the solution for 1 hour 20 minutes. At times exceeding 2 hours of bubbling, magnetite was obtained at phase fractions of 98+%. At times ≤ 1 hour, a mixture of phases was obtained.

Maghemite was synthesised as a transformation product of magnetite, prepared as described above with 2 hours of stirring and bubbling. The magnetite sample was loaded into an open alumina boat and placed in a preheated oven at 250 °C for 5 hours, before being removed to cool rapidly to room temperature.

11.3 Matlab script – Raman averaging

11.3.1 Main file - Spectral averaging

```
% Written by W.G.Rowley, University of Birmingham 2017
%
% Raman spectrum Averaging script
% Takes a directory of tab seperated variable text files and an image
% corresponding to a map produced by WiRE raman software. It will
average
% all spectra corresponding to pixels above a set intensity value in
the
% map image (set with thresh variable).
%
% To use:
% 1.export your map image from WiRE using right click->export image,
%   this should be a bmp with the same number of pixels as you have
spectra
%   in the map
% 2. use file->multidataset save to export the full list of spectra as
txt
%   files
%   dirvar is the path to the directory containing the text files, Im
is the
%   bmp image which has been imported to matlab as a variable
% 3. Set thresh such that it is below the pixel value of the areas
that
%   you want to average, but above those of the area you want to
ignore
% 4.Finally, modify the for loop on line 46 such that the '%u' falls
in line
%   with the spectrum number on each text file.
%   e.g. 'Test_A_1_X_11243_Y_414_Z_312_Time_0' would be
%   '%*s %*s %u %*s %*s %*s %*s %*s %*s %*s %*s'
function [xout, yout] = RMNAVG(dirvar, Im)

%Threshold for including spectrum in averaging | N.B. this is a pixel
%intensity value ranging from 1-255, so 0.5 is 128, 0.75 is 191 etc.
thresh = 100;
%%process
%read spectra
%average spectra
%output (display)
%% Initialise
Im = Im(:,:,1)';%delete pointless colour channels & transpose
k=0;
j=0;
ImIndexLength = size(Im,1)*size(Im,2);
%Get total # of expected spectra
fnames = dir(strcat([dirvar, '\*.txt']));
%Get file name list
if length(fnames) == 0
    disp('Bad Filename');
    return
end
[xout,~] = readspec(fnames(1).name);
%Extract list of wavenumbers (x axis)
```

```

Indexlist = zeros(ImIndexLength, 1);
%Initialise list of indices
speclist = zeros(ImIndexLength,size(xout,1));
%Initialise list of spectra for averaging
if ImIndexLength ~= size(fnames)
%Check to make sure that your image size is the same as the number of
spectra in the folder
    disp('Image dimensions do not match length of file list');
    return
end

%% extract the spectrum indices from the filenames as they don't
line up with array indices when imported
for i = 1:ImIndexLength
    %Indexlist(i) = cell2mat(textscan(fnames(i).name, '%s %s %s %s
%s %s %s %s %s %s %s %s %s %s %s %s', 'delimiter',
'_' ));
    %oceanwater
    %Indexlist(i) = cell2mat(textscan(fnames(i).name, '%s %s %s %s
%s %s %s %s %s %s %s %s %s %s %s %s', 'delimiter', '_'));
    %nacl
    Indexlist(i) = cell2mat(textscan(fnames(i).name, '%s %s %s %s
%s %s %s %s %s %s %s %s %s %s %s %s', 'delimiter', '_'));
    %magh
end
% set(gca, 'xlim',[0,1600])
%% read the spectra for relevant indices (Image intensity over
threshold set at start of script)
for i=1:ImIndexLength
    clear tempname
    tempname = fnames(Indexlist == i-1).name;
    if exist('tempname','var') ~= 0
        if Im(i) >= thresh
            [~,tempy] = readspec(tempname);
            tempy = abs(tempy./max(tempy));
            if isnan(tempy)
                tempy = zeros(size(xout,1),1);
            end

            %
            figure(A1);
            %
            hold on
            %
            plot(xout, tempy,'b');
            %Im(i)=255;
            % disp(strcat([num2str(i), ' of ', num2str(ImIndexLength),
' spectra scanned']));
            %else Im(i) =0;
            if tempy == 0 %sometimes there will be error spectra
(all zeroes), ignore them.
                k=k-1;
                i
            end
            speclist(i,:) = tempy;
            k=k+1;
        else
            %
            [~,tempy] = readspec(tempname);
            %
            figure(A2);
            %
            hold on
            %
            plot(xout, tempy,'r');

```

```

        j = j+1;
    end
end
end
%imshow(Im)
%speclist(speclist==0)=[];
speclist=reshape(speclist,k,size(xout,1));
yout = mean(speclist,1);
%Actually average the spectra
figure;plot(xout,yout, 'k')
%plot it
set(gca, 'ylim',[0,inf]);
disp(strcat(['Averaged ', num2str(k) , ' spectra']));
end

```

11.3.2 Dependency – import csv spectral from directory

```

function [Wavenumber,Counts] = readspec(filename, startRow, endRow)
%IMPORTFILE Import numeric data from a text file as column vectors.
% [WAVENUMBER,COUNTS] = IMPORTFILE(FILENAME) Reads data from text
file
% FILENAME for the default selection.
%
% [WAVENUMBER,COUNTS] = IMPORTFILE(FILENAME, STARTROW, ENDROW) Reads
data
% from rows STARTROW through ENDROW of text file FILENAME.
%
% Example:
% [Wavenumber,Counts] = importfile('06-09-
16_test2_ocean_10s_2aq_100pw_28um-28um_mapping - truncate-
baselinesub_1__X_-22228.9__Y_-15589.7__Z_-6566.34__Time_20.txt',1,
981);
%
% See also TEXTSCAN.

% Auto-generated by MATLAB on 2017/05/03 10:33:27

%% Initialize variables.
delimiter = '\t';
if nargin<=2
    startRow = 1;
    endRow = inf;
end

%% Format for each line of text:
% column1: double (%f)
% column2: double (%f)
% For more information, see the TEXTSCAN documentation.
formatSpec = '%f%f%[\n\r]';

%% Open the text file.
fileID = fopen(filename,'r');

%% Read columns of data according to the format.

```

```

% This call is based on the structure of the file used to generate
this
% code. If an error occurs for a different file, try regenerating the
code
% from the Import Tool.
dataArray = textscan(fileID, formatSpec, endRow(1)-startRow(1)+1,
'Delimiter', delimiter, 'HeaderLines', startRow(1)-1, 'ReturnOnError',
false, 'EndOfLine', '\r\n');
for block=2:length(startRow)
    frewind(fileID);
    dataArrayBlock = textscan(fileID, formatSpec, endRow(block)-
startRow(block)+1, 'Delimiter', delimiter, 'HeaderLines',
startRow(block)-1, 'ReturnOnError', false, 'EndOfLine', '\r\n');
    for col=1:length(dataArray)
        dataArray[80] = [dataArray[80];dataArrayBlock[80]];
    end
end

%% Close the text file.
fclose(fileID);

%% Post processing for unimportable data.
% No unimportable data rules were applied during the import, so no
post
% processing code is included. To generate code which works for
% unimportable data, select unimportable cells in a file and
regenerate the
% script.

%% Allocate imported array to column variable names
Wavenumber = dataArray(:, 1);
Counts = dataArray(:, 2);

```

11.4 Matlab scripts – Hyperspectral image processing

Scripts for importing hyperspectral images into matlab and plotting specific spectra from a hyperspectral image

11.4.1 Principal component analysis

```

%function [eigenvectors, secpricom] = PCA_ndim(I)
% this function takes a hyperspectral image, calculates the principle
components and
% plots these as an image

close all
X = [];
% To make it faster we will re-size the image to be smaller
%I = imresize(I,0.25);

% get size of image

```

```

[nr,nc,d]=size(I);

% Convert to a double variable
I = double(I);

% extract the colours
for i = 1:d
In = I(:,:,i);

% instead of a matrix, we want a long list of pixel intensity
In = reshape(In,nr*nc,1);

% This bit is where we calculate the PCA
In = In-mean(In);
In(In==Inf)=0;
In(In== -Inf)=0;
In(isnan(In))=0;
X = [X, In];
end
[U,S,V]=svd(cov(X));

eigenvectors= U'*X';

% and plot it!
figure;
for i = 1 : 5
    subplot(1,5,i);
    imagesc(reshape(eigenvectors(i,:),nr,nc));axis equal;axis
tight;colormap gray;
end
firpricom =reshape(eigenvectors(1,:),nr,nc);
secpricom = reshape(eigenvectors(2,:),nr,nc);
thirpricom = reshape(eigenvectors(3,:),nr,nc);
fourpricom = reshape(eigenvectors(4,:),nr,nc);
fifpricom = reshape(eigenvectors(5,:),nr,nc);
%subplot(1,3,3);
%imagesc(reshape(eigenvectors(2,:)-(eigenvectors(1,:)./4),nr,nc));axis
equal;axis tight
%end

```

11.5 Matlab scripts – Image processing

11.5.1 Acquire rust area by Red-Blue colour channel subtraction

```

% Takes an image; finds, labels pits by deposition area based on red-
blue
% colour channel subtraction, boxes is optional
%% I is a x*y*3 RGB image vector i.e. I = imread('IMAGE.NAME');
function output = colourfindrgb(I, boxes);
if exist('boxes') == 0
    boxes = false;
end

```

```

%%classifying part
%get size of image
[nr,nc,d]=size(I);

% Convert to a double variable
I = double(I);

% extract the colours
IR = double(I(:,:,1));
IG = double(I(:,:,2));
IB = double(I(:,:,3));

thresh = IR-IB;          %for R-B
thresh(thresh < 30) = 0;  %thresh of 30

%Dust and Assign labels to each region of connected components
conncomps = bwconncomp(thresh);
dust = cellfun(@numel,conncomps.PixelIdxList);
thresh(cat(1, conncomps.PixelIdxList{dust<100}))=0;

almconncomp_im = bwdist(thresh) <= 50;
L2 = labelmatrix(bwconncomp(almconncomp_im));
%Reduce areas to their original sizes
L2(~thresh) = 255;

%Extract Areas and Centroids and plot. We also have the option to
colour
%the plot based on label area
s = regionprops(L2, 'Area', 'Centroid', 'Extrema', 'BoundingBox');
figure;
imshow(L2);
%imshow(label2rgb(L2, 'jet', 'w','shuffle')); % colour

%clean up output image
%L2(L2~=255) = 1;

%Initialise output variables
Area = zeros(1,length(s));
Centroid = zeros(2,length(s));
Extrema = zeros(8,2,length(s));
BB = zeros(4, length(s));

%Populate output variables from struct and amend plot with desired
%features.
hold on;
for i = 1:(length(s)-1);
    if s(i).Area > 100 %&& s(i).Area < 1000000
        Area(:,i) = s(i).Area;
        Centroid(:,i) = s(i).Centroid;
        Extrema(:, :, i) = s(i).Extrema;
        BB(:,i) = s(i).BoundingBox;
        if boxes == true
            %plot(Centroid(1,i),Centroid(2,i),'b*');
%Mark the centroid of each region
            %plot(Extrema(:,1,i), Extrema(:,2,i), 'r+');
%Mark the extremeties of each region

```



```

        rectangle('Position',BB(:,i));
%Draw a square around each region
        %viscircles(rot90(Centroid(:,i)), (Centroid(2,i)-BB(2,i)));
%Draw a circle around each region
    end
end
end
%%output and close
output = struct('Areas', Area, 'Centroid', Centroid, 'Extrema',
Extrema, 'BoundingBox', BB, 'Im', L2);
hold off
end

```

11.5.2 Acquire rust area by principal component analysis

```

% Takes an image; finds, labels pits by deposition area based on
principle
% component analysis, boxes is optional
%% I is a x*y*3 RGB image vector i.e. I = imread('IMAGE.NAME');
function output = pitfind(I, boxes);
if exist('boxes') == 0
    boxes = false;
end
%%PCA portion
%get size of image
[nr,nc,d]=size(I);

% Convert to a double variable
I = double(I);

% extract the colours
IR = I(:, :, 1);
IG = I(:, :, 2);
IB = I(:, :, 3);

% instead of a matrix, we want a long list of pixel intensity
IR = reshape(IR,nr*nc,1);
IG = reshape(IG,nr*nc,1);
IB = reshape(IB,nr*nc,1);

% This bit is where we calculate the PCA;
%we first centre the data by subtracting the mean of each channel from
each channel
IR = IR-mean(IR);
IG = IG-mean(IG);
IB = IB-mean(IB);

%These then get put in a single matrix
X = [IR, IG, IB];

%Single value decomposition of the covariance matrix is performed
[U,S,V]=svd(cov(X));

%the eigenvectors are then extracted by multiplying the transpose of
the

```

```

%unitary matrix U by the transpose of X.
eigenvectors= U'*X';

%the second principle component (second channel) is extracted from the
%eigenvector and reshaped back into the original resolution of the
image
%(nr, nc)
secpricom = reshape(eigenvectors(2,:),nr,nc);

%clearvars -except secpricom I

%%Regionfinding portion
%Thresholding, all pixels of less than 50 intensity are set to zero
thresh = secpricom;
thresh(thresh < 20) = 0;

%Dust and Assign labels to each region of connected components
conncomps = bwconncomp(thresh);
dust = cellfun(@numel,conncomps.PixelIdxList);
thresh(cat(1, conncomps.PixelIdxList{dust<100}))=0;

almconncomp_im = bwdist(thresh) <= 2;
L2 = labelmatrix(bwconncomp(almconncomp_im));
%Reduce areas to their original sizes
L2(~thresh) = 255;

%Extract Areas and Centroids and plot. We also have the option to
colour
%the plot based on label area
s = regionprops(L2, 'Area', 'Centroid', 'Extrema', 'BoundingBox');
figure;
imshow(L2);
%imshow(label2rgb(L2, 'jet', 'w','shuffle')); %colour

%clean up output image
%L2(L2~=255) = 1;

%Initialise output variables
Area = zeros(1,length(s));
Centroid = zeros(2,length(s));
Extrema = zeros(8,2,length(s));
BB = zeros(4, length(s));

%Populate output variables from struct and amend plot with desired
%features.
hold on;
for i = 1:(length(s)-1);
    if s(i).Area > 100 %&& s(i).Area < 1000000
        Area(:,i) = s(i).Area;
        Centroid(:,i) = s(i).Centroid;
        Extrema(:, :, i) = s(i).Extrema;
        BB(:,i) = s(i).BoundingBox;
        if boxes == true
            %plot(Centroid(1,i),Centroid(2,i),'b*');
%Mark the centroid of each region

```

```

        plot(Extrema(:,1,i), Extrema(:,2,i), 'r+');
%Mark the extremeties of each region
        rectangle('Position',BB(:,i));
%Draw a square around each region
        viscircles(rot90(Centroid(:,i)), (Centroid(2,i)-BB(2,i)));
%Draw a circle around each region
    end
end
end
%output and close
output = struct('Areas', Area, 'Centroid', Centroid, 'Extrema',
Extrema, 'BoundingBox', BB, 'Im', L2);
hold off
end

```

11.5.3 Acquire rust area by HSV thresholding

```

% Takes an image; finds, labels pits by deposition area based on HSV
thresholding, boxes is optional
%% I is a x*y*3 RGB image vector i.e. I = imread('IMAGE.NAME');
function output = colourfindhsv(I, boxes);
if exist('boxes') == 0
    boxes = false;
end
%%classifying part
%get size of image

[nr,nc,d]=size(I);

% Convert to hsv
I = rgb2hsv(I);

% extract the variables
Ih = I(:,:,1);
Is = I(:,:,2);
Iv = I(:,:,3);

thresh = Is; %doing everything via the saturation
channel
thresh(Ih > 0.15) = 0; %eliminate H that's not red
thresh(Is < 0.2) = 0; %threshold of 0.2S

%Dust and Assign labels to each region of connected components
conncomps = bwconncomp(thresh);
dust = cellfun(@numel,conncomps.PixelIdxList);
thresh(cat(1, conncomps.PixelIdxList{dust<100}))=0;

almconncomp_im = bwdist(thresh) <= 50;
L2 = labelmatrix(bwconncomp(almconncomp_im));
%Reduce areas to their original sizes
L2(~thresh) = 255;

```

```

%Extract Areas and Centroids and plot. We also have the option to
colour
%the plot based on label area
s = regionprops(L2, 'Area', 'Centroid', 'Extrema', 'BoundingBox');
figure;
imshow(L2);
%imshow(label2rgb(L2, 'jet', 'w','shuffle')); %colour
%clean up output image
%L2(L2~=255) = 1;

%Initialise output variables
Area = zeros(1,length(s));
Centroid = zeros(2,length(s));
Extrema = zeros(8,2,length(s));
BB = zeros(4, length(s));

%Populate output variables from struct and amend plot with desired
%features.
hold on;
for i = 1:(length(s)-1);
    if s(i).Area > 100 %&& s(i).Area < 1000000
        Area(:,i) = s(i).Area;
        Centroid(:,i) = s(i).Centroid;
        Extrema(:, :, i) = s(i).Extrema;
        BB(:,i) = s(i).BoundingBox;
        if boxes == true
            %plot(Centroid(1,i),Centroid(2,i),'b*');
%Mark the centroid of each region
            %plot(Extrema(:,1,i), Extrema(:,2,i), 'r+');
%Mark the extremeties of each region
            rectangle('Position',BB(:,i));
%Draw a square around each region
            %viscircles(rot90(Centroid(:,i)), (Centroid(2,i)-BB(2,i)));
%Draw a circle around each region
        end
    end
end
%%output and close
output = struct('Areas', Area, 'Centroid', Centroid, 'Extrema',
Extrema, 'BoundingBox', BB, 'Im', L2);
hold off
end

```

11.5.4 Rust area analysis by $L^*a^*b^*$ thresholding

```

% Takes an image; finds, labels pits by deposition area based on
 $L^*a^*b^*$  thresholding, boxes is optional
%% I is a  $x*y*3$  RGB image vector i.e.  $I = \text{imread}('IMAGE.NAME');$ 
function output = colourfindlab(I, boxes);
if exist('boxes') == 0
    boxes = false;

```

```

end
%%classifying part
%get size of image

[nr,nc,d]=size(I);

% Convert to lab
I = rgb2lab(I);

% extract the variables
I1 = I(:,:,1);
Ia = I(:,:,2);
Ib = I(:,:,3);

thresh = Ib; %doing everything via the b* channel
thresh(thresh < 20) = 0;

%Dust and Assign labels to each region of connected components
conncomps = bwconncomp(thresh);
dust = cellfun(@numel,conncomps.PixelIdxList);
thresh(cat(1, conncomps.PixelIdxList{dust<100}))=0;

almconncomp_im = bwdist(thresh) <= 50;
L2 = labelmatrix(bwconncomp(almconncomp_im));
%Reduce areas to their original sizes
L2(~thresh) = 255;

%Extract Areas and Centroids and plot. We also have the option to
colour
%the plot based on label area
s = regionprops(L2, 'Area', 'Centroid', 'Extrema', 'BoundingBox');
figure;
imshow(L2);
%imshow(label2rgb(L2, 'jet', 'w','shuffle')); % colour

%clean up output image
%L2(L2~=255) = 1;

%Initialise output variables
Area = zeros(1,length(s));
Centroid = zeros(2,length(s));
Extrema = zeros(8,2,length(s));
BB = zeros(4, length(s));

%Populate output variables from struct and amend plot with desired
%features.
hold on;
for i = 1:(length(s)-1);
    if s(i).Area > 100 %&& s(i).Area < 1000000
        Area(:,i) = s(i).Area;
        Centroid(:,i) = s(i).Centroid;
        Extrema(:, :, i) = s(i).Extrema;
        BB(:,i) = s(i).BoundingBox;
        if boxes == true
            %plot(Centroid(1,i),Centroid(2,i),'b*');
%Mark the centroid of each region

```

```

        %plot(Extrema(:,1,i), Extrema(:,2,i), 'r+');
%Mark the extremeties of each region
        rectangle('Position',BB(:,i));
%Draw a square around each region
        %viscircles(rot90(Centroid(:,i)), (Centroid(2,i)-BB(2,i)));
%Draw a circle around each region
        end
    end
end
%%output and close
output = struct('Areas', Area, 'Centroid', Centroid, 'Extrema',
Extrema, 'BoundingBox', BB, 'Im', L2);
hold off
end

```

11.5.5 Supplemental figures (Chapter 6)

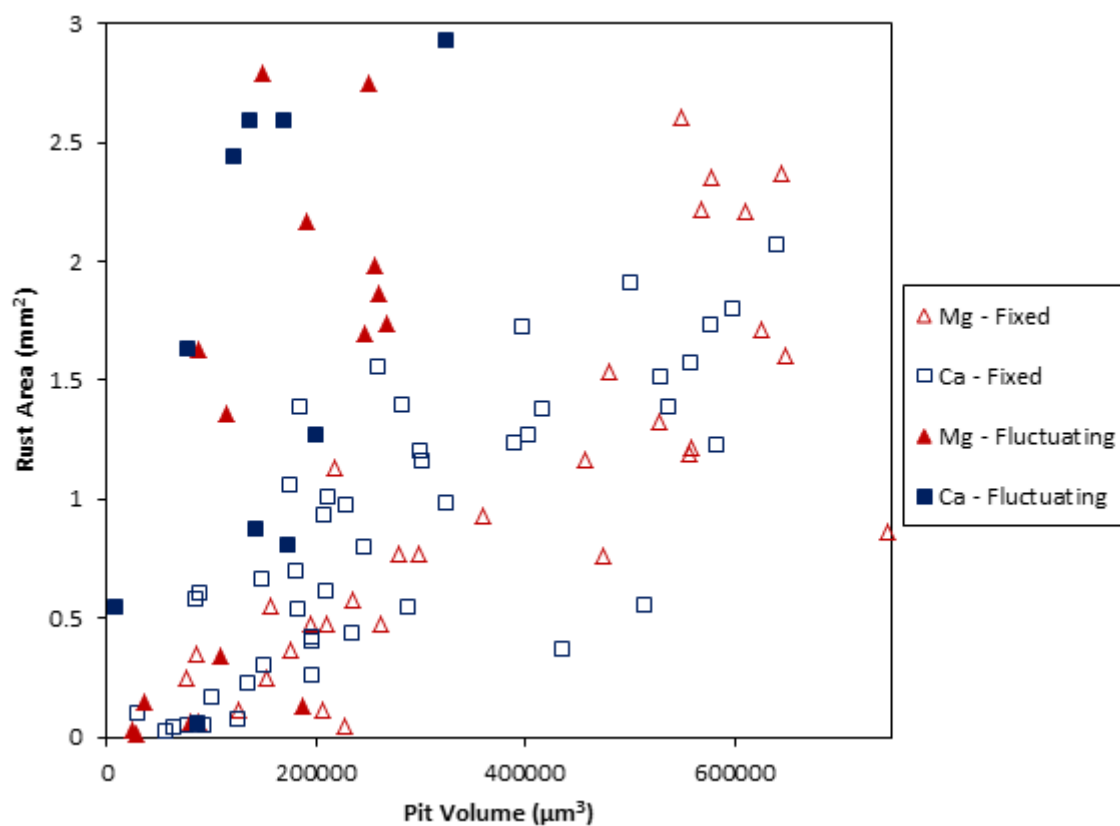


Figure 74 Zoom of lower left region of Figure 66. Pit volume is compared to rust area for both MgCl_2 and CaCl_2 droplets exposed for 2 weeks under either fixed conditions (46% RH and 30°C) or fluctuating ambient (19-49% RH and $19\text{-}24^\circ\text{C}$).

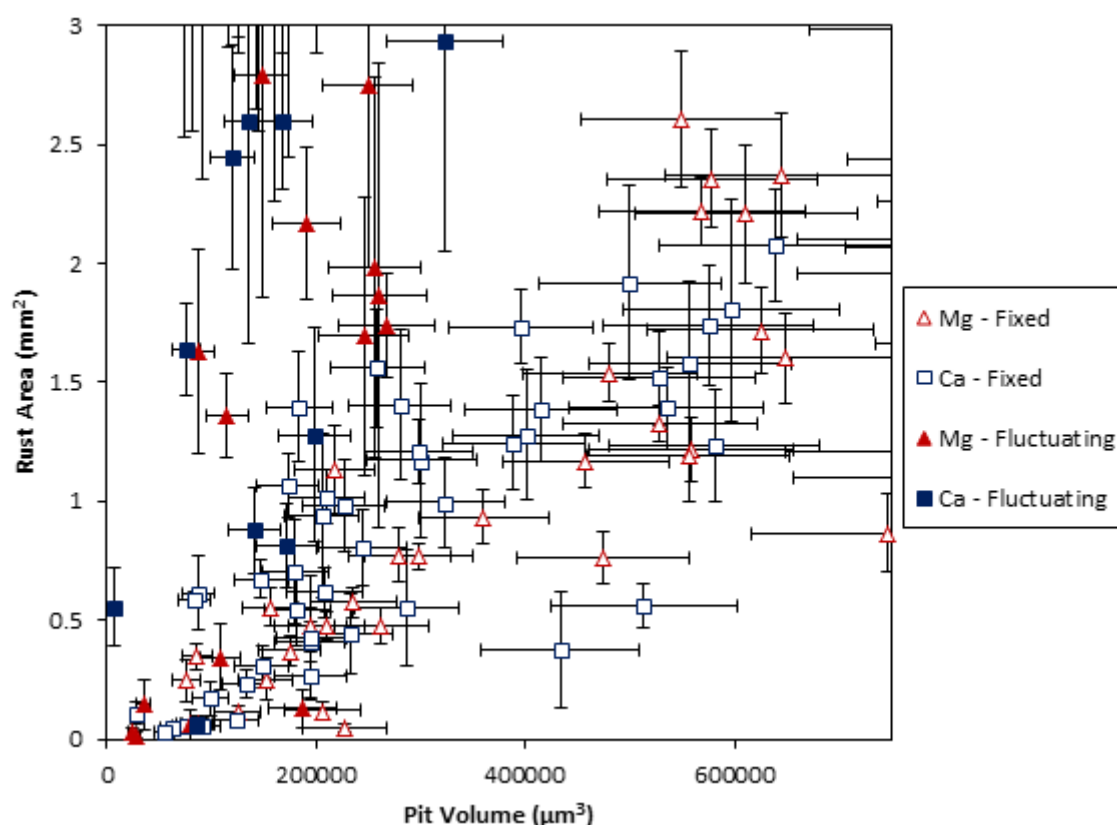


Figure 75 Zoom of the lower left portion of Figure 71. Pit volume is compared to rust area for both MgCl_2 and CaCl_2 droplets exposed for 2 weeks under either fixed conditions (46% RH and 30°C) or fluctuating ambient (19-49% RH and $19-24^\circ\text{C}$). Error bars show standard deviation of pit volume measurements (x) and standard deviation of area measurements acquired through different threshold-based techniques (y).

Figure 75 clarifies the areas of Figure 71 corresponding to pit volumes of less than $500,000 \mu\text{m}^3$ and rust areas of less than 2 mm^2 . A linear relationship is present for droplets exposed to fixed conditions; no relationship is present for fluctuating ambient droplets. .

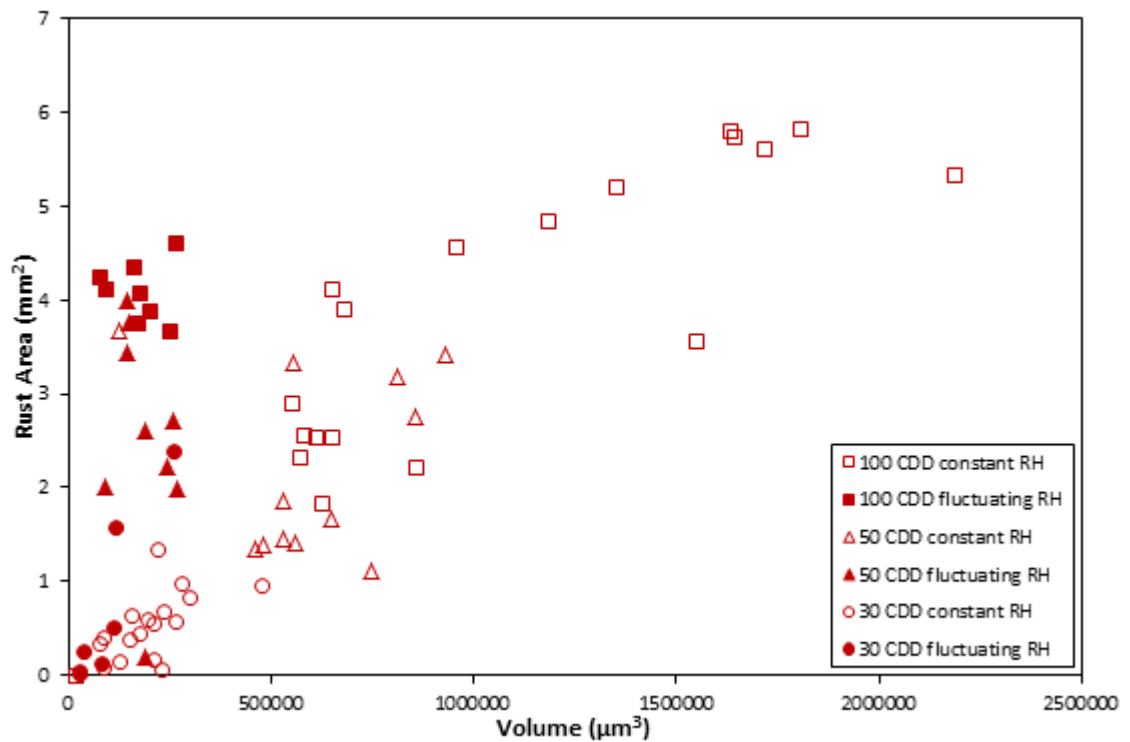


Figure 76 Distribution of pit volume and rust area for MgCl_2 droplets for a range of chloride deposition densities and for fluctuating and ambient RH

Figure 76 shows the distribution of pit volumes with respect to rust area for MgCl_2 droplets, split by CDD. A linear relationship is present for all droplets in fixed conditions, while fluctuating conditions have a maximum measured pit volume of $400,000 \mu\text{m}^3$. Higher CDDs are also associated with a larger visible rust area in all conditions and also a higher pit volume in the case of droplets exposed in fixed conditions.

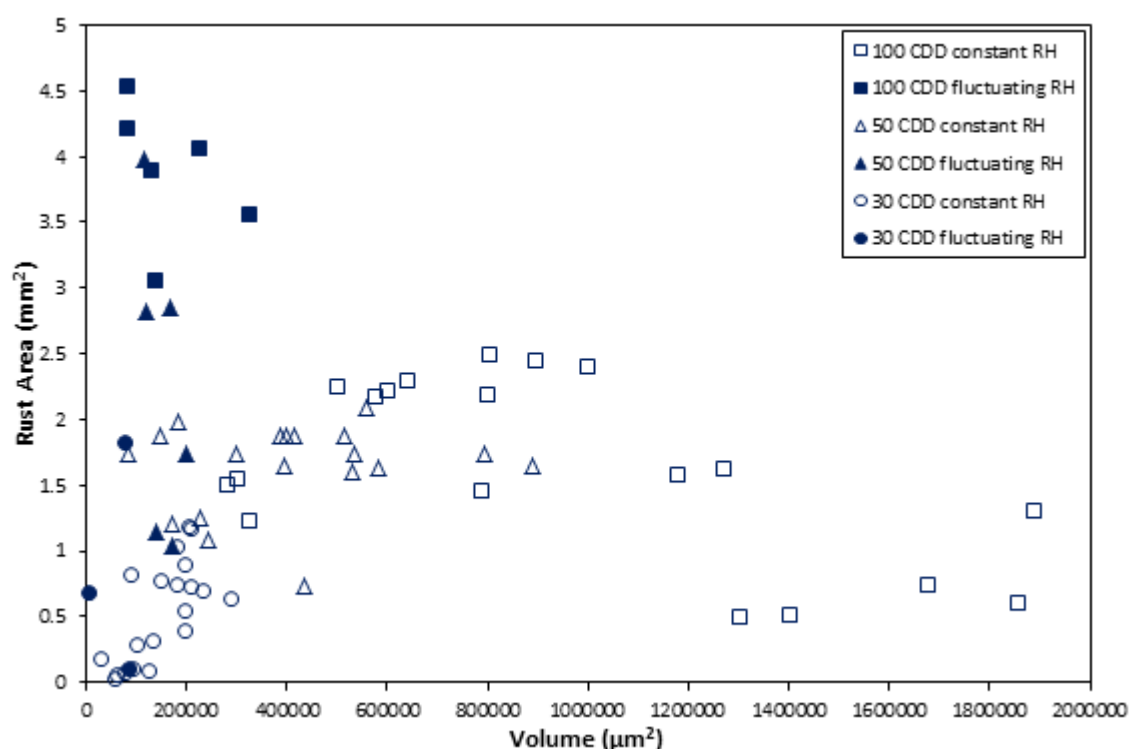


Figure 77 Distribution of pit volume and rust area for CaCl_2 droplets under a range of chloride deposition densities and for fluctuating and ambient RH

Figure 77 shows the distribution of pit volumes with respect to rust area for MgCl_2 droplets, split by CDD. In fixed conditions, higher CDDs are associated with larger pit volume and rust area for 20 and 50 μgcm^{-2} droplets, but 100 μgcm^{-2} have a lower rust area than would be expected. For fluctuating ambient conditions, higher CDD is associated with a larger rust area, but not an increase in pit volume.

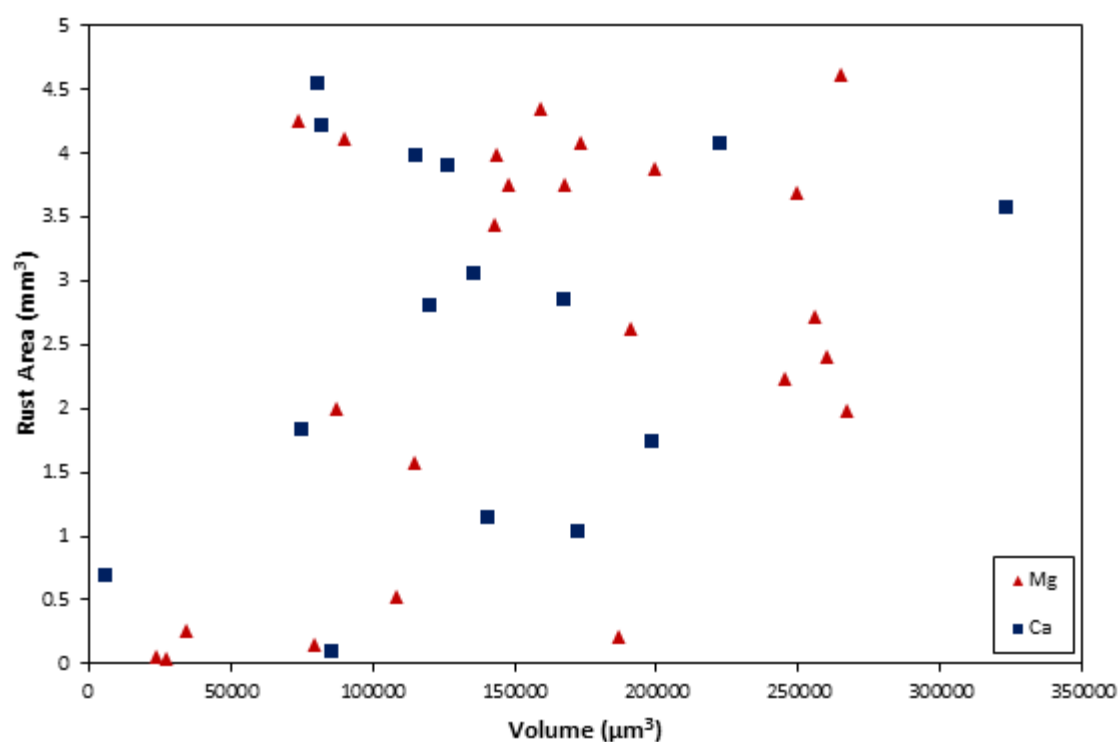


Figure 78 comparison of pit volume vs rust area for both MgCl_2 and CaCl_2 droplets exposed for 2 weeks for fluctuating ambient conditions only(19-49% RH and 19-24°C).

Figure 78 shows the distribution of droplets corroded in fluctuating ambient conditions. No correlation is present.